Effect of deposition conditions and doping on the structure, optical properties and photocatalytic activity of d.c. magnetron sputtered TiO_2 thin films

Karin Eufinger

Proefschrift voorgelegd tot het behalen van de graad van
Doctor in de Wetenschappen: Natuurkunde

Promotor: Prof. Dr. D. Poelman
Copromotor: Prof. Dr. ir. R. De Gryse

Maart 2007

To my two Grandmothers,
who if times had been different both would have been a medical doctor

To Guy, Johanna and Frank

Acknowledgements

First of all I would like to thank my advisors Dirk Poelman and Roger De Gryse for giving me the opportunity to conduct this research and write this thesis as well as the fruitful discussions in understanding the obtained results.

This thesis would not have been what it is now without the assistance and support of others, especially since the results were obtained in the frame work of two different projects. The first was a Concerted Research Action (GOA) financed by the Ghent University on the elimination of volatile organic compounds. The second was an exchange program of the Flemish government (AWI) between the Ghent University and the ITME in Poland on the development of photocatalytically active TiO_2 thin films.

I would also like to thank the other people involved in these two research projects, most of all Hilde Poelman at our department, Maria Olea, Veerle Balcaen, Philippe Heynderickx and Guy Marin at the Laboratorium voor Petrochemie for their support throughout the project. I would also like to thank Monica Dan, whom I could ask for advice on the OmniStar. I also have to thank two people from ITME, Poland, namely Jaček Jagielsky for performing the ion implantation and especially Henryk Tomaszewski for making the mixed oxide targets, performing most of the sputtering experiments with these targets as well as most of the photocatalytic measurements of the doped films. He also prepared the TiO_2 films for ion implantation.

Further I would like to thank everyone who helped along with my project, lending their assistance where my own capabilities came short.

I am indebted to Alex Colpaert, who managed to transfer my ideas on how the photocatalysis chamber had to look like and function into a workable set up. Without his technical assistance it would not have been possible to have such a reliable reactor for photocatalytic testing. And, of course, I need to thank Gilbert Notebaert for machining the necessary parts.

Special thanks also go to Philippe Smet for getting me started on the optical transmission measurements. He also performed the luminescence and lamp emission measurements, and helped to interpret the data.

I would also like to thank Els Janssen who performed some of the initial studies for photocatalytic thin film deposition during her thesis (Licentiaat).

Further I would like to thank Diederik Depla for the many discussions concerning (reactive) sputtering and thin film deposition and Stijn Mahieu and Pieter Gekiere for understanding thin film growth and crystallization.

I am also thankful for Ulric Demeter who performed the ESCA measurements. Many thanks also to Olivier Janssens for performing the SEM and XRD measurements and the many discussions we had on how to interpret the data received.

I would like to thank my good friend and fellow chemistry student Anke Blume ,who now works for the Degussa AG, Germany, for arranging to have a sample of Degussa P25 TiO_2 powder sent to me.

I also would like to thank all other colleagues at the S1, including those who have come and gone over the years, for the nice working atmosphere. And whom I may not forget is Nadine, who always knew how to deal with administrative tasks.

Finally I would like to thank my family, who even on long distance have always been supportive. Especially I need to thank my husband Guy who has supported me throughout my work on this thesis, and my children Johanna and Frank, who especially over the last year had to live with a very busy and absent minded mom.

Karin Eufinger,
Gent, January 2007

Table of contents

List of acronyms

ASTM:	American Society for Testing and Materials
ESCA (XPS)	Electron Spectroscopy for Chemical Analysis (X-ray Photoelectron Spectroscopy)
DOS	Density Of States
EDX (EDS)	Energy Dispersive X-ray analysis (Energy Dispersive x-ray Spectroscopy)
EPMA	Electron Probe Micro Analysis
ESR	Electron Spin Resonance
(E)XAFS	(Extended) X-ray Absorption Fine Structure
FWHM	Full Width at Half Maximum
GC	Gas Chromatograph(y)
GSC	Gas Specific Calibration
HPLC	High Performance Liquid Chromatograph(y)
IR	Infra Red
IUPAC	International Union of Pure and Applied Chemistry
MCD	Multiple Concentration Detection
MID	Multiple Ion Detection
MS	Mass Spectrometry/ Spectrometer
NHE	Normal Hydrogen Electrode
NIST	National Institute of Standards and Technology (U.S.A)
(PE-)CVD	(Plasma Enhanced-) Chemical Vapor Deposition
PVD	Physical Vapor Deposition
QSE	Quantum Size Effect
RBS	Rutherford Back Scattering
SEM	Scanning Electron Microscopy
SIMS	Secondary Ion Mass Spectroscopy
TEM	Transmission Electron Microscopy
UV	Ultra Violet
VIS	Visible
VOC	Volatile Organic Compound
XAS	X-ray Absorption Spectroscopy
XRD	X-ray Diffraction

1 Introduction

The importance of TiO_2 as a photocatalytic material was discovered by Fujishima and Honda in 1972, who observed the photocatalytic splitting of water on TiO_2 electrodes [Fujishima72]. In the photocatalytic process the TiO_2 is activated by illumination with (UV) light having an energy higher than the band gap (E_g = 3.2 eV for anatase, 3.0 eV for rutile), e.g. [Schiavello97]. The photocatalytic breakdown reaction proceeds via intermediate steps ending in the mineralization of the organic to water, CO_2 and mineral acids. The initial step is the electron-hole pair formation, followed by their separation. The electrons can be used for reduction, the holes for oxidation processes, e.g. [Schiavello97]. The lifetimes of the electron and the hole have an influence on how well they can be utilized for the subsequent redox-reaction. Structural imperfections in the TiO_2 lattice generate trap sites and recombination centers, leading to a decrease of the electron and hole concentration, e.g. [Anpo03, Carp04, Fernández-García04]. In 1995 it was discovered that TiO_2 shows a photoactivated superhydrophilic effect, when illuminated with UV light its contact angle with water approaches zero [Fujishima00, Carp04]. This behavior is often taken identical to photocatalytic activity, in reality the two are related but may not be confused.

In recent years, applications to environmental clean up have been one of the most active areas in heterogeneous photocatalysis, e.g. [Linsebigler95, Mills97, Fujishima00, Carp04, Fernández-García04]. Here one looks at the photo-degradation of hydrocarbons either in water or in air using suspended small particles or thin films of TiO_2. There are several advantages of this material over other photocatalytically active semiconductors: TiO_2 is low cost, chemically inert, highly photoactive, as well as self-regenerating and can easily be recycled. Additionally, the redox potential of the H_2O/ *OH couple (-2.8 eV) lies within its band gap energy, e.g. [Schiavello97].

TiO_2 has several naturally occurring modifications, the most common ones being anatase, brookite and rutile. Most research with respect to photocatalysis is performed using anatase, e.g. [Linsebigler95, Mills97, Fujishima00, Carp04, Fernández-García04], while in all other areas rutile has been much more thoroughly characterized (e.g. electronic behavior, bulk structural investigations). This is mostly due to preparation methods. While it is easier to obtain anatase than rutile in fine powder form at low temperatures around 773-873 K (400-500°C), it is impossible to obtain anything but rutile using standard ceramic processing which requires temperatures of up to 2000 K (ca. 1700°C). This lies well above the transition

temperature (1073 K/ 800°C) to the thermodynamically most stable phase, namely rutile. Very little is known about the brookite phase as it has been studied little up to now [Carp04].

The highly active Degussa P25 powder has become standard for comparing the photocatalytic activity of TiO_2 powders. It is fine grained (<100 nm), containing a mixture of anatase, rutile and amorphous TiO_2, with an anatase to rutile ratio of about 75%:25%, e.g. [Carp04, Demeestere03, Okimura01, Ohno03].

While materials obtained at low temperatures are fine grained (nano-crystalline), because little grain growth can occur, the grain growth at temperatures above 1073 K (800°C) can be substantial. As a result the nature of the surface and its size are usually very different for anatase and rutile powders. Since for a catalyst its active surface area is important, it is difficult to compare the activity of different materials if they do not have the same surface area.

Generating a large surface area for a TiO_2 powder or thin films means reducing the grain size. Most photocatalytic materials are nanocrystalline, i.e. have a grain or crystallite size below 100 nm. When the grain size decreases below about 10 nm, grain boundaries, which present a defective lattice, start to dominate the material. Defects in the lattice structure are detrimental to the photocatalytic activity as they act as trap sites for the photogenerated charge carriers, increasing their chance of recombination. This is why the highly defective amorphous state is expected to show no significant or a very low photocatalytic activity, e.g. [Carp04, Fernández-García04, Karches02, Linsebigler95]. In general, amorphous TiO_2 has been studied little.

One major problem, especially for indoor applications, is that TiO_2 absorbs only near-UV light: the band gap energies of anatase and rutile correspond to the wavelengths of 387 and 413 nm, respectively, so that only 4-10% of solar radiation can be utilized. Efforts have therefore been made to introduce dopant materials into TiO_2 to shift its band gap to lower energies. It has been tried to predict the efficiency of a dopant by performing band gap calculations, e.g. [Asahi01]. Unfortunately the electronic changes induced by the dopant are not straightforward: defect states can be generated in the band gap, which can degenerate to a narrowing of the band gap. Another difficulty is that TiO_2 is a partially ionic material for which the band theory is not strictly applicable. Also it is not clear which dopant levels are beneficial for improving the photocatalytic activity of TiO_2: usually dopant concentrations are on the order of %, not in the ppb range or lower as normally used in the semiconductor industry. Such high concentrations of additives will not only generate electronic but also structural changes, pos-

sibly also segregate to form second phases. Since these will also influence the photocatalytic activity it becomes more difficult to interpret the effect of the dopant.

Even though many studies exist on how the processing conditions influence the photocatalytic activity of TiO_2 little systematic studies exist where it is tried to relate the photocatalytic activity of a given thin film to its structural and optical properties. This was the major goal of this thesis. The thin film deposition technique chosen was d.c. magnetron sputtering from substoichiometric TiO_{2-x} ceramic targets. This technique allows to control the thin film structure by varying the deposition parameters. Using TiO_{2-x} targets allowed for sputtering in pure Ar to obtain stoichiometric TiO_2 thin films. The varied deposition parameters were the applied d.c. power and the Ar-pressure during deposition. The as deposited thin films were XRD amorphous and could be crystallized by heating to temperatures above 573 to 673 K, depending on the deposition parameters.

A second goal was to investigate the effect of additives on the structural development, and on the optical and photocatalytic properties of TiO_2 thin films. These films were obtained by deposition from M_2O_3/ TiO_{2-x} mixed oxide targets (M = Fe, Nd, V) and by ion implantation (Fe, Nd) into as deposited TiO_2 thin films. The deposition parameters that resulted in the best photocatalytic activity for pure TiO_2 thin films were chosen for investigating the effect of dopant concentration. This concentration varied for the mixed oxide targets between 1 and 10 at%. For ion implantation it was aimed at introducing the dopants into the top 40 nm of the thin film in concentrations between 0.5 and 2 at%.

The third goal of this thesis was to develop a reliable reactor and procedure for testing the photocatalytic activity of the (doped) TiO_2 thin films. Although a variety of methods exists for testing the photocatalytic activity of TiO_2, it was opted to use a specialized reactor. This allowed to perform the testing under controlled conditions (humidity, reaction temperature, etc.). Therefore, this part of the thesis included designing and constructing the reactor as well as choosing the analysis technique to be used for monitoring the photocatalytic breakdown reaction.

In the following chapters first the theoretical background for understanding the photocatalytic activity of (doped) TiO_2 will be given (chapter 2). Then the experimental techniques and procedures used are described (chapter 3). In the final chapter 4 the experimental results are presented and discussed. This chapter is subdivided into four main sections, which discuss the development of the photocatalytic test reactor (4.1), the thin film deposition (4.2), the study of the TiO_2 thin films (4.3) and the effect of doping (4.4).

2 Theoretical background

In this chapter the theoretical backgrounds relevant to this thesis will be introduced. First the material TiO_2 will be introduced (section 2.1). Then the optical properties of transparent semiconductor thin films in general, and TiO_2 in specific, will be discussed together with methods for measuring them (section 2.2). In section 2.3 the photoactivation of TiO_2 is described, including a short introduction to relevant photoinduced processes for light activated TiO_2, namely photovoltaic and photo-induced superhydrophilic activity. The process of photocatalysis with TiO_2 will be elaborated on in section 2.4, followed by the discussion of the effect of the catalyst structure on its photocatalytic activity (section 2.5). The effect of dopant addition to the structure, optical properties and photocatalytic activity of TiO_2 is the topic of section 2.6. In section 2.7 methods for measuring the photocatalytic activity of TiO_2 will be introduced, including reactor design and interpretation of kinetic data of photocatalytic breakdown reactions. In the end two sections are devoted to thin film preparation: First thin films deposition by d.c. magnetron sputtering is discussed (section 2.8), followed by a brief description of ion implantation as a technique for introducing dopants into TiO_2 thin films (section 2.9).

2.1 General aspects of TiO_2

In this section the abundance (section 2.1.1), modifications (section 2.1.2), chemical activity (section 2.1.3) and applications (section 2.1.4) of TiO_2 will be discussed briefly to familiarize the reader with the general properties of TiO_2.

2.1.1 Abundance

The short overview given in this section is based on a more detailed one given in [Carp04]. Titanium is one of the more abundant metals on earth (exceeded only by aluminum, iron and magnesium); it constitutes about 0.63% of the earths crust. Titanium is only found bound to other elements, occurring primarily in minerals like rutile, ilmenite ($FeTiO_3$), leucoxene, sphene or tianite ($CaTiSiO_5$), anatase, brookite, perovskite ($CaTiO_3$) and other titanates, and it is found in iron ore. The most important mineral titanium sources are rutile (containing 93 - 96% TiO_2), ilmenite (44 - 70% TiO_2) and leucoxene (< 90% TiO_2).

To produce pure TiO_2, two methods exist, the sulfate and the chlorine process. In the sulfate process ilmenite is dissolved with sulfuric acid to iron and titanium sulfates. From this

solution titanium hydroxide is precipitated and calcined to the oxide at 900°C (1173 K). This process yields only anatase unless rutile seed crystals are used. The purity of the TiO_2 is also rather poor. For the chloride process crude TiO_2 is first separated from the ores which is then reacted with chlorine to produce $TiCl_4$. This is purified and then re-oxidized, yielding highly pure TiO_2, while recycling the chlorine gas.

2.1.2 Titania modifications

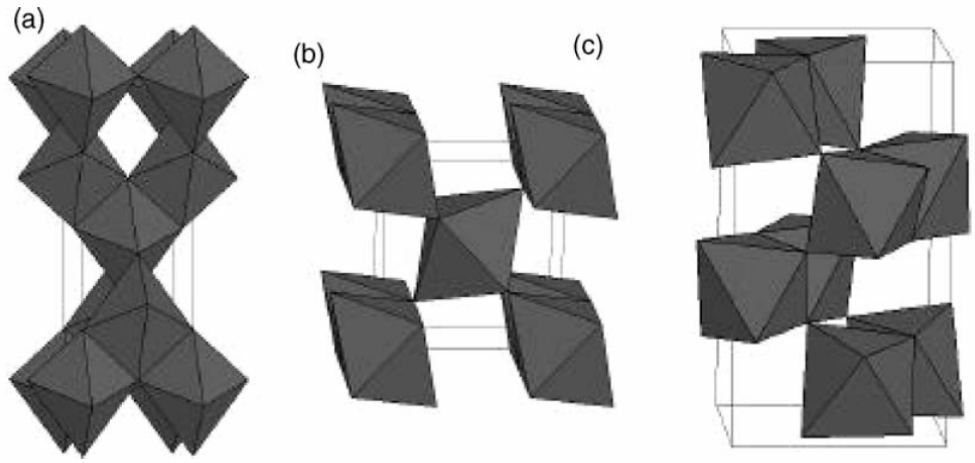

Figure 2. 1:
Crystal structures of the most common TiO_2 modifications found in nature: a) anatase, b) rutile, c) brookite.

Four polymorphs of TiO_2 are found in nature, namely anatase (tetragonal), rutile (tetragonal), brookite (orthorhombic) and TiO_2 (B) (monoclinic). The first three are the most abundant and, therefore, most studied modifications. Their crystal structures are shown in Figure 2. 1.

Two high pressure forms have been synthesized starting from rutile, namely TiO_2 (II) (PbO_2 structure) and TiO_2 (H) (hollandite structure $[Ba(Mn^{4+}Mn^{2+})_8O_{16}]$). These modifications are not relevant in the context of this thesis and will not be discussed any further.

Rutile is usually stated to be the thermodynamically most stable form of TiO_2 at all temperatures and pressures up to 60 kbar (6 GPa). There are only small differences in Gibbs free energy between anatase, brookite and rutile (4-20 kJ/mol) meaning that the metastable polymorphs are almost as stable as rutile at normal pressures and temperatures. While there is no discussion about the bulk materials, there is a controversy in literature to which polymorph is the most stable one when the grain size of the material is (very) small [Carp04, Fernández-García04, Zhu05]. Experiments have shown that the relative phase stability may reverse when

particle sizes decrease to sufficiently low values due to surface energy effects. For decreasing size the surface area of the particles increases, which affects surface free energy and surface stress. When comparing TiO_2 modifications at the same grain size it is found that for the smallest grain sizes (below 11 nm according to [Carp04] or below 15 nm according to [Fernández-García04]) anatase is the most stable phase. There is no discussion that above 35 nm rutile is the most stable phase (i.e. bulk properties are reached with respect to phase stability). For intermediate grain sizes, between 11 (15) and 35 nm, there is discussion whether brookite is the most stable phase [Carp04], or whether both rutile and brookite are stable due to their very close free energy values [Fernández-García04].

In [Fernández-García04] the phase stability in nanomaterials is linked to the undercoordinated Ti positions at the surface which affect the surface energy. It is argued that a 4-fold coordination leads to a higher surface energy than a 5-fold coordination. In XAS (x-ray absorption spectroscopy) studies only 5-fold coordination was found in nano-materials. Literature studies showed that, although nanostructured anatase, brookite and rutile had been prepared, a single phase for particle sizes in the 2-15 nm range is only possible for anatase. It was found that rutile was mostly prepared with the help of mineralizers or in presence of Cl^-, but that the minimum particle size was limited to 10-20 nm. Brookite samples were usually obtained with larger particle size and often not in their pure crystalline form.

The most studied phase transition is the one between anatase and rutile. The transition enthalpy is low (-1.3 to -6.0 ±0.8 kJ/mol), so that at room temperature anatase is kinetically stable. But at temperatures above 600°C (873 K) bulk anatase shows a measurable transformation speed which accelerates towards 800°C (1073 K), above which the rutile phase is stable. The transformation temperature is influenced by the concentration of lattice and surface defects (including impurities/dopants), by the particle size and by applying high pressures. Usually small particles show stronger grain growth due to the higher inner grain pressure, which promotes the transformation to rutile. If grain growth is inhibited, e.g. by a SiO_2 intra-grain matrix, small particles will show a higher transformation temperature [Carp04, Fernández-García04]. Also secondary particle size (e.g. agglomerates) and the presence of a poorly crystalline or amorphous phase play a role [Fernández-García04].

Overall rutile is the best characterized modification, especially in bulk form. It is the only phase where large single crystals can be easily obtained. Anatase is less well investigated, while little is known about brookite. Since there is a growing interest in anatase due to its higher catalytic activity (see chapter 1), more of its properties, especially in nano-structural

form are being known. There is also growing interest in brookite since it also seems to have promising catalytic properties [Kominami03, Zallen06].

2.1.3 Chemical activity

TiO_2 is a rather inert oxide, which is harmless in the human body and digestive system [Carp04, Mills97]. New studies are questioning this assurance though, since it is becoming more and more evident that nanostructured materials behave different from their bulk forms in this respect. A recent study on mouse cells investigating the effect of nanosized TiO_2, which is typically used in sunscreen, showed that the nanoparticles can alter the cell material of the brain [Ball06a]. It is expected that nanomaterials can travel freely in the human or animal body. It is known that the chemical activity of nanosized structures differs from their bulk behavior, but the area of nanoscience is still rather new so that the extent of their differences is not completely known yet.

As mentioned above TiO_2 is used for applications in thermally and photo-activated catalysis, where it shows a good stability against poisoning for many reactions [Mills97, Carp04]. Especially towards photocatalysis it is important to note that it is not degraded under illumination, i.e. the photocatalytic activation is reversible. Care must only be taken when using the metastable forms of anatase or brookite: they should not be used above the transition temperature to rutile (see section 2.1.2).

2.1.4 Applications of TiO_2

About 98% of the worlds production is used for making white pigments, only the remaining approx. 2% is used to make Ti-metal, welding rod coatings, fluxes and other products [Carp04].

TiO_2 has received special attention due to its chemical stability, non-toxicity, low cost and other properties like its high refractive index, high dielectric constant, superior catalytic properties. Table 2. 1 summarizes the properties of TiO_2 and the resulting applications (taken from [Carp04]).

Property	**Material type**	**Crystal phase**	**application**
Dielectric constant	1) bulk 2) thin film	rutile amorphous	Capacitors
Biocompatibility	thick/thin film	rutile	Bone substituent, reinforcing mechanical supports
Refractive index: High reflectivity	1) powder 2) thin film	mostly rutile rutile	White pigment (paint, cosmetics) optical interference coatings
Dependence of electrical conductivity on concentration of surface species	thin film	rutile, other	Gas sensing
Chemical activity (1)	powder, granulate, thin film	anatase, rutile	Thermally activated catalyst
Chemical activity (2)	powder, thin film	anatase, rutile, (brookite)	Photo-activated catalyst (at room temperature)
Superhydrophilicity, amphiphilicity (sec. 2.3.2.2)	thin film	anatase, rutile,	Self-cleaning, anti-fogging

Table 2. 1: Applications of TiO_2.

2.2 Optical properties of TiO_2

The optical transmission spectrum of TiO_2 is characterized by a strong absorption edge between 380 and 420 nm due to the band gap at 3.2 and 3.0 eV for anatase and rutile, respectively [Carp04, Fujishima00, Mills97]. While the optical properties of rutile have been thoroughly investigated and are easily found back in literature, there is only a limited amount of information available on anatase. For rutile the optical transmission remains high for higher wavelengths before it decreases at 4 µm [www1].

2.2.1 Optical transmission measurements

A characteristic feature of the optical transmission spectrum of thin films is the presence of interference fringes. Due to multiple partial reflection of the transmitted beam at the film/ substrate and film/ air interface interference of the transmitted and the reflected beams occurs. Analysis of the height and the spacing of these fringes allows to determine the refractive index and the thickness of the analyzed film. Since a lower film thickness reduces the number of fringes formed, a minimum film thickness is usually required for this analysis. On the other hand, if the film is too thick (i.e. several tens of µm), the fringes will become too densely spaced, so that from a certain thickness on the fringe-free transmission spectrum of the bulk material results. This thickness depends on the flatness of the sample (surface) and the resolution used for the measurement. The calculation of the refractive index will be discussed in section 2.2.2.

The band gap of a material is reflected as a decrease in transmission to zero, caused by the absorption edge. The calculation of the optical absorption from transmission measurements will be discussed in section 2.2.3. The band gap and how it is calculated from the optical absorption is then discussed in section 2.2.4.

2.2.2 Refractive index

2.2.2.1 The refractive index of TiO_2

Both rutile and anatase have a high refractive index, which increases strongly towards the absorption edge in the near UV. For rutile the refractive index remains rather stable at higher wavelengths until it decreases significantly above 3 µm [www1, www2]. Both materials are also birefringent, meaning that for the single crystal two refractive indexes are measured, one ordinary and one extraordinary, n_o and n_e, respectively. For a polycrystalline thin film one

will measure an averaged refractive index, though. Since the refractive index is dependent on the wavelength of the incoming light, it is important to report the conditions under which the measurement was performed. For rutile single crystal values of $n_o = 2.65$ and $n_e = 2.9$ at 549 nm [www1] and for anatase values of $n_o = 2.49$ and $n_e = 2.56$ at 589 nm are reported. In [Schiller80] the refractive indices for magnetron sputtered anatase and rutile thin films are reported in the wavelength range from 400-1000 nm. From these data values of 2.34 (anatase) and 2.73 (rutile), both at 550 nm, could be extracted. The value for anatase seems rather low when comparing to the single crystal values. One reason could be a lower density in the film (section 2.2.2.3).

2.2.2.2 Measurement of the refractive index:

As already discussed above, the refractive index can be extracted from the transmission measurements of thin films due to the occurrence of interference fringes. There exist different methods which are discussed in more detail in [Poelman03]. Two of these methods, namely the envelope method (also named after Swanepoel) and the Lorentz classical oscillator method, were suggested to be the most useful for non-ideal thin films and shall be discussed here. Further details can be found in [Poelman03]. Both methods allow to determine the refractive index *n* and extinction coefficient *K* using a single transmission measurement.

a. Envelope method (Swanepoel)

The envelope method was introduced by Manifacier et al [Manifacier76] and further developed by Swanepoel [Swanepoel83]. Here envelopes around the maxima, T_M, and minima, T_m, of the transmission spectrum are constructed, which are then considered as continuous spectra vs. the wavelength, namely $T_M(\lambda)$ and $T_m(\lambda)$, respectively. The parameters *n* and *K* can then be calculated from $T_M(\lambda)$ and $T_m(\lambda)$ at each wavelength.

b. Lorentz classical oscillator model:

In the classical oscillator model *n* and *K* can be described by the following two equations:

$$n^2 - K^2 = \varepsilon_\infty + \frac{A\lambda^2}{\lambda^2 - \lambda_0^2 + g\lambda^2/(\lambda^2 - \lambda_0^2)} \qquad (2.1)$$

and

$$2nk = \frac{A\sqrt{g}\lambda^3}{(\lambda^2 - \lambda_0^2)^2 + g\lambda^2} \qquad (2.2)$$

with λ_0 the oscillator central wavelength, A the oscillator strength and g the damping factor. In equation (2.2) the expression on the right hand side represents the dielectric function at infinite energy (zero wavelength). The easiest way to solve the two equations for n and K is numerical.

2.2.2.3 Effect of additives on the refractive index:

The refractive index is a material constant. To calculate the refractive index for mixed compounds using the indices of the individual components, several expressions have been developed. A frequently used one is the Lorenz-Lorentz equation [www3]:

$$\frac{n^2-1}{n^2+2}\ \frac{M}{\rho}=\sum_{i=1}^{m}\left(\frac{n_i^2-1}{n_i^2+2}\ \frac{f_i M_i}{\rho_i}\right) \qquad \text{with } \sum_{i=1}^{m} f_i = 1 \tag{2.3}$$

where n is the refractive index of a composite material of average molecular weight M and density ρ. This composite material can be viewed as consisting of m materials, each having the mole fraction f_i, the molecular weight M_i and the density ρ_i.

A porous material can be seen as a special case of a composite material: one can model it as a mixture of a given material with air. Since the refractive index of air can be approximated as equal to 1, equation (2.3) reduces to:

$$1-\frac{P}{100}=\frac{n^2-1}{n_i-1}\ \frac{n_i^2+2}{n^2+2} \tag{2.4}$$

with P denoting the porosity in %, defined as

$$P=1-\left(\frac{M_i}{\rho_i}\ \frac{\rho}{M}\right) \tag{2.5}$$

Expression (2.5) allows the calculation of the film porosity from the refractive index if there are no other influences like second phases or dopants. Nevertheless, any calculation of the porosity should also be taken as an estimate only.

2.2.3 Optical absorption

From the optical transmission measurement the optical absorption can be calculated according to equation (2.6), but only in the absence of interference fringes:

$$T=\frac{(1-R)^2 e^{-\alpha(\lambda)d}}{1-R^2 e^{-2\alpha(\lambda)d}} \tag{2.6}$$

with T the corrected transmission of the thin film (see equation (2.8)), R the reflectance, d the film thickness and $\alpha(\lambda)$ the absorption coefficient at wavelength λ [Pankove71].

If the product $\alpha(\lambda)d$ is large (which is the case for the absorption at wavelengths close to the absorption edge) equation (2.6) reduces to:

$$T \approx (1-R)^2 e^{-\alpha(\lambda)d} \tag{2.6a}$$

and the reflectance R can be approximated by:

$$R \approx 2\left(\frac{n-1}{n+1}\right)^2 \tag{2.7}$$

The corrected transmission of a thin film coated onto a glass substrate must first be calculated from the measured transmission T_m (which includes the transmission of the glass, T_g).

$$T = \frac{T_m}{T_g} \tag{2.8}$$

Transforming equation (2.6)a allows to calculate the optical absorption from transmission measurements close to the optical absorption edge when no interference fringes are present in the chosen wavelength range:

$$\alpha(\lambda) = -\frac{1}{d}\ln\frac{T}{(1-R)^2} \tag{2.6b}$$

2.2.4 Band gap

The electronic band gap of a semiconductor is the energy spacing between its valence and its conduction band. In a pure metal no such spacing exists and the electrons can move freely in the material. In semiconductors the electrons from the valence band need a certain activation energy, the energy equivalent to the band gap, to be promoted to the conduction band. A material is defined as an insulator if the band gap is sufficiently high so that, for all practical uses, electron transition between the valence and the conduction band is impossible.

For low band gap semiconductors thermal energy can be sufficient to activate conduction. In all semiconductors the band gap transition can be facilitated with light, i.e. these materials are photo-activated. Here the illumination with light having an energy higher than the band gap generates an electron/ hole pair. This process will be discussed further in this section. The fate of the electron/ hole pair will be discussed in more detail in section 2.3.1.

2.2.4.1 Optical resonance phenomena

When the optical absorption of a material is measured one observes so-called absorption edges. These are caused by electronic resonance phenomena in the material [Pankove71]**.** The resonance absorption results in a discontinuity in the refractive index *n* and a maximum in the extinction coefficient *K*. One can distinguish between two types of resonance phenomena:

a. Atomic (ionic) polarization, lattice vibrations:

These result in a small displacement of the ionic sub-lattices against each other. They occur in a frequency range of 10^{11}-10^{14} Hz (λ = 3 mm – 3 μm), i.e. microwave to IR. One of the characteristics is that the refractive index *n* remains > 1 for frequencies lower and higher than the resonance frequency.

b. Electronic polarization:

This is characterized by a displacement of the electron cloud with respect to the atomic nucleus/ nuclei of an atom/ molecule. The observed frequency range lies around 10^{15}-10^{16} Hz (λ = 300 – 30 nm), which lies in the UV part of the spectrum. One of the characteristics is that at the resonance frequency the refractive index changes from > 1 to < 1 when increasing the frequency of the incident light.

Visible light (λ = 380 to 780 nm, ν = 7.89 to 3.85x10^{14} Hz) falls between the two categories. This is why most insulators are transparent in the visible light range.

One can use the classical oscillator theory to describe the changes of the refractive index n for both ionic as well as electronic polarization (see section 2.2.1.1).

2.2.4.2 Resonance absorption in TiO_2

As already mentioned, light absorption causes the transition of an electron across the band gap, which results in the generation of an electron/ hole pair [Fujishima00, Serpone99].

$$TiO_2 \xrightarrow{h\nu} TiO_2\,(e^-/h^+) \rightarrow e^-_{cb} + h^+_{vb} \qquad (2.9)$$

with ***cb*** denoting the conduction band and ***vb*** the valence band. This equation can also be written as:

$$Ti_{Ti} + O_O \xrightarrow{h\nu} (Ti_{Ti}e^-) + (O_O h^+) \qquad (2.10)$$

Therefore, the just formed electron/ hole pair is a state where the electron cloud is distributed in such a way as to that there is a nominally negative charge on the Ti and a nominally positive charge on the O.

Looking back at the definitions for resonance phenomena under the illumination with light the formation of the electron/ hole pair originates from the displacement of the electron cloud around a Ti-O bond. Therefore, it can be classified as an electronic polarization resonance phenomenon.

The polarizability of a bond can be understood when looking at its nature. A purely ionic bond results in the complete separation into two ions. The electron cloud is completely localized around the anion, so that polarization of the bond is not possible. In contrast, for a purely covalent bond a completely delocalized electron cloud is present between the two atoms. This type of bond can be polarized by displacing the electron cloud. In general, the ionic character of a bond increases with the difference in electronegativity between the two atoms involved. Transition metal oxides in their higher oxidation states, like TiO_2, are characterized by having partially covalent bonds between the metal and the oxygen. These bonds can be polarized by re-distribution of the electron cloud. When discussing the band theory of semiconductors one assumption is the complete covalent nature of the bonds. This does not apply for ionic crystals where the nature of the bonds is only partially covalent. Therefore one has to take care with applying the band theory to (partially) ionic crystals like TiO_2 [Schiavello97].

2.2.4.3 Effect of lattice defects

Lattice defects can be introduced in the form of dislocations, grain boundaries, vacancies or foreign atoms. They will cause a disturbance in the oxygen and/ or titanium sub-lattices, depending on their size, charge and position. Next to causing lattice strain, the charge of the lattice site can be changed. Some of these lattice defects can have a variable charge (e.g. vacancies and transition metal ions) and, therefore, can act as trap sites for charge carriers. An example are oxygen vacancies, which present a double positively charged lattice site. They can act as an electron trap site, changing their charge to single positive.

Defects can create new states inside the band gap. If these defect states are close to the band edges, they allow the electrons to go either from the Ti valence band to the new electronic state just below the conduction band (donor levels), or to go from a new electronic state just above the valence band (acceptor levels) to the conduction band. In both cases the energy

needed to promote an electron to the conduction band is reduced. The states inside the band gap created by defects will be discussed in more detail in section 2.5.

Another important issue is the crystallite and grain size of the material. With decreasing particle size the influence of the particle surface becomes more important, which also means that the number of lattice defects increases. The small (confined) size of the particle also leads to the breaking up of the continuum of the electronic levels in the conduction as well as the valence band into discrete energy levels. Such structures will also be discussed in more detail in section 2.5.

2.2.4.4 Band gap transition modes

As already discussed, the band gap of a semiconductor results in the resonance absorption of light having a wavelength λ_{bg} which corresponds to at least E_{bg}. There are two main types of band gap transition in semiconductors [Pankove71]. These will be first described briefly before discussing the band gap of TiO_2, and whether the nature of the band gap transition depends on its crystal structure.

(i) Direct band gap transition:

Here the electronic transition from the valence to the conduction band is electrically dipole allowed. In some materials direct transitions are forbidden for the wave vector $\underline{k}$ having the value 0, but are allowed for values of $\underline{k} \neq 0$. Here one speaks about a '*direct forbidden*' as compared to a '*direct allowed*' transition.

(ii) Indirect band gap transition:

Here the electronic transition from valence to conduction band is electrically dipole forbidden and the transition is phonon assisted, i.e. both energy and momentum of the electron-hole pair created are changed in the transition. Therefore, absorption and emission of light are weaker compared to those of direct band gap semiconductors, since they involve a change in momentum. Again, one distinguishes between allowed and forbidden transitions.

2.2.4.5 Calculation of the band gap from the optical absorption:

The dependence of the band gap energy on the optical transmission is given by equation (2.11) [Miao02]:

$$B\left(h\nu - E_{bg}\right)^{m} = \left(4 \cdot \pi \cdot K / \lambda\right)\, h\nu \qquad (2.11)$$

with B a constant, m a value representing the optical transmission mode and $h\nu$ the photon energy (in eV). The term $(4\pi K/\lambda)$ is identical to the absorption coefficient $\alpha(\lambda)$, where K is the imaginary part of the refractive index, and λ is the wavelength of the incoming light. Strictly speaking this formula is only valid for direct transitions. For indirect transitions a second energy term (the phonon energy) must be introduced into the left hand side of equation (2.11) [Pankove71]. Since the phonon energy is small (of the order of 20 meV), it is usually neglected when fitting the absorption spectra. The constant m depends on the optical transition mode having the values as listed in Table 2. 2.

m	**Transition mode**
1/2	direct allowed
3/2	direct forbidden
2	indirect allowed
3	indirect forbidden

Table 2. 2: Values of the exponent *m* from equation (2.11) for different band gap transition modes.

Equation (2.11) can be transformed to:

$$B^{1/m} \cdot h\upsilon - B^{1/m} E_{bg} = (\alpha \cdot h\upsilon)^{1/m} \qquad (2.12)$$

By plotting the right side of equation (2.12) against the light energy $(h\nu)$ one should receive a straight line for the correct choice of m. The band gap energy E_{bg} can be calculated by dividing the y-axis intercept of this line by its slope. Care must be taken to eliminate edge effects which are caused by a high noise level at high absorptions (low transmission) and the presence of interference fringes at wavelengths above/ at the absorption edge (high transmission).

A second source of errors comes from the influence of defects on the absorption coefficient. If the rate of increase of the absorption coefficient at the absorption edge is changed the calculated value for the band gap will be changed, too. For thin films one will never observe the sharp decrease of α at the absorption edge as seen in bulk materials. The reason is the limited thickness of the film.

2.2.4.6 Band gap transition in TiO_2

There is some discussion on the nature of the band gap transition in anatase thin films. Little information exists on the nature of the band gap transition for single crystal anatase. Band gap calculations of G. Cangiani [Cangiani03] have shown that for rutile the minimal band gap

is direct having a (calculated) energy of 1.86 eV, and that a relevant indirect band gap has an only slightly higher (calculated) energy of 1.89 eV. Calculations reported in [Daude77] yield the same conclusion; in [Mathieu1978] experimental values of 3.034 eV and 3.049 eV (latter at 1.6 K) are reported for the direct forbidden and indirect allowed band gap transition in rutile. Due to the nature of the band gap calculations absolute values for band gap energies cannot be obtained but the relative differences in band gap energies between different transitions are claimed to be real.

For anatase a minimal band gap energy of 2.11 eV was calculated by G. Cangiani [Cangiani03], the nature of this transition being stated as definitely indirect. The closest direct gap was calculated to be at 2.57 eV. The indirect nature of the band gap in anatase is also stated in [Dumitriu00]. Experimental results of the band gap in single crystal anatase have yielded a value of 3.2 eV (section 2.2). No reports of experimentally determining the nature of the band gap transition in anatase could be found. Since the structural differences between anatase and rutile are very few, it is commonly assumed that the electronic properties of anatase and rutile are similar (see for example [Berger93, Carp04, Mills97]). That this is not completely true is shown by the differences obtained for band gap calculations. One has to be very careful, therefore, when comparing results reported in literature.

2.3 Photo-excitation of TiO_2

2.3.1 Mechanism of photo-excitation

2.3.1.1 Generating charge carriers

As already discussed in section 2.2.3 irradiation of the semiconductor TiO_2 with light having an energy larger than the band gap ($E \geq E_{bg}$) will generate an electron/ hole pair, according to equation (2.9), p 14. The electron and hole can recombine (anihilate) or dissociate into a conduction band electron and a valence band hole. The formation of the electron/ hole pair can, therefore, be interpreted as the breaking of one bond between Ti and O. When the electron/ hole pair dissociates the one electron will be located at the Ti^{4+}, forming a Ti^{3+}, while the other electron will be located at the O forming a radical state O^{-*}. This becomes more clear when rewriting equation (2.9), p. 14, in the Kröger-Vink notation (see section 2.6.2.1). Here $'$ denotes a negative and $^{\bullet}$ a positive charge on the respective lattice site. $\mathbf{V_x}$ is used to mark a vacancy on the lattice site X. The change in nominal oxidation state is also shown.

$$Ti_{Ti} + O_O \xrightarrow{h\nu} Ti'_{Ti} + O^{\bullet}_O = (Ti_{Ti}e^-) + (O_O h^+) \qquad (2.13)$$

with oxidation states: +4 -2 +3 -1

An electron associated with a Ti^{4+} therefore means that reduced Ti^{3+} is generated, accordingly the association of the hole with O^{2-} means the reduction to O^-. If two holes are associated with the O^{2-} this is equivalent to the formation of atomic O, so that actually reduction of the material under the loss of oxygen occurs:

$$Ti_{Ti} + 2\ O_O \xrightarrow{h\nu} Ti'_{Ti} + 1/2\ V^{\bullet\bullet}_O + 3/2\ O_O + 1/2\ O_2\ (g) \qquad (2.14)$$

The negative charge on the Ti (i.e. Ti^{3+}) represents a polaron state that can be conducted through the Ti-sublattice. The positive charge on the O (i.e. the bonded radical O^*) should be rather instable, so that oxygen vacancy formation will be an option, corresponding to a reduction of the TiO_2 to Ti_2O_3.

2.3.1.2 Reactions of the charge carriers

During their lifetime the separated charge carriers can recombine or migrate to the surface. Hereby they can become trapped (temporarily or quasi permanently) at bulk or surface

trap sites. In equations (2.15) to (2.18) below the possible reactions of the separated electron and hole are shown [Serpone99].

$$e^-_{cb} + h^+_{vb} \rightarrow e^-_{tr} + h^+_{tr} \quad \text{(lattice and/ or surface trapping)} \quad (2.15)$$

$$e^-_{cb} + h^+_{vb}\ (\text{and/ or } h^+_{tr}) \rightarrow \text{recombination} \quad (h\nu_1 \text{ and phonon emission}) \quad (2.16)$$

$$e^-_{cb}\ (\text{and/ or } e^-_{tr}) + h^+_{vb} \rightarrow \text{recombination} \quad (h\nu_2 \text{ and phonon emission}) \quad (2.17)$$

$$e^-_{tr} + h^+_{tr} \rightarrow \text{recombination} \quad (h\nu_3 \text{ and phonon emission}) \quad (2.18)$$

with ***cb*** denoting the conduction band, ***vb*** the valence band and ***tr*** a trap site. The indices on the light energy ($h\nu_x$) denote that light of a different wavelength is emitted for the different processes (equations (2.16) to (2.18)).

Trap sites can facilitate separation or recombination of the charge carriers, depending on whether they act only on one or on both carriers. If the trap sites are too deep, the chance of the carrier to leave the site becomes rather low, so that it is lost to the photocatalytic process [Fujishima00].

Literature is not so clear about the possible trap sites for electrons and holes. They can also differ between bulk and surface. Most authors agree that Ti^{4+} is a trap site for electrons, forming the polaron state Ti^{3+}. Also mentioned are oxygen vacancies. Some sources list these as trap sites for holes, though they are also known to attract electrons [Serpone99]. In general, defect sites act as trap sites and also as recombination centers for charge carriers.

In [Colbeau-Justin03] the charge carrier lifetimes in TiO_2 powders were determined by transient photoconductivity measurements. Here a rather slow decay of the transient photocurrent was observed for anatase which was attributed to hole trapping at the surface of the powder which resulted in a reduced electron/hole recombination rate.

Electrons trapped at the surface are scavenged by adsorbed oxygen, which inhibits the formation of Ti^{3+} sites [Linsebigler95]. This re-oxidation closes the catalytic cycle which started with reducing Ti^{4+} by illumination with UV light. Concerning the trapped holes it is not clear which species at the surface are exactly associated with them. Postulated are, among others, O^-, O_3^-, and $^*OH$ radicals [Carp04, Fujishima00, Linsebigler95], which will then further react with the organic substances present at the surface: the organic is oxidized, and the radical is reduced, closing the other part of the catalytic cycle. These two processes will be discussed in more detail in section 2.4.2. Surface hydroxyl groups are present on the TiO_2

surface due to saturation of the terminating O with water molecules from the ambient air. ozone radicals (O_3^-) can be formed from chemisorbed O_2.

2.3.2 Photoinduced processes for light activated TiO_2

There are three different photoinduced processes possible for light activated TiO_2, namely photovoltaic effect, photoinduced superhydrophilicity and photocatalysis. The first process is used for energy generation, the second for self cleaning applications and the third for promoting chemical reactions. Latter includes air and water cleaning (removal of organic compounds present in low concentrations in air and water), but also synthesis of organic compounds. In this section a short description of the photovoltaic and the photoinduced superhydrophilic effect in TiO_2 will be given. Since photocatalysis is one of the main topics of this work, it will be discussed in detail in section 2.4.

2.3.2.1 Photovoltaic cells

A photovoltaic cell can produce electricity from (sun-)light. The electrons excited into the conduction band after illumination (see section 2.3.1.) can be extracted to an outer circuit, thus generating an electric current. Usually some type of doping is needed to extend the lifetime of the electron and hole (see also section 2.6) to enhance the effectiveness of the cell. At present, most commercial solar cells consist of (doped) Si, which have a high efficiency but some serious drawbacks which increase their cost. First, the low doping levels require high purity base material. Second, encapsulation to prevent oxidation in air is needed. The alternative GaAs, is even more expensive. Both materials have band gaps matched with solar light emission.

A different approach is to use a wide band gap metal oxide (TiO_2 or ZnO) together with a suitable organic chromophore (light absorbing dye), which are then called organic, hybrid or dye sensitized solar cells [Carp04, Fujishima00, Mills97]. Since both components are relatively cheap the price of the solar cell is drastically reduced. In a dye sensitized solar cell the organic chromophore is excited by visible light and injects electrons into the conduction band of the metal oxide. To close the circuit an electron has to be returned to the system. The major drawback is the low conductivity of the organic compound, limiting the travel distance of the charge carriers. Therefore the thickness of the dye has to be kept as low as possible, which can best be accomplished by coating nanocrystalline TiO_2 with a monolayer of dye [Carp04, Mills97]. Here a liquid electrolyte is used for regeneration of the dye, which poses a problem

for commercial applications. Work is in progress to use either a conducting polymer matrix or to find conducting dyes.

2.3.2.2 Photoinduced superhydrophilicity (PSH)

Some semiconductors also exhibit a photo-induced superhydrophilic effect (PSH). Here the contact angle of the semiconductor with water approaches zero after exposure to ultra-band gap irradiation, a process that can be reversed by storing the semiconductor in the dark [Fujishima00, Mills02]. Actually, the effect is such that the surface turns both hydrophilic (low contact angle with water/ polar fluid) as well as oleophilic (low contact angle with oil/ non-polar fluid), so that one speaks of an amphiphilic effect (low contact angle towards both water/ polar fluid *and* oil/ non-polar fluid) [Carp04, Fujishima00].

In literature one is cautious about any link between photocatalytic activity and photo-induced superhydrophilicity; only few studies discuss this issue [Fujishima00, Guan05]. There are semiconductors with high photocatalytic activity but negligible PSH activity (e.g. strontium titanate), and there are semiconductors, which can exhibit a high or low photocatalytic activity, but usually always a high PSH activity, e.g. TiO_2 [Fujishima00, Mills02]. PSH is also observed in amorphous TiO_2 [Nakamura00a, Nakamura00b].

As already discussed in section 2.3 illumination of TiO_2 with ultra-band gap light generates an electron-hole pair that can recombine or react with surface species. At the TiO_2 surface the available species are Ti^{4+} and bridging O^{2-} groups. Photo-generated electrons reduce the surface Ti^{4+} to hydrophilic Ti^{3+}, while photo-generated holes oxidize the bridging O^{2-} groups to oxygen, leaving oxygen vacancies behind [Carp04, Fujishima00]; this is equivalent to the material being reduced at the surface. Subsequently the oxygen vacancies are filled by water molecules which produce adsorbed OH groups, increasing the hydrophilic nature of the surface. The process is reversed slowly in the dark: the Ti^{3+} sites are re-oxidized to Ti^{4+} by ambient oxygen, and the vacancies are filled by the O^{2-} generated as a consequence of this reaction [Mills02]. The rate of this reverse process can be enhanced by subjecting the film to ultrasound or mechanical abrasion [Kamei00, Sakai98]. Freshly prepared films almost always show a high wettability [Guan05].

Studies have shown that SiO_2/ TiO_2 mixed or layered oxide films have an increased hydrophilicity and/ or a retarded hydrophopic regeneration in the dark [Guan05, Hattori00, Miyashita03]. Usually there is an optimum amount of SiO_2.

Investigations on rutile have shown, that the hydrophilicizing rate depends on the crystal plane of the surface [Carp04, Fujishima00]. It is suggested that the hydrophilicizing process is some kind of photocorrosion, i.e. the first exposure to UV light evokes an irreversible change of the surface.

2.4 Photocatalysis

2.4.1 Definition of terms

Before discussing the subject of photocatalysis the reader is introduced to the most important terms of chemical reactions and how they are influenced by a catalyst. First, we want to recollect the definition of a chemical reaction and the energy transfer involved. Then, the role a catalyst plays during a chemical reaction will be highlighted. After this the special features of photocatalytic reactions will be discussed in more detail.

2.4.1.1 Chemical reactions

Chemical reactions can be divided into two classes, namely electron transfer reactions between two species and intra-molecular bond re-arrangement. Latter can only occur in complex molecules, so that the electron transfer reactions are by far the most abundant. Here reactant 1 transfers one or more electron(s) to reactant 2, i.e. reactant 1 looses one or more electron(s), meaning it is *oxidized*. On the other hand, reactant 2 gains one or more electron(s), meaning it is *reduced*. Therefore, these reactions are also referred to as '*redox reactions*'. A simple example is the oxidation of Ti to TiO_2, where one Ti atom transfers nominally 4 electrons to two oxygen atoms forming TiO_2:

$$\overset{0}{Ti} + \overset{0}{O} = \overset{+4}{Ti}\overset{-2}{O_2} \qquad (2.19)$$

A chemical reaction will have to go through a transition state, where the electron transfer takes place, before ending in a final state of lower energy (for spontaneous, i.e. exergonic reactions). The energy difference between the ground state of the separate reactants and the transition state is the activation energy ΔE_a of the chemical reaction:

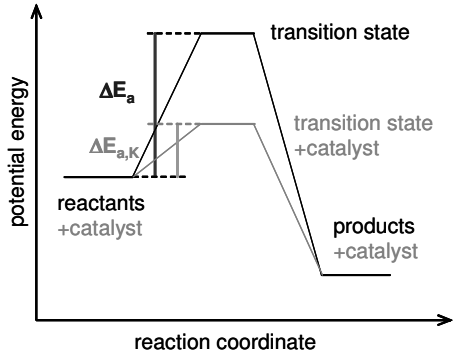

Figure 2. 2:
Energy profile of a chemical reaction with and without catalyst.

2.4.1.2 Catalyzed chemical reaction:

A chemical reaction is called '*catalyzed*' when the activation energy of the process is lowered and, as a result, the reaction rate is enhanced. This is done by involving a third partner in the reaction, the ***catalyst***, which enables the reaction to proceed through one or more transition states which are lower in energy than the original transition state (Figure 2. 2). The enhancement of the reaction rate follows from the Arrhenius equation:

$$\ln k = - E_A/RT \qquad (2.20)$$

with k the reaction rate and E_A the (molar) activation energy of the reaction. R is the universal gas constant and T the reaction temperature.

In its original meaning, the catalyst is returned to its original state after the reaction is completed, i.e. the catalyst participates *without being consumed*. In reality the lifetime of a catalyst is limited due to alteration of its state, referred to as '*catalyst poisoning*'. Therefore, usually a '*turn-over number*' is defined, which gives the number of reaction cycles that can be catalyzed before the catalyst becomes inactive.

The catalyst can be present in the same phase as the reactants, one then speaks of '*homogeneous catalysis*'. Reactants and/or products can also be in different phases, e.g. two liquid phases, with the catalyst present at the interface; here one speaks of '*phase transfer catalysis*'.

If the two reactants are in the same phase but the catalyst comprises a second phase, one speaks of '*heterogeneous catalysis*'. Here the reaction takes place at the surface of the catalysts, to which the reactants are absorbed. It is this type of process which is active in semiconductor photocatalysis.

2.4.1.3 Photocatalysis

The word '*photocatalysis*' implements the involvement of light in the catalytic process. As such it does not specify whether the light is used to activate the catalysts or by invoking changes in one of the reactants.

2.4.1.4 Heterogeneous semiconductor photocatalysis

Heterogeneous semiconductor photocatalysis describes a process where a semiconductor particulate (CdS, TiO_2, ZnO, WO_3, etc.) is activated by illumination with UV-visible light suitable to its band gap energy ($\geq E_{bg}$) to catalyze a redox reaction at its surface. The illumination results in resonance absorption in the semiconductor as stated in section 2.2.4.2, generat-

ing conduction band electrons (e^-) and valence band holes (h^+), as discussed in section 2.3.1. The charge carriers can recombine, become trapped or can migrate to the particulate/ solution (air) interface where they are available for redox reactions.

2.4.2 Photocatalyzed redox reactions

In a photocatalyst, the electrons have a reduction potential reflected by the energy level of the bottom of the conduction band, while the holes have an oxidizing potential reflected by the top of the valence band. Therefore, the redox potential of the adsorbed redox couples must be situated between these two energy levels, i.e. within the band gap of the semiconductor [Carp04, Mills97, Schiavello97].

This is illustrated by Figure 2. 3 below, adapted from [Serpone99], which shows the oxidation of an organic molecule (denoted 'OR') in the presence of oxygen. The hole is transferred in the form of an OH^+ radical to the organic molecule while the electron is scavenged by an oxygen molecule. The defect states in TiO_2 will be discussed in more detail in section 2.5.1.

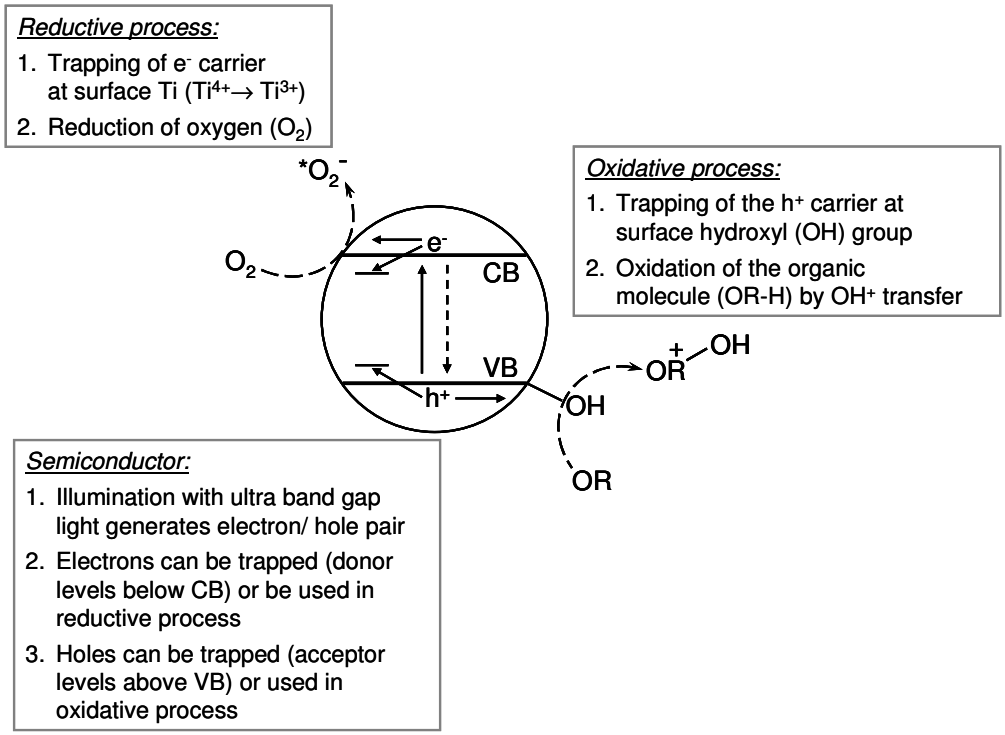

Figure 2. 3:

Schematic of redox reactions occurring during photocatalysis of TiO_2 and an organic molecule (OR), adapted from [Serpone99]. The levels inside the band gap denote possible trap centers (donor and acceptor states). The conduction and valence band are denoted by CB and VB, respectively.

When looking at reactions in water, the positions of the band edges can be reported by using the normal hydrogen electrode (NHE) as reference (Figure 2. 4). Indicated in the figure are also the positions of the redox couples for water splitting. Other chemical reactions also have redox couples that are referred to the NHE, so that a suitable semiconductor can be found. One has to remember, though, that for reactions in water the redox potential is influenced by the pH of the solution, which can also influence surface states on the solid semiconductor. Figure 2. 4 can therefore only be used as a guideline.

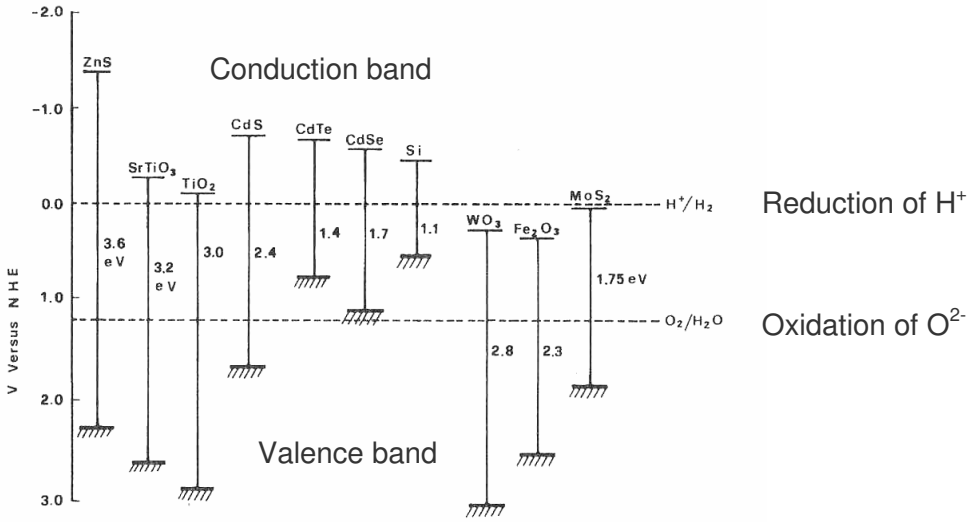

Figure 2. 4:

Position of the band edges of selected semiconductors in contact with an aqueous electrolyte (from [Schiavello97]). The hatched lines indicate the bottom of the valence band. The position of the H^+/H^2 and O_2/H_2O redox couples, which are important for water splitting, are also indicated.

Unfortunately Figure 2. 4 is not applicable to reactions in the gas phase as no standards as the NHE have been defined. Here, among others, the value of the redox potential difference will depend on the extent of interaction between the two phases as well as the composition of the gas phase. This includes the degree of chemisorption, the gas pressure and the humidity.

2.4.2.1 Photocatalytic breakdown reactions

The most cited photocatalytic redox reaction is the mineralization of an organic substance in the presence of oxygen, i.e. its complete oxidation to CO_2, H_2O and mineral acids, which can be summarized by equation (2.21):

$$\text{Organic} + O_2 \xrightarrow[\text{semiconductor}]{h\nu \geq \text{bandgap energy}} CO_2 + H_2O + \text{mineral acids} \qquad (2.21)$$

Mineral acids are generated if there are hetero-atoms, such as S, N, and Cl present in the organic. This catalytic process is exergonic ($\Delta G < 0$), as shown in Figure 2. 2, p. 24, and the energy of the photons is not used in the reaction other than to excite the catalyst. Since the net energy balance of the reaction is positive, the energy released after the reaction needs to be dissipated as heat or in other form.

Other examples of photocatalytic 'breakdown' reactions are partial oxidation reactions, of e.g. alcohols to aldehydes or ketones. Exergonic redox reactions can, therefore, also be applied for synthesizing new organic molecules. This includes photocatalytically assisted polymerization [Damm05]. A good overview is given in [Carp04].

These processes should not be confused with the endergonic (non-spontaneous) synthesis discussed in the next section.

2.4.2.2 Photocatalytically assisted synthesis

The process described by equation (2.21) can be reversed, i.e. hydrocarbons can be built from their parts. In this case the reaction is not spontaneous, but endergonic ($\Delta G > 0$) so that the process is actually a real photosynthesis or a photocatalytically assisted synthesis. Here the energy of the photons is stored in the product(s) of the reaction.

The most studied reaction of this kind is the production of hydrogen from water (water splitting). The first to report this were Fujishima and Honda, as mentioned in the introduction, chapter 1. According to Figure 2. 4, p. 27, this should be possible (the redox potential of water is shown to lie within the band gap of TiO_2). Newer results have shown, though, that the location of the band gap of pure TiO_2 is not completely matched with the position of the redox potential of water, but the reaction can proceed through modifying the process or the catalyst [Carp04, Mills97].

Other examples are the so-called photo-fixation of nitrogen, where ammonia is formed (together with NO_x) and the photo-reduction of CO_2 ('artificial photosynthesis'). Both are controversial, as the amount of products formed is usually in the range of the detection limit due to the presence of impurities [Carp04, Mills97].

This synthesis should not be confused with what is termed in biology as 'photosynthesis', which is a natural reaction under sunlight assisted by chlorophyll.

2.4.3 Reaction kinetics of the photocatalytic breakdown of organic substances with TiO_2

2.4.3.1 General

All chemical reactions involving the (photo-)catalyst will take place at its surface. More precisely there are so-called '*active sites*' present at the surface which are the only surface sites that can be involved in the process. The number of active sites (per unit area or unit mass of catalyst) will, therefore, influence the catalytic activity of the catalyst. Important will also be the time involved for completing the reaction. Any reaction at the surface of the catalyst involves the following steps, which are characterized by a specific reaction rate:

1) Adsorption of the reactants
2) Reaction of the reactants with the catalyst (i.e. transfer of electron/ hole to the reactants)
3) Combination of the reactants (if part of the reaction)
4) Desorption of the reactants

The definition of an active site will differ from one organic substance to another and depends on the environment of the catalyst (gas or liquid). Since the adsorbed molecules can be mobile on the catalyst surface, active sites may also migrate. As for the catalyst TiO_2, every Ti^{4+} associated with an electron (i.e. a Ti^{3+}) is a potential active site for the reduction process, while every hydroxyl group associated with a hole (i.e. a hydroxyl radical) is an active site for the reduction process (section 2.3.1.2). On an ideal catalyst surface all active sites will be available to the reaction. In reality there will be other molecules present at the catalyst surface. Depending on whether they are weakly or strongly bonded to the active sites, as compared to the target molecule(s), they can block the active sites, i.e. *poison* the catalyst.

A good description of the general reaction kinetics and the influence of external parameters like temperature and initial substrate concentration can be found in [Mills97] and [Carp04]. A summary will be given here and in the next section 2.4.4.

The kinetics of photo-mineralization of organic substances by oxygen, using TiO_2 and steady state illumination, in general follow the Langmuir-Hinshelwood kinetic scheme:

$$R_i = \frac{-d[S]_i}{dt} = \frac{k(S)\cdot K(S)\cdot [S]_i}{1+K(S)\cdot [S]_i} \qquad (2.22)$$

with R_i the initial rate of substrate removal, $[S]_i$ the initial concentration of the organic, *K(S)* is taken to be the Langmuir adsorption constant of species *S* on the surface of TiO_2 and *k(S)* is a proportionality constant providing a measure of the intrinsic reactivity of the photo-activated surface with *S*.

The discussed kinetics were found to be valid for batch reactors. They can usually also be applied to flow reactors, but here an additional dependence of *k(S)* on the flow has been found. As a result, flow reactors are not considered to be as helpful as batch reactors in the evaluation of the fundamental kinetic parameters associated with semiconductor sensitized photo-processes.

2.4.3.2 Specific reaction kinetics

The general reaction order (towards component *A*) is defined as:

$$v = -d[A] / dt = k\,[A]^a \qquad (2.23)$$

with *v* the reaction rate, *[A]* the concentration of component *A*, *k* the reaction constant and *a* the reaction order.

a. Zero order reaction

Here the exponent *a* from equation (2.23) is zero, so that one yields $v = k$, which in integrated form yields:

$$[A] = [A]_0 - kt \qquad (2.24)$$

which means that one observes a linear decay of component *A*.

b. First order reaction

Here the exponent *a* from equation (2.23) is one, so the resulting reaction equation is:

$$v = k\,[A] \qquad (2.25)$$

which in integrated form yields:

$$[A] = [A]_0\, e^{-kt} \qquad (2.25)a$$

so that the result is an exponential decay of component A.

In summary, one observes that for a zero order reaction the reaction rate *v* is constant and identical to the rate constant *k*, while for a first order reaction *v* is dependent on *[A]*.

2.4.3.3 Method of the initial rates (determination of the rate law) [Atkins90]

This method is often used together with the isolation method (where all components but the one to be investigated are in large excess). For the method of the initial rates the reaction rate is measured at the beginning of the reaction for several different initial concentrations of reactants. If the rate law for a reaction with *A* isolated is:

$$v = k\,[A]^a \tag{2.26}$$

then it follows for the initial rate:

$$v_0 = k\,[A]_0^a \tag{2.27}$$

Since usually a logarithmic plot is chosen, one transforms equation (to:

$$\ln v_0 = \ln k + a \ln [A]_0 \tag{2.28}$$

so that a plot of $\ln v_0$ against $\ln [A]_0$ should yield straight lines with slope a. The initial reaction rate v_0 must be determined as $\Delta[A]/\Delta t$ from the initial part of the decay curve, i.e. as tangent to the curve at $[A] = [A]_0$.

2.4.4 Influence of external parameters on the photocatalytic breakdown of organic substances

In this section the influence of external factors on the kinetics of the reaction will be discussed. Their influence on the structure of the catalyst (e.g. in the case of water) will be discussed in section 2.5. There are a variety of external parameters having an influence on a given photocatalytic breakdown reaction. There are several important factors, which are usually quite dependent on the circumstances chosen by the individual research group, namely initial concentration of the organic test substance, level of humidity and the UV intensity. While the first factor is rather straightforward to control, the latter two are not. The level of humidity is not always controlled, especially when working in ambient air. The UV intensity usually has a strong influence but many times cannot be determined accurately due to the experimental settings. Even though the power of the UV lamp used is known, the number of photons per area arriving at the catalyst surface is unknown. This is due to the unknown loss of radiation upon passing through air/ filters/ reactor window, but also due to the unknown loss of radiation due to reflection of light at the catalyst surface or transmission of light through the catalyst without being absorbed. Therefore it is difficult to determine the number of photons actually absorbed by the photocatalyst. Nevertheless, the effect of humidity and UV-intensity can be studied on a comparative basis.

2.4.4.1 Effect of oxygen concentration

A major player in the reaction is oxygen. Considering gas phase photocatalysis, mostly air or an atmosphere containing the same amount of oxygen as air is used, so that its concentration can be taken constant. There are studies though, that investigate the effect of the oxygen concentration in the reactor atmosphere [Carp04, Einaga99]. It was found that the presence of oxygen is necessary for photocatalytic oxidation to take place, which is also reflected in the mechanism described in sections 2.3.1.2 and 2.4.2. It is not sufficient to use the lattice oxygen of the TiO_2 and later replenish it as can be done for catalysts used for thermal oxidation.

A description of the influence of the oxygen partial pressure on the reaction kinetics is given in [Mills97]. In summary, the factor *k(S)* of equation (2.22), p. 29, is proportional to the fraction of O_2 adsorbed on TiO_2, denoted as $f(O_2)$, where:

$$f(O_2) = K_{O2}\,[O_2] / (1 + K_{O2}\,[O_2]) \qquad (2.29)$$

with K_{O2} the Langmuir adsorption coefficient for O_2 on the semiconductor. There seem to be no competing species to O_2, which adsorbs onto Ti^{3+} sites.

2.4.4.2 Effect of temperature

Another factor that is studied little is the effect of temperature, as most studies take place at room temperature. The overall process of semiconductor photocatalysis is usually not found to be particularly temperature sensitive, since reported activation energies lie in the range of 5-16 kJ/mol. Increasing the temperature may increase the oxidation rate but should also lower the adsorption isotherms of the organic substance and O_2. Most photocatalytic experiments are carried out with the fraction of adsorbed oxygen $f(O_2) \approx 1$ (i.e. saturated O_2 atmosphere) and the concentration of the organic substance, $[S]_i$, is low. Here an increase in temperature will mostly effect the rate of oxidation of the organic substance at the interface. Only if $[S]_i$ were large ($> 10^{-3}$ mol/dm^3) and p_{O2} were small (< 0.05 atm), then the rate of electron transfer to oxygen may become the rate determining step that could be effected by a temperature change [Carp04, Mills97].

2.4.4.3 UV intensity/ photon flux

It was found that the factor *k(S)* of equation (2.22), p. 29, is proportional to $(I_a)^{\theta}$, with I_a the rate of light absorption and θ a power term, which is equal to 0.5 or 1 at high or low light intensity, respectively [Mills97]. This means that at high light intensity the reaction rate is half order with respect to the photon flux, while it is first order at low light intensities. The

fact that two different dependencies are found for high and low photon fluxes is also reported in [Carp04]. In the first order regime, which is observed for fluxes up to about 25 mW/ cm^2, the electron-hole pairs are consumed more rapidly by chemical reactions than by recombination. On the other hand, in the half order regime observed at higher photon fluxes, the recombination rate is predominant.

2.4.4.4 Initial concentration of the organic test substance

For high concentrations of the organic substance ($[S]_i > 10^{-3}$ mol/dm^3) the kinetics are found to be zero order (i.e. no dependence) while for low concentrations ($[S]_i < 10^{-3}$ mol/dm^3) they are found to be first order (i.e. linearly dependent) with respect to the degradation of the organic [Carp04, Mills97]. According to [Carp04] there are two reasons for the saturation of the dependence of the initial degradation rate on the initial concentration of the organic, observed for higher initial concentrations. The first reason is the saturation of the adsorption places on the catalyst surface. The second reason is the rate determining step of the reaction. For low initial concentration of the organic this step is the reaction of the charge carriers with the organic at the catalyst surface, which depends linearly on the initial concentration of the organic. For high initial concentrations of the organic the rate determining steps are the generation and migration of the charge carriers to the surface of the catalyst, which is independent of the initial concentration of the organic.

One should take into account that 'high' and 'low' concentrations of the organic substance may vary with the system to be investigated i.e. the amount of active photocatalyst present in the chamber. Since the concentration of the organic substance decreases during the reaction it may also be possible to see a change in reaction kinetics during the reaction after a certain lower limit of organic has been reached, i.e. a transition from zero to first order, showing an initial linear decay converting to an exponential one.

2.4.4.5 Relative humidity in chamber atmosphere

The relative humidity is an important factor as the presence of water can strongly influence the photocatalytic reaction [Einaga99, Martra99]. This is not surprising, since the surface hydroxyl groups are known to play a role in trapping the hole which was generated by UV illumination (section 2.3.1.2). Water is always present in ambient air, and is difficult to remove completely even when working in a dry atmosphere. The reason for this is that the TiO_2 surface is almost always exposed to air before being tested. As a result, the investigations on

the effect of water vapor on the photocatalytic efficiency of a given breakdown reaction are in many cases controversial [Carp04].

The effect of water vapor on the photocatalytic breakdown rate depends on its concentration, the type of organic substance and the other process parameters. Physisorption of water plays an important role, since this water can attract or repel organic substances or occupy surface active sites. Chemisorption of water leads to the formation of surface hydroxyl groups. Since the surface hydroxyl radicals play a role in the catalysts activity (section 2.3.1.2) their number must remain around a certain level. Too many hydroxyl groups result in blocking the surface to other molecules (e.g. the organic to be oxidized), inhibiting the reaction. This is the case, among others, for saturated hydrocarbons, alcohols and aldehydes, [Einaga02, Kim02a, Vorontsov04]. An example is the breakdown of ethanol:

$$CH_3CH_2OH + 3\ O_2 = 2\ CO_2 + 3\ H_2O \qquad (2.30)$$

In other cases the hydroxyl groups are consumed to complete the oxidation reaction like in the case of unsaturated aliphatic (e.g. cyclohexene) and aromatic molecules (e.g. benzene, toluene) [Augugliaro99, Einaga99, Einaga02, Kim02a, Lichtin98, Martra99], as an example the breakdown of toluene is shown in equation (2.31):

$$2\ C_6H_6CH_3 + 18.5\ O_2 = 14\ CO_2 + 9\ H_2O \qquad (2.31)$$

In these cases the absence of sufficient water leads to catalyst deactivation (poisoning), where a tar like deposit (i.e. aromatic or unsaturated aliphatic poly-condensates) is formed on the catalyst surface. Usually the catalyst poisoning can be reversed by illumination in humid air [Einaga99], but in some cases irreversible poisoning is reported [Augugliaro99]. For some organic molecules traces of water are reported to be beneficial while large amounts are not (trichloretylene TCE) [Kim02a].

The importance of a hydroxylated surface was shown by experiments, where the TiO_2 surface was dried in-situ prior to being subjected to a photocatalytic reaction in air [Augugliaro99]. Here it was found that the surface can be completely dehydroxylated by heating in a dry atmosphere at a temperature of 873 K. When the catalyst was then exposed to water only physisorbed hydroxyl groups were observed with IR, which could be removed by outgassing in dry air at room temperature. The influence of the catalyst surface structure on surface hydroxylation will be discussed further in section 2.5.2.1.

2.4.4.6 Strongly adsorbed reaction products

Another rather common problem is the strong adsorption of reaction products. Different molecules can require different active sites [Ching04, Vorontsov04], so that a product may block a site which is active for the original organic substance, but not for the product. This will also result in poisoning of the catalyst surface. An example is the reaction of alcohols to aldehydes or ketones [Schiavello97]. In [Cao04] the blocking effect of chemisorbed CO_2 is discussed.

2.5 Effect of structure on the photocatalytic activity of TiO_2

As was already indicated in previous sections the structure of TiO_2 has a strong influence on its photocatalytic activity. Real life TiO_2 cannot be used in a defect free single crystal form for obvious reasons (single crystals of anatase are difficult to obtain). But in order to understand the intrinsic properties investigations on single crystal material are very helpful. Unfortunately, most studies are performed on polycrystalline material, the defect state of which is usually not well defined. In this section it will be attempted to discuss the influence of individual defects on the TiO_2 structure and activity, but, as will become clear, many defects do not occur alone but only together with other defects.

The defects will be split into internal defects (i.e. within the grains/ the bulk of the material) and surface defects (i.e. on the grain/ bulk surface of the material), which will be discussed in sections 2.5.1 and 2.5.2, respectively. Sometimes a surface can be seen as a strong defect zone of the bulk, so that there will be some overlap in the discussions. Since the issue of particle size falls between the two categories, it will be treated separately in section 2.5.3. Another factor that influences the photocatalytic activity of thin films is their thickness. This will be discussed in section 2.5.4.

The effect of doping will be treated separately since it has a rather complex and global effect on the structure of TiO_2. A separate section (2.6) will be devoted to this subject alone.

2.5.1 Internal defects (bulk of the material)

2.5.1.1 Deviations from the ideal crystal lattice

Any real material will not have a perfect crystal structure. Even in a single crystal one finds point defects (misplaced lattice atoms/ ions, vacancies, foreign atoms/ ions) and dislocations. In polycrystalline materials defects are added due to the presence of grain and crystallite boundaries. Any interruption of the perfect crystal lattice will affect the band structure of the material. If the size of the defect state is different from its host a lattice distortion (i.e. strain) is introduced. This will have some effect on the width of the band gap, just like temperature which increases the lattice vibrations. The effect of uniaxial stress on the band gap of single crystal rutile was studied by [Mathieu78]. Here a pressure coefficient of $dE_g/dP = 1.19 \cdot 10^{-6}$ eV/bar was found for the band gap. As result, a uniaxial pressure of 1 GPa (which is the order of internal stress generated in thin films) would cause an increase in the

band gap energy of 0.01 eV. This is a rather small value and at the edge of being measurable. The issue of lattice strain will be discussed in more detail in section 2.5.1.5.

If the electronic state of the defect (i.e. its charge) is different from its host, it will introduce energy states in the band gap. A defect which (i) provides more electrons to the conduction band than the lattice position it occupies or (ii) generates a defect which provides such electrons, it is called a ***donor***. Examples for latter are defects resulting in the formation of Ti^{3+}, which increases the number of electrons in the conduction band. If the defect (i) provides less electrons than the lattice site it occupies or (ii) takes electrons from the valence band where it creates holes, it is called an ***acceptor***. Examples are defects resulting in the formation of oxygen vacancies which can capture (trap) electrons, reducing their number in the conduction band. The effect of oxygen vacancies will be further discussed in section 2.5.1.4, doping will be discussed further in section 2.6.

Donor states are found just below the conduction band, while acceptor states are found just above the valence band. Defect levels deep inside the band gap are ***trap sites***, both for electrons as well as holes. The definition of a trap site is not straightforward, though, since all levels inside the band gap have the potential to be trap sites. The deeper the trap site lies within the band gap the higher its trapping power, i.e. the lower the chance is that the trapped charge carrier can leave the trap within its lifetime. But also the donor and acceptor levels close to the band edges can act as trap sites. As already discussed in section 2.3.1.2 trap sites enhance the separation of the electron/ hole pair, but if the charge carrier is too strongly bonded it is not available for the photocatalytic redox reaction. As a result the activity enhancement by the defect depends strongly on its nature, and the presence of other defects.

2.5.1.2 Crystallinity

The degree of crystallinity was found to be an important factor influencing the photocatalytic activity of TiO_2. One must also take into account that grain size and crystallite size may not be identical, so that the effective degree of crystallinity depends on the actual crystallite size and the ratio between crystalline and amorphous phase present in the material. One has to keep in mind that the crystallite size is defined by the domain (within a grain) which has the same crystallographic orientation. A grain is defined by the presence of (visible) grain boundaries. Therefore, it is possible to have different crystallites within one grain. The main difficulty is to influence the crystallite size without changing the grain size of the material, because increasing the temperature to promote crystal growth in anatase TiO_2 will result in

grain growth and/ or transformation to the rutile structure. Careful studies using SiO_2 as grain growth inhibiting additive have shown that a higher degree of crystallinity results in a higher photocatalytic reactivity [Jung99, Jung02, Jung04]. The grain growth inhibiting properties of SiO_2 also retard the anatase to rutile transformation which allows annealing at higher temperatures, resulting in improved crystallinity [Carp04].

When decreasing the grain size the degree of crystallinity is reduced due to the introduction of defects in the form of grain boundaries. This becomes important for grain sizes below ca. 10 to 20 nm [Carp04].

The amorphous phase represents the highest state of disorder, i.e. has a completely random structure [Takeda01]. With TiO_2 the definition of amorphous is difficult, as there is always some degree of local ordering observed. Here we will define '*amorphous*' as the TiO_2 phase where no signal can be detected in XRD. This states only that the material has crystalline domains of a size below the XRD detection limit (< 3-5 nm). Usually grains around 5 nm are detected as very broad peaks around the position expected from the diffraction spectrum of the material. The absence of any XRD signal can be caused not only by a very small crystallite size but also by a very low degree of crystallinity. One can, therefore, state that XRD '*amorphous*' TiO_2 contains a certain degree of local ordering which can extend to crystallites of grain size smaller than 3 nm, which may or may not be enclosed by a matrix of low structural ordering.

Very little is known on the electronic structure of '*amorphous*' TiO_2. Most discussions agree that the high defect state should result in poor charge carrier conduction, e.g. [Fallet06, Fernández-García04]. In [Fernández-García04] it is claimed that for such type of material (which they count as nano-crystalline TiO_2) one observes a direct-forbidden band-gap transition as compared to the indirect allowed transition observed in well crystallized anatase. This will be discussed further in detail in section 2.5.3. Completely amorphous TiO_2 is expected not to show any photocatalytic activity [Damm05, Fallet06]. As a result, only rarely the photocatalytic activity of amorphous films or powders is measured, e.g. [Fallet06, Zeman03].

2.5.1.3 Crystal structure

Another important factor is the crystal structure of the catalyst. Even though the crystal lattice of rutile and anatase are similar there are a few significant differences. The phase stability was already discussed in section 2.1.2. The difference in band gap and optical transition mode were discussed in section 2.2.4.4. It was also found that rutile and anatase have different

numbers of active sites [Carp04], and in rutile it was shown that the crystal facets at the surface have different numbers of active sites [Fujishima00, Lowekamp98]. The reason is that different crystal facets have different coordination numbers (CN) for the Ti and O at the surface, so that a different number of bonds will have to be saturated by absorption of O_2 and H_2O from the air. This leads to a different degree of surface hydroxylation. The same should be expected for anatase, but no such studies were found in literature. As a result a different photocatalytic activity of the two crystal phases as well as for different crystal facets of a given crystal phase may be expected (also refer to sections 2.5.2.2 and 2.5.2.3).

A common observation is that anatase always shows good photocatalytic activity while rutile shows good photocatalytic activity in some cases [Yin04] but almost zero activity in other cases [Carp04, Schiavello97]. The small difference in band gap of rutile and anatase (3.0 and 3.2 eV, respectively) cannot explain their different activity. A main difference, though, is their recombination rate of photoinduced electrons and holes, which is higher for rutile [Schiavello97]. Other reasons for the low reactivity of rutile lay in the high firing temperatures needed to obtain this crystal phase, which causes the irreversible loss of surface hydroxylation (section 2.4.4.5) and increased crystal growth (section 2.5.1.2).

It was also found that a combination of the two crystal phases leads to an enhancement of the photocatalytic activity in many cases [Miyagi04, Ohno01, Ohno03]. A good example is the P25 powder from Degussa. This material has become a reference photocatalyst and will be discussed in more detail in section 2.7.1.2. According to [Ohno03, Miyagi04] it is the interface of the two phases that yields the highly active sites.

Brookite has been studied to a much less extent. A study on single crystal brookite, which had a pale brown color, yielded a band gap of 1.9 eV, which was claimed to be indirect [Zallen06]. Since it is difficult to obtain in pure form (section 2.1.2) not enough is known to compare its photocatalytic activity to that of anatase and rutile. A comparative study is described in [Kominami03] where powders were synthesized and compared to Degussa P25. Since the band gap is substantially lower than that of anatase and rutile it can expected that its photocatalytic behavior will be quite different.

As discussed in section 2.1.2 the relative stability of the three different TiO_2 modifications is particle size dependent. While anatase is found usually with small crystal/grain size, rutile can be found with large crystal/grain size. Since also the grain size has an effect on the photocatalytic activity (section 2.5.3), it can be difficult to separate these effects.

2.5.1.4 The effect of oxygen vacancies (stoichiometry)

Oxygen vacancies in TiO_2 are present if the material is not completely stoichiometric or can be generated by doping (see section 2.6). Therefore, oxygen vacancies will not be occurring on their own but only in combination with one or more defects (e.g. dopant, reduced Ti^{3+}). It can, therefore, be expected that the effect of oxygen vacancies can vary, depending on the exact circumstances of their occurrence.

Indications that oxygen vacancies are detrimental to the photocatalytic activity were found by [Takeda01] and [Liu05] for d.c. magnetron sputtered TiO_2 films. Post oxidation of films using ^{18}O tracer and subsequent SIMS analysis showed that with increasing amount of incorporated tracer the photocatalytic activity decreases [Takeda01]. From this it was concluded that the decrease in photocatalytic activity is linked to the increase in defects associated with oxygen vacancies in the film. In [Liu05] the photocatalytic activity was linked to the thin film stoichiometry determined by ESCA showing a decrease in photocatalytic activity with decreasing oxygen content. In both cases the conclusion was that for optimum photocatalytic performance the films must be fully stoichiometric.

Density of states (DOS) calculations performed by [Takeda01] showed no effect of single oxygen vacancies, but that for double oxygen vacancies energy levels inside the band gap were generated. It was suggested that these energy levels can act as recombination centers for the charge carriers, decreasing their concentration and, therefore, the photocatalytic activity of the material.

On the other hand, band gap calculations by [Wang05a] for anatase showed that oxygen vacancies introduced shallow donor states in the band gap. The authors expect these to increase the photocatalytic activity of TiO_2.

In [Zhang03b] preparation of a visible light active photocatalyst of reduced TiO_2 is claimed. The color of the catalyst is reported to be yellow; traces of N were also found. Possibly the presence of N causes the VIS light photocatalytic activity (see section 2.6.2.2). The results are confirmed, though by [Ihara03] where commercially available anatase powder was reduced in a H_2-plasma to have a O/Ti ration of 0.68 (ESCA estimate). This powder had a yellowish color and showed a red shift of the optical absorption edge and VIS light photocatalytic activity. An electron spin resonance (ESR) signal of $g = 2.003$ found by the authors was assigned to electrons trapped on an oxygen deficient site [Ihara03].

In [Beermann02] the trapping of electrons in nanostructured TiO_2 was studied by photocurrent transients. Here the results obtained with a 420-480 nm bias light were explained by assuming the generation of additional traps by this light. These traps were considered deep as they decreased the number of electrons in the conduction band. The authors discuss the possibility of the nature of these sites: One missing surface O generates two adjacent Ti^{3+}. These strongly attract O_2, forming Ti^{4+}-O_2^-. When this site attracts an electron the peroxide Ti^{4+} - O_2^{2-} is formed, which has a yellow color.

In conclusion, one needs to say that the effect of oxygen vacancies on the photocatalytic activity of TiO_2 is not clear. Presumably other factors play a role in why sometimes a positive and sometimes a negative effect is observed. This issue will be discussed further in section 2.6 on doping.

2.5.1.5 Lattice strain

Some early studies looked at the influence of an applied external stress on the band gap transition of TiO_2 (rutile) [Mathieu78]. It was found that the band gap increased with increasing applied (uniaxial) stress, yielding a pressure coefficient of dE_g/dP of $-1.19 \cdot 10^{-6}$ eV/ bar. Additionally, a stress induced splitting of the indirect band gap transition was found for an applied [100] stress (i.e. along the a axis of the crystal).

In [Miao05] the high band gap of 3.4 eV observed for magnetron sputtered anatase TiO_2 thin films as compared to the bulk value of 3.2 eV is attributed to the distortion of the TiO_2 unit cell. The authors also performed experiments and ab-initio calculations [Wunderlich04a-b] to determine the influence of lattice distortions (i.e. lattice strain) on the band gap of rutile and anatase TiO_2. They found that the band gap increases with decreasing lattice constant *a* and increasing lattice constant *c*. This was confirmed by experimental results to which the simulations showed an excellent fit. From the presented graph one can extract a dependence of the band gap E_g on the lattice strain ε of $\Delta E_g/\varepsilon = 1.6$ eV/ -0.177 = - 9.040 eV (with the lattice strain ε defined as $\Delta a/a$). To find the resulting dependence of the band gap on stress applied uniaxially along the a axis, i.e. $\Delta E_g/\sigma$, one needs to divide $\Delta E_g/\varepsilon$ by the Young's modulus *E* of anatase ($\sigma = E\,\varepsilon$). Using an average value of 185 GPa [Anderson97] for *E* the resulting stress is 2.8 GPa (2.8×10^4 bar). One receives for the dependence of the band gap on the applied stress in anatase a value of $-4.89 \cdot 10^{-6}$ eV/ bar, which is on the order of the value obtained in [Mathieu78] for rutile, showing good agreement between the stress measurements

and the strain calculations, considering that rutile has a higher Young's modulus than anatase [Anderson97].

The studies in [Wunderlich04b] show that, on the other hand, an increase in lattice constant *a* and decrease in lattice constant *c* would lead to a decrease in band gap energy. The authors suggest the possibility to induce such changes in lattice constants by depositing highly nanoporous anatase. They cite confirming results from other studies where it was found that nanoporous anatase shows a lower band gap than the bulk [Diallo05].

2.5.2 External defects (grain/ catalyst surface)

2.5.2.1 Surface roughness

Surface roughness increases the effective surface area of the material. This increases the number of active sites of the catalyst but also the number of defects. Since surface roughness is in many cases a macroscopic phenomenon, its increase is usually caused by a decrease in grain/primary particle size, especially in the case of powder catalysts. The effects of particle size will be discussed further in section 2.5.3.

One study reports that the surface roughness of TiO_2 can be changed under the influence of UV light [Katsumata06].

2.5.2.2 Crystal facets

In a study on the photocatalytic activity of rutile it was observed that the {101} crystal facets showed a much higher reactivity than the other facets [Lowekamp98].

Studies with preferentially oriented anatase thin films have shown various results, although mostly a preferential (112) orientation was reported to be favorable [Byun00, Kim02b, Tokita03], in another case it was (220) [Weinberger95]. In both cases only the out-of-plane orientation of the thin films was reported, not the faceting of their surfaces. In all cases, though, other structural changes occurred together with the crystallographic orientation, which could also influence the photocatalytic activity of the thin films.

2.5.2.3 Surface hydroxylation

The influence of water on the photocatalytic breakdown of organic substances was already discussed in section 2.4.4.5. The degree of surface hydroxylation not only depends on the relative humidity but also the structure of the catalyst surface. Hydroxyl groups are formed by water dissociation, so that it is favorable to have paired acid/ base sites situated at the appro-

priate distance [Carp04]. Sites with acid character are titania cations with lower coordination numbers: They initially bind the water molecules. Sites with basic character are exposed bridging oxygen which then accept the proton. From this it is understandable that the catalyst preparation conditions were found to play a major role in surface hydroxylation [Carp04, Sakthivel06].

The coordination number of Ti depends on the crystal facet forming the surface [Fujishima00]. Since Ti^{3+} has a lower coordination number, sub-stoichiometric surfaces are expected to show an increased surface hydroxylation, which has been verified in experiments [Carp04]. Si also has a lower coordination number (4), it is also observed that its addition to TiO_2 increases the degree of surface hydroxylation [Guan05]. Other additives like SO_4^{2-} and Cl^- influence the surface acid/base character [Carp04]. The behavior of these additives seems more complex, though, their reactivity depending on the nature of the organic studied in the breakdown reaction. A more thorough discussion of the effect of dopants on the photocatalytic activity of TiO_2 will be given in section 2.6.

2.5.3 Particle size

For very small particles (< 35 nm) their size has an effect on the crystallographic phase stability and the chemical activity. In general, research has shown that particles/grains in the nanometer range, which has been defined as < 100 nm, show a physical and chemical behavior different from larger grain sized material. It has become common to call such materials *nanostructured*, with *nanoparticles* being ultrafine dispersed particles and *nanocrystalline materials* being polycrystalline bulk materials with a fine grain/ crystallite size. Unfortunately, the terms 'crystal' and 'grain' are sometimes used as synonyms even though they describe something completely different. One has to keep in mind, too, that the primary particles can agglomerate to form secondary particles of > 100 nm size. We will here use '*particle*' for the primary and '*agglomerate*' for the secondary particle.

2.5.3.1 General effects of reduced particle size

a. Chemical activity

Nano-powders reach sizes of the order of biological molecules so that their activity in the human body is expected to differ from that of bulk material [Ball06a, Hove06]. With nanostructured materials the surface area is large compared to the bulk of the particle. This changes the Gibbs free energy of the material which controls its chemical activity. On the

other hand, the large surface area itself increases the catalytic activity of the nanostructured material by offering more places (active sites) for the reaction to take place.

As already discussed, the surface presents a defect state due to the presence of dangling bonds on the TiO_2 surface, so that sometimes one speaks of an increased number of oxygen vacancies. It is argued that this is why nanosized TiO_2 has a higher density of oxygen vacancies than large grain size TiO_2, as nanostructured materials have a higher surface to bulk ratio [Fernández-García04].

b. Optical and electronic properties

The fact that the particle dimension is smaller than the wavelength of visible light (ca. 400-700 nm) also results in different interaction with such light. One observes that the degree of light scattering is decreased, i.e. that more of the light can be absorbed [Mills97, Cornu02].

The small particle size also has the advantage that the charge carriers do not have to migrate far before they reach the surface, where they are needed for the catalyzed redox reaction. On the other hand the small particle size is associated with a higher number of defects in form of surfaces [Carp04], while the number of internal defects is decreased [Tjong04]. Since defects act as trap sites, the number of free charge carriers is expected to decrease. This can offset the positive influence of the short carrier migration distance. Therefore it is argued, that for optimum efficiency there is a critical size below which the surface recombination of electrons and holes becomes dominant due to the increased surface to volume ratio [Li02].

c. Mechanical properties

It is well known that the mechanical strength of a material increases with decreasing grain size. Therefore, nanocrystalline solids show a strongly increased mechanical hardness [Tjong04]. This aspect is normally of less relevance for (photo)catalysts, since here less dense structures are needed, which per definition have a lower mechanical stability.

For thin films the method of deposition plays an important role as it determines the adhesion of the film to the substrate as well as the general strength of the film (see also section 2.8.1).

2.5.3.2 Effect of particle size on the electronic properties (band gap)

a. Definition of terms

In covalent semiconductors quantum mechanical calculations show a transition from semiconductor to molecular properties for decreasing particle sizes. This means that the band structure of the semiconductor breaks up into discrete quantum levels. The transition point should be where the particle size reaches the order of the de Broglie wavelength of the charge carriers in the semiconductor. For most semiconductors this lies in the range of 5-25 nm, the exact value being dependent on the respective material [Mills97]. This change in electronic structure is commonly referred to as '*Quantum size effect*' (QSE) or '*Q-effect*', the respective particles are called '*Q-particles*'. The most wide-spread, simple theoretical framework to study the influence of confinement effects and how they depend on the primary particle size is the so-called '*effective mass approximation*' (EMA). More comprehensive discussions of the quantum size effect and the EMA are given in [Dumitriu00, Fernández-García04, Linsebigler95, Madhusudan Reddy02, Mills97, Schiavello97]; the original theoretical framework was developed by Brus in his work on CdS clusters [Monticone00]. The complete discussion of this theory goes beyond the scope of this thesis, but the most important points shall be repeated here. This theory is commonly used to explain the observed blue shift of the band gap in small grained anatase.

The bonding in TiO_2 is partially ionic. As a result, semiconductor band theory and molecular orbital (MO) theory, both of which are strictly speaking only valid for covalent bonding, must be applied with care to this material. There are some indications that the ionic nature of the bond increases with decreasing particle size [Fernández-García04]. In general, one can expect small grained TiO_2 to show a strong deviation from covalent behavior.

Another important issue concerning the application of the description of the quantum size effect to real materials is that it is, strictly seen, only applicable to free particles, e.g. a colloidal suspension. This condition is not fulfilled in the case of suspended agglomerated particles or crystals/ grains in a thin film. As a result, this theory can only be taken as an approximation. In point c the difficulties of applying it to the experimental results obtained for TiO_2 will be discussed.

b. Theoretical considerations

The electrons and holes produced in Q-particles are confined in a potential well of small geometrical dimensions. They do not experience the electronic delocalization present in a

bulk semiconductor possessing conduction and valence band, but instead, the confinement produces a quantization of discrete electronic states and increases the effective band gap of the semiconductor. As a result one observes a blue shift in the absorption and emission spectra of the material.

The dependence of the energy shift, ΔE, of the band gap on the particle size can be predicted by the three-dimensional confinement model based on the *effective mass approximation* (EMA). From experimental work it is customary to identify three different energy regions as a function of the average crystalline radius (R) of the secondary particle (i.e. agglomerated primary particles) [Fernández-García04]. Indeed, one looks how its size relates to the exciton (electron/ hole pair) Bohr radius a_B of the extended/bulk semiconductor, which is defined as $a_B = a_e + a_h$ (with a_e the electron and a_h the hole Bohr radius, respectively).

(1) $R > a_B$ or weak confinement region

This is the regime of weak confinement where the dominant energy is the Coulomb term. Here, size quantization of the motion of the exciton (the electron-hole pair is treated as quasi-particle) occurs.

(2) $R < a_B$ or strong confinement region

Here the Coulomb term can be treated as perturbation and electrons and holes are treated as confined independent particles. This means that the exciton is not formed, and the dominant factor is the separate size quantization of electron and hole. The change in band gap can be described by:

$$\Delta E = \frac{\hbar^2 \pi^2}{2R^2}\left[\frac{1}{m_e^*} + \frac{1}{m_h^*}\right] - \frac{1.786 \cdot e^2}{\varepsilon \cdot R} - 0.284 \cdot E_{RY} \qquad (2.32)$$

where $\hbar = 1.0545 \times 10^{-34}$ Js (reduced Planck's constant), R = particle radius, m_e^* = effective electron mass, m_h^* = effective hole mass, ε = dielectric constant, E_{RY} = effective Rydberg energy [$E_{RY} = e^4/2\varepsilon^2h^2(1/m_e^* + 1/m_h^*)$].

The equation consists of a first term, which represents the energy of localization, a second term, which represents the Coulomb attraction, and a third term, which represents the correlation effect. It follows from equation (2.32) that, at first approximation, the optical band gap energy should show an inverse squared dependence on the primary particle size, if strong quantum confinement dominates the energy behavior of the band gap in metal oxide semiconductors [Fernández-García04].

The effective band gap *E(R)* of the particle of size *R* is then determined by:

$$E(R) = \Delta E + E_g^{bulk} \qquad (2.33)$$

In [Fernández-García04] it is stated that the formulas developed by EMA overestimate the *E(R)* energy; they can be corrected by using an effective bond-order model (EBOM).

(3) Intermediate region

The region between weak and strong confinement has not been thoroughly investigated, as it was studied for some specific materials only.

c. Experimental studies

Measuring the influence of nanostructure in metal oxides using optical spectroscopy is mostly confined to the absorption onset energy. The reason is that the inhomogeneous broadening resulting from the particle size distribution induces broadening of the spectrum. This limits the study of the shape of the optical absorption spectrum. The onset of the optical absorption spectrum occurs at the so-called first exciton or optical band gap energy [Fernández-García04].

The increase in effective band gap and, consequently, the blue shift in the absorption threshold can become quite dramatic for bulk semiconductors with very small band gaps (e.g. PbS) [Linsebigler95]. The quantum size effect could also be verified for Fe_2O_3 and CdO but not for Cu_2O, CeO_2 and anatase TiO_2 [Fernández-García04]. While in some cases anatase TiO_2 is reported to show the quantum size effect, it was found to behave very differently from above discussion. In [Fernández-García04] the suspicion is raised, whether the presence of impurities or amorphous phases could be the reason for the blue shift of the band gap of TiO_2.

An example for the proof of the quantum size behavior is given in [Madhusudan Reddy02], where the effect of grain size on the band gap in nanocrystalline TiO_2 powder was determined. XRD and TEM analysis were used for estimating the grain size of self made (as calcined and reduced in H_2) and commercial TiO_2 powder. This yielded 5-10 nm (XRD) and 10-15 nm (TEM) for the self made powder and 39 nm (XRD) and 35-40 nm (TEM) for the commercial powder. The estimate of the particle size from the shift in absorption edge for UV adsorption spectra of powder suspended in water yielded a value of 7 nm when using equations (2.32) and (2.33) with $E_{RY} = 4.3 \times 10^{-39}$ J (calculated effective Rydberg energy), $\varepsilon = 86$ (dielectric constant of anatase). The authors take this as proof of the quantum size effect. For an average particle size of 5-10 nm the change in band gap energy was calculated to be

ΔE = 0.1-0.2 eV, i.e. E_g would be 3.3-3.4 eV. For a grain size of 39 nm the band gap energy was calculated to be about 3.2 eV (i.e. unchanged).

On the other hand, careful studies in [Monticone00] using colloidal powders showed no shift in band gap with decrease in particle size (measured by XRD). The authors attribute this behavior to a change in charge carrier mobility with decreasing particle size. They warn, therefore, not to use a measured shift in band gap energy to determine the particle size, as other factors could also cause such a shift.

2.5.3.3 Nature of the band gap transition

There is some discussion in literature about the nature of the band gap transition in nanostructured and amorphous TiO_2. Some authors [Fernández-García04, Madhusudan Reddy02] claim that for small grain sizes the band gap transition becomes direct. In [Madhusudan Reddy02] this was decided on basis of which value for *m* yielded the best results for fitting equation (2.12), p. 17, of section 2.2.4.4 to the experimental data. The authors suggest that photoluminescence studies could be used to support the observations in this study.

In [Fernández-García04] a possible explanation is given for the direct band gap transition of nanostructured anatase TiO_2. It is argued that the confinement of charge carriers in a limited space causes their wave functions to spread out in momentum space, in turn increasing the likelihood of radiative transitions for bulk indirect semiconductors. In [Li02] it is argued, though, that the enhancement of absorption observed in small nanocrystals is the result of the very high surface to volume ratio. Here the share of surface atoms is sufficiently high to increase the chance of surface absorption, which increases the light absorption in total. Both arguments are actually based on the fact that a direct transition shows a stronger light absorption than an indirect transition.

The transition to a direct band gap material of nanostructured anatase is interesting due to the fact that the absorption at threshold and the emission of light is much stronger for the direct system. This should result in a more efficient management of light and in improving the photochemical and/or physical performances of the nanostructured materials.

2.5.3.4 Effect of particle size on the photocatalytic activity of TiO_2

Overall there is quite some discussion about the effect of particle size on the photocatalytic activity of nanostructured TiO_2. The reason is probably that the different effects resulting from the small particle size have different influences so that, depending on the TiO_2 deposi-

tion conditions, other effects can dominate. Additionally, in most studies the particle size is poorly defined or has a large spread (e.g. due to agglomeration), so that dependencies cannot be found in a proper way.

The factors listed in section 2.5.3.1 already show both positive and negative effects on the availability of charge carriers at the surface which can offset the higher number of active sites due to the higher surface area. Any blue shift of the band gap will increase the redox potential of the semiconductor but will reduce its solar light absorption or make it necessary to use a UV lamp of higher frequency. This reduces in practice the efficiency of the catalyst. On the other hand, an enhancement in light absorption due to the shift to a direct band gap transition as discussed in section 2.5.3.3 would be beneficial. Unfortunately, so far no solid proof that the general photocatalytic efficiency of TiO_2 Q-particles (significantly) exceeds that of their larger counterparts could be provided. Factors like a well developed anatase crystal structure have been found to show a much larger influence (section 2.5.1).

2.5.4 Film thickness

Not much is reported on the effect of thickness on the photocatalytic activity of thin films besides some short studies included in [Jung05, Tada97], even though some authors are aware of the influence and correct for the variations in sample thickness [Fallet06]. In order to study the true influence of film thickness it is important that the structure of the film does not change with film thickness, which was not the case e.g. in [Jung05]. Here very thick films up to 15 µm thickness were studied, and the film growth occurred in 2 stages. First a small sized columnar structure was formed which then grew into large size columns. After a film thickness of 2 µm the large sized structure was fully developed. Since most thin films studied for photocatalytic applications are < 1 µm, such structures are not representative.

In [Tada97] thin films with thickness between 50 and 250 nm were studied. Here it was found that the photocatalytic activity reached its maximum at ca. 140 nm, after which the activity remained constant. In [Nam04] a saturation film thickness of ca. 360-430 nm is reported. This indicates that the film thickness, above which the photocatalytic activity is no longer (strongly) dependent on the film thickness, is dependent on the thin film preparation techniques as well as the experimental setup for testing their photocatalytic activity. In [Tada97] thin films were illuminated both from the front and the backside (i.e. through the glass substrate). In the second case the maximum in photocatalytic activity was reached for a lower film thickness. The authors reasoned that the maximum (i.e. leveling off) in photocata-

lytic activity observed when illuminating from the front side is linked to the increasing light absorption in the film. On the other hand, they argue, the maximum observed when illuminating from the back is linked to the diffusion length of the charge carriers, i.e. the time the charge carriers need to migrate from the film/substrate interface to the surface of the film as compared to their recombination rate. The problem with this argumentation is, that adsorption depth and recombination before reaching the surface will play a role in both cases. The experiments reported and discussed in [Tada97] would indicate, that the depth limit due to recombination is lower than the absorption depth. In such a case, though, no discrepancy should be observed between the two measurements, since any charge carriers generated deeper than the maximum diffusion length will not reach the surface. Only if the carriers could originate from deeper than the absorption depth, one should be able to measure a difference between backside (i.e. through the substrate) and front illumination. In this case illumination from the back side should yield a larger film thickness before the maximum in photoactivity is reached; as the charge carriers are generated deeper in the film than the absorption depth. The reason for the observations in [Tada97] could be due to light absorption in or absorption at the glass substrate diminishing the amount of light reaching the film from the backside, decreasing the effective absorption depth. In any case it is understandable that the film structure influences the photocatalytic activity. Columnar grains allow light to be guided deeper into the material, and charge carriers have the possibility to migrate to the side-surface of a column which can be reached by the reactants due to the open structure of the film. This is why the films described in [Jung05] can show such a high photocatalytic activity.

2.6 Doping

2.6.1 General considerations

Doping is the process of adding small amounts of a second material without forming a second phase. The definition of a '*small amount*' of material can vary widely: while the semiconductor industry defines this as a '*controlled impurity*' reaching levels of maximum 10^{-10} at%, ceramic research uses the term for concentrations up to several at%. In this thesis the second definition is applied.

The distribution of the dopant in the crystals/ grains of the matrix material can be homogeneous or heterogeneous. In latter case one speaks of dopant segregation, which is usually unwanted. Heterogeneous dopant distribution can occur due to the processing conditions: Either the dopant is added in an inhomogeneous way or it segregates during a heat treatment step. When large amounts of the dopant material are added, either a mixed oxide (i.e. a new structure) or a second phase can form, which may or may not be a mixed oxide, depending on the mutual solubility limits of the two components. In these cases one speaks of mixed oxide formation rather than doping.

Noble metals or other semiconductor compounds (like CdS) can be added to TiO_2 with the aim to keep them as a finely dispersed second phase on the TiO_2 particle surface. This creates a semiconductor/ metal (e.g. TiO_2/ Pt) or semiconductor/ semiconductor (e.g. TiO_2/ CdS) junction which facilitates charge separation. It is an important method for enhancing the photocatalytic activity of TiO_2 but goes beyond the scope of this work and will not be discussed any further.

There are two major reasons for introducing dopants into TiO_2 in order to improve the photocatalytic activity:

1) To increase the quantum efficiency, i.e. to increase the number of photons effectively used for the catalyzed redox reaction. This can only be done by increasing the lifetime of the separated charge carriers (electron and hole) by inducing trap sites. These trap sites should only be so-called '*shallow*', i.e. their energy level should not be deep in the band gap. If the charge carrier is too tightly bound to the trap site it is not able to migrate to the surface and participate in the redox-reaction so that re-combination with its counter part occurs eventually. Shallow trap sites allow the lifetime of the charge carriers to increase while the charge carrier remains mobile, and thus available for redox reactions. Additionally, if the

trap sites generate localized levels within the band gap, the semiconductor can absorb extra light making it more efficient.

2) To decrease the band gap energy (i.e. red shift the optical absorption edge) enabling photocatalytic activity under visible light illumination. This makes it possible to use the photocatalyst in sunlight, eliminating the necessity to use UV lamps.

Additional effects of introducing dopants can be an increase in electrical conductivity and the compensation of other defects. These may also influence the photocatalytic activity of the semiconductor.

It was found that the controlled introduction of shallow trap sites was rather difficult so that the main focus of current research has turned to red shifting the optical band gap.

In [Asahi01] the requirements for generating visible light activity by the introduction of dopants are nicely stated:

(i) Doping should produce states in the band gap of TiO_2 that absorb visible light.

(ii) The CBM [conduction band minimum], including lower lying impurity states, should be as high as that of TiO_2 or higher than the H_2/ H_2O level to ensure its photocatalytic activity.

(iii) The states in the gap should overlap sufficiently with the band states of TiO_2 to transfer photoexcited carriers to reactive sites at the catalyst surface within their lifetime.

The conclusion in [Asahi01] is that anion (e.g. N^{3-}) rather than cation doping should be used, since latter often gives quite localized *d* states deep in the band gap of TiO_2 so that recombination centers are formed. Since their conclusions were based on theoretical conclusions, research in the direction of cation doping continues nevertheless as there is still a discrepancy between theoretical band gap calculations and experimental findings.

In this study it was chosen to look at the addition of V, Fe and Nd. Former two are well investigated dopants while latter has shown some promising initial results, as will be discussed further in section 2.6.5.

In order to elucidate this matter further, some general aspects of doping are discussed first. The addition of a dopant, i.e. a foreign atom/ion will, in the first place, affect the crystal lattice structure of the matrix, forming a defect. The exact nature of the defect depends on the position the dopant atom/ion takes in the lattice. This is discussed in more detail in section 2.6.2. In the second place the distribution of the dopant in the grain is important. Inho-

mogeneous dopant distribution can influence grain growth and facilitate the development of space charge regions, which is discussed further in section 2.6.3. In the third place the addition of a dopant alters the nature of the catalyst surface, due to the presence of a different atom/ ion and the altered defect state. Dopant segregation can also lead to a surface concentration that is different from the bulk. These issues are discussed in section 2.6.4.

It is clear from the above discussion that the distribution of the dopant in the TiO_2 catalyst structure is important. This distribution is controlled by the preparation method of the catalyst (e.g. homogeneous or non-homogeneous powder or film formation, post-deposition anneal treatments for crystallization). Even though the initial distribution of the dopant is homogeneous, a later heat treatment can change this distribution due to segregation. The dopant can be expected to behave differently when distributed homogeneously throughout the grain than when segregated at the grain boundaries. Concentrations of dopant on the grain surface may, therefore, not be identical to concentrations in the bulk of the grain and different from the total introduced dopant amount. Additionally, the dopant concentration in itself may have an influence on its distribution due to solubility limitations.

2.6.2 Defect formation in the crystal lattice

Foreign atoms are associated with defect formation in the original crystal lattice. In the case of TiO_2 there are two possibilities for dopant introduction: (i) the dopant is introduced as a metal oxide $MO_{n/2}$, with the cation M^{n+} replacing Ti^{4+} or (ii) a dopant anion is introduced to replace O^{2-}.

To determine which lattice position the cation can occupy one needs to look at its size. The following discussion can only be an approximation as ion sizes are not constant for a given ion. They depend on the coordination environment defined by the site the ion occupies in the crystal lattice: The type and number of the ligands surrounding it as well as the nature of the bonding between them. Fact is, that the ion adjusts its size to the lattice place it occupies. The ion sizes quoted in the following are average values for a coordination number of 6.

The octahedral site occupied by the Ti-ions in anatase is slightly distorted as to have a square base (best defined by the diagonal of 0.378 nm which is identical to the lattice constant *a*) and a long axis (0.398 nm). There are interstitial sites in the anatase structure, which can be described by a strongly distorted octahedron or a square bi-pyramid with the same square base as the TiO_6 octahedrons (diagonal = 0.378 nm) but have a long axis of 0.555 nm [Software1]. As a result these square bi-pyramids have a larger volume but still the same square base as the

TiO_6 octahedrons. Therefore, larger cations can be expected to occupy the larger interstitial site but will most likely cause a distortion of the square base of the bi-pyramide. Cations smaller than or similar in size to Ti^{4+} can occupy the cation lattice site. Some cations can take both positions due to their intermediate size.

As already indicated above, dopant anions normally only occupy the O^{2-} positions. If the anion is reported to go interstitial it is normally not introduced as anion but as oxo-anion (i.e. as cation with bonding to nearby O). An example is the introduction of NO^{-}, which is discussed in the section on N-doping into TiO_2.

According to its valence and its occupation site, vacancies in the cation or anion lattice or charge carriers must be created for charge balance. We can rephrase the definition of donor and acceptor doping, as given in section 2.5.1.1. If a metal ion with a valence lower than the lattice cation is introduced, one speaks of '*acceptor doping*', since this type of doping is usually associated with hole formation [Pankove71]. If the valence of the introduced cation is higher than that of the lattice cation one speaks of *'donor doping*', since this type of doping is associated with electron formation. This occurs under loss of oxygen. The electron can be associated with the Ti^{4+}, forming a Ti^{3+} state, which is identical to reduction of the TiO_2 to Ti_2O_3. Since for anion doping the charge is negative, a lower valence leads to donor doping, while a higher valence leads to acceptor doping.

In both acceptor as well as donor doping normally not only a charge defect is associated with the foreign ion, but also a size defect, since the ionic radii of dopant ion and lattice ion deviate to some extent. If a cation is substituted interstitially its charge will always be higher than the lattice site (which is equivalent to zero), so that the result is always donor doping. In this case there is a lattice distortion associated with the defect. If an ion of the same valence is introduced on the lattice site there is no nominal charge defect, but a lattice distortion will usually be formed due to the size difference.

Any lattice distortion will affect the polarizability of the cation-anion bond. If the electronegativity of the dopant ion is different from the lattice ion (which is normally the case) the polarizability of the bond between anion and cation also changes. The result is a local difference in resonance light absorption which results in a different optical band gap. From an electronic point of view, any lattice defect introduces an energy state in the band gap, a donor introduces a state (just) below the conduction band, while an acceptor introduces a state (just) above the valence band. There is disagreement on the exact depth of the defect state in the band gap as will be discussed in the section on cation doping. The states in the band gap may

facilitate the formation of an electron/ hole pair and increase the number of charge carriers, but they also may act as trap sites, decreasing the number of charge carriers, especially when they are deep in the band gap. In [Carp04] it is argued that the charge carrier trapping outweighs any positive benefits. On the other hand, the donor/ acceptor states in the band gap also lower the energy needed to form the electron/ hole pair, i.e. the effective activation energy of the catalyst. One expects to find these extra levels in optical transmission measurements as steps in the optical absorption edge.

A high number of dopant ions will eventually result in a broadening of the new band which will merge with the closest intrinsic band at very high concentrations [Pankove71]. One then receives a so-called 'degenerated' semiconductor. The result can be a shifted band gap energy compared to pure TiO_2. As already mentioned, the dopant concentrations in ceramics are usually quite high so that degeneration of the dopant levels can be expected.

Since the nature of the individual dopant as well as its concentration and distribution determine the defect structure of the crystal, it will also influence the electronic and optical properties of the resulting TiO_2 crystal. The experimental findings and theoretical band calculations for the selected dopants are given in section 2.6.5.

2.6.2.1 Cation doping

In the following the defect equations for adding a cation (as metal-oxide) to the TiO_2 lattice will be developed. The equations are formulated in the Kröger-Vink notation, with the left hand side of the equation giving the 'free' additive, and the right hand side of the equation showing how the additive is incorporated into the TiO_2 lattice. Therefore, on the left hand side the subscript denotes the stoichiometry of the added oxide. On the right hand side the subscript denotes the lattice position, the superscript denotes the charges with ' = negative charge and $^{\bullet}$ = positive charge with respect to the lattice site. A vacancy is denoted by *V*, the metal ion is denoted by *M*. The variable *n* gives the charge of the metal ion (e.g. for Ti^{4+} n = 4). As an example, an oxygen vacancy, which is double positively charged with respect to the oxygen ion normally on this lattice site, is written as $V_O^{\bullet\bullet}$. The radius of the cation is denoted by *R*.

<u>A. Substitutional ($R[M^{n+}] \approx R[Ti^{4+}]$)</u>:

a) M^{n+} has valence lower than Ti^{4+} (n < 4):

$$MO_{n/2} \xrightarrow{TiO_2} M_{Ti}^{(4-n)'} + n/2\ O_O + (4-n)/2\ V_O^{\bullet\bullet} \qquad (2.34)$$

The result is the formation of oxygen vacancies. One refers to acceptor doping in this case (section 2.6.2).

b) M^{n+} has valence equal to Ti^{4+} (n = 4):

$$MO_2 \xrightarrow{TiO_2} M_{Ti} + 2O_O \qquad (2.35)$$

Here no vacancies and no charged sites are formed. The only defect is a lattice distortion due to the different size of the foreign cation or difference in bonding between cation and anion (more or less ionic).

c) M^{n+} has valence higher than Ti^{4+} (n > 4):

$$MO_{n/2} \xrightarrow{TiO_2} M_{Ti}^{(n-4)\bullet} + (n\text{-}4)/2\ O_O + (n\text{-}4)/4\ V_{Ti}^{''''} \qquad (2.36)$$

$$MO_{n/2} \xrightarrow{TiO_2} M_{Ti}^{(n-4)\bullet} + 2\ O_O + (n\text{-}4)e' + (n\text{-}4)/4\ O_2\ (g) \qquad (2.37)$$

Here there is the possibility of forming a Ti-vacancy, or the formation of an electron for charge compensation (accompanied by loss of oxygen). One refers to donor doping in this case (section 2.6.2).

<u>B. Interstitial ($R[M^{n+}] > R[Ti^{4+}]$)</u>:

$$MO_{n/2} \xrightarrow{TiO_2} M_i^{n\bullet} + n/2O_O + V_{Ti}^{''''} + (4\text{-}n)\ V_O^{\bullet\bullet} \qquad (2.38)$$

$$MO_{n/2} \xrightarrow{TiO_2} M_i^{n\bullet} + ne' + n/4\ O_2\ (g) \qquad (2.39)$$

Here one has the possibility of forming both a Ti- and an O-vacancy (2.38), or electrons (2.39) for charge compensation. One can see, respectively, that the number of O-vacancies decreases (2.38), or the number of electrons increases (2.39), with the valence of the introduced interstitial. As already mentioned, interstitial cations are always donor dopants in TiO_2. Strictly speaking equation (2.39) is only valid for ions with an oxidation state of maximum +4. Usually higher oxidation states will lead to a smaller ionic radius so that such ions will be found on the Ti^{4+}-site.

The possibilities for cation doping are as large as the metallic part of the periodic table. A variety of these have been tested, probably with exception of the most toxic or the most difficult to obtain metals. Since it goes beyond the scope of this thesis to discuss all possible dopants the focus will be on the ones selected to be investigated in this study. Probably the most investigated additive is Fe_2O_3. Among other popular dopants are VO_x and Nd_2O_3. SiO_2 is also a frequently used additive, which has no effect on the electronic structure while influ-

encing the microstructure strongly, especially when added in high concentration leading to mixed oxide formation. Addition of SiO_2 was discussed briefly in section 2.5.1.2.

In the following table the relevant cation sizes for Ti and the different dopants discussed are listed; for further explanations please refer to the text.

	5+	**4+**	**3+**	**2+**
Ti	-	0.0605	0.067	N.A
Fe (high spin, hs)	-	N.A.	0.0645	0.078
Fe (low spin, ls)	-	N.A.	0.055	0.061
V	0.054	0.058	0.064	N.A.
Nd	-	-	0.0983	-

Table 2. 3: Cation sizes of Ti, Fe, V and Nd in nm [Greenwood84], 'N.A.' denotes that the ionic radius is not of interest here, '-' denotes that this ion does not exist.

a. Effect of Fe_2O_3 addition on the properties of anatase TiO_2

First we shall look at some general properties of Fe ions. Since Fe is in the middle of the 3d-row of the periodic table it is strongly affected by its coordination, i.e. its crystal field. Even though the crystal field theory is mostly used to explain the color and magnetic nature of transition metal ions in (aqueous) solution, it can also be applied, to some extent, to the solid state. In the crystal field theory the ligands coordinated to the transition metal ion cause a weak or strong field around it, which results in splitting of the energy levels of the five d-orbitals. In an octahedral coordination two orbitals are rendered energetically higher than the other three while in tetrahedral surroundings three orbitals are rendered energetically higher [Greenwood84]. A sketch of the crystal field splitting of the orbitals is given in Appendix A1. In a weak crystal field the electrons will be distributed over all orbitals, the energy difference between them being lower than the spin-coupling of two electrons in one orbital. The result is the maximum number of free spins, i.e. a '*high spin*' (*hs*) complex. In a strong crystal field filling of the lower energy orbitals first is energetically favored, so that the lowest number of free spins is obtained, i.e. a '*low spin*' (*ls*) complex. The filling of the orbitals for this case is also shown in Appendix A1.

As listed in Table 2. 3 the ionic radius of Fe^{3+} (d^5) depends on its electronic configuration. It is in any case similar in size to Ti^{4+}, so that it is commonly assumed that Fe^{3+} is present on the Ti^{4+} site [Carp04], although there are claims that it occupies interstitial sites [Fernández-García04]. Event though the +3 state is the most stable in an oxidized surrounding (as given

in TiO_2), easy transfer to the +2 state [Greenwood84] is possible. The latter has an ionic radius comparable to that of Ti^{3+}, but somewhat larger than that of Ti^{4+}. Therefore, one would expect the Fe^{2+} ion to go to an interstitial site.

As a result we can formulate the following possible defect equations for Fe-doping of TiO_2, taking into account the two different oxidation states:

A. Substitutional:

$$Fe^{3+}: \quad FeO_{3/2} \xrightarrow{TiO_2} Fe_{Ti}^{'} + 3/2\ O_O + 1/2\ V_O^{\bullet\bullet} \qquad (2.40)$$

$$Fe^{2+}: \quad FeO \xrightarrow{TiO_2} Fe_{Ti}^{''} + O_O + V_O^{\bullet\bullet} \qquad (2.41)$$

B. Interstitial:

$$Fe^{3+}: \quad FeO_{3/2} \xrightarrow{TiO_2} Fe_i^{\bullet\bullet\bullet} + 3/2 O_O + V_{Ti}^{''''} + 1/2\ V_O^{\bullet\bullet} \qquad (2.42)$$

$$FeO_{3/2} \xrightarrow{TiO_2} Fe_i^{\bullet\bullet\bullet} + 3e^{'} + 3/4\ O_2\ (g) \qquad (2.43)$$

$$Fe^{2+}: \quad FeO \xrightarrow{TiO_2} Fe_i^{\bullet\bullet} + O_O + V_{Ti}^{''''} + V_O^{\bullet\bullet} \qquad (2.44)$$

$$FeO \xrightarrow{TiO_2} Fe_i^{\bullet\bullet} + 2e^{'} + 1/2\ O_2\ (g) \qquad (2.45)$$

From the defect equations shown above one can see that substitutional doping of Fe needs to be compensated by the generation of oxygen vacancies in the ratio of 1 Fe^{3+} / ½ $V_O^{\bullet\bullet}$ and 1 Fe^{2+} / 1 $V_O^{\bullet\bullet}$. Interstitial doping of Fe has to be compensated by the formation of titanium and oxygen vacancies or the loss of oxygen combined with the reduction of Ti^{4+} to Ti^{3+} (generation of electrons). Substitutional doping leads to the formation of acceptor states while interstitial doping leads to the formation of donor states.

The presence of Fe^{3+} or Fe^{2+} on the Ti^{4+}-site presents an electronic defect of lower charge which must be compensated by an oxygen vacancy (see equations (2.40) and (2.41)). Both ions still have *d* electrons which can participate in electronic conduction, but both Fe^{3+} and Fe^{2+} as well as the accompanying oxygen vacancy form acceptor states. There is little information about the defect position of these two ions in the TiO_2 band structure, normally it is stated that Fe^{3+} creates states deep in the TiO_2 band gap [Asahi01]. For Fe^{2+} and Fe^{3+} present on an interstitial site, both would form a donor state (positive charge on the lattice position) which can be compensated by the formation of a Ti-vacancy [Fernández-García04], as one can see in the defect equations (2.42) and (2.44). Due to the difference in cation size one

would expect Fe^{3+} to substitute a Ti^{4+}, while Fe^{2+} would go to an interstitial site, so that former would comprise an acceptor state while latter would form a donor state.

Both Fe^{2+} and Fe^{3+} form a rather covalent bond with oxygen as compared to Ti^{4+} [Greenwood84] which means that the bond is easier to polarize.

According to [Carp04] Fe^{3+} has a half filled d^5 electronic configuration (in *hs* state) which is especially stable. In order to validate this statement one needs to look at the crystal field of Fe in an octahedral coordination by oxygen. Oxygen ligands have a weak crystal field splitting [Greenwood84], so that the high spin configuration will be adapted, i.e. all five d electrons indeed remain unpaired. Accepting or releasing an electron destroys this stable configuration which decreases the stability of the Fe^{2+} (and Fe^{4+}) state, so that Fe^{3+} should form a shallow trap site, which should facilitate the electron/ hole separation [Carp04]. As a result it is most likely that Fe substitutes in the +3 state onto a Ti^{4+} lattice site. One therefore expects it to act as acceptor dopant, according to equation (2.40). This is also supported by the cation size.

b. Effect of VO_x addition on the properties of anatase TiO_2

V has been applied as dopant to influence the properties of photocatalytic TiO_2. Since the vanadia/ anatase system has been studied rather intensely, it is known that VO_2 can grow isomorph onto anatase TiO_2 [Gao04, Gao06]. The interface between V_2O_5 and TiO_2 will show reduction of V to the +4 state [Eurocat97, Vittadini05]. Therefore it is commonly assumed that V substitutes onto the Ti^{4+} state having also the oxidation state +4. The ionic radii of the two V ions are both are smaller than Ti^{4+} (Table 2. 3, p. 57) so that substitution is possible.

V^{4+} can still be further reduced to the +3 state, which is less likely under oxidizing conditions, meaning that the V^{4+} state can be both an electron donor as well as an electron acceptor. The cation size of V^{3+} is still compatible with that of Ti^{4+} (Table 2. 3, p. 57), so that substitution is likely.

One can formulate the following defect equations for the substitution of V^{n+} (n = 3, 4, 5) into TiO_2 (here ***V*** denotes Vanadium and **V** denotes a vacancy):

Substitutional:

$$V^{3+}:\ VO_{3/2} \xrightarrow{TiO_2} V_{Ti}^{'} + 3/2\ O_O + 1/2\ V_O^{\bullet\bullet} \qquad (2.46)$$

$$V^{4+}:\ VO_2 \xrightarrow{TiO_2} V_{Ti} + 2\ O_O \qquad (2.47)$$

$$V^{5+}:\ VO_{5/2} \xrightarrow{TiO_2} V_{Ti}^{\bullet} + 1/2\ O_O + 1/4\ V_{Ti}^{''''} \quad (2.48)$$

$$VO_{5/2} \xrightarrow{TiO_2} V_{Ti}^{\bullet} + 2\ O_O + 1e' + 1/4\ O_2\ (g) \quad (2.49)$$

As a result, the Vanadium ion will comprise an acceptor dopant when in the +3 state, a donor dopant in the +5 state and a charge neutral dopant when in the +4 state.

As with all transition metal oxides, the ionic character of the bond with oxygen decreases with increasing oxidation state, i.e. its polarizability increases [Greenwood84].

c. Effect of Nd_2O_3 addition on the properties of anatase TiO_2:

Neodymium is a frequently used rare earth dopant which has a stable oxidation state of +3 due to its electron configuration (even though sometimes the possibility of reduction to the +2 state is reported [Greenwood84]). Its ionic radius is substantially larger than that of Ti^{4+} (Table 2. 3, p. 57), so that substitution on the Ti^{4+} site is rather unlikely. Therefore, it is normally assumed that it is present in an interstitial site.

The following defect equations can be formulated for the incorporation of Nd^{3+} onto interstitial sites in TiO_2:

Interstitial:

$$NdO_{3/2} \xrightarrow{TiO_2} Nd_i^{\bullet\bullet\bullet} + 3/2 O_O + V_{Ti}^{''''} + 1/2\ V_O^{\bullet\bullet} \quad (2.50)$$

$$NdO_{3/2} \xrightarrow{TiO_2} Nd_i^{\bullet\bullet\bullet} + 3e' + 3/4\ O_2\ (g) \quad (2.51)$$

One can see that either Ti-vacancies or electrons need to be generated for charge compensation, which makes Nd^{3+} a donor dopant.

Nd follows the chemistry of yttrium (Y) in having a rather low electro-negativity, so that its bond with oxygen has a rather ionic character, i.e. is little polarizable. Since Nd is a rare earth element its electronic behavior is dominated by its 4f electrons, the +3 state having the electron configuration $4f^3$ [Greenwood84]. This makes it a good candidate to red shift the absorption edge of TiO_2 [Carp04]. Due to the 4f electrons Nd^{3+} shows good photoluminescence, which is utilized in e.g. Nd-YAG lasers.

Rare earth ions are known for their ability to form complexes with various Lewis bases [Carp04], which makes them interesting to be present at the catalyst surface to interact with organic substances.

2.6.2.2 Anion doping

According to the defect equations for cation doping into the TiO_2 lattice one can develop the defect equations for anion doping. Here we need to look at the replacement of O_2^- or the interstitial doping of the anion. In many cases care has to be given to the exact nature of the incorporated additive, as most anionic dopants can also form oxo-anions. An example is doping with nitrogen, where oxo-anions like NO^- can be formed. The nitrogen is then actually incorporated as cation, namely N^{3+}. This is usually the case when the anion is reported to go interstitial. In this chapter we want to consider true anion doping by N^{3-} and S^{2-}, which are the most studied anionic dopants after they were found to be promising according to calculations performed by [Asahi01].

According to the defect equations formulated for the incorporation of cations as metal oxides we will look at the incorporation of the anions A using a nominal Ti^{4+}-A^{n-}compound.

<u>A. Substitutional ($R[A^{n-}] \approx R[O^{2-}]$)</u>:

a) A^{n-} has valence lower than O^{2-} (i.e. n = 1):

$$Ti_{1/2}A_2 \xrightarrow{TiO_2} 1/2\ Ti_{Ti} + 1/2\ V_{Ti}^{''''} + 2\ A_O^{\bullet} \qquad (2.52)$$

$$Ti_{1/2}A_2 \xrightarrow{TiO_2} 1/2\ Ti_{Ti} + 2\ e' + 2\ A_O^{\bullet} \qquad (2.52)a$$

The result is the formation of titanium vacancies or electrons, resulting in donor doping.

b) A^{n-} has valence equal to O^{2-} (n = 2):

$$TiA_2 \xrightarrow{TiO_2} Ti_{Ti} + 2A_O \qquad (2.53)$$

Here no vacancies and no charged sites are formed. The only defect will be a lattice distortion due to the different size of the foreign anion or difference in bonding between cation and anion (more or less ionic).

c) A^{n-} has valence higher than O^{2-} ($4 \geq n > 2$):

$$Ti_{n/4}A \xrightarrow{TiO_2} n/4\ Ti_{Ti} + (4\text{-}n)/4\ V_{Ti}^{''''} + A_O^{(n-2)'} + V_O^{\bullet\bullet} \qquad (2.54)$$

Here oxygen vacancies are formed resulting in acceptor doping.

<u>B. Interstitial ($R[A^{n-}] > R[O^{2-}]$)</u>:

$$Ti_{n/4}A \xrightarrow{TiO_2} Ti_{Ti} + (4\text{-}n)/4\ V_{Ti}^{''''} + A_i^{n'} + 2\ V_O^{\bullet\bullet} \qquad (2.55)$$

Since the interstitial anionic defect always has a negative charge, it always generates oxygen vacancies, i.e. is an acceptor dopant.

a. Effect of N addition on the photocatalytic activity of TiO_2

The addition of N to TiO_2 has become a very popular means to induce a red shift of the light absorption due to narrowing of the band gap [Carp04]. Films and powders of $TiO_{2-x}N_x$ show an improvement over pure TiO_2 in visible light (< 500 nm). Various methods have been employed to introduce N into TiO_2 [Carp04]. Nitrogen as dopant can be incorporated as N^{3-} or NO_x^- species, and also as N_2. Here we will look at the incorporation of N^{3-}, which is mostly assumed to substitute for O^{2-} since this type of N incorporation has been found to be the reason for the VIS light photocatalytic activity. The ionic radii of N^{3-} (0.146 nm) and O^{2-} (0.140 nm) match rather well [Greenwood84] and the two ions are iso-electronic, i.e. contain the same number of electrons in their shell.

Since N has a lower electro-negativity than O, the nature of the Ti-N bond is less ionic, i.e. it will be easier to polarize the bond. While TiO_2 is a transparent and colorless insulator, TiN is a metallic conductor and opaque [Greenwood84]. From the chemical formula it is already clear that in the former Ti is present in the 4+ state while in latter it is present in the 3+ state, so that the presence of N changes the stable oxidation state of Ti.

For the incorporation of N^{3-} into the TiO_2 lattice one can formulate the following defect equations. Formally, the anion will be added as Ti^{4+}-N^{3-} compound (not to be confused with TiN, where Ti is in the 3+ state).

A. Substitutional:

$$Ti_{3/4}N \xrightarrow{TiO_2} Ti_{Ti} + 1/4\ V_{Ti}^{''''} + N_O^{'} + V_O^{\bullet\bullet} \qquad (2.56)$$

B. Interstitial:

$$Ti_{3/4}N \xrightarrow{TiO_2} Ti_{Ti} + 1/4\ V_{Ti}^{''''} + N_i^{'''} + 2\ V_O^{\bullet\bullet} \qquad (2.57)$$

In both cases titanium and oxygen vacancies are created together for compensating the charge defect. More oxygen vacancies are created in the case of interstitial incorporation.

b. Effect of S addition on the photocatalytic activity of TiO_2

When adding S to TiO_2 there are different possible dopant states: S can be substituting as S^{2-} for O^{2-} , which is not straightforward due to the large difference in ionic radii, being 0.184 nm for S^{2-} and 0.140 nm for O^{2-}. The other possibilities are that S is incorporated in the

form of SO_4^{2-} or SO_3^{2-}, were S is in the oxidation state of +6 or +4, which can happen even unintentionally when a wet chemical process involving the use of sulfates/sulfites is used.

2.6.3 Defect segregation in TiO_2 – formation of a space-charge region

When there is a separation of the charged defects between grain bulk and grain boundary, a so-called '*space charge region*' develops. This will aid in separating the electron-hole pair formed by UV-illumination in TiO_2. Such a charge separation can occur due to processing, but mostly occurs due to diffusional effects during heat treatment [Weibel06b]. From dopant cations it is known that they tend to segregate to the grain boundaries. No information about anion segregation was found.

If a donor dopant segregates to the grain boundary a positive charge develops there, whereas a negative charge develops in the bulk of the grain. The resulting electric field draws electrons to the grain surface and holes to the grain bulk. This is the opposite of what is desirable for photocatalysis where the holes are needed at the grain surface to oxidize the organic.

For acceptor doping the space charge region leads to the opposite, drawing the holes to the surface and the electrons to the grain bulk. Even though now the holes would be available for oxidation of the organic, the electrons are nevertheless needed for the reduction of the ambient oxygen to close the redox-cycle (see section 2.4.2). This is often forgotten in arguments stating that acceptor doping is beneficial to improve the photocatalytic activity of TiO_2.

In conclusion, dopant segregation, especially that of donors, should not be beneficial for photocatalysis since both electron and hole are necessary for the photocatalytic process. Additionally one has to remember, that metal ions or oxygen vacancies can be electron/hole trap sites, which extends the lifetime of the electron/ hole. But in general the trap site is too deep so that the charge carrier is no longer available for the redox reaction [Asahi01].

It is difficult to predict dopant segregation in the nano-crystalline anatase materials used for photocatalysis. Usually the behavior of dopants or other defects [Bak03a-d] is studied for high temperature equillibria [Wang2004], where rutile is the stable phase and grain sizes are large (> 1 µm). In [Wang2004] rutile TiO_2 was doped with 0.025-0.3 mol% Y^{3+} (sintered at a temperature of 1300°C for up to 14 h). Here a segregation region of a few nm was found in grains of 6-7 µm size which means that the space charge region is on the order of 0.1% of the grain diameter. In nano-crystalline anatase TiO_2 a space charge region of a few nm would amount to 10-100% of the grain diameter, so that here the dopant distribution would be inhomogeneous throughout the whole grain. In [Fernández-García04] it is predicted that for this

reason the degree of segregation should be reduced with decreasing grain size. Additionally, the anneal temperatures of anatase lie in the range of 300-600°C (as to avoid transformation to rutile), which results in a much lower diffusion rate and, therefore, degree of segregation.

Experiments on doping of nanostructured materials have shown, though, that it is very difficult to actually introduce dopants into nanocrystalline grains [Ball06b]. Since the diffusion length to the crystallite surface is small, dopants can reach it easily, a state which seems energetically more favorable. This has been verified by electronic band calculations that showed that the introduction of a foreign atom/ion into a nanocrystal increases its energy, making it energetically not favorable [Ball06b]. The process of impurity elimination by nanocrystals is referred to as '*self purification*'.

According to [Carp04] the extent of the space charge layer should be identical to the penetration depth of UV light in the material, which depends on the absorption coefficient α of the material and the wavelength of the UV light (see also Figure 4.67, p.219). For nanocrystalline TiO_2 this penetration depth was found to be larger than 150-400 nm (see section 2.5.4), which is larger than the grain size in nano-structured materials (< 100 nm). This means that a useful space charge layer can never be developed within the grains. Since most films or powder agglomerates also have a thickness in the sub-micrometer range, there is also not the possibility to develop any space charge region throughout the thin film or agglomerate. In conclusion, charge carrier separation due to the formation of a space charge region can not be accomplished in nano-structured materials.

2.6.4 Effects on the surface structure

The introduction of a dopant will also affect the surface structure of the TiO_2 photocatalyst. Since segregation most likely occurs due to solubility limits, the defect structure and dopant concentration of the surface and sub-surface may differ from that of the bulk.

Apart from the foreign ions being present at the surface, which themselves can have a different chemical activity, the surface will show an altered charge carrier concentration and availability, as already discussed in section 2.6.3. The oxygen vacancy concentration may also be affected due to the cation segregation. As a result the number of surface hydroxyl groups can be changed, which mounts to a change in catalytically active surface sites.

The presence of a second phase will result in a mixture of two semiconductor phases. If two semiconductors having a different band gap are in contact with each other (heterojunc-

tion) an electrical potential gradient is created, which enhances the electron-hole separation. One has to keep in mind that a different reaction mechanism for photocatalytic breakdown may be observed for such a two-phase semiconductor.

2.6.5 Reported experimental results

There are many reports on the effect of a variety of dopants on the photocatalytic effect of TiO_2. Some studies try to be systematic by changing only one parameter, namely the dopant concentration in the starting materials. But in many cases the finally studied material (after all processing steps) shows a change in more than one parameter (e.g. additional micro-structural and oxidation state changes induced by the dopant addition). This, and the fact that usually little is reported on the distribution (or even the actual concentration) of the dopant in the final material, makes it sometimes difficult to interpret the results. Additionally, the exact reaction conditions for testing the photocatalytic activity are also rarely standardized (see chapter 2.7). As a result contradictory results for the same dopant seem to be obtained between research groups, most of which can be resolved when comparing them in more detail.

Most studies have focused on doped powders (or, to a less extent, on thin films) applied for the removal of pollutants in a watery suspension. Little is reported on doped thin films used for air cleaning, although this is being increasingly more investigated.

The addition of cationic dopants has been studied for decades while the addition of anionic dopants, such as N and S, has only rather recently been focused on. Cationic and anionic dopants are discussed in sections 2.6.5.1 and 2.6.5.2, respectively. Since sodium plays a special role, as it can be introduced unintended due to the choice of substrate, this issue will be treated separately in section 2.6.6.

When looking at the electronic properties, doping will influence two factors (section 2.6.1), namely (i) the charge carrier separation and mobility and (ii) the absorption edge. The first factor will affect the number of photons which can be utilized for the chemical redox-reaction while the second will change the wavelength of the light needed to activate the catalyst, mostly trying to shift the absorption edge towards visible light.

As already mentioned, doping can also influence the catalyst structure, e.g. by changing the anatase to rutile transformation temperature or influencing the crystallization process. These issues will not be discussed in detail here since the focus of this section lies on the electronic and optical properties of doped TiO_2. Additionally, very little is reported on the actual influence of the dopant on the film/ powder structure. One important issue that will be dis-

cussed, though, is the effect of the dopant on the number of oxygen vacancies and the reduction of Ti^{4+} to Ti^{3+} (i.e. the stoichiometry).

Finally it must be stated that the effect of the dopant can differ for the specific organic breakdown reaction observed: the reactivity may be changed and different breakdown pathways may be observed. This issue will not be discussed here since the main focus of this thesis lies on the structural characterization of (doped-) TiO_2. It is an important factor, though, to keep in mind when comparing results between different research groups as often different organic test substances and different experimental set-ups are used.

When discussing the effect of a specific dopant, the conclusions of the authors of the according study will be given, but also the, sometimes on the side line, reported structural changes shall be pointed out, in an attempt to separate out the pure electronic effects.

2.6.5.1 Cation doping

a. Effect of Fe_2O_3 addition on the properties of anatase TiO_2

The effect of the addition of Fe-ions to TiO_2 is not always clear and contradictory effects on the photocatalytic activity are reported. This is likely due to the fact that hydroxylated Fe(III) species (which form in water) are active UV-absorbers, which can enhance the photocatalytic activity of TiO_2 when absorbed to its surface, e.g. [Franch04]. Due to processing conditions Fe(III)-oxide or salts can remain at the surface of the final TiO_2 catalyst, which can hydrolyze in water. This results in the presence of Fe^{3+} species attached to the surface of TiO_2 or in the solution and not to Fe^{3+} doped into the lattice of TiO_2. Care must be taken that these two different methods for modifying the activity of TiO_2 are not confused, which may have happened unintended in the past. When carefully looking at the effects due to true Fe-doping the results seem more consistent. One of the issues that has not been answered completely yet is which oxidation state the Fe ions have and which position they take in the TiO_2 lattice, and whether their oxidation state is fixed or variable.

When looking at the different reports on the effect of Fe-doping on the structure and properties of TiO_2 thin films and powders a number of common results independent of the method can be found:

1. The incorporation of Fe into the TiO_2 lattice promotes the anatase to rutile transformation. A gradual increase in rutile contents with increasing Fe content was observed at otherwise unchanged deposition conditions [Bally98, Weibel06a, Zhang03a-c] for Fe concentrations

above a certain threshold value (0.32 to 15 at%). The reason for the increasing phase stability of rutile with Fe-content is, according to [Wang06b] due to the higher tolerance of rutile towards defects (e.g. vacancies and/or interstitial cations) which comes from the difference in crystal structure. The lower number of edge sharing TiO_6 -octahedrons in rutile should make it more easy to compensate deformation of the octahedrons. In one case amorphous films were deposited when Fe was incorporated into TiO_2 as compared to the deposition of undoped films [Carneiro05].

2. For the oxidation state and the lattice position of the incorporated Fe it is mostly assumed that it is substituting into Ti^{4+} sites as Fe^{3+}, due to its ionic radius [Bally98, Carneiro05, Li02, Wang06b, Zhang03a-c], which was mentioned in the general discussion. In one study XAFS measurements were performed [Chiker03, Yamashita03] which indeed found Fe to be present as Fe^{3+} in an octahedral O surrounding. A.R. Bally et. al [Bally98], though, are careful and state "Fe atoms do not behave as simple substitutional impurities replacing Ti atoms in the oxide lattice". One has to remember that many interpretations are based on above mentioned assumptions.

3. Band gap calculations [Chiker03, Yamashita03] showed that the presence of implanted Fe^{3+} decreases the band gap of TiO_2. This is confirmed by experimental observations of an increasing red-shift of the absorption edge [Bally98, Carneiro05, Chiker03, Wang06b, Yamashita03, Zhang03a-c] with increasing Fe content. In one case this was interpreted as a result of the increasing rutile content (which has a lower band gap than anatase) [Bally98].

4. Thermoelectric power measurements performed by [Bally98] showed n-type conduction for undoped and a trace amount of Fe dopant. For 0.13 at% a mixed n- and p-type conduction was found, which became pure p-type conduction for higher concentrations. This would mean that at low Fe-concentrations donor doping and at high Fe-concentrations acceptor doping is observed.

5. The location of the Fe ions with respect to the bulk seems important for the photocatalytic activity: it seems that the Fe should be present in the bulk but not at the surface of the sample in order to observe good VIS photocatalytic activity [Chiker03, Yamashita03]. Such inhomogeneous distribution of Fe was achieved by sub-surface implantation into powder compacts of anatase TiO_2 [Chiker03, Yamashita03] and these materials showed no difference in UV activity as compared to pure TiO_2. On the other hand homogeneous distribution of Fe in TiO_2 resulted in very little [Chiker03, Yamashita03] VIS activity and

a deterioration of the UV activity [Chiker03, Li02, Yamashita03]. In other cases an improved UV activity is found, but only for small Fe concentrations [Carneiro05, Zhang03a-c]. Usually these materials also showed a very small grain size.

6. There are two reasons given for the increased photocatalytic activity at very low Fe concentrations which is followed by a decrease in photocatalytic activity for increasing Fe concentrations: The first is [Zhang03a-c], that at low concentrations the increase in Fe-content is beneficial, until the solubility limit in anatase is reached. Higher concentrations of Fe result in its enrichment at the surface which deteriorates the photocatalytic activity. The second reason is, that there is a balance of oxygen vacancies to Fe^{3+} trap sites [Carneiro05, Zhang03a-c], with the increasing number of Fe^{3+} trap sites being detrimental to the photocatalytic activity.

In conclusion, when looking at the information found in literature there is one important result that is reflected in all studies, namely that the main effect of Fe-doping is the red shift in the optical absorption edge. This indeed enables the materials to utilize sunlight more efficiently, as was shown in [Chiker03, Yamashita03]. All references indicate that the positive effect of Fe seems to be valid only for concentrations below 1 at%, which is linked to its solubility limit in TiO_2. The exception is the study discussed in [Chiker03, Yamashita03] where the negative effect was found already at much lower concentrations.

As for the position and oxidation state of the Fe in the TiO_2 lattice, it is mostly assumed that Fe^{3+} substitutes for Ti^{4+} based on its ionic size, resulting in acceptor doping. In [Chiker03, Yamashita03] EXAFS measurements confirmed this hypothesis. Most studies report that using ESCA was not successful due to a too low response of the Fe signal at dopant levels below 1 at%, making detailed investigations difficult or impossible. In point 4. it is indicated that the defect situation is different for very low and moderate to high Fe concentrations. The n-type (donor) doping at very low concentrations indicates, according to equations (2.40) to (2.45), p. 58, that the Fe is incorporated interstitially and not substitutionally as commonly assumed.

Some authors discuss the importance of oxygen vacancies that are formed together with the introduction of Fe. When looking at the defect equations (2.40) to (2.45) and considering the fact that Fe is found to be incorporated on substitutional sites in the 3+ state it is necessary that oxygen vacancies are formed in order to compensate for the charge defect of the cation. The ratio between Fe^{3+} and oxygen vacancies needs to be 2:1. Any change in this ratio can only be achieved by increasing the number of oxygen vacancies which must be accompanied

by electron/Ti^{3+} formation accompanied by the loss of O_2. According to the defect equations (2.40) to (2.45), p. 58, one would expect a lower ratio between Fe^{3+} and oxygen vacancies for interstitial doping, due to the possibility for electronic compensation. Here oxygen vacancies are also accompanied by titanium vacancies.

Interesting is the hypothesis that it is the oxygen vacancies, whose formation is induced by Fe-doping, who are influencing the photocatalytic activity in a positive manner. This would indicate that formation of electrons for charge compensation is negative.

With regard to the photocatalytic process, there seems agreement among the studies that the charge-trapping properties of the Fe-ions are detrimental under UV-illumination. Since TiO_2 has little activity in visible light, any band-gap shift to lower energy will potentially increase the photocatalytic activity. In [Chiker03, Yamashita03] it was emphasized that the Fe should be implanted into the bulk of the material, leaving the surface more similar to undoped TiO_2. This leaves the conclusion that the presence of Fe on the surface is detrimental to the photocatalytic activity. If this is true, then bulk doping of Fe^{3+} facilitates the adsorption of VIS light and the Fe-free surface allows the catalytic surface properties of pure TiO_2 to be undisturbed, which is mentioned in [Anpo03]. The defect structure of the bulk is not discussed, but presumably is the same as for other films of the same dopant concentration. The positive effect of Fe in the thin films may therefore be due to the same reasons as observed by [Bally98], namely the different defect structure observed at very low concentrations.

b. Effect of VO_x addition on the properties of anatase TiO_2

It was found that SiO_2 supported V_2O_5 is photocatalytically active under UV and VIS light [Ismail03, Takenaka97, Wada98], the exact wavelength depending on the organic substrate to be removed [Wada98]. According to [Takenaka97, Wada98] unsupported V_2O_5 showed no photocatalytic activity.

V-doped anatase TiO_2 ($V_{0.05}Ti_{0.95}O_2$) was found to be ferromagnetic up to a temperature of 400 K [Hong05]. The oxidation state of the incorporated V was not determined, but the ferromagnetism was suspected to be due to V being in a lower oxidation state (+4 and/or +3) rather than due to the presence of V-clusters. Electronic structure calculations [Wang05b] looking at the presence of V^{4+} ions in the anatase structure showed that ferromagnetism would occur in such a material. This material is interesting for enhanced separation in slurry reactors (where a powder is suspended in water) by applying an external magnetic field [Carp04].

From the reports on the effect of V-doping into anatase TiO_2 on the optical and photocatalytic properties one can find the following results:

1. EXAFS results obtained by [Anpo03, Yamashita02] led to the conclusion that V-doping of TiO_2 by high energy ion implantation followed by annealing resulted in substitutional incorporation of V^{4+} and V^{3+} onto Ti^{4+} sites. These materials showed a low presence of V at the surface and good VIS and UV photocatalytic activity, which was the best at a dopant level of $13.2x10^{-7}$ mol/g-cat (ca. 0.01 mol%).
2. Comparison of experimental results and calculations showed a narrowing of the electronic band gap due to the long distance interaction of the implanted ions rather than the formation of impurity energy levels due to metal oxide cluster formation [Anpo03].
3. A red shift of the optical absorption edge which increases with V-content is found [Anpo03, Yamashita02]. However, in [Yamashita02] this is reported to be the case only up to a certain dopant level.
4. Standard wet chemical doping techniques show that V is incorporated as V^{4+} and V^{5+}, whereby the V^{5+} content increases with the amount of V added [Iketani04].
5. V^{5+} is not beneficial for VIS photocatalytic activity [Iketani04] because it has a low solubility in TiO_2 and, therefore, segregates to the grain boundaries.
6. No detrimental effect of V-doping was found under UV illumination [Iketani04].

To conclude, there is not much literature on V-doped TiO_2 for photocatalytic applications available. From the existing studies it seems that the amount and distribution of the dopant are important as well as its oxidation state. V should be present in small amounts below 1% [Iketani04] or even below 0.01% [Yamashita02]. Higher concentrations of V seem to favor formation of V^{5+} and segregation of the dopant to the thin film surface, both of which is stated to be detrimental to the photocatalytic activity [Anpo03, Yamashita02]. The main influence of the introduction of V is that it induces a red shift in the absorption edge which shifts the activity of the photocatalyst to VIS. Looking at the defect equations (2.46) to (2.49), p. 59-60, V^{4+} does not result in a charge defect, while V^{5+} is a donor dopant on the Ti^{4+} site. Charge defects are usually reported to be detrimental to the photocatalytic activity, which also makes V^{4+} more favorable as dopant.

c. Effect of Nd_2O_3 addition on the properties of anatase TiO_2

From the little information that could be found on the effect of Nd-doping into TiO_2 the following main points could be extracted:

1. With ESCA the oxidation state of Nd was concluded to be 3+ while the Ti remained in the oxidation state 4+ [Ismat Shah02, Li02].
2. It is assumed that Nd^{3+} will be in an interstitial position [Ismat Shah02, Li02].
3. An increase in photocatalytic activity in VIS was found [Ismat Shah02, Li02], which the authors see as a result of the following argumentation: The high oxygen affinity of the Nd-O bond creates a local positive charge on the Ti and /or creates an oxygen vacancy. Both would form an electron trap site which would increase the lifetime of the holes.
4. Calculations showed that in Nd-doped TiO_2 there are highly localized Nd 4f states present in the band gap region which resulted in the formation of donor states [Wang05a]. There is no information on what their effect on band gap transitions would be.

To conclude, the effect of Nd^{3+} doping on the photocatalytic activity of TiO_2 has not been investigated much. Band gap calculations showed that donor states are formed in the band gap of TiO_2. The formation of donor states is predicted by the defect equation (2.50), p. 60. As discussed before these are expected to act as (hole) trap sites, diminishing the photocatalytic activity of TiO_2. The opposite was found in [Ismat Shah02, Li02], where a positive effect of Nd-doping was found. This was claimed to be due to the oxygen affinity of Nd resulting in a positive charge on the Ti (which could be interpreted as the breaking of a Ti-O bond where both electrons are taken by the O) or formation of an oxygen vacancy, both would attract electrons. According to the defect equations formation of an oxygen vacancy is a possibility, which should be accompanied by a Ti-vacancy. In literature not much is discussed about the effect or the possibility of forming Ti-vacancies. These have a very high charge and most likely a high energy of formation will be associated with them. The reduction of Ti^{4+} is another possibility for compensating the charge defect introduced by the Nd^{3+}. According to the defect equation (2.50), p. 60, this would involve the breaking of one Ti-O bond and the loss of oxygen.

d. Concluding remarks on cation doping

When looking at the experimental and computational results reported on the different cation dopants, some common points become clear:

1. Only in (very) low dopant concentrations (< 1 at%) a positive effect on the photocatalytic activity is seen. As already discussed in section 2.6.2 for low dopant concentration discrete dopant levels are observed which merge for high dopant concentrations. Possibly the presence of discrete dopant levels is beneficial (low dopant concentration), but not that they merge to form a continuous band at high concentration. For very low dopant levels the impurities present in the base material become important, so that one will have to work with highly pure TiO_2 to measure the true effect of doping.
2. Charge neutral, followed by donor doping are more beneficial than acceptor doping for cations. The reason could be that the number of oxygen vacancies should be as low as possible.
3. Ion implantation results indicate that it may be best to keep the surface of the thin films dopant free as to preserve the reactivity of the undoped TiO_2 surface.

Nevertheless there are still quite some unanswered questions. If such small dopant levels have to be investigated it will be important to find methods for ensuring that high purity TiO_2 is studied and that these low dopant levels can be detected. Before studying the effect of doping, it will be necessary, though to fully understand the properties of the semiconductor TiO_2 on its own.

2.6.5.2 Anion doping

a. Effect of N addition to the photocatalytic activity of TiO_2

Since doping of TiO_2 with N has become popular the last years due to the fact that such materials showed good photocatalytic activity under VIS light a great variety of literature concerning this issue exists. Again, many publications just discuss the effect of N-addition to TiO_2, or the making of TiO_xN_y thin films or powders and testing their photocatalytic activities. The number of publications discussing the connection between the type of N-species incorporated into TiO_2 and their influence on its optical and photocatalytic properties is already less. In the following overview we will discuss mostly latter papers and focus on the type of N-doping that actually results in VIS light photocatalytic activity.

The influence of N-doping on the optical and photocatalytic properties of anatase TiO_2 can be summarized to the following points:

1. Electronic band structure calculations by [Wang05a] find a reduction of the band gap energy for N-doped TiO_2. No N-induced states in the band gap are generated which could

act as trap sites. In contrast to these results, calculations by [Long06] found that the introduction of substitutional N^{3-} into the anatase lattice resulted in the formation of three N 2p states located in the band gap close to the top of the valence band. These states are claimed to be responsible for the VIS light activity and have a shallow acceptor character (meaning that they lie close to the valence band) which improves charge separation. Electronic band calculations by [Asahi01] showed that substitutional doping with N will be the most effective way of red-shifting the light absorption since the p states of N can mix with the O 2p states, and its ionic size is favorable. On the other hand the same authors investigated interstitial doping of N and a combination of substitutional and interstitial doping of N, which corresponds to the introduction of molecular NO^- or N_2. They found that it results in the formation of bonding states below the O 2p valence band and antibonding states deep in the band gap. Both were found to be well screened and not interacting with the band states of TiO_2 so that they could not be active for photocatalysis.

2. Calculated absorption edges of substitutional doping of N^{3-} show a red shift of the absorption edge [Asahi01] which is confirmed by experiments on N-doped TiO_2 [Asahi01, Ihara03, Prabakar06, Wong06]. Also, observations of, the optical band gap (indirect transition assumed) [Prabakar06, Tanemura05], and of VIS photocatalytic activity when N is doped substitutional onto O^{2-}-sites as N^{3-} [Asahi01, Ihara03, Prabakar06] confirm the calculations. These effects increase with increasing N-content for low levels of N incorporation (< 5 at%). Also higher UV activity is observed [Chen04].

3. Interstitially doped N does not influence the VIS photocatalytic activity [Asahi01].

4. NO^- doping into TiO_2 does not affect the VIS photocatalytic activity [Ihara03].

5. In one study it was proposed that the oxygen deficiency created by N-doping is causing the VIS photocatalytic activity [Ihara03] because also VIS activity was observed in reduced TiO_2 which contains oxygen vacancies. It is proposed that the N resides at the grain boundaries stabilizing the formed oxygen vacancies by preventing re-oxidation during heat treatment. This is also brought forth by [Belver06a-b], where it is stated that oxygen vacancies in the bulk of the film cause the VIS photocatalytic activity. In the studied films no shift in optical absorption edge was found by localized states at the bottom of the conduction band. The authors suspect that the observed VIS photocatalytic activity is explained by an oxygen vacancy/ N-impurity interaction, which would result in the presence

of a defect derived density of unoccupied states located in the band gap at 2.0-2.5 eV above the valence band edge.

6. High amounts of oxygen vacancies are detrimental to the photocatalytic activity [Belver06a-b, Prabakar06].
7. The number of oxygen vacancies increases with increasing N-content in the films [Prabakar06].
8. Calculations by [Valentin05] have shown that the energy for introducing oxygen vacancies is substantially reduced due to N-doping, so that latter is likely to be accompanied by the formation of oxygen vacancies.
9. High amounts of N-doping induce structural changes which reduce the photocatalytic activity [Asahi01, Chen04].
10. As already discussed in section 2.5.1, good crystallinity [Wong06] and low local disordering [Belver06a-b] are important.
11. Formation of TiN must be avoided as it is a completely different material with metallic properties (opaque) [Tanemura05, Wong06] and it has no photocatalytic activity [Wong06].

In conclusion, substitutional doping of TiO_2 with N^{3-} has been predicted to generate a VIS light active photocatalyst which has been confirmed by experimental results. The defect equations (2.56) and (2.57), p. 62 show that four times more oxygen vacancies are created for interstitial than for substitutional doping of N. The reason for the higher activity of latter could, therefore, be linked to the lower amount of oxygen vacancies, as already found in the case of cation doping.

The most important is the controlled incorporation of nitrogen in a manner summarized nicely by [Wong06]: “Films with the maximum amount of substitutional nitrogen under minimum deterioration of anatase TiO_2 and without formation of TiN could be a rule to obtain the best visible light induced photocatalytic activity.”

b. Effect of S addition on the photocatalytic activity of TiO_2

The reports on studies of doping S into TiO_2 give a wide variety of results since they cover all possible oxidation states of S. Annealing of S^{2-}doped TiO_2 can result in oxidation of S to +4 or +6 [Ohno04, Takeshita06]. Latter authors propose that the S^{4+} is substituting for Ti^{4+}, which means that a charge neutral defect is created. Band gap calculations as well as

experimental results show that this type of doping results in a red-shift of the optical absorption edge as well as VIS light photocatalytic activity.

Calcination of TiO_2 impregnated with SO_4^- was found to be detrimental to the photocatalytic activity [Colón03, Ohno04]. In this case S^{6+} is present, yielding a donor state independent on whether it is substitutional or interstitial.

Calculations by [Asahi01] showed that substitutional doping of TiO_2 with S^{2-} should result in a similar narrowing of the band gap as N^{3-}-doping, but the much larger formation energy (due to its large ion size) should make incorporation of S^{2-} into TiO_2 much more difficult. The stable sulfide of Ti is TiS_2, i.e. Ti remains in the oxidation state +4. This material is a semiconductor with a rather covalent nature of the bond [Lindic05].

As a result, care has to be taken that the species of incorporated S is known so that it can be related to the observed optical and photocatalytic properties.

2.6.6 Na contamination

A special case of impurity doping is Na^+ contamination. Early studies discovered that the photocatalytic activities of annealed TiO_2 thin films depended strongly on the type of substrate used [Fernández95], where it was suspected that ions diffusing into the film during annealing influenced its activity. In [Tada97] the diffusion of Na^+ into the TiO_2 thin film from soda-lime glass was measured by ESCA depth profiling and a direct link between its lower photocatalytic activity and the Na-concentration was made. It was suggested that Na^+ acted as recombination center for electrons and holes.

As a result investigators started using soda-lime free substrates or a SiO_2 barrier coating [Mills03, Takeda01] when a heat treatment step is needed after deposition, to avoid incorporation of Na^+. It must be noted that also an uptake of Si from any kind of glass is observed [Tada97], which can have a beneficial effect (section 2.5.1.2).

Na^+ has an ionic radius of 0.095 nm [Greenwood84], which is rather large compared to the ionic radius of Ti^{4+} (0.0605 nm) so that one expects interstitial incorporation into the Ti-lattice. This makes it, according to the defect equation (2.38), p. 56, a donor dopant. According to [Nam04] Na^+ forms a shallow donor state in TiO_2, which makes it a rather unlikely recombination center. Since Na^+ has a high affinity to oxygen, reduction to Na^0 is rather unlikely [Greenwood84]. The Na-O bond is highly ionic and polarization of this bond is rather unlikely.

Some authors investigated the effect of a soda-lime glass substrate [Nam04] when heat treating TiO_2 films or of Na doping on TiO_2 powder [Bessekhouad2004, Zielinska2005]. In [Nam04] the resulting decrease in photocatalytic activity was related to the effect of Na^+ on the grain growth in the thin film upon heat treatment. Na^+ was found to retard the crystallization of anatase while increasing the particle size in the film. The photocatalytic activity was found to be correlated to the particle size within the films, rather than their Na content, the photocatalytic activity increasing with decreasing particle size. So the authors conclude that Na^+ in the films influences the photocatalytic activity by changing the particle size and not by acting as recombination center.

In [Bessekhouad2004] $NaNO_3$ was co-precipitated with TiO_2 and pure TiO_2 was first precipitated and then impregnated with $NaNO_3$ at a dopant level of 1-5%. The films were calcined at temperatures above 400°C for crystallization and dopant incorporation. No effect of Na^+ on the anatase crystallization was observed. It was found that Na^+ ions dissolved into water when the powders were immersed. The photocatalytic activity was found to decrease for two different organic molecules tested, while towards a third the photocatalytic activity improved with increasing Na-content. In total the authors concluded that the addition of Na^+ to TiO_2 is beneficial. They state that perhaps the uptake of other elements from the glass in combination with Na^+ (co-doping) is the reason for the negative behavior observed by other investigators rather than an effect of Na^+ alone. If one looks at their results, though, it seems that the positive effect of Na^+ addition is strongly dependent on the organic used as test substance. Also the fact that Na^+ dissolved into water shows that it was not incorporated into the TiO_2 lattice but remained absorbed on the surface of the powder. Since only one of the three tested substances showed a positive effect of Na^+, their results are not so much different from other groups.

In [Zielinska2005] anatase TiO_2 powder impregnated with 20 wt% NaOH and calcined at 550°C was studied. The powder was found to be a mixture of anatase and a second phase (Na-titanate) and showed a decreased photocatalytic activity. The final concentration of Na was not determined. This makes it rather difficult to compare this study to the others.

In conclusion one can say that concerning the effect of Na^+ on the properties of TiO_2 the best strategy is to avoid any Na-contamination by the correct choice of substrate.

2.7 Measuring the photocatalytic activity of TiO_2

In order to determine the activity of a photocatalyst it is necessary to develop an experimental procedure to either directly measure the conversion of light energy into the lowering of the activation energy (Figure 2. 2, p. 24) or to compare the evolution of a chemical reaction between different catalysts and/ or organic substances. Former is rather difficult, if not impossible to measure directly, while latter gives only indirect evidence of the catalyst activity. In the following it is discussed how the efficiency of a photocatalyst should be determined in an ideal setting and how this can be implemented in an actual experimental setting (2.7.1). Then follows a discussion on the two general types of chemical reactors which are mostly implemented (2.7.2), what methods are used to analyze the reaction mixture (2.7.3) and the commonly used types of UV-light sources (2.7.4). In the end there is a discussion on the types of photo-reactors used in literature (2.7.5).

2.7.1 Determining the efficiency of a photocatalyst

It is a rather complex procedure to determine the efficiency of a photocatalyst quantitatively. Standard definitions and procedures were established and are recommended by the IUPAC (International Union of Pure and Applied Chemistry) and a very detailed discussion of the procedures can be found in [Salinaro99, Serpone99]. Unfortunately most experimental settings are not compatible with the strict requirements stated by the IUPAC so that a more qualitative approach must be applied. We will therefore discuss only the implementation of this method for heterogeneous catalysis (section 2.7.1.1), recommended standards (section 2.7.1.2) and evaluate the specific problems faced in less ideal, e.g. industrial settings (section 2.7.1.3). This discussion was done for catalysis in liquids, but in [Salinaro99, Serpone99] it is claimed to be applicable for the gas phase as well. Some adjustments are necessary, though, which are discussed in section 2.7.5.

2.7.1.1 Heterogeneous photochemistry (solid suspended in a liquid phase)

As already discussed in the introduction, determining the absolute photonic efficiency is not straightforward. One therefore defines the '*relative photonic efficiency', ξ_r*, which allows for avoiding unnecessary errors and is independent of defining reactor geometry, light source, catalyst properties, etc., so that it can be used for comparing results between laboratories. It is applicable to any type of heterogeneous medium used.

The relative photonic efficiency ξ_r refers to the removal of the organic test substance so that it is related to (i) an acceptable standard process, (ii) a standard photocatalyst material and (iii) a standard 'secondary actinometer' (for determining the incident photon flow) in the photocatalyzed process. ξ_r is determined by relating the *initial rate of degradation of the organic test substance,* R^{in}*(test substance)* to the *initial rate of degradation of a standard* R^{in}*(standard)* for constant incident photon flow $R_{o,\lambda}$ reaching the reactor (using the same reactor geometry):

$$\xi_r = \frac{R^{in}(\text{test substance})}{R^{in}(\text{standard})} \qquad \frac{[\text{mol min}^{-1}]}{[\text{mol min}^{-1}]} \tag{2.58}$$

Ultimately ξ_r can be converted to the photochemically defined *quantum yield* Φ once the *true quantum yield for the standard* $\Phi_{standard}$ for a given photocatalyst has been determined:

$$\Phi = \xi_r \, \Phi_{standard} \tag{2.59}$$

Experiments using phenol as standard have shown that $\Phi_{standard}$ is approx. 10% for the TiO_2 photocatalyst [Salinaro99, Serpone99].

2.7.1.2 Recommended standards

a. Standard organic test substance

The standard *phenol* can be used for other *aromatic* substances (e.g. benzene derivatives). When using an *aliphatic substance* (alkane derivatives) a different standard may be needed. Here the photodegradation of *formic acid* is recommended.

Both of these suggestions will be difficult to implement in the gas phase, though, since both phenol and formic acid have a rather low vapor pressure. In this case a different organic test substance is needed as standard. No recommendations have been given for gas phase reactions yet.

b. Standard catalyst material (TiO_2)

Degussa P25 has been accepted by most researchers as standard for testing the photocatalytic activity of nanostructured TiO_2 powder. It is made by flame hydrolysis of $TiCl_4$ in the presence of hydrogen and oxygen, at temperatures above 1200ºC. The TiO_2 powder is then treated with steam to remove all HCl, which is produced as part of the reaction. The product is 99.5% pure TiO_2 [Cornu02]. The crystalline phases were determined to be 70-80% anatase and correspondingly 30-20% rutile [Beermann02, Cornu02, Ohno01, Salinaro99], a small

fraction of amorphous TiO_2 was also found [Cornu02, Ohno01]. On the crystallite size there is less agreement in literature, some state the crystallites have a size in the range of 21-30 nm [Beermann02, Cornu02, Mills02], forming aggregates of approximately 0.1 µm in diameter [Cornu02, Mills02]. Others state a crystallite size of 50 to 200 nm [Salinaro99]. In [Ohno01] the structure of the Degussa P25 powder was investigated by TEM and showed crystallites of ca. 25 and 85 nm for anatase and rutile, respectively. The crystallites are stated to be cubic with rounded edges and non-porous [Cornu02]. As impurities, traces of SiO_2, Al_2O_3, HCl and Fe are listed [Salinaro99]. The surface area was found to be between ca. 50 m^2/g [Cornu02, Ohno01] and ≈ 55 m^2/g [Salinaro99] (non-porous, BET specific surface area).

When looking for a standard for thin film catalysts it becomes more difficult. In literature two different options are discussed (i) a layer of P25 spin coated onto a reference surface and (ii) an anatase thin film deposited onto SiO_2 coated glass (Pilkington Active™) [Mills02, Mills03]. The latter material is rather thin (15 nm) so that it has a weak photocatalytic response (section 2.5.4). The use of a spin coated layer of Degussa P25 is also problematic due to the structure of the powder and the difficulty to control its thickness. So far no real standard for a TiO_2 thin film catalyst exists.

c. Standard procedure to determine quantum yields

The standard procedure to determine quantum yields, also referred to as the '*method of relative photonic efficiency*' is described in more detail in [Serpone99]. Here a brief summary will be given.

First the quantum yield for the degradation of phenol Φ_{ph} in an aqueous suspension (low loading) of Degussa P25 TiO_2 must be determined. Then, in order to determine the relative photonic efficiencies of other organic test substances, one uses the following procedure, where all reactions must be performed under exactly the same circumstances:

- First one determines the initial rate of disappearance of phenol, R^{in}*(phenol)*, in mol/min (a zero order reaction).
- Secondly one determines the initial rate of disappearance of the organic being examined, R^{in}*(test substance)*, also in mol/ min.
- The relative photonic efficiency, ξ_r is subsequently determined according to equation (2.58), p. 78.

– Given the quantum yield for the initial photodegradation of phenol, Φ_{ph}, which was determined to be 0.14 ± 0.02 at 365 nm by [Salinaro99, Serpone99] one calculates the quantum yield for the initial photodegradation of the organic under examination (also at 365 nm irradiation) according to equation (2.59), p. 78.

2.7.1.3 Industrial setting

In an industrial environment, where the efficiency of a given process is a significant component to determine its economic viability, various figures of merit have been proposed. It must be taken into account that for the process, e.g. for the oxidative degradation, not only the simple disappearance of the pollutant but also the conversion of total organic carbon (TOC) into inorganic carbon (CO_2) is important. Sometimes the process is viewed as complete when the organic substance has not been broken down completely but at least to the level of environmentally friendly products. These figures of merit do not discuss the fundamental quantity that describes the extent to which the absorbed photon (the efficiency) contributes to drive a certain event [Serpone99]. Therefore, values have to be interpreted carefully, as they cannot be compared between different settings.

2.7.2 Chemical reactor types (selection)

For determining the activity of a given photocatalyst two types of chemical reactors are frequently applied, namely the batch reactor and the plug flow reactor [Marin2000]. In the following two sections there will be a brief description of the two reactor types and how they are applied for photocatalytic reactions. In the end there will be a discussion on the advantages and disadvantages of these two reactor types.

2.7.2.1 Batch reactor

The batch reactor is run in a discontinuous mode, i.e. it is filled with reactants and reaction medium and then sealed. The reactor content is stirred to ensure temperature and concentration homogeneity throughout the reactor. The kinetics of such a batch reactor are rather simple, since no flow has to be taken into account.

If one looks at a simple two-step reaction

$$A \xrightarrow{k_1} Q \xrightarrow{k_2} P \tag{2.60}$$

with k_1 and k_2 the reactions rates of the respective reaction steps, and if both are irreversible and of first order, then we have in a constant volume:

$$dC_A/dt = -k_1 C_A \quad (2.61)$$

$$dC_Q/dt = k_1 C_A - k_2 C_Q \quad (2.62)$$

With the initial values of $C_A = C_{Ao}$ and $C_Q = 0$ at $t = 0$, integration of equations (2.61) and (2.62) yields:

$$C_A = C_{A,o} \cdot e^{-k_1 t} \quad (2.63)$$

$$C_Q = \frac{C_{A,o} k_1}{k_2 - k_1} \left(e^{-k_1 t} - e^{-k_2 t} \right) \quad (2.64)$$

and the concentration of *P* follows from the total mass balance according to:

$$C_P(t) = C_{A,o} - C_A(t) - C_Q(t) \quad (2.65)$$

As a result one obtains the concentration profiles as a function of the batch time as shown in Figure 2. 5:

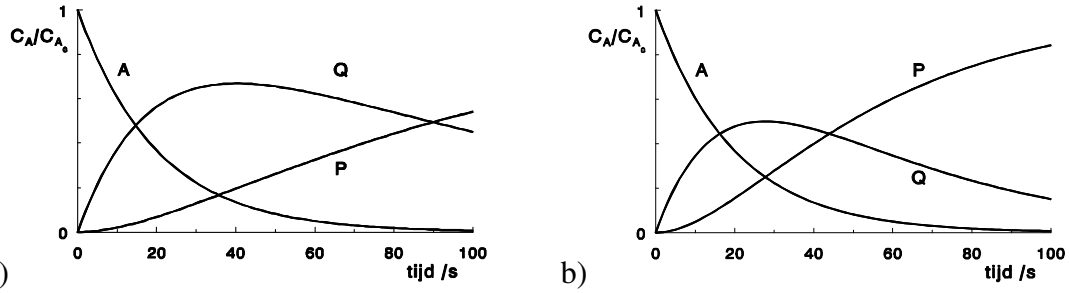

Figure 2. 5:

Concentration profiles vs. batch time for a first order reaction in a batch reactor. Left: results for $k_1 = 0.05\ s^{-1}$ and $k_2 = 0.01\ s^{-1}$, right: results for $k_1 = 0.05\ s^{-1}$ and $k_2 = 0.025\ s^{-1}$ [Marin2000].

2.7.2.2 Plug flow reactor

The plug flow reactor is run in a continuous mode, i.e. reactants and reaction medium are added to and removed from the reactor continuously. The reactor housing is usually a long tube with a length to diameter ratio of 10 to 1 000. This aspect ratio is the result of heat transfer requirements. In the ideal plug flow reactor the added ingredients are assumed to flow through the tube as a '*plug*', i.e. there is no concentration gradient in the radial direction. Since the reactants react on their way through the reactor, there will be a concentration gradient in axial (i.e. flow) direction. Another assumption in the flow reactor is that only forced convection is present. Since there is a continuous flow through the reactor, there is a specific time τ_o (the residence time) during which each fluid element remains in the reactor. In the ideal plug flow reactor there will be no spread in the residence time. Since there is a continu-

ous flow through the reactor one needs to take flow parameters in addition to the chemical terms into account when describing the reaction kinetics in the reactor.

The typical concentration profile for a reactant *A* entering the reactor with concentration $C_{A,o}$ and leaving the reactor with concentration $C_{A,L}$ is shown in Figure 2. 6.

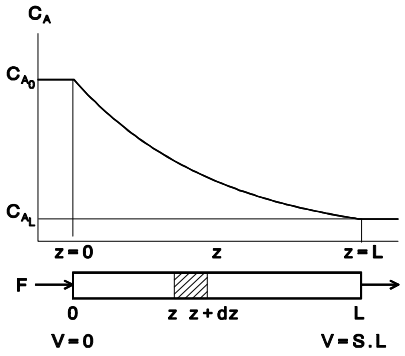

Figure 2. 6:
Concentration profile of component *A* when passing through an ideal plug flow reactor [Marin2000].

The residence time τ_o is defined by:

$$\tau_o = V\, C_{Ao} / F_{Ao} \tag{2.66}$$

with *V* the reactor volume, and $F_{A,o}$ the molar feed flow of *A*. For the two-step irreversible reaction shown in equation (2.60), p. 80, one receives the following expressions for the initial reactant *A* and the intermediate *Q*:

$$C_{A,L} = \frac{C_{A,o}}{1 + k_1 \tau_o} \tag{2.67}$$

$$C_{Q,L} = \frac{C_{A,o} k_1 \tau_o}{(1 + k_1 \tau_o) + (1 + k_2 \tau_o)} \tag{2.68}$$

Also, here C_P follows from the total mass balance given in equation (2.65), p. 81.

Figure 2. 7 shows the concentration profiles as a function of the residence time τ_o. This concentration profile is quite similar to the one observed for the batch reactor (Figure 2. 5) if one exchanges residence time with batch time.

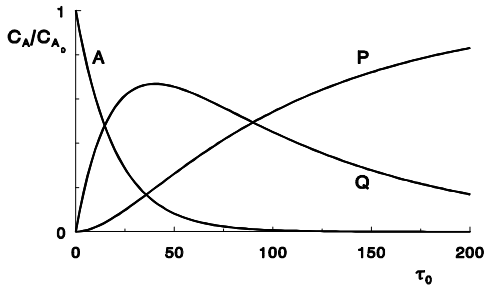

Figure 2. 7:
Concentration profile for an irreversible two-step reaction following first order kinetics for constant reaction volume in a plug flow reactor ($k_1 = 2\ k_2$) [Marin2000].

2.7.2.3 Comparison between the two reactor types

The batch reactor has as disadvantage that it cannot be run in a continuous way. This means it is not applicable for photocatalytic cleaning of air or water. But the advantage of the closed system is its simple design and easy kinetics. All one needs to test is the best combination of initial reactant concentration and catalyst surface area for a given reactor volume.

For designing a flow reactor the reaction kinetics must, in principle, already be known in order to design the reactor, i.e. to have the correct ratio between catalyst surface, concentration of reactants, the total flow through the reactor and the reactor diameter/ length ratio. In this thesis it was, therefore, opted to work with a batch reactor.

2.7.3 Analysis of the reaction process

2.7.3.1 Determining the reaction kinetics of a given photocatalyzed reaction

When starting to work with a new photocatalyst or a new organic substance determining the reaction kinetics of a given photocatalyzed reaction actually needs to be the first step in investigating a photocatalytic process. One needs to follow the evolution of the concentrations of initial reactants, possible intermediates and the final products. It is also important to study the effects of external parameters, like catalyst temperature, total catalyst surface area, concentration of organic substance, as well as other ingredients in the liquid or gaseous medium, e.g. oxygen content, water content (in air).

2.7.3.2 Measuring the initial reaction rate

In order to compare the photocatalytic activity of different catalysts towards a given organic or of one catalyst towards different organics one can use the method of initial decay of the organic substance, as described in section 2.7.1. Here the change in concentration of the

organic is followed in time and the tangent of the initial decay is determined. As seen in Figure 2. 8 this can be done by using the initial linear part of the decay curve (if the data points are spaced sufficiently close):

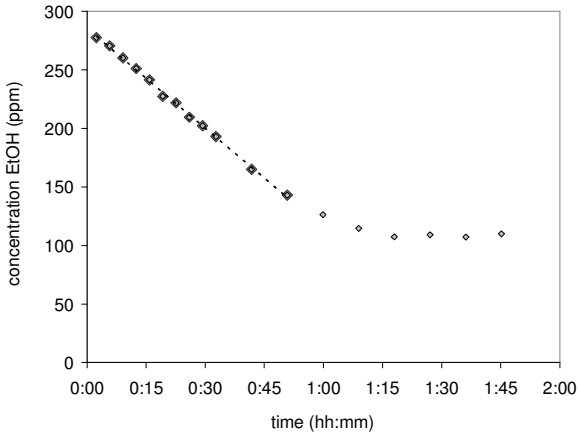

Figure 2. 8:
Determining the initial reaction rate of the decay of the organic substance in a photocatalytic reaction.

Following the reasoning in section 2.7.1 one can then define a standard to which all the other catalysts/organic substances can be compared. In order to compare with researchers from other laboratories one will have to follow the procedure as outlined.

In the case of testing the reactivity of photocatalytic thin films in the gas phase the use of phenol, which was the suggested standard in section 2.7.1.2, is difficult. It is easily dissolved in water, but since it is a solid it is not straight forward to evaporate it into the gas phase at room temperature. It will be necessary to define a good standard for testing the photocatalytic activity in air, which has not been done so far.

2.7.3.3 Analysis techniques

In order to determine the reaction kinetics of a given chemical process or to follow the concentration(s) of (a) chosen compound(s) one needs to be able to follow accurately the concentrations of the initial feed, any intermediates and the final products in time. In many cases the reaction is rather complex, so that identifying the individual components can be quite a challenge. In the most cases it is opted to follow the decrease in concentration of the organic test substance.

In the following some frequently used techniques implemented in the analysis of photocatalytic reactions are discussed briefly, together with their advantages and disadvantages. There exists a wealth of other analysis tools to determine the nature of a mixture of com-

pounds and it goes beyond the scope of this thesis to discuss them all. Their applicability will depend on the ease of sampling the reaction mixture and speed of analysis needed to follow the respective breakdown reaction.

a. Chromatography

Depending on whether a liquid or gas phase reaction is followed HPLC (high performance liquid chromatography) or gas chromatography (GC) is used. In both cases a sample of the reactor contents is injected into the analysis system. First it is passed over a column which is coated with an absorbing solid, the so-called '*stationary phase*'. From this column it is eluated (flushed) with a flowing '*mobile*' phase, i.e. a liquid or a carrier gas. Due to differences in the interaction of the compounds in the injected mixture between the mobile and the stationary phase the compounds can be separated, so that they leave the column after different residence times. In the case of HPLC the composition of the mobile phase is varied, by using a changing mixture of liquids. In gas chromatography the adherence of the compounds to the stationary phase is changed by varying the temperature of the column. The separated compounds are then identified according to a specific detector signal or their residence time on the column.

Unfortunately the degree of separation depends on the nature of the compounds and the stationary phase of the column as well as on the mobile phase. For each reaction mixture one needs to find the best combination of the three. Some compounds can 'poison' the column, i.e. they remain on the column instead of being eluated (e.g. water). This causes signal spreading and down time of the equipment when the column has to be regenerated.

The analysis time is also an important point. A so-called '*micro-GC*' can have a rather fast analysis times of less than 5 min, but standard chromatographic analysis times are close to 10 min per sample, if not longer. In order to take measurement points with a shorter spacing in time one needs to have a sample storage loop where the samples can wait to be analyzed.

b. Mass Spectrometry

A mass spectrometer works at gas pressures below 0.01 Pa (10^{-4} mbar). This means that the mixture to be analyzed needs to be vaporized and reduced in pressure. Therefore, this technique is easier to apply to volatile compounds. Each individual component of the mixture has its own specific mass spectrum, corresponding to the ion fragments that are formed in the analyzer. When analyzing a mixture of compounds, though, the resulting spectrum can become rather complex. Usually one will try to identify a signal which is specific for one com-

pound and follow its intensity in time. The advantage of the mass spectrometer is its fast measurement speed, which lies below 1 min.

A mass spectrometer can also be used as a detector in gas chromatography. A combination of these two techniques is very interesting, since the mass spectrometer allows direct and instant analysis of the eluated compound. Major drawbacks are the slow sampling rate of the GC and the price of the equipment.

c. Infrared (transmission) spectroscopy

Infrared (IR) spectroscopy is usually applied for analysis of gas phase reactions. Part of the reactor gasses is sampled to an analysis cell where a spectrum of the mixture is recorded. Here the disadvantages and advantages are the same as for mass spectrometry, namely the complex nature of signals received from a gas mixture and the fast measurement time, respectively. An additional problem is that IR spectroscopy is not very sensitive so that either relatively high concentrations or a large gas volume are needed to get a strong enough signal.

d. UV-VIS (transmission) spectroscopy

Here a light absorbing organic compound is used which is discolored by photocatalytic breakdown/ oxidation. The most frequently used compound is methylene blue, but also rhodamine B and malachite green have been used. Especially for methylene blue there is a problem with interpreting the discoloration because it may not happen only due to photocatalytic breakdown but also due to reduction of the compound to its colorless form as a result of electron transfer reactions [Yates06].

2.7.4 Light source

For the photocatalytic reaction the choice of light source for activating the photocatalyst is important. As already mentioned the semiconductor needs to be illuminated with light having an energy higher than the band gap to generate the electron/hole pair which activates the chemical process. For TiO_2 this means that the light source must contain wavelengths below 387 nm (anatase) or 413 nm (rutile). This means that UV-intense light sources must be chosen. On the other hand, the light source may not contain too energetic wavelengths (< 250 nm), since these can directly cause photolysis of organic compounds. It is therefore always important to check the effect of the UV light source on the organic substance to be investigated without a catalyst present.

A second important factor is the intensity of the UV light. As discussed in section 2.4.4.3 it is observed that the photocatalytic activity does not increase continuously with increasing UV intensity, but levels off at a certain saturation value. Also, especially for applications for air and water cleaning, low intensity irradiation is desired from economical point of view. Here one tries to use the UV from sunlight (outdoors) or black light bulbs (indoors).

For research purposes it is interesting, though, to use a more intense light source whose intensity can be regulated either by changing the power of the lamp or by inserting light filters into the illumination pathway.

2.7.5 Photocatalytic reactor types

There exist many different types of photocatalytic reactors. They are based on the two chemical reactor types discussed in section 2.7.2. A good overview is given in chapter 6 of [Schiavello97] and a detailed discussion goes beyond the scope of this thesis. Here only some points relevant to choosing the correct reactor type will be discussed. When designing a photoreactor one needs to consider several issues. The first is the aim of the photoreactor: will it be used for air or water cleaning, for studying the breakdown mechanism of organic substances or for testing different photocatalyst/ organic substance combinations.

2.7.5.1 Reactors used for air/water cleaning

Photocatalytic reactors can be used for removing small concentrations of organic pollutants from water or air. The reactor set-up and the manner of implementing the catalyst in the reactor have to be adjusted for the two different media.

The catalyst can be in form of an unsupported powder, powder or a thin film supported onto a porous carrier or on a flat substrate. In all cases the active surface or active volume of the catalysts is determined by the following factors: (1) penetration depth of the activating light into the bulk of the catalysts, (2) the depth from which the electrons/holes can reach the surface (3) availability of the surface to the organic substance (pore sizes) i.e. the effective active surface. Point (1) and (2) are material characteristics, with point (1) also being a characteristic of the frequency of the incoming light. Point (3) will be related to the (micro-) structure of the (un-)supported catalyst.

Another important factor is the amount of light that can be taken up by the catalyst, which depends on: (1) light scattering on the catalyst surface, (2) light reaching catalyst material deeper in the reactor. The first point is related to the (micro-)structure of the (un-)supported

catalyst. Point (2) will be influenced by the reactor design and is especially important in the case of suspended powders. The aim is to get light to all the catalyst in the chamber, i.e. keep the reactor depth as low as possible. For suspended powders one tries to keep the reactor thickness even lower than 5 cm since the intensity of UV light decreases strongly with depth inside the suspension.

When using suspended powder reactors care has to be taken to remove the powder from the water/air stream. The advantage of suspended powders is that they have a very high surface area. Supported thin films have only a low surface area, but they are easy to separate from the medium to be cleaned. It is easier to implement suspended powders in a liquid phase than in a gas phase. A liquid suspension can be sustained in a batch or a flow reactor, while a suspension of particles in air can only be sustained for a high flow rate, which is not possible in a batch reactor. As a result mostly thin film catalysts are used for air cleaning studies.

For investigating supported thin film catalysts two types of reactor design exist. In the first the coating is directly applied to the UV-transparent reactor walls. These are usually tube reactors of a diameter/wall-to-wall thickness of around 5 cm and are illuminated by a cylindrical array of lamps. In the second reactor type the film is deposited onto a carrier material and is positioned close to a UV-transparent window in the reactor wall, at a distance which ensures sufficient air/water flow to pass between the layer and the window.

Since light has to enter the reactor all or some walls of the reactor will have to be made of glass or polymer which is stable and transparent to the needed light wavelength. In many cases standard window glass is not sufficiently transparent to UV light and a different, usually more expensive, glass type must be chosen.

2.7.5.2 Reactors used for testing the breakdown of organic substances

When starting to work with a new photocatalyst or a new organic substance, determining the reaction kinetics is the first step in investigating the photocatalytic process. At the basis of each more complex reactor design lays the knowledge of the kinetics of the reaction to be performed in the reactor. Therefore one needs a simple reactor design for determining the kinetics. As already discussed, a batch reactor is often the best choice. Here one can follow the evolution of the concentrations of initial reactants, possible intermediates and the final products. One can easily study effects of external parameters, like catalyst temperature, total catalyst surface area, concentration of organic substance, as well as other ingredients in the liquid or gaseous medium, e.g. oxygen content, water content (in air).

The best analysis method for determining the concentration evolution of all ingredients in the batch reactor is chromatography in combination with a mass spectrometer. Here the reactor content is sampled at regular intervals in time and a full analysis of all the components is then performed. This analysis method may be too slow for a fast reaction, so that a method more compatible with the reaction rate needs to be chosen.

2.7.5.3 Reactors used for testing different photocatalyst/ or organic substance combinations

When testing the reactivity of different photocatalysts towards one specific organic test substance or the activity of one specific catalyst towards different organic test substances one uses the method of the initial reaction rate to compare reactivities. For this purpose a batch reactor as well as a flow reactor can be used. When using a batch reactor knowledge of the specific reaction process is not needed. This is different in the case of designing a flow reactor where the time frame of the reaction needs to be taken into account. In most cases it is, therefore, easier to use a batch reactor.

2.7.5.4 Special considerations comparing powder and thin film catalysts

It is not straightforward to compare powder and thin film catalysts since normally different methods are used to measure their photocatalytic activity. It is possible to immobilize a powder onto a substrate, i.e. deposit it as a thin film, but adhesion will be weak and the method of deposition will strongly influence the character of the powder coating. Consequently, it can be very difficult to compare powder thin films that were not made in exactly the same way (i.e. compare between laboratories) (section 2.7.1.2).

2.7.5.5 Special considerations for liquid phase (water) and gas phase (air) reactors

A catalyst in contact with water or air has a completely different surface structure. In water the pH (i.e. the acid/base character of the solution) has a profound influence on the chemical reaction occurring during photocatalysis. In air one cannot speak of a pH since no ions are present. Here one finds that there is a profound influence of the relative humidity on the reaction rate for some organic substances (see section 2.4.4.5). It is, therefore, very difficult to compare reactions in water with reactions in air.

In water care must be given to the amount of free oxygen present. Often no mentioning of this is given in publications, as oxygen is constantly replenished due to the type of reactor used (e.g. a jar stirred in air).

In air care must be given to the relative humidity, which must be known and taken into account when comparing measurements. Therefore, it is usually not interesting to use untreated ambient air as here the level of humidity is not controlled.

2.8 Deposition of TiO_2 thin films by reactive d.c. magnetron sputtering

2.8.1 Ceramic thin film deposition techniques

There are a variety of thin film deposition techniques for TiO_2. They can roughly be divided into two general areas (1) wet chemical and (2) vapor deposition. The wet chemical technique employed mostly is sol-gel [Carp04, Takeda01]. In earlier years the limitations of the wet process were due to the fact that the films had to be calcined at temperatures between 500-600°C, in order to achieve good stoichiometry and crystallinity [Nam04], which limited the applicable substrate materials. Newer investigations showed that these high temperatures needed for crystallization were due to the wrong substrate choice and caused by Na-contamination of the films (see section 2.6.6). Further development of the sol-gel technique has also lead to procedures which can yield crystalline TiO_2 powders at temperatures lower than 200°C [Fallet06]. For good bonding of a sol-gel film with a glass substrate temperatures above 400°C are still necessary, though [Carp04].

Vapor deposition techniques include chemical vapor deposition (without or with plasma enhancement, i.e. CVD or PECVD) and physical vapor deposition, including electron beam evaporation and (magnetron) sputtering. With (PE-)CVD powders as well as thin films can be deposited, depending on the processing conditions. Physical vapor deposition (PVD) techniques are used exclusively for thin film deposition. The main advantage of vapor deposition techniques, especially PVD, is that good adhesion of the film to the substrate can be achieved. A second advantage of vapor deposition techniques is that the process conditions can be controlled to yield crystalline thin films without substrate heating. Sometimes substrate self heating can occur during the process.

An important issue is the choice of substrate material. It must be compatible with the deposition conditions (e.g. low out-gassing pressure for PVD, chemical environment for CVD) as to remain inert and undamaged during deposition. The substrate must also be resistant to the temperatures required for calcination/crystallization of the thin film. Important examples are polymer substrates which have a rather low temperature resistance (max. 150°C). Polymers can also pose a problem in vacuum chambers due to out-gassing of e.g. water.

At the elevated temperatures needed for calcination/crystallization, diffusion from the substrate to the thin film and vice versa can occur. A known problem is the sodium diffusion

from soda-lime glass into TiO_2 films (section 2.6.6). As already discussed there, if higher temperatures are necessary for deposition or calcination it is advisable to use a sufficiently thick buffer layer of e.g. SiO_2 or use alkali-free glass substrates.

Generating doped TiO_2 films can be done by incorporating the dopant during the thin film deposition process or by post-deposition techniques like ion implantation. In this work TiO_2 thin films were deposited by d.c. magnetron sputtering from sub-stoichiometric TiO_{2-x} targets. The dopants were introduced into the films by (i) sputtering from MO_y/ TiO_{2-x} sub-stoichiometric mixed oxide targets and (ii) ion implantation into as-deposited, sputtered TiO_2 thin films.

In the next sections first the technique of (reactive) d.c. magnetron sputtering (2.8.2) will be described, followed by a brief discussion on the growth of thin films using this technique. Then follows a section on the control of the TiO_2 thin film structure (2.8.3) by the deposition parameters. In the end there is a section on the sputter deposition of doped TiO_2 thin films from mixed oxide targets (2.8.4). Ion implantation is discussed in a separate chapter (2.9).

2.8.2 D.C. magnetron sputtering

2.8.2.1 General description

D.c. magnetron sputtering is a physical vapor deposition technique, which is operated in a vacuum system at total gas pressures of 0.1-1.0 Pa. The technique is a further development of glow discharge sputtering, by positioning the discharge in a magnetic field [Chapman80, Westwood03].

A d.c. electrical field is applied to a gas (usually Ar) at low pressure, which results in a glow discharge (plasma) generated between the electrodes. The cathode is a plate of the material to be deposited, the anode can be a second plate, but it may have any form or position or may even be the chamber walls. The plasma consists of ionized Ar (Ar^+) and electrons (e^-). The Ar^+ ions are accelerated towards the target and impact onto it, causing a disturbance at the target (sub-) surface which can lead to the ejection of a target atom and/or electron. The Ar^+ ions are neutralized and the atoms can remain implanted in the target or migrate back out [Chapman80, Westwood03]. The electrons emitted from the target are used to sustain the discharge by ionizing Ar-atoms to form new Ar^+ [Chapman80, Westwood03]. The target atoms fly off into the chamber, where most are scattered by the gas particles present. As a result, the degree of scattering increases with the amount of gas present in the chamber, i.e. the gas pres-

sure. The sputtered particles collect on every surface in the chamber (Figure 2. 9). For thin film deposition one places a substrate in front of the target to collect most of the sputtered atoms, so that a thin film is formed. Figure 2. 9 shows a sketch of the d.c. glow discharge and magnetron sputtering process:

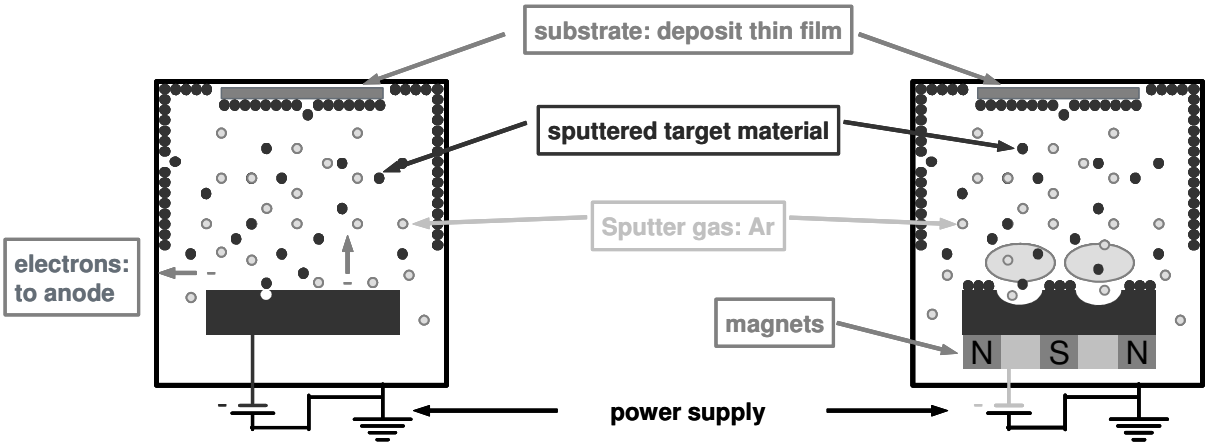

Figure 2. 9:
Sketch of the d.c. glow discharge (left) and d.c. magnetron discharge (right) sputtering processes.

The difference between a standard glow discharge and a magnetron discharge is the presence of a magnetic field above the cathode in the latter. This magnetic field confines the electrons, and, therefore, confines and enhances the plasma. This means that the discharge can be operated at lower gas pressures (10-100 Pa for a diode compared to 0.1-1.0 Pa for a magnetron) and lower discharge voltages (1000-3000 V for a diode, 300-500 V for a magnetron). The lower discharge pressure means less scattering of the sputtered target atoms, and the higher plasma intensity means more target atoms being sputtered, which together results in a higher deposition rate of the thin film (section 2.8.3). The lower discharge voltage of the magnetron discharge also means that the Ar-ions are impacting at lower energies at the target. As a result the sputtered particles leave the target with lower energies. The more confined plasma means that the substrate is usually outside the plasma zone (this can be varied, though), which has implications for the thin film growth (section 2.8.3).

The plasma confinement also results in only part of the target being bombarded by the Ar^+-ions (where the magnetic and electric field lines are perpendicular) [Westwood03], which is referred to as '*race track*' or '*erosion groove*' of the target.

2.8.2.2 Reactive d.c. magnetron sputtering

If the sputtering gas is inert, it will not undergo any chemical reaction with the target material so that the composition of the thin film is controlled by the target composition. When a second gas which can react with the target material, is added to the sputtering gas one speaks of '*reactive sputtering*' (Figure 2. 10).

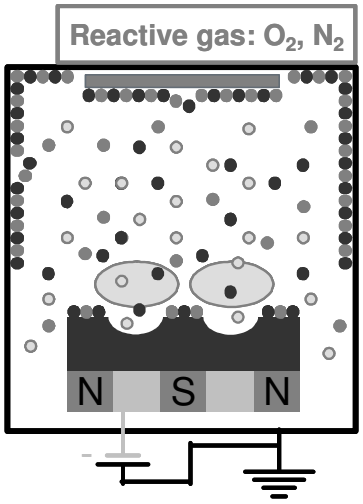

Figure 2. 10:
Sketch of the reactive d.c. magnetron sputtering process.

The addition of the reactive gas has some profound implications for the sputtering process and, therefore, for the deposition of the thin film. The reactive gas will react with the target material to form a compound. This happens at all surfaces of the sputtering system, including target and substrate. The amount of compound formation depends on the amount of reactive gas introduced into the chamber. For small amounts of reactive gas the system can usually buffer by consuming all the reactive gas due to compound formation at the internal chamber surfaces (gettering), i.e. in the plasma remains essentially the inert gas. This means that the target area bombarded during sputtering (race track) does not change much in composition. The sputtering and film deposition conditions are similar to those of the pure metal so that one still speaks of '*metallic sputtering*'. When the buffer capacity is reached, reactive gas will remain free in the chamber, changing the plasma composition. This changes also the composition of the race track, resulting in compound formation. The change in race track composition leads to a change in secondary electron emission from the target [Depla06b]. This, together with the change in plasma composition, causes a change in the impedance of the discharge circuit. As a result, the discharge voltage changes (at constant applied power or current). Important is also that the compound formation in the race track results in a reduction of the sput-

ter rate, which reduces the uptake of reactive gas, leading to an avalanche effect so that the system jumps to the '*reactive sputtering*' state [Berg05, Safi00, Sproul05].

The total gas pressure, as well as the discharge voltage, will, therefore, follow a non-linear dependence on the reactive gas flow, with a sudden transition between metallic and reactive sputtering regime. Figure 2. 11 below shows the discharge voltage and total pressure in dependence of the oxygen flow for sputtering of Al in Ar/ O_2. This is one of the most studied reactive sputtering systems. Since Al_2O_3 has a higher secondary electron emission coefficient than pure Al, the discharge voltage (at constant applied power or current) decreases upon transition to the reactive state.

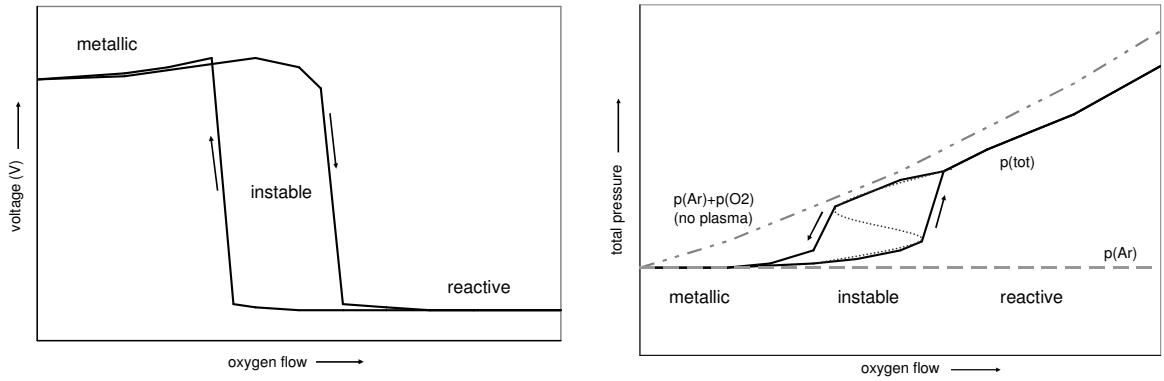

Figure 2. 11:
Dependence of the discharge voltage and the total gas pressure p(tot) on oxygen flow for sputtering of Al in Ar/ O_2, at constant power, using mass flow control for introducing the reactive gas. Note that p(Ar) and p(O_2) stand for the partial pressures of Ar and O_2, respectively. In the figure for the total gas pressure the S-shaped curve (dotted line) observed for using partial pressure control for the reactive gas flow has been indicated inside the 'instable' zone.

As one can see from Figure 2. 11 the system reacts differently on flow reversal. Since the system has a lower ability for gettering reactive gas in the reactive state, a lower reactive gas influx is needed for the system to return to the metallic state. This leads to a hysteresis behavior of the deposition parameters with reactive gas flow [Berg05, Safi00, Sproul05].

Since the sputter rate of the metal is reduced in the reactive state, the thin film deposition rate is also reduced substantially [Berg05, Safi00, Sproul05]. Since the transition between the two states is abrupt, there is only a limited possibility to deposit in the '*in-between*' state. Usually the area inside the hysteresis loop is termed '*instable*' since fluctuations in the deposition conditions can cause the transfer from metallic to reactive mode and vice versa.

Films deposited in the metallic mode are normally sub-stoichiometric, while films deposited in the reactive mode are stoichiometric. The low deposition rate is unattractive, though,

so that methods have been studied and are implemented to sputter at a higher rate in a (semi-) metallic state and still deposit a stoichiometric thin film. One method is to use a partial pressure control of the reactive gas instead of a flow control [Berg05, Safi00, Sproul05]. Here one does not observe the abrupt transition as for mass flow control but an S-shaped curve is followed (Figure 2. 11), so that sputtering in the normally instable regime becomes stable. A second possibility is to introduce the oxygen locally at the substrate, which can yield an oxidized film at the substrate while keeping the target in the metallic state [Safi00]. In the case of TiO_2 thin film deposition it is possible to use a ceramic sub-stoichiometric TiO_{2-x} target, which will be discussed further in section 2.8.4.2.

Substrate requirements:

Since sputtering is a low pressure deposition method, it is best for flat surfaces. Objects that can be rotated (cylinder), or tumbled (beads) can also be coated, but at a much lower deposition speed (since only the part of the surface facing the magnetron is coated).

2.8.3 Structural development during film growth

A well known and much referred to model for thin film growth by physical vapor deposition is the model from Thornton [Thornton77]. Here the different types of microstructure developed when depositing thick metallic films at different substrate temperatures T (referenced to the melting temperature of the metal T_m) and inert gas pressures are described. The model is based on a previous model by Movchan-Demchishin, which was developed for electron-beam evaporated metals. In this latter model the thin film growth is divided into three distinctive zones (1-3):

Zone 1 growth occurs at substrate temperatures of $T/T_m < 0.3$ and is described as a microstructure consisting of 'tapered crystals with domed tops which are separated by void boundaries'. The internal structure of the crystals is described as poorly defined. The crystal growth process proceeds with a low activation energy and, therefore, little surface diffusion.

Zone 2 growth occurs at temperatures of $0.3 < T/T_m < 0.5$ and is described as a microstructure consisting of 'columnar grains separated by distinct, dense, inter-crystalline boundaries'. The grain growth process proceeds with an activation energy equal to that of surface diffusion. Such metallic films behave similar to cast metals.

Zone 3 growth occurs at temperatures of $0.5 < T/T_m < 1$ and is described as a microstructure consisting of equiaxed grains with a bright surface. The grain growth activation energies show

that the process is controlled by bulk diffusion. Structure and properties of the layers correspond to those of a fully annealed metal.

Thornton extended this model for sputtering, where an inert gas is present (i.e. the chamber pressure is higher than for evaporation), by adding an additional axis to account for the sputtering gas (Figure 2. 12). Additionally he takes into account the effect of substrate roughness when discussing the thin film growth.

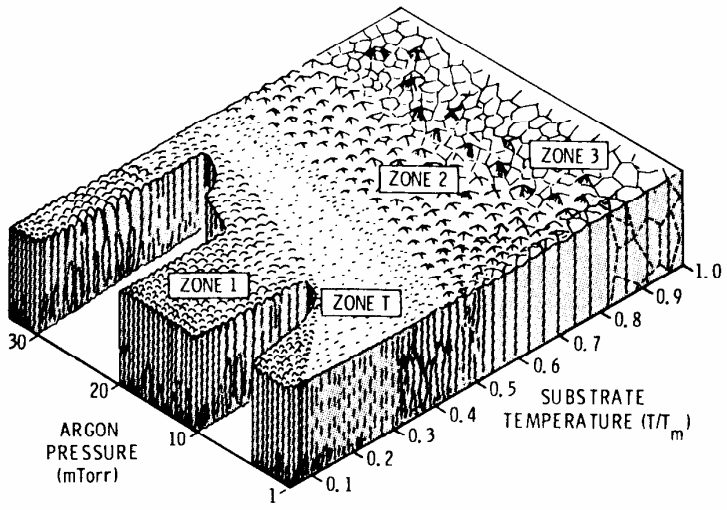

Figure 2. 12:
Thornton model for film growth [Thornton78].

According to the Thornton model **Zone 1** growth is promoted by substrate roughness and high gas pressure. Also a transition zone between Zones 1 and 2, called **Zone T**, is introduced, which is defined as the limiting form of the Zone 1 structure at zero T/ T_m on infinitely smooth substrates. Zone T is described as 'consisting of a dense array of poorly defined fibrous grains without voided boundaries' and as a 'Zone 1 structure with crystal sizes that are difficult to resolve and appear fibrous, and with boundaries that are sufficiently dense to yield respectable mechanical properties'. Otherwise the structure zones follow the characteristics as defined in the Movchan-Demchishin model. Another important observation of Thornton is that the influence of the inert gas pressure diminishes with increasing substrate temperature, so that it has no influence anymore at T/ T_m approaching unity.

A major shortcoming of the two models discussed above is that they are defined by the microstructural appearance of the film with respect to the substrate temperature. In [Mahieu06a-b] the mechanisms for atomic diffusion active during film growth were studied and it was found that they are a more accurate parameter for defining the crystal growth

zones. In the following a summary of this new model will be given; in order to distinguish from the growth zones as defined in [Thornton78] the growth zones as defined in [Mahieu06a-b] will be labeled with a suffix *M*. The microstructural aspects of the model are summarized in Figure 2. 13.

Zone 1_M is defined by low atom mobility inside the film, i.e. arriving atoms cannot move between grains. Depending on the kinetic energy of the arriving atoms and the temperature a different film structure develops, so that Zone 1_M is subdivided into three categories a-c.

Zone 1_Ma occurs at very low temperatures and low kinetic energy of the arriving atoms. The film follows a so-called 'hit and stick' growth (ballistic deposition), which means that the atoms cannot move on the substrate after they arrived. Nucleation is not possible, so that an amorphous structure results. A columnar, rough film develops due to statistical roughening and self-shadowing, leading to a low density film. Such films can be expected when sputtering onto an unheated substrate (with low self-heating during the process) combined with a rather high chamber pressure (which results in strong particle scattering).

Zone 1_Mb occurs at low substrate temperatures with energetic species bombarding the substrate. This can cause already present atoms to be knocked into a new position. These energetic species are present during sputtering as compared to evaporation. They can be accelerated ions (charged substrate), reflected ions (from the target) or fast neutrals (e.g. sputtered particles). The resulting film will have a higher density, but still be amorphous or show repeated nucleation. No preferential out-of-plane orientation will develop. Such a film can be expected when sputtering onto an unheated substrate (with low self-heating during the process) at standard sputtering pressures.

Zone 1_Mc results when the temperature of the substrate is high enough to allow nucleation into crystalline islands. These grow according to their kinetically determined most stable growth shape. Densely packed crystalline columns with no preferential out-of-plane orientation will develop. Such a film can be expected if moderate self-heating during sputtering occurs or the substrate is moderately heated.

Zone T_M again takes a position between Zone 1_M and Zone 2_M. Here inter-grain diffusion of the atoms is possible, aiding the crystal growth and allowing for evolutionary control of the crystal orientation. Initially the film nucleates and starts growing with a random orientation in the bottom. With time, evolutionary overgrowth occurs and as a result V-shaped columnar grains showing a preferred out-of-plane orientation develop.

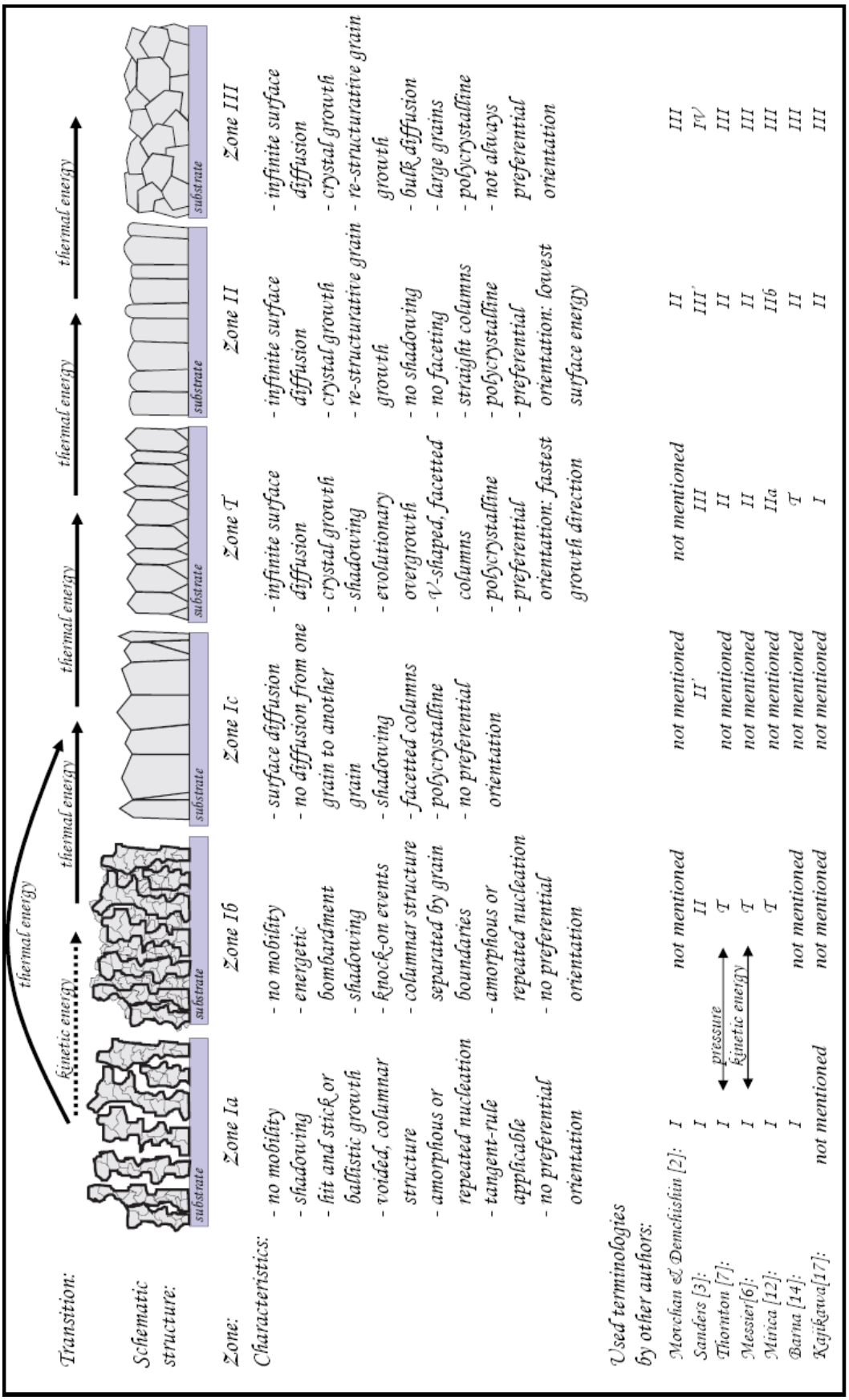

Figure 2. 13:

Thin film structure growth zone model as described in [Mahieu06a-b].

In Zone 2_M grain boundary diffusion is possible, leading to grain growth and re-structuring. The result is the growth of straight columns starting at the bottom of the film without showing evolutionary overgrowth. The columns also show a preferred out-of-plane orientation.

In Zone 3_M grain growth is determined by bulk diffusion, which is not related to the deposition process anymore. Here the standard grain growth and crystallization processes as for sintering bulk materials are followed. The polycrystalline structure shown in Figure 2. 13 is, strictly speaking, only valid for films containing impurities which enable the formation of grain boundaries. For highly pure thin films in principle a single crystal film should be developed.

2.8.4 Deposition of TiO_2 thin films by d.c. sputtering

2.8.4.1 Sputtering from a metal Ti target

For the deposition of TiO_2 thin films using d.c. magnetron sputtering either metal Ti or ceramic sub-stoichiometric TiO_{2-x} can be used as target material. In most cases a mixture of oxygen and argon is used as sputter gas, with the ratio adjusted to yield stoichiometric TiO_2 films, while in some cases pure O_2 is used [Takeda01].

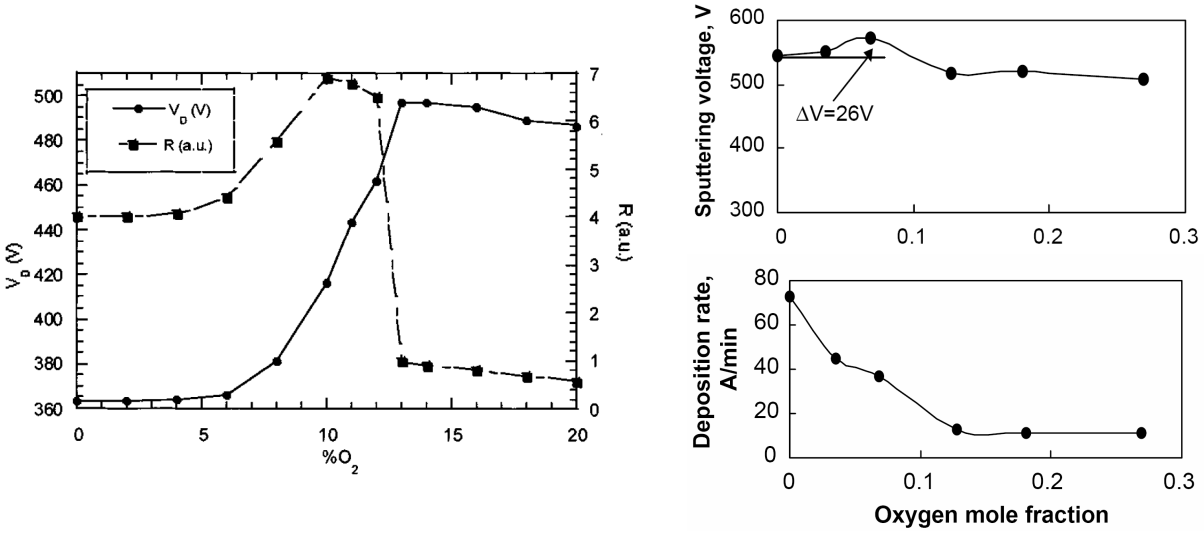

Figure 2. 14:
Dependence of discharge voltage V and deposition rate R on the oxygen flow for Ti sputtered in Ar/ O_2 (left, from [Vancoppenolle99]) and TiO_{2-x} sputtered in Ar (right, from [Tomaszewski03]).

When sputtering metallic Ti in Ar/ O_2 atmosphere, a voltage and pressure hysteresis behavior similar to that of sputtering Al in Ar/ O_2 is developed [Kinbara92]. A profound difference is seen for the discharge voltage, which increases upon transition from the metallic to the

reactive sputtering regime (Figure 2. 14) [Vancoppenolle99]. The reason for this is still being investigated, but it is suspected to lie in the different nature of the TiO_2 which is easily reduced upon Ar-bombardment as compared to Al_2O_3 [Depla06a].

The hysteresis behavior of the Ti-Ar/O_2 system leads to an instable regime for intermediate flows, which can only be avoided by using the methods described in section 2.8.2.2 (reactive sputtering).

2.8.4.2 Sputtering from a ceramic sub-stoichiometric TiO_{2-x} target

An alternative method is to use a sub-stoichiometric oxide target. This is possible for TiO_2 as it is easy to obtain ceramic (TiO_{2-x}) material in the sub-stoichiometric state having a high conductivity [Ohsaki99, Ohsaki01, Tachibana00, Tomaszewski03]. The sputtering behavior is quite different from a metallic target: a much smaller effect of the discharge voltage on the oxygen flow is observed [Depla06a, Kominami03, Tomaszewski03], resulting in a small and gradual transition (Figure 2. 14) as compared to the abrupt change seen for the metal. In [Depla06a] a series of TiO_{2-x} targets from metallic Ti to $TiO_{1.75}$ was studied. Here one can see the gradual transition from the strong voltage change observed with a metallic target to the almost steady discharge voltage for the ceramic $TiO_{1.75}$.

In [Poelman04] the deposition rate of the $TiO_{1.75}$ target in pure Ar is 50% of the metallic deposition rate and 3x that of the fully reactive rate. In [Persoone05] also a high deposition rate is reported for sputtering of a TiO_x ($1.5 < x < 1.7$) target in pure Ar. In [Ohsaki99] the deposition rate of TiO_{2-x} in pure Ar is reported to be 6 x that of the rate in the fully reactive mode. It seems that, when sputtered in pure Ar, the oxide target operates in the transition region of the metallic target [Depla06a]. With increasing oxygen flow the same sputtering conditions as for the metallic target are reached [Depla06a]. The absence of the hysteresis behavior means that no instable sputtering regime exists, so that the deposition process does not require sophisticated process control for depositing stoichiometric films under stable sputtering conditions at high deposition speed [Persoone05, Poelman04].

2.8.4.3 Control of the film structure

Sputtering is a medium-energy deposition technique. Depending on the shape and nature of the plasma, the position of the substrate with respect to the plasma and the biasing of the substrate, charged ions can reach the substrate, influencing the film structure. Important issues

for depositing photocatalytic TiO_2 are crystallinity, stoichiometry (degree of oxidation), density and surface morphology (section 2.5).

For growing TiO_2 thin films in particular, the effect of the energy of the ions impacting on the substrate is discussed by N. Martin et al [Martin01]. They observed that for very low ion energies (< 0.1 eV) the dominating processes induced by the impact are physisorption and thermal desorption. For ions with energies in the range of 1-10 eV (typically low pressure regime) the energy of the ion impacts corresponds to the energies of chemical reactions. In [Martin01] it is argued that in latter case the bombardment of the growing surface with low energy ions can create new nucleation sites. This would reduce the defect density in the film and disturb the columnar growth (low total pressure regime). In contrast, when the ions are deposited with a (very) low ion bombardment energy (high total pressure regime) they develop a structure with open grain boundaries and large columns [Martin01]. Growing such open structured columnar grains of (anatase) TiO_2 is especially interesting for photocatalytically active films. These films show good crystallinity and a rough surface structure with voids between the columns, which enlarges the surface area of the catalyst [Byun00].

Crystallization of the anatase structure can occur during deposition (usually with elevated substrate temperature) or by subsequent heat treatment (post deposition anneal treatment) of the as-deposited amorphous film. Latter will be discussed in section 2.8.4.4. Elevated substrate temperatures during deposition can be obtained by external heating or can originate from the sputtering process itself (self-heating) due to a high particle bombardment and heat of condensation.

In literature one can find TiO_2 thin film deposition using diode or magnetron sputtering, both in r.f. and d.c., with magnetron sputtering also in mid-frequency or pulsed dc sputtering mode. In the following only magnetron sputtering will be discussed in more detail. Diode discharges are quite different from magnetron discharges due to their higher gas pressures and discharge voltages.

With respect to the different sputtering modes one finds that d.c. sputtering almost exclusively leads to the deposition of the amorphous or the anatase structure. Pulsed d.c. and r.f. sputtering can also yield rutile or mixed anatase – rutile structures. This is not surprising as for these latter techniques the deposition speed is lower at the same power, resulting in a higher energy per sputtered particle. Therefore, it is more easy to yield thermodynamically stable thin films, i.e. the rutile structure.

All sputtering methods can yield amorphous thin films. For the crystalline phases very often preferential orientations are observed, but they vary according to the deposition conditions. Since no clear line could be found in the relationship between the developed preferential orientation and the deposition conditions (the strongest influence is the respective research group) this issue will not be discussed in detail.

In the following sections the general trends are discussed. The investigated range of parameters is summarized per reference in Appendix A2.

a. Amorphous or weakly crystalline TiO_2

Under most standard sputtering conditions and the substrate at room temperature the films follow the Zone 1_Ma or 1_Mb type growth (see section 2.8.4.4). This means that the TiO_2 films are either non-crystalline or have only small nucleation sites, i.e. they are XRD amorphous or show only a very low degree of crystallinity [Baroch05]. The conditions for this type of growth were a low or zero particle mobility due to a low particle energy. This is reflected in the experimental observations: For r.f. sputtering the amorphous phase (or low crystallinity) is favored by low pressures [Asanuma03, Zeman02] and high pressures [Yamagishi03]. For d.c. sputtering this is the case for a high target-to-substrate distance [Barnes05, Takahashi02, Takahashi06], high pressure [Barnes05, Kim02c, Takahashi06], a low d.c. power [Kim02c] and low oxygen content in the sputter gas [Liu05]. The first three parameters correspond to a low deposition speed. With respect to the oxygen content it must lie in the range for reactive sputtering (to obtain stoichiometric films) so that per definition the deposition speed is low.

The only unexpected result is that in [Asanuma03, Zeman02] the amorphous phase is observed at low deposition pressures, which should yield more energetic particles and, therefore crystalline films. Evidently there must be other factors playing a role in this study.

b. Rutile

Rutile is commonly observed for magnetron sputtering in the r.f. and pulsed d.c. mode. Here one observes that the rutile phase is favored at low pressures [Asanuma03, Miao02, Okimura01, Yamagishi03, Zeman02] and high pressures (for low power) [Asanuma03], and at low O_2 content in the sputter gas (at low total pressures) [Zeman02]. In [Yamagishi03] it is argued that a higher rutile content is caused by the presence of ionized species in the plasma and a higher energy of the impacting atoms. It is commonly thought that the degree of ionization is higher than in d.c. plasmas, which could explain why rutile formation is observed mostly in r.f. and pulsed or mid-frequency sputtering. As discussed in section 2.8.3 the energy

of the particles forming the thin film increases with decreasing pressure due to scattering with the gas particles. Also, some degree of sample heating is observed under r.f. sputtering, which can reach 240°C [Okimura01]. Both factors favor growth of crystalline rutile as the thermodynamically more stable phase.

A.R. Bally et al have used iron doping to promote rutile formation [Bally98]. They found that for an iron content > 0.32 at% the films started to show rutile crystallization. For smaller iron concentrations only anatase was formed. However, they used a high amount of oxygen (33%) in the sputtering atmosphere.

Very recently it was reported that an almost pure rutile film was obtained using d.c. magnetron sputtering [Vale06]. Here also a low O_2-flow and low gas pressure were applied. Unfortunately, no comparative study was performed and not sufficient information was given to estimate the particle energy so that this study cannot be compared to others.

c. Anatase

For r.f. sputtering the formation of anatase falls between the conditions listed for rutile and amorphous TiO_2.

For d.c. sputtering it was found that the crystallization of anatase was promoted by decreasing the target-to-substrate distance [Barnes05, Takahashi02, Takahashi06], decreasing the sputtering pressure [Barnes05, Kim02c, Takahashi02, Takahashi06, Zhang04], increasing d.c. power [Barnes05, Kim02c], and increasing the O_2 content [Liu05] up to a critical value [Kim02c]. All films showed some degree of preferred orientation, which was strongly influenced by the sputtering pressure and the O_2 content in the sputtering gas, but less influenced by the applied d.c. power. Usually some degree of sample heating occurred due to the sputtering process, which could reach 130°C [Zhang04]. The results indicate that there is no difference using Ti or TiO_{2-x} as target material.

In the above listed references it is suggested that factors favoring energy loss of the sputtered particles (so that they arrive at the substrate with a lower energy) will reduce the crystallinity in the film. Straightforward factors are a higher sputtering pressure [Kim02c, Takahashi06], a higher target-to-substrate distance [Takahashi06] and a very high oxygen content (which was combined with an increased total pressure) [Kim02c]. The effect of the applied d.c. power is more complex: with increasing d.c. power the energy each individual particle carries increases little since the discharge voltage (which delivers the energy) is not affected strongly (see equation (4.8), p. 163). On the other hand, increasing the discharge

power leads to an increase in discharge current, so that more particles are sputtered and more particles arrive at the substrate during a given interval in time. As a result the total energy delivered to the film increases, which is probably what is meant by "there is more energy in the particles with increasing d.c. power" stated in [Kim02c]. This effect is smaller than the effect of pressure, target-to-substrate distance and O_2 content.

In [Barnes05] a different argumentation is used: here it is claimed that nucleation of TiO_2 occurs in the gas phase forming clusters which grow according to their charging status and travel time to the substrate. The authors claim that they have been able to collect these clusters on TEM grids at short sputtering times. This claim is contradictory to any theory on thin film growth and plasma chemistry where it is stated that oxide formation in the gas phase is energetically forbidden [Smith94]: the large reaction enthalpy freed upon the formation of a Ti-O bond in the gas phase would immediately result in the decomposition of the bond. A third partner is needed to take up this energy to stabilize the molecule formed. Since a three body collision is statistically very unlikely in the gas phase under the low pressure conditions during sputtering any reaction between Ti and O can only occur at a solid surface, i.e. the substrate, chamber walls, etc. The reasoning followed in [Barnes05] will, therefore, not be discussed any further here.

2.8.4.4 Crystallization behavior of heat treated XRD amorphous TiO_2 thin films deposited by magnetron sputtering

The crystallization behavior of sputtered TiO_2 thin films upon heat treatment has received little attention in literature. Usually only the temperatures needed for crystallization and anatase-to-rutile transformation and how these are influenced by grain size and additives/impurities are of interest. A very nice study concerning the post-microstructural evolution of sputter deposited TiO_2 thin films was performed by [Martin97]. Here XRD amorphous TiO_2 thin films were deposited by reactive r.f. magnetron sputtering in Ar/O_2 and subsequently annealed at different temperatures. The temperature of the substrate was assumed to remain largely unaffected by the sputtering process. The substrate material was silicon, the film thickness 6000 Å. Crystallization of randomly oriented anatase was observed at 300°C. At 700°C some rutile crystallized together with (101) out of plane preferentially oriented anatase. This latter finding is interesting in that a preferred orientation results from an 'amorphous' film.

In [Zheng01] XRD amorphous TiO_2 thin films were deposited by d.c. magnetron sputtering in Ar/O_2 and subsequently annealed at different temperatures. Films annealed at 300°C show a strong (220) preferred orientation, which becomes less pronounced when annealing at 500°C. The authors do not comment on this preferred orientation. The fact that the material was crystallized on microscope-slide glass, which is a soda-lime glass, should influence the crystallization, too (section 2.6.6).

In [Wang06a] XRD amorphous TiO_2 thin films were deposited by r.f. magnetron sputtering in pure Ar using a TiO_2 target. The XRD spectrum of a film annealed in pure O_2 at 600°C shows a preferred (004) orientation, it is mentioned that anatase crystallizes also at 400°C. The preferred orientation is not discussed by the authors.

When comparing the three different studies no clear line can be found between the deposition conditions and the developed preferred orientation after annealing of the XRD amorphous films. In the three different studies three different preferred orientations were observed. In each study all sputtering parameters were fixed, in one study the effect of anneal temperature was investigated. In that study the reason for the observed preferred orientation is not discussed, but the authors refer to this orientation being formed in as deposited films. They do not take into account that a variety of preferred orientations is observed in as-deposited anatase as discussed in section 2.8.4.3.

2.8.4.5 Sputtering from mixed oxide targets

There are different methods for introducing dopants into a thin film by sputtering. One is co-sputtering with two targets: one for the TiO_2 matrix, one for the dopant. Care has to be given that the sputtering direction of the two magnetrons is aligned well to yield a homogeneous film. The relative amount of dopant in the film can be controlled by adjusting the power/ current to the individual magnetrons. A problem during reactive sputtering using two metallic targets can be the points of transition from metallic to reactive state which may not be the same for the two different targets, making it more difficult to control the process [Moradi91].

A better method is using a compound target. There are different examples: (i) small sheets of dopant-metal are placed on a Ti target [Carneiro05, Zhang03a-c], (ii) dopant powder is filled into holes drilled into the target [Bally98], (iii) a mixed compound target is used [Wang06a]. The most important issue is to ensure that the dopant is homogeneously distributed in the film. For this the dopant material must be distributed as homogeneously over the

target as possible. Increasing the target-to-substrate distance also aids in a more homogeneous distribution of the sputtered components. Since the sputter rate between the different target components may differ, the dopant distribution in the target has to be chosen such that the desired dopant concentration is obtained in the thin film.

For two dopants used in this study, namely Fe and Nd, the corresponding metal is ferromagnetic which will influence the sputtering process, because ferromagnetic targets change the magnetic field in their vicinity. Also Nd is difficult to handle in the metallic form due to its high affinity to oxygen. Since it was opted in this thesis to use TiO_{2-x} targets to deposit pure TiO_2 films, it was decided to deposit doped films using mixed oxide MO_y/ TiO_{2-x} targets, which could be obtained by standard ceramic processing techniques.

2.9 Ion implantation

During ion implantation a surface is bombarded with highly energetic ions with the goal to implant them into the (sub-)surface region, without removing any of the material being treated (which would be sputtering) [Wikipedia1, www4].

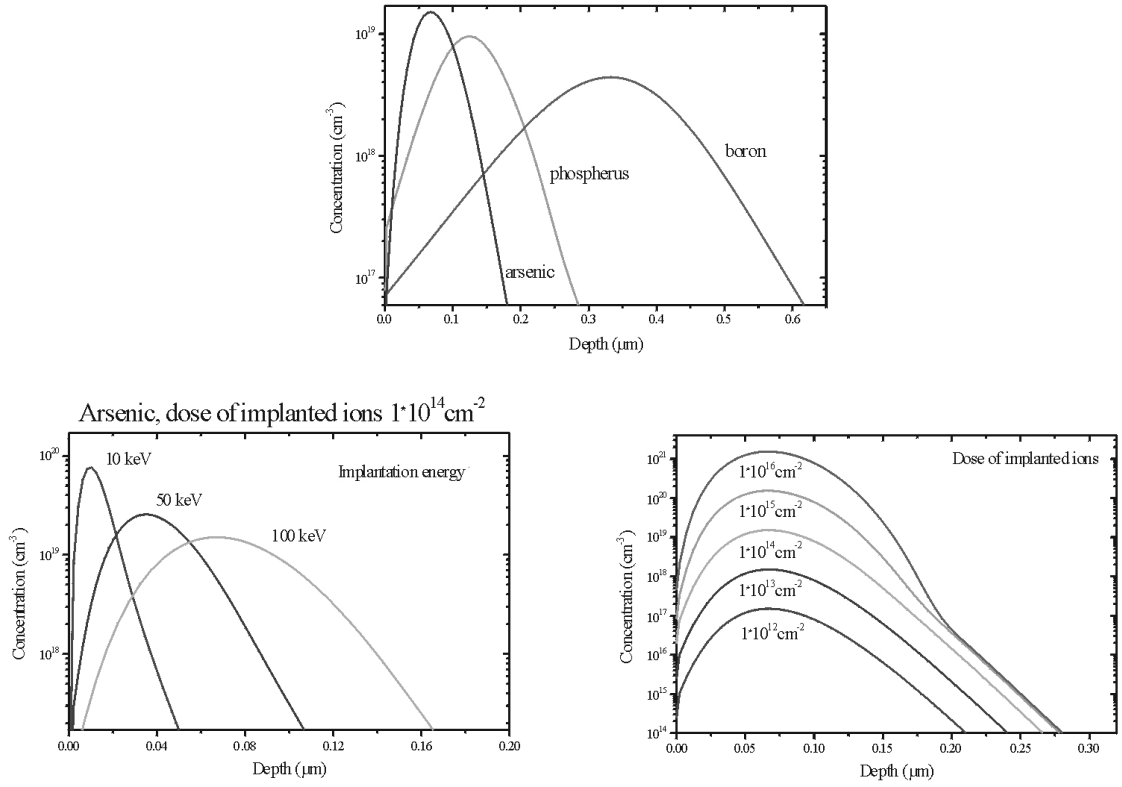

Figure 2. 15:

Top: Dependence of the ion implantation profile on the atomic weight of the ions for B, P and As in Si
Bottom: Dependence of the ion implantation profile on the ion energy (left) and dose (right) for As in Si [www4].

Ion implantation is only suitable for introducing foreign ions into a narrow region close to the sample surface. Typical implantation doses are 10^{11} to 10^{18} cm^{-2}. Typical acceleration energies are several keV to several hundred keV, with special equipment one can reach several MeV. The implantation depth and range in the substrate depend on the mass of the implanted ions, their energy, the mass of the substrate atoms, the crystal structure of the substrate and the direction of incidence of the ion beam. Some examples, which are of importance in the semiconductor industry are shown in Figure 2. 15.

Important is also the stopping power (i.e. the interaction of the solid with the implanted ion) of the substrate material being implanted, which depends on its chemistry, nature of bonding, crystal structure, etc., but also the implanted species. For calculating implantation profiles software like SRIM/ TRIM (www.srim.org) can be used. Care has to be taken though, that theoretical calculation does not yield exact implantation profiles [www4]. In ionic and especially partially ionic solids the nature of the chemical bond between the components is often not clear. For a pure ionic bond the stopping cross section of the solid can be calculated by adding the individual stopping cross sections of the components (weighed by their stoichiometry) [Möller01]. This is not strictly valid anymore in solids with mixed ionic/ covalent bonding like TiO_2.

To implant a larger surface area an energetic ion beam is scanned over the sample surface or spread to cover the complete surface. The concentration in the material is calculated by the ion dose delivered to a specific sample volume (i.e. surface times implantation depth).

Since the implanted ions have a large energy before impact, they disrupt the structure of the material, i.e. the layer altered by implantation can be expected to have a low degree of crystallinity. This altered layer may be deeper than the implantation depth of the ions due to knock-on effects of the implanted ions. The extent of the structural damage caused by Ion implantation increases with increasing ion energy. Annealing is then often used for structural relaxation, but this may not necessarily end up to be re-crystallization of the amorphized material but can result in segregation of the implanted material and formation of second phases (de-mixing).

3 Experimental

3.1 Photocatalytic reactor

3.1.1 Choice of reactor type

Since the reactivity of the sputtered thin films was unknown, it was chosen to use a batch reactor. As discussed in section 2.7.2 this reactor type is the best for determining the kinetics of a reaction. To design a plug flow reactor one needs to take into account the flow of the reactants and carrier gas as well as the reaction kinetics. Since latter were not known, it would not be possible to design a plug flow reactor properly. The investigations on the photocatalytic activity of the sputter deposited thin films were performed under the frame work of a larger project, which studied the removal of volatile organic compounds (VOC's) from air. Therefore, the TiO_2 thin films were tested in a gaseous atmosphere.

For the analysis of the chamber atmosphere it was chosen to use an atmospheric gas analyzer based on mass spectroscopy. This technique allows for short data spacing times (section 2.7.3.3) in a more convenient way than when using a gas chromatograph.

3.1.2 Basic reactor setup

As mentioned above, the catalytic reaction was followed with an atmospheric gas analyzer which included a mass spectrometer. To be able to control all factors influencing the photocatalytic activity of TiO_2 (humidity, organic impurities, CO_2, etc.) it was chosen not to work in ambient air, the composition and pressure of which is subject to daily and, especially, seasonal fluctuations. An example is the difference in humidity which can reach 100 % on a hot summer day just before a thunderstorm and be very low on a cold, clear day in winter. Synthetic dry air (ca. 80 % N_2 + 20 % O_2) was not a good alternative because the mass of N_2 (28 amu) lies in the vicinity of many organic fragments. Therefore, it was opted to replace N_2 with Ar (40 amu), so that the basic atmosphere was an air substitute consisting of 80% Ar and 20 % O_2. The amount of oxygen in this atmosphere is high enough to be considered as remaining constant throughout the photocatalytic breakdown reaction.

In order to replace the chamber atmosphere it was necessary to completely remove any ambient air from the chamber before filling it with the air substitute gas mixture. Therefore, the reaction chamber was in essence a vacuum chamber.

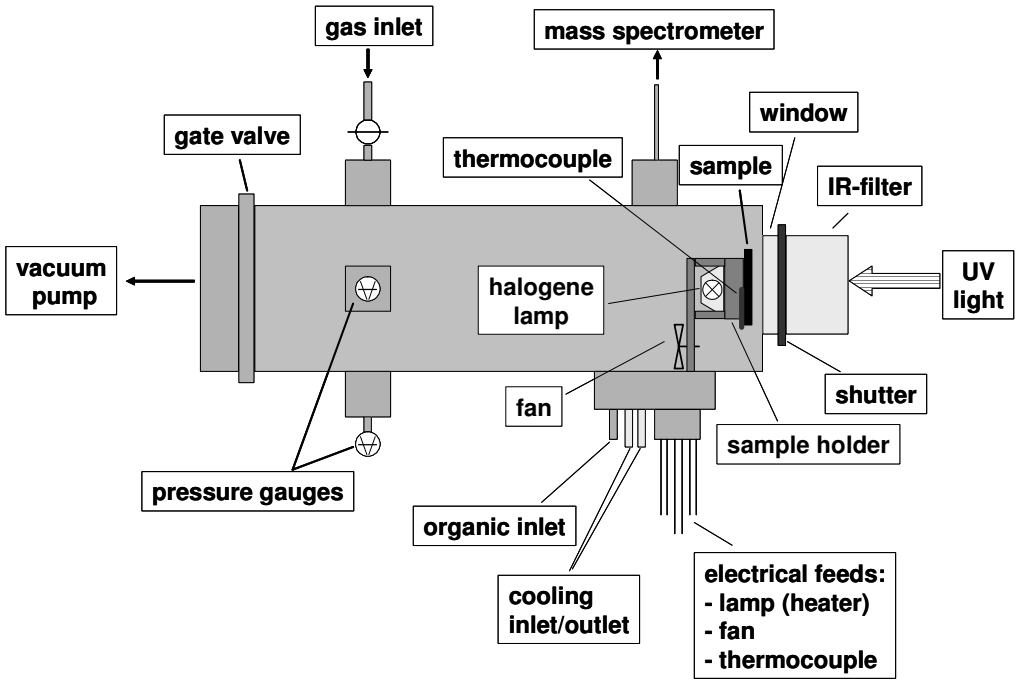

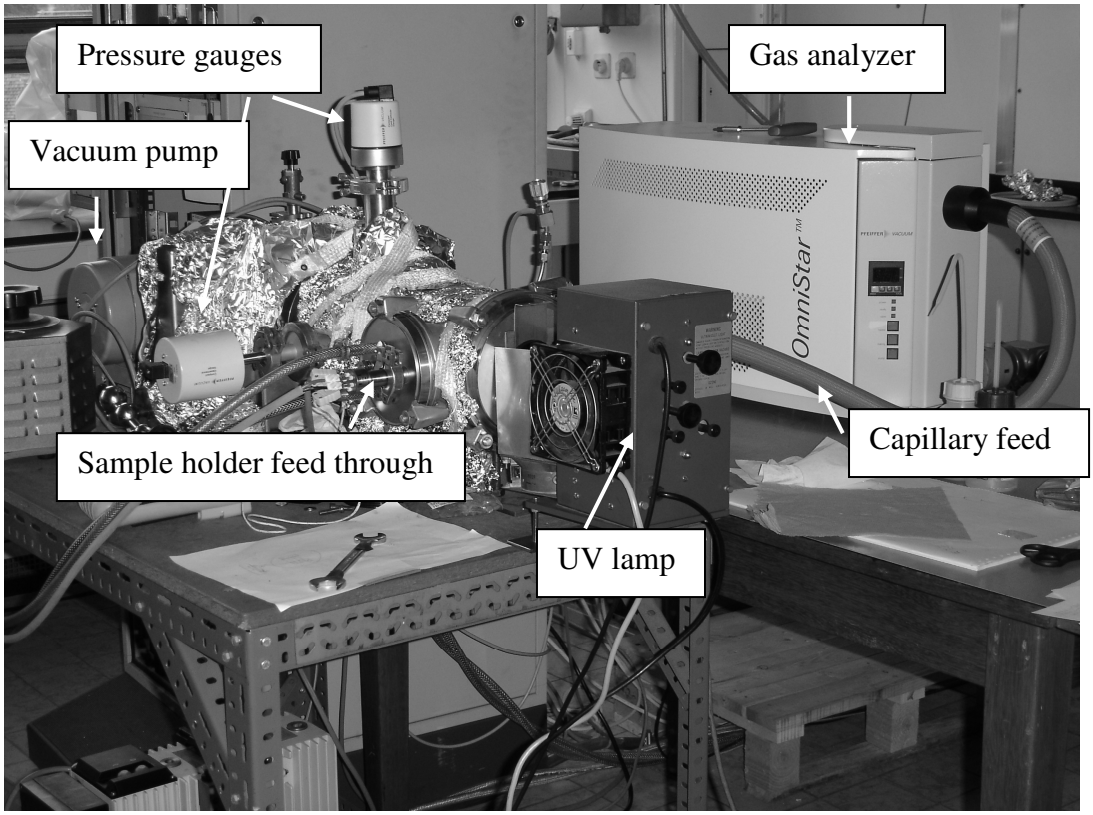

Figure 3. 1:
Top: Sketch of the setup of the photocatalytic reaction chamber.
Bottom: Photograph of the complete setup showing the reaction chamber (left, back), UV-lamp (front) and gas analyzer (right, back).

The chamber walls and flanges were all made of stainless steel, therefore no light could enter the reactor other than through the UV-transparent window. The flanges between turbo-molecular pump, gate valve and reactor were Conflat, using Cu-rings, while all other flanges were ISO-KF, using VITON o-rings. The Conflat seals are vacuum/ air tight but the VITON seals allow low, albeit detectable, gas diffusion. Due to the necessity to open and close some flanges rather frequently it was not feasible to seal these with Cu-rings. The volume of the reaction chamber was determined from its geometry to be 8.75 dm^3.

The pumping system, containing an oil-free pre-vacuum and a turbo-molecular pump, could be separated from the reaction chamber by a vacuum/ air tight gate valve. A cold cathode gauge (Pfeiffer Vacuum IKR 251) was used to determine the base pressure reached on evacuating (normally $<10^{-3}$ Pa). The pressure of the gas filled chamber, which was kept at 1050 mbar for most experiments (section 4.1.1.1), was measured with a compact capacitance gauge (Pfeiffer Vacuum CMR 271).

Before starting the illumination of the reaction chamber the UV-transparent window was completely closed off with a shutter to prevent light from entering the chamber. The UV-lamp had a focusing lens allowing to de-focus the beam over most of the rectangular sample area (3.1 x 2.5 cm^2). In order to minimize IR radiation from the UV-lamp to enter the chamber a filter (tube of 6 cm length, filled with water) was placed in front of the window. This water filter was cooled with an external fan. In total, the sample was positioned at a distance of 15 cm from the UV-lamp. In order to guarantee a homogeneous gas concentration throughout the reaction chamber a high speed fan was mounted below the sample holder.

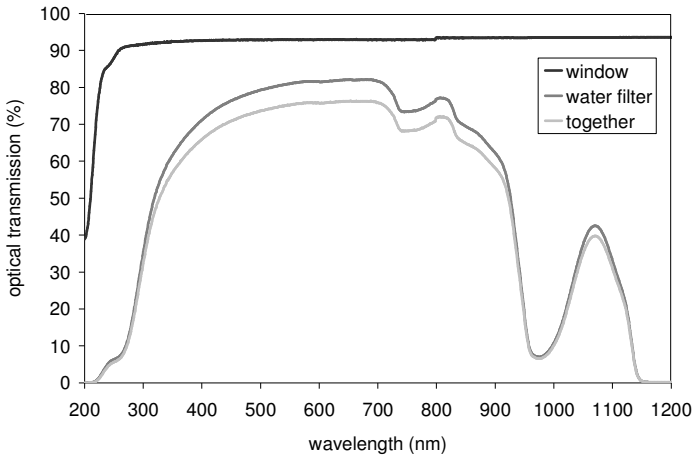

Figure 3. 2:
Transmission spectrum of the UV-transparent window, the water filter and both together.

The UV transparent window (quartz glass) had a transmittance of > 90 % at wavelengths above 300 nm, but together with the water filter the transmittance dropped from ca. 65 % at 400 nm to ca. 30 % at 300 nm, as can be seen in Figure 3. 2. The intensity of the light as admitted to the reaction chamber is discussed in section 3.1.2.1.

Initial experiments were performed with a non-temperature controlled sample holder. A thermocouple (copper-alumel) was placed behind the sample (being in close contact to it) to monitor the sample temperature using a manual hand-held read out. It was observed that there was a large temperature change at the sample upon starting the illumination with UV light. The temperature change was also found not to be the same for all samples, and did not remain constant with illumination time. It was, therefore, necessary to modify the sample holder to allow for controlling the sample temperature.

It was also found that it was necessary to heat the sample holder to the reaction temperature before starting the UV illumination (section 4.1.4.4). When the pre-heated sample stage was illuminated by UV light, a temperature rise of 1-2°C occurred, if it became too high there was the possibility to use compressed air to cool the sample stage.

Initial experiments were performed with manual control of the heater, but since the temperature fluctuations were difficult to control a PD (proportional derivative) -controller was installed; it was then no longer necessary to cool the stage with compressed air when starting the UV illumination.

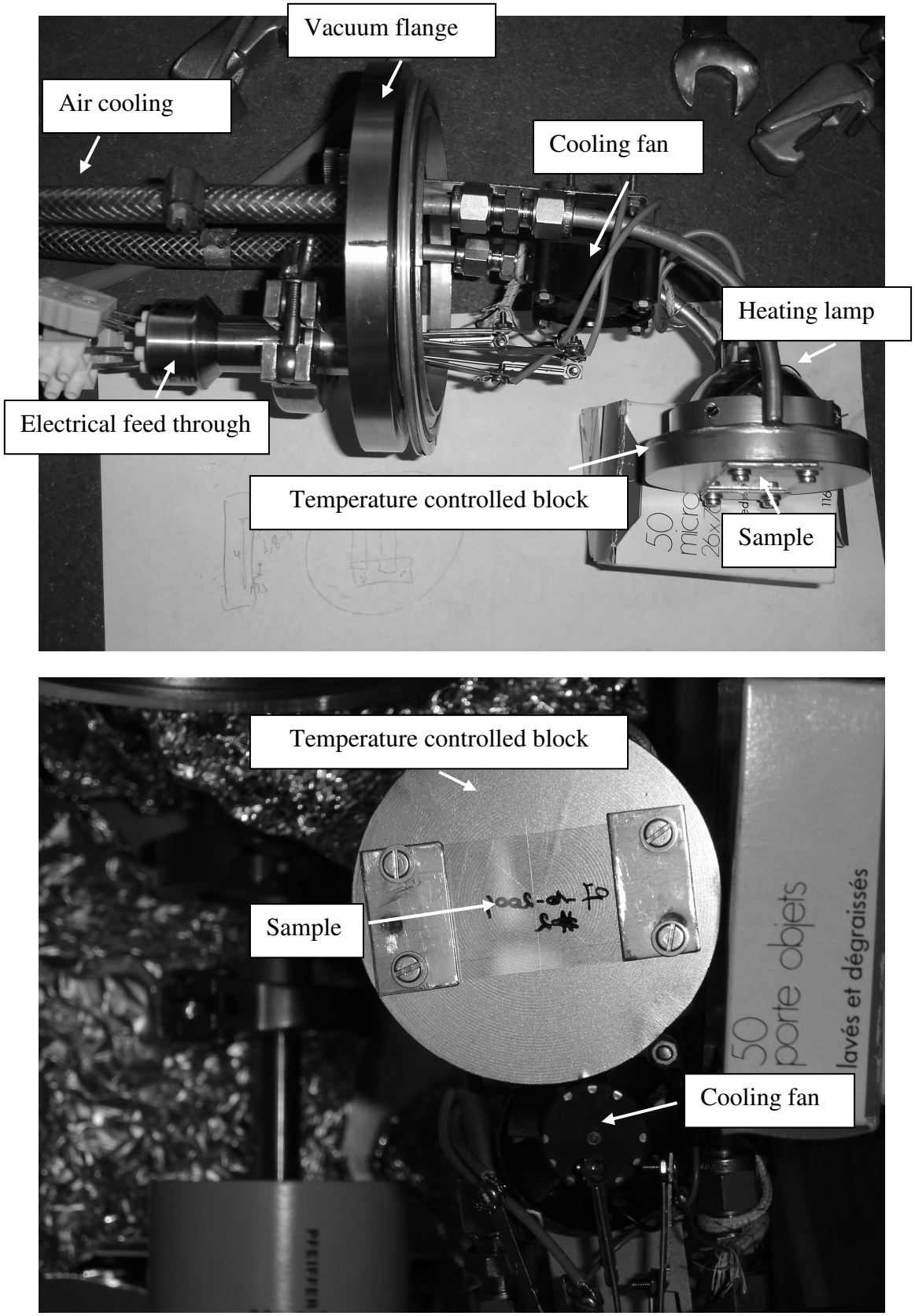

Figure 3. 3:
Heated sample holder of photocatalysis chamber: side view (top), detail of sample holder (bottom).

3.1.2.1 UV lamp

The UV lamp used is a mercury high pressure short arc lamp (Osram HBO 200 W/2 in an Oriel arc lamp housing). The emission spectrum of the lamp alone, together with the water filter and together with both water filter and window (Figure 3. 4) was measured with a FS920 spectrofluorimeter (Edinburgh Instruments).

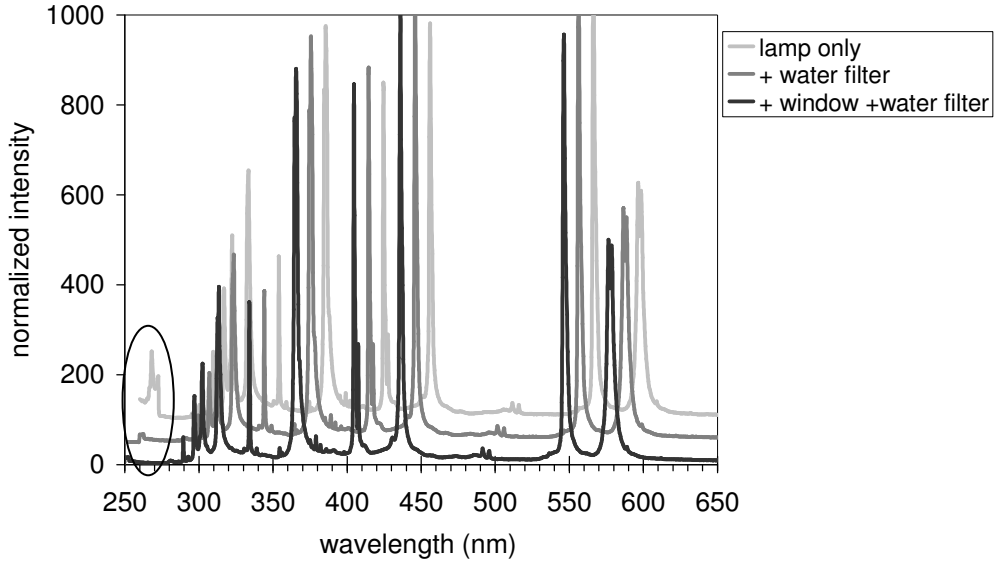

Figure 3. 4:
Emission spectrum of the UV lamp used for illuminating the thin films in the photocatalysis chamber, measured alone, together with the water filter and together with both water filter and window. The peak at ca. 255 nm is cut off by the water filter (circled). The normalized intensity is proportional to the number of photons emitted per nm.

As one can see the emission spectrum of the lamp is not continuous but has the distinct emission lines of Hg. These are 253.652, 296.728, 302.150, 313.155, 334.148 and 365.015 nm in the near UV, and 404.656 and 407.783 nm (violet), 435.833 nm (blue), 546.074 nm (green), 576.960 and 579.066 nm (yellow) in the visible part of the spectrum. The emission peak of the lamp at 253.652 nm (circled in Figure 3. 4) is cut off by the water filter. Even though the transmission spectra (Figure 3. 2), p.111, indicate that the absorption of the water filter increases at wavelengths below 400 nm, the measured relative peak intensity of the emitted light is influenced little, as can be seen in Figure 3. 4. The emission spectrum of the dark curve (lamp + water filter + window) is identical to the light received by the thin film inside the photocatalysis chamber.

The peaks in the visible are of too long wavelength for activation of anatase TiO_2 (E_g = 3.2 eV, corresponding to light of a wavelength λ = 387 nm). Therefore, only the four

peak ranges in the UV can be used for excitation of the anatase TiO_2, namely 300, 313, 330 and 365 nm. Latter is, by far, the most intense line.

The line at 406 nm (violet) is able to activate rutile ($E_g = 3.02$ eV, corresponding to $\lambda = 413$ nm). For doped TiO_2 there is a possibility that the effective band gap shifts to even lower energies or that localized absorption bands occur. Then, also lines in the visible light region are able to activate the material.

In Figure 3. 5 the normalized intensity of the light effectively entering the photocatalysis chamber, proportional to the number of photons emitted per eV, is shown. This allows to estimate the relative photon energy utilized for photocatalysis. It was possible to calibrate the intensity measured by the spectrofluorimeter to the power received. The spot size of the light was set as to illuminate the complete sample area so that all incoming light was utilized.

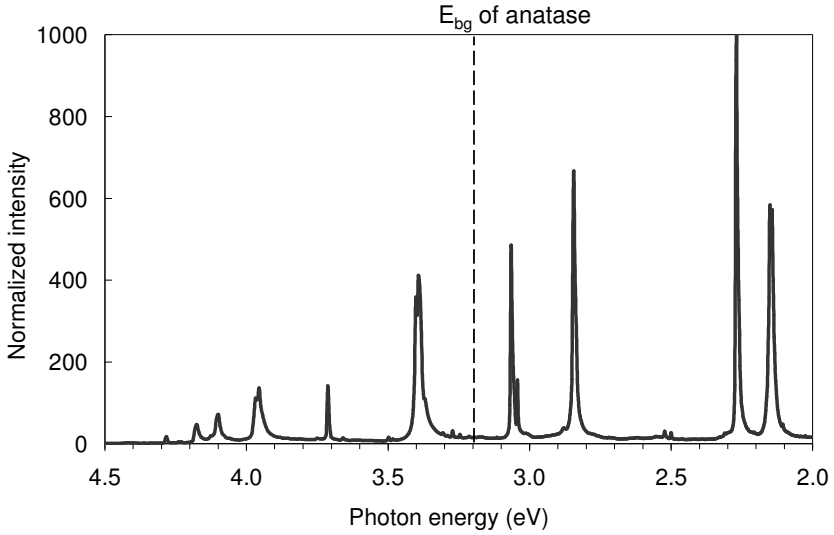

Figure 3. 5:
Emission spectrum of the light used for illuminating the thin films in the photocatalysis chamber (UV-lamp + water filter + window). The normalized intensity here is proportional to the number of photons emitted per eV. The band gap energy of anatase at 3.2 eV is indicated by the dotted line.

The total power received at the sample from the lamp (after passing through the water filter and the window) was calculated to be 8.45 ± 2 W. With a sample area of 7.75 cm² this amounts to a power density of ca. 1.09 ± 0.26 W/cm² for all incoming light energies. The percentage of light received at photon energies higher than 3.2 eV (the band gap of anatase) is about 62 %, which corresponds to a power density of 0.676 ± 0.160 W/cm² for the light effectively usable for photocatalysis. Shifting the band gap to values above 3.4 eV will reduce the number of photons that can be utilized because the high intensity line at this energy (365 nm) becomes inactive.

The calculations of the band gap energy can be verified by measuring the relative contribution of the different peaks in the emission spectrum to the photocatalytic process. For this one can use so-called cut-off filters which transmit only light of a higher wavelength (lower energy). These cut-off filters were inserted between the chamber window (shutter) and the water filter (Figure 3. 1), p. 110. Cut-off filters for the wavelengths 345 and 395 nm where used for both Degussa P25 reference coatings and TiO_2 thin films deposited at an Ar-pressure of 1.4 Pa and a sputtering power of 60 W (please refer to section 3.2.2.2 for the thin film deposition conditions). For thin films deposited from Fe_2O_3/ TiO_2 mixed oxide targets a different set of cut-off filters was used, namely 395, 420 and 455 nm, to test whether there was some contribution from visible light to their photocatalytic activity. The respective transmission spectra of all cut-off filters are shown in Figure 3. 6. As one can see, the cut-off is not instantaneous but has a certain interval.

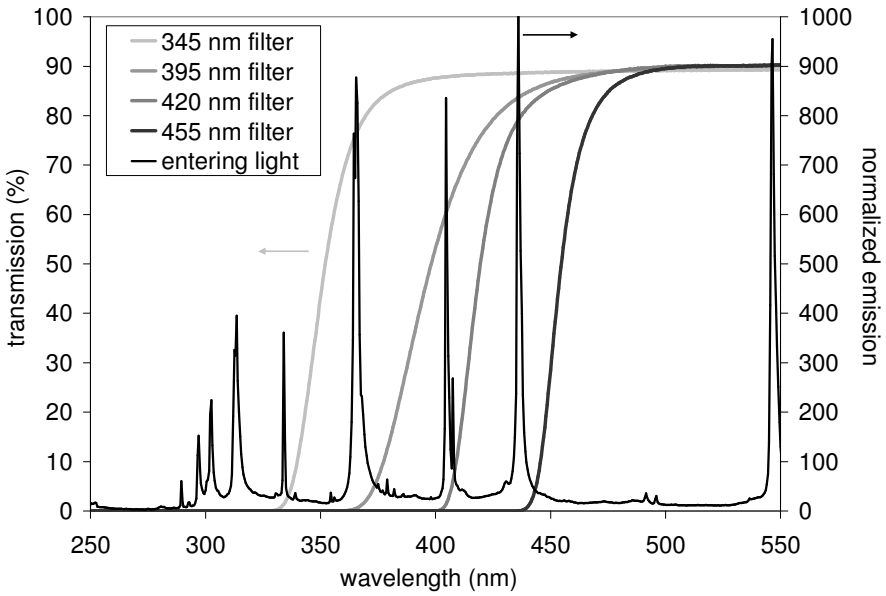

Figure 3. 6: Transmission spectra of different cut-off filters together with the spectrum of the light entering the chamber without filter (from Figure 3. 4, p. 114).

All filters but the one for 455 nm cut some of the lower frequency line whose activity was to be tested, so that one has to take into account these transmission losses. What is also important to note is that the maximum transmission of the filters is about 90 % due to reflection losses.

From the normalized intensity as a function of the photon energy (shown in Figure 3. 5,p. 115, for the light entering through the chamber window) one can calculate the relative number of photons. If one takes the number of photons entering the chamber without

any cut-off filter to be 100 % one can calculate the percentage of photons entering the chamber when using a cut-off filter. These results are shown in Table 3. 1.

% of photons entering the reaction chamber	**unfiltered (% of total unfiltered)**	**345 nm cut-off filter (% of total unfiltered)**	**395 nm cut-off filter (% of total unfiltered)**
Total amount	100	72.9	56.5
Photons > 3.02 eV	42.0	21.3	5.374
Photons > 3.2 eV	33.5	13.8	0.467
Photons > 3.5 eV	16.3	0.436	0
Photons 365 nm line	18.0	10.6	0.104

Table 3. 1: Relative number of photons entering the chamber when using cut-off filters, related to the total unfiltered value (in %).

The photon energies of 2.95, 3.2 and 3.5 eV are smaller than the peaks observed at 405, 365 and 335 nm, respectively, so that the number of photons above this energy includes the respective lines. The line at 365 nm is listed separately since it is the most energetic of the complete lamp spectrum.

One can clearly see from Table 3. 1 that the remaining amounts of photons after the insertion of the 345 and 395 nm cut-off filter are 72.9 and 56.5 %, respectively. If one looks at the remaining amount of photons present in the UV (> 3.2 eV) one gets respectively 13.8 and 0.467 % of the original amount emitted by the lamp (including water filter and window). Since only UV light with an energy above 3.2 eV is expected to be activating the anatase TiO_2 thin films, one can expect the photocatalytic activity to be decreased strongly after inserting the cut-off filters. Especially the low photon amount admitted through the 395 nm cut-off filter should reduce the photocatalytic activity to close to zero.

Since the Degussa P25 powder is a mixture of rutile and anatase the question arises whether the line at 405 nm could still be active (the band gap of rutile is 3.02 eV). Unfortunately this line is reduced in intensity by the 395 nm cut-off filter, leaving only a small percentage of photons passing below 3.02 eV, namely 5.374 %.

Obviously, not only the number of photons available at a certain energy is important for determining the photocatalytic activity. When increasing the photon energy above the band gap of a thin film, the absorption only increases gradually and, for example, light with a wavelength of 300 nm will be absorbed much more effectively than 365 nm in anatase.

3.1.3 Analysis of the chamber atmosphere with an atmospheric gas analyzer

3.1.3.1 Pfeiffer Vacuum OmniStar

The analysis of the chamber atmosphere was performed with the OmniStar atmospheric gas analyzer (Pfeiffer Vacuum) containing a mass spectrometer (Pfeiffer Vacuum Prisma QMS200M). Figure 3. 7 below shows the set-up of the Omnistar [Pfeiffer02].

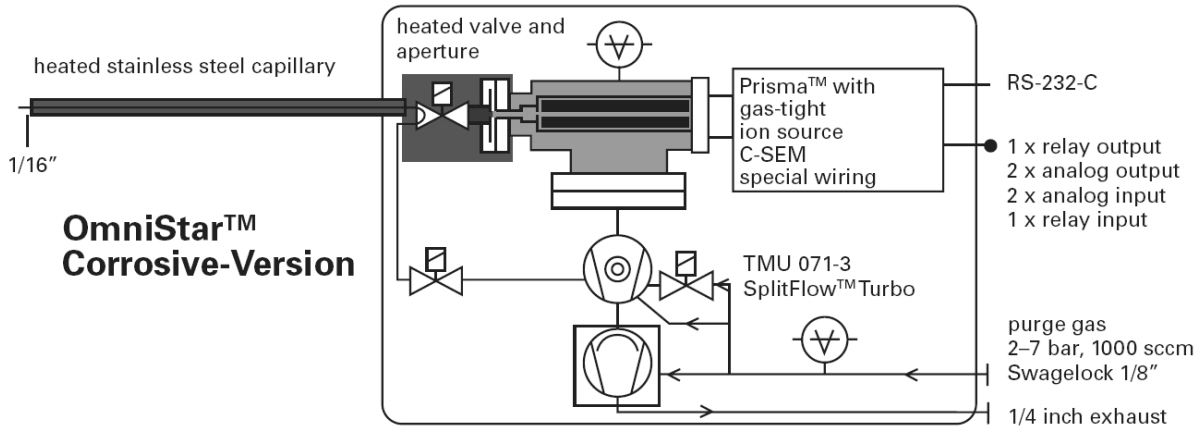

Figure 3. 7:
Set up of OmniStar gas analyzer, taken from [Pfeiffer02].

The heart of the equipment is a mass spectrometer (Prisma QMS200M), which is differentially pumped by a turbo-molecular and membrane pre-vacuum pump. The pressure is dropped in two stages, first via the capillary to 10^2 Pa, then via the aperture to 10^{-3} Pa. The capillary can sample gasses at a pressure from ca. 1.1 to 0.75 x 10^5 Pa (i.e. around atmospheric pressure).

As indicated in Figure 3. 7 there is an inlet valve to close off the capillary, which is an important feature. For one, the gas analyzer has to be closed off during evacuation of the reaction chamber, for another it enables sampling the reaction chamber atmosphere in intervals. Since the flow sampled through the capillary is ca. 2 sccm, it means that for prolonged measurement times there would be an appreciable loss of pressure in the reactor if the capillary was sampling continuously: The loss would amount to ca. 15 mbar/ hour or 360 mbar/ day.

The capillary is made of stainless steel and can be heated to temperatures up to 200°C to minimize adhesion of the gas components to the capillary walls. For all experiments discussed in this thesis the capillary was heated to a temperature of 120°C, which was sufficient for the components present in the reaction chamber.

The mass spectrometer has a range of 0-200 amu. There are two types of detectors in this instrument, a faraday and a channeltron (SEM) detector. The main difference between the two is the stronger signal amplification in the channeltron resulting in a higher sensitivity. This comes at the cost of a decreased signal stability. Initial tests showed a drift in the channeltron signal with time compared to the stable faraday detector. According to the manufacturer this is normal and is averaged out for quantitative measurements (section 3.1.3.3). Experiments showed that the sensitivity of the channeltron was needed for measuring concentrations in the ppm range with the required accuracy. The theoretical detection limit of < 1 ppm could not be achieved in practice, though. The real noise level was found to be ca. 10-15 ppm for the ethanol signal at 45 amu.

3.1.3.2 QuadStar software

The QuadStar software allows communication between a personal computer and the OmniStar. With this software calibrations and measurements can be performed manually, but it is also possible to program a complete calibration and measurement routine. This latter feature was implemented in this thesis, the final programmed sequence will be discussed in section 3.1.3.5.

3.1.3.3 Monitoring the chamber atmosphere

The chamber atmosphere was monitored using two different measurement procedures possible with the OmniStar. The first procedure is a standard mass spectrum ('*scan analog*'), where the mass/charge value is scanned over a given range. The second procedure allows following qualitatively ('*multiple ion detection*', MID) or quantitatively ('*multiple concentration detection*', MCD) a given component which has a peak with a maximum ion current at a certain mass/charge value (in further referred to as '*mass point*'). The measured mass point usually does not coincide exactly with the actual mass/charge value of the ion due to instrumental influences. It is, therefore, necessary to define the point of maximum ion current before performing a measurement, which is done by choosing the appropriate calibration sequence ('*mass scale calibration*', MSC) in the QuadStar software.

For qualitative analysis (MID) the maximum ion current at the mass point is followed. For quantitative analysis (MCD) the ion current of the component must be calibrated against the according ion current of a standard gas ('*gas specific calibration*', GSC) by determining its respective calibration factor *K* according to:

$$\frac{c(A)}{c(ST)} \cdot K(A) = \frac{I(A)}{I(ST)} \qquad (3.1)$$

with *c(A)* and *c(ST)* the concentration of compound *A* and the standard *ST*. The ion current of compound *A* and the standard *ST* are *I(A)* and *I(ST)*, respectively. *K(A)* is the calibration factor of compound *A*. During measurement the concentration of a compound is then calculated with equation (3.1), using the calibration factor *K* determined earlier. Here the standard was Ar which has its main peak at 40 amu. Two other concentrations were followed, namely O_2 (32 amu) and the organic test substance. The concentrations of Ar and O_2 were 80 and 20 vol% as determined by the pre-mixed gas supply so that following the O_2-concentration was just a control feature. The initial concentration of the organic test substance was fixed by the amount injected.

Since external factors (e.g. temperature) can influence the measurement it is best to perform the GSC calibration close in time to and under the same conditions as the actual measurement. It was, therefore, opted to perform a GSC calibration at the beginning of each experiment, before illumination with UV light was started.

3.1.3.4 Initial chamber characterization experiments

For initial chamber characterization experiments mass spectra were recorded over the range of 0-50, 0-80 or 0-100 amu, depending on the type of organic test substance used. This allowed for finding suitable mass points for following the concentration of the organic test substance as well as breakdown products (using the MCD function). It was chosen to calibrate only for the concentration of the initial test substance. It would be rather complicated to calibrate for all possible intermediate and final products. It was chosen to follow latter using the qualitative ion current measurement (MID) function. These initial tests were performed to determine the most suitable organic test substance from several possible ones, namely ethanol, acetone, isopropanol, methanol and propane. The final choice was for ethanol (section 4.1.2.2).

3.1.3.5 Photocatalytic breakdown reaction

To study the complete breakdown reaction several mass points corresponding to original test substance, intermediate and final products were followed (including Ar and O_2). Also a mass spectrum over the range of 0-80 amu was recorded as additional control. For determining the photocatalytic activity only the initial part of the reaction was needed (section 2.7.3.2).

Therefore, the number of mass points was limited to those needed for calibration and some additional ones to follow up on the reaction using the MCD/ MID function. This procedure allowed for a shorter measurement per point in time (which will be referred to as '*data point*' or '*measurement cycle*' in the following).

The sample size of the tested films was 31 x 25 mm, which corresponds to the most homogeneous sample area on the sputtered glass slides (section 4.2.2.4). Initial tests were performed using a spin coated layer of Degussa P25, which allowed for optimizing the test procedure. Especially for following the complete breakdown reaction it was interesting to have a short time spacing between data points (measurement cycles) in time for the initial part of the reaction, which meant that every 3-4 min a measurement was performed. As the reaction proceeded, its speed slowed down and measurements could be taken at larger time intervals. This means that the measurement program was split into two parts: in each a different time interval between the data points could be chosen. For best reproducibility of the photocatalytic testing, it was opted to write a measurement program as outlined in the flow chart (Figure 3. 8) and not to perform each measurement individually.

First the chamber was evacuated, flushed and backfilled to a specific pressure with an Ar : O_2 = 80% : 20% mixture (specialty gas, Air Liquide, Belgium). Then the measurement program was started. In the beginning some setup routines were run to ensure optimal performance of the OmniStar. This included ensuring that the filament, which is needed for generating ions in the mass spectrometer, and the channeltron detector were warmed up sufficiently. Then the input parameters were requested: These included the number of data points and waiting period between them for the first and the second part of the measurement program, the amount of ethanol to be injected (could be chosen from an offered set of values) and the time to wait for homogenization. The homogenization period was needed to equilibrate the ethanol in the chamber and was standard chosen to be 30 min.

Before injection of the ethanol two control measurements (mass spectrum of the analysis chamber, MCD/ MID measurement of the Ar/ O_2 atmosphere before ethanol injection) were executed to check for abnormalities. After the ethanol injection and the homogenization period had passed, the gas specific calibration (GSC) was performed for Ar, O_2 and ethanol. Then a first measurement cycle in the dark was performed, immediately after which the UV illumination was started by opening the shutter. The UV lamp was routinely turned on during the last 5 min of the homogenization period to allow it to reach full power before admission of light to the reaction chamber.

If the time interval between two successive measurement cycles was more than two minutes the capillary was closed in the time between. Since during initial experiments a not temperature controlled heating stage was used the step '*turn on heater for sample stage*' was not applicable. For determining the working pressure in the chamber and the temperature of the sample stage please refer to sections 4.1.1 and 4.1.4.4, respectively.

For each measurement cycle the recorded data were written to a mass spectrum as well as a mass point/concentration file. Latter was displayed and monitored real time using the QuadStar display window. If at the end of the program more measurement points were needed, the program could be restarted and run without the calibration routine. After the experiment was completed the data could be exported for further analysis with spread sheet software.

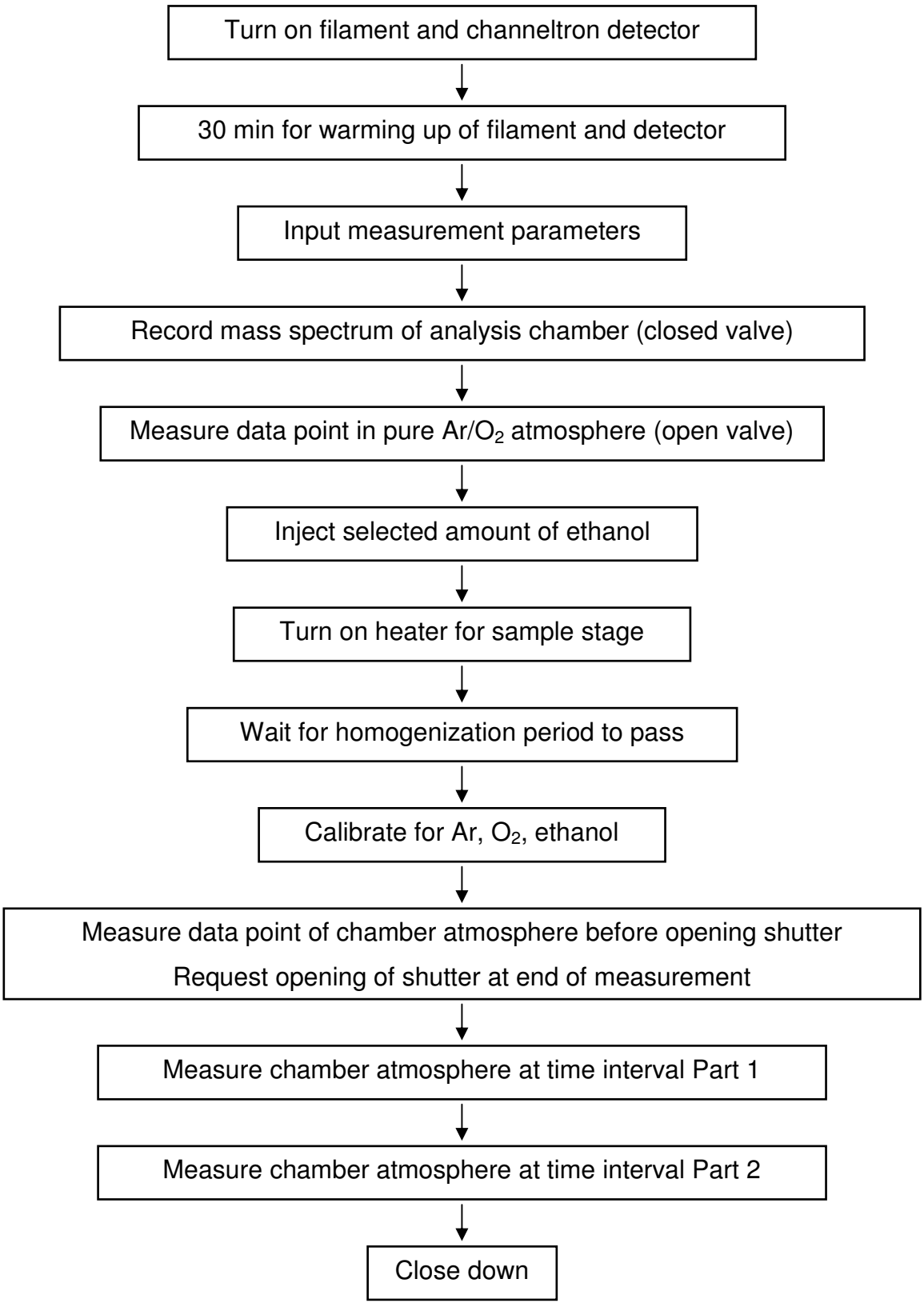

Figure 3. 8:
Flow chart of measurement program used for photocatalysis measurements.

3.2 Thin film deposition

In this part, the different types of films deposited, and the methods used, will be discussed. Two different types of substrates were used, namely standard microscope slide glass (Fiers-Roth) which is a standard soda-lime glass, and alkali free AF45 (PGO, Germany). The films to be used for ion implantation were deposited onto low sodium Corning7059 (Corning Industries).

In the following sections the production of the reference films (section 3.2.1), the sputter deposition (section 3.2.2), the ion implantation of sputtered films (section 3.2.3) and the post deposition anneal treatment (section 3.2.4) will be discussed.

3.2.1 Deposition of reference catalyst P25

To obtain a reference catalyst Degussa P25 powder (Degussa AG, Germany) was spin coated onto microscope glass slide substrates (Fiers-Roth, Belgium) following a procedure adapted from [Mills03]. Four different suspensions in de-ionized water were prepared at different times, two with 0.5 g/ 10 ml and two with 1.0 g/ 10 ml. The first three, also referred to as slurry 1, 2 and 3, were used for the initial calibration experiments discussed in section 4.1.6.2 as well as for control measurements whenever the reaction chamber was started up after an extended downtime. The last suspension was used for the experiments on the dependence of the photocatalytic activity on film thickness (section 4.3.6.1). To prepare the thin films the suspension was spread onto the substrate with dimensions of 3.8 x 2.5 cm and spin coated at 4000 rpm for 15 s using a photoresist spinner. In some cases a second coating was applied to increase the film thickness. From the last suspension up to four coatings were applied per sample. The films were then dried for some days at room temperature in air.

3.2.2 D.C. magnetron sputter deposition of TiO_2 thin films

As mentioned in section 2.8 TiO_2 thin films can be deposited by d.c. magnetron sputtering from metallic Ti or semi-conducting, ceramic TiO_{2-x} targets. After some initial testing it was opted to use the ceramic TiO_{2-x} targets in this study due to the higher deposition speed for stoichiometric films and the better process stability. Using sintered ceramic targets also allowed for dopant introduction during target processing. In the following paragraphs the target fabrication and characterization (section 3.2.2.1) and the thin film deposition process (section 3.2.2.2) are discussed in more detail.

3.2.2.1 Target fabrication (at ITME) and characterization

The ceramic (mixed oxide) TiO_{2-x} targets were prepared at ITME (Poland) using powders of TiO_2 (Ferro electronic materials, U.S.A.), Nd_2O_3 (Metal Rare Earth Ltd, China), Fe_2O_3 (Aldrich, U.S.A.), V_2O_3 (Aldrich, U.S.A.). For both pure TiO_{2-x} and mixed oxide targets the powders were ball milled together with water for 24 h. After drying, all powders were uniaxially pressed into shape and then compacted by cold isostatic pressing. These compacts were sintered at 1733 K (Nd_2O_3 additive), 1623 K (pure TiO_2, Fe_2O_3 additive) or 1773 K (V_2O_3 additive) in a vacuum furnace in order to obtain sub-stoichiometric TiO_{2-x} targets. Different sintering temperatures were necessary due to the nature of the additive. The sintered discs were then machined into sputtering targets having a diameter of 50 mm and thickness of 3 and 6 mm. For the pure TiO_2 targets RBS analysis yielded a stoichiometry of $TiO_{1.75}$ [Tomaszewski03].

The targets were characterized by XRD analysis (section 3.3.1) to determine their crystallographic phase formation. The resistivity of the target material was measured by the Van der Pauw technique using a four point probe setup [Schroder98] using small pellets processed identical to the targets.

3.2.2.2 Thin film deposition

The thin film deposition was performed in a custom made sputtering chamber of ca. 50 dm^3 (Figure 3. 9). The pumping unit consisted of a turbo-molecular pump (Pfeiffer Vacuum TPU300), backed by a rotary vane pump (Alcatel T_v2033). The pressure in the chamber was monitored by a compact process ion gauge (Pfeiffer Vacuum IMR265). The chamber was evacuated to a base pressure of $< 10^{-5}$ mbar. Ar was used as sputter gas, and was introduced at a fixed flow of 25 sccm using a 50 sccm range mass flow controller (MKS). The Ar pressure was adjusted using a throttle valve (VAT series 61 control butterfly). Oxygen could then be added through a second mass flow controller (MKS).

For characterization of the sputtering behavior of the targets the dependence of the discharge behavior and the deposition rate on the discharge gas characteristics (Ar-pressure, O_2-flow rate) were determined.

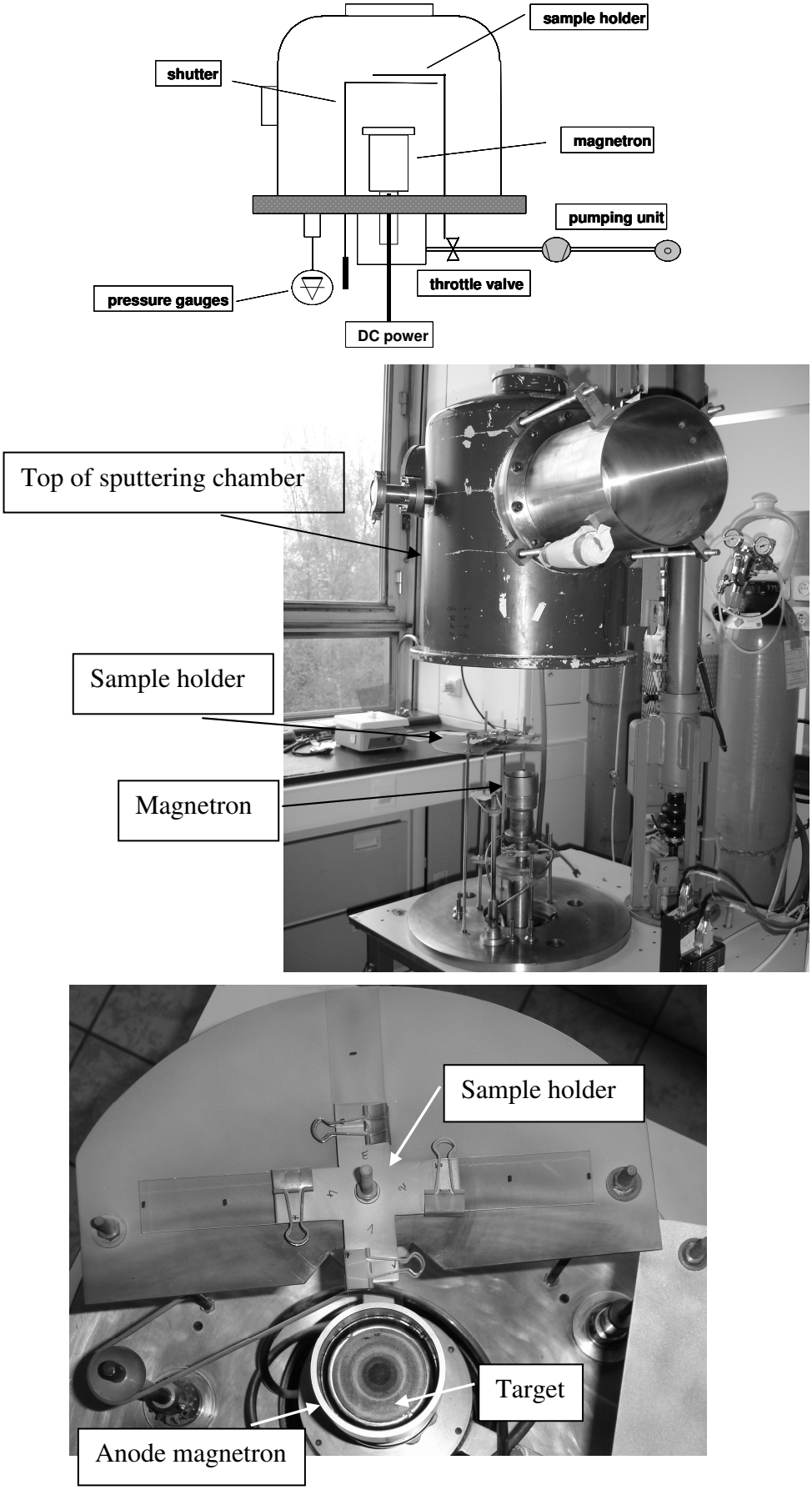

Figure 3. 9:
Top: sketch of sputtering chamber, Center: photograph showing open chamber.
Bottom: detail of sputtering chamber showing target, magnetron and sample holder.

For the actual thin film deposition the pressure of argon was varied in a range between 0.47 and 2.2 Pa. It was found that no oxygen addition was needed to yield stoichiometric films. The applied d.c. power (Huettinger PFG1500DC) was varied from 60 to 180 W. Thin films were deposited at fixed deposition times (for calibration of the deposition rate) or fixed film thickness (for thin film analysis). The standard film thickness was 350-400 nm, which allowed good optical analysis and measurement of the photocatalytic reactivity.

3.2.3 Ion implantation of Fe and Nd (ITME)

Ion implantation of Fe and Nd into as deposited TiO_2 thin films was performed at ITME (Poland) using Fe and Nd metal as ion source. The implantation energies were determined by the operator as to yield a homogeneously implanted zone of 40 nm depth starting from the thin film surface. Three different ion concentrations for this implanted zone were chosen, namely 0.5, 1.0 and 2.0 at%. To achieve this flat concentration profile two implantation steps using different ion energies were used. For Fe the first step was performed at 45 keV with fluencies of $3 \cdot 10^{14}$, $6 \cdot 10^{14}$ and $1.2 \cdot 10^{15}$ and the second step was performed at 85 keV with fluencies of $1.85 \cdot 10^{14}$, $3.7 \cdot 10^{14}$ and $7.4 \cdot 10^{15}$. For Nd the first step was performed at 50 keV with fluencies of $3 \cdot 10^{14}$, $6 \cdot 10^{14}$ and $1.2 \cdot 10^{15}$ and the second step was performed at 150 keV with fluencies of $1.83 \cdot 10^{15}$, $2.6 \cdot 10^{15}$ and $5.2 \cdot 10^{15}$.

The complete sputtered area was implanted. For each implantation condition two samples were prepared: one was analyzed as received while the second was first subjected to an anneal treatment at 673 K/ 1 h (see also next section). Only for the measurement of the photocatalytic activity the same sample was first tested as received, then heat treated and re-tested.

3.2.4 Post deposition anneal treatment for layer crystallization

Since all as deposited films were XRD amorphous (section 4.3) it was necessary to apply post deposition annealing to crystallize the layers. Anneal temperatures between 523 and 773 K were investigated, as well as anneal times between 0.25 and 2 h. Annealing was performed in a small box oven (Heraeus, Germany), with manual temperature control. The temperature was measured with a chromel-alumel thermocouple using a hand-held read out. The samples were placed into the cold oven and ramped at a speed of ca. 10 K/ min up to a temperature of ca. 50 K below the chosen anneal temperature. The heating rate was then reduced to minimize overshooting the temperature. The samples were held for the respective anneal time at this temperature, which could vary with ±5 K due to the manual control. The oven was

then switched off and left to cool down with the door opened. After ca. 30 min (when the temperature had decreased by ca. 100 K) the samples were removed. Only the sample annealed for 0.25 h was treated differently: it was placed into the preheated oven (673 K) to ensure a short anneal time.

3.3 Thin film characterization techniques used

3.3.1 XRD

The crystallinity of the thin films was investigated with an x-ray diffractometer (Siemens Kristalloflex DS5000) using CuKα radiation at 40 kV and 40 mA working in the θ-2θ mode. A measurement of 2 h over a 2θ range of 20-60° yielded sufficient information on the crystal structure of the thin films. For the ion implanted films a longer measurement time of 8 h was chosen.

The crystallite size of the annealed films was estimated using the Scherrer formula [Cullity78]:

$$\Delta(2\theta) - A = \frac{B \cdot \lambda}{D \cdot \cos\theta} \qquad (3.2)$$

with 2θ the diffraction angle, D the grain size, B a correction factor for the crystallite shape (taken to be 0.9 in anatase), A the instrumental broadening factor, λ the wavelength of the x-ray tube (for CuK_α λ = 0.154056 nm). $\Delta(2\theta)$ is the full width at half maximum (FWHM) of the diffraction peak. The instrumental broadening factor A increases with increasing slit width and diffraction angle 2θ. Values of 0.075 and 0.1 for A were used to calculate the crystallite size from the (101) and (004) reflections, respectively. These values were taken from a calibration curve of the diffractometer. One has to keep in mind that in this way one determines the thickness of the crystallites perpendicular to the surface of the thin film.

The length of the lattice constant c was estimated from the position of the (004) diffraction peak using Bragg's law [Cullity78]:

$$n\,\lambda = 2\,d\,\sin\theta \qquad (3.3)$$

with n the order of the diffraction peak, and d the diffraction plane spacing. For the (004) reflection one has $n = 4$ and the lattice constant c is identical to $4d$. Using the reference value c_o (calculated from the (004) reflection peak at 37.801° from the ASTM spectrum for anatase) one can calculate the lattice strain $\Delta c = (c - c_o)/c_o$.

The lattice constant *a* was estimated using the more general formula:

$$d_{(hkl)} = \frac{a}{\sqrt{h^2 + k^2 + l^2 \, a^2 / c^2}} \tag{3.4}$$

which is resolved for the (101) diffraction peak as:

$$a = \frac{d_{(101)}}{\sqrt{1 - d_{(101)}^2 \; c^2}} \tag{3.5}$$

The fact, that the $d_{(004)}$ and $d_{(101)}$ spacing were not shifted by the same angle or even in the same direction, was used to verify that there was not just a simple shift in the XRD spectrum due to an instrumental error.

Both the FWHM and the diffraction plain spacing *d* were determined from the θ-2θ raw data using the software package of the diffractometer.

3.3.2 Film thickness

The film thickness was determined by two different methods. The first was by using a profilometer (Taylor-Hobson Talystep). In order to determine the reproducibility of the film thickness all samples deposited were measured.

The second method was to calculate the thickness from the interference fringes using the method of Swanepoel, which also yielded the refractive index (section 2.2.2.2).

3.3.3 SEM

SEM analysis of the film top surface as well as of a fractured cross sectional surface was performed using an environmental SEM (FEI Quanta 200F FEG-SEM), both before and after annealing. It was necessary to perform the analysis in the low vacuum mode (120 Pa water atmosphere) due to charging of the sample surface. The maximum useful magnification was 240 000x for top surface and 80 000x for cross sectional surface analysis. The cross sections were viewed under a tilt angle of 10°. Secondary electron (SE) images were used in all cases.

3.3.4 ESCA

ESCA analysis (Perkin Elmer PHI ESCA 5500) was performed to determine the stoichiometry and dopant level of the thin films. When determining the oxidation state *n* of Ti^{n+} species care must be taken on how the analysis of TiO_2 surfaces is performed due to the

ease of reduction of this compound under ion beam sputtering in vacuum (which is commonly used for cleaning the sample surface) [Hashimoto02]. It was, therefore, opted not to perform any ion beam cleaning. The Ti2p peak was analyzed for the presence of lower oxidation states of Ti using a peak fit routine.

Fe, Nd and V dopant concentrations were determined from the Fe2p, Nd4d and V2p peaks, respectively. The time per energy window was chosen as to allow maximum time to go to measurement of the dopant. For each analysis also a survey spectrum over the energy window of 0-1400 eV was taken. For the individual components multiplex spectra over the following energy windows were taken: 475-450 eV for Ti2p, 295-277 eV for C1s, 540-522 eV for O1s, 140-110 eV for Nd4d, 750-695 eV for Fe2p and 535-505 eV for V2p.

3.3.5 Optical transmission

Optical transmission measurements were performed with a UV-VIS-NIR spectrophotometer (Varian Cary 500) in transmission mode using a measurement and a reference beam. Since the layer thickness was not sufficiently homogeneous over the complete sample area it was chosen to measure through an aperture of ∅ 5 mm for both measurement and reference beam.

For determining the refractive index the measured wavelength range was 250-2000 nm. The refractive index was calculated from the interference fringes using the method of Swanepoel (section 2.2.2.2). This also allowed to calculated the film thickness at the point of measurement. The porosity could be calculated according to equation (2.5), p. 12.

For determining the optical band gap the measurement range was restricted to 250-450 nm (i.e. around the absorption edge). In order to enhance the measured signal, the intensity of the reference beam was reduced by inserting a wire-mesh into its path. To calculate the optical band gap it was necessary to first calculate the optical absorption using equation (2.6)b, p. 12, correcting for absorption of the substrate, reflection losses and sample thickness.

The band gap energy was determined using equation (2.12), p. 17, and a value for m, according to table 2.2, p. 17. When using the correct value for m one can obtain a linear fit to part of the curve (there are non-linear parts to the curve due to increasing absorption and interference fringes). One then gets the band gap energy E_{bg} by dividing the y-axis intercept by the slope. Since there still is some discussion on the mode of the band gap transition in anatase and amorphous TiO_2 (section 2.2.4.6) different values for m where tried to obtain the best fit.

4 Results and discussion

This chapter consists of 4 parts: The first discusses the development and characterization of the photocatalysis chamber and an appropriate photocatalytic testing procedure for thin films (section 4.1) . In the second part the d.c. magnetron sputtering characteristics of the ceramic TiO_{2-x} targets and the M_2O_3-TiO_{2-x} mixed oxide targets (M=Fe, Nd) are described (section 4.2). In the third part the dependence of the thin film characteristics on the sputtering parameters for TiO_2 films is discussed (section 4.3), while the fourth and last part is devoted to the influence of additives on the thin film characteristics (section 4.4).

4.1 Design and characterization of the photocatalytic test reactor

In this section the initial design and testing of the photocatalytic test reactor is discussed. The first issues addressed were the proper use of the atmospheric gas analyzer and the general feasibility of the concept of the reaction chamber (section 4.1.1). Secondly, the testing of different organic substances to find a suitable one for thin film testing in the given environment is described (section 4.1.2). Then the initial reaction process characterization (section 4.1.3), the breakdown mechanism for ethanol (4.1.4) and the influence of external parameters (section 4.1.5) will be discussed. The last section (4.1.6) is devoted to the final experimental design, choice of reference catalyst and data analysis for testing of the sputter deposited thin films.

4.1.1 Initial reactor testing

4.1.1.1 Testing in pure Ar

Initial testing of the photocatalytic test reactor and the gas analyzer was performed in a pure Ar atmosphere which has a simpler mass spectrum than the argon/ oxygen gas mixture used for the photocatalytic breakdown measurements. During these tests only the mass spectrum of the chamber atmosphere was recorded at fixed time intervals to monitor the changes with time over the complete mass/ charge range. The spectra were recorded with the faraday detector.

The reactor design evolved with the experience gained in the testing period, the initial reactor testing was performed with a reactor setup similar to the one shown in Figure 3.1, p. 110. At this stage a more simple sample holder was used which did not allow for tempera-

ture control. No UV light was used at this point, and all experiments were performed in the dark (window closed off by shutter).

a. Stability of reactor atmosphere with time

Due to the construction of the reaction chamber (using rubber o-ring seals) there was a chance that surrounding air (ca. 80% N_2 and 20% O_2) could enter the chamber through the seals after it was filled with the controlled atmosphere. For this purpose the purity of the chamber atmosphere (pure Ar) and how it changed with time was observed for a period of up to 19 h. This was done for two different chamber pressures, namely 975 and 1050 mbar which are, respectively, below and above the standard atmospheric pressure of 1013 mbar.

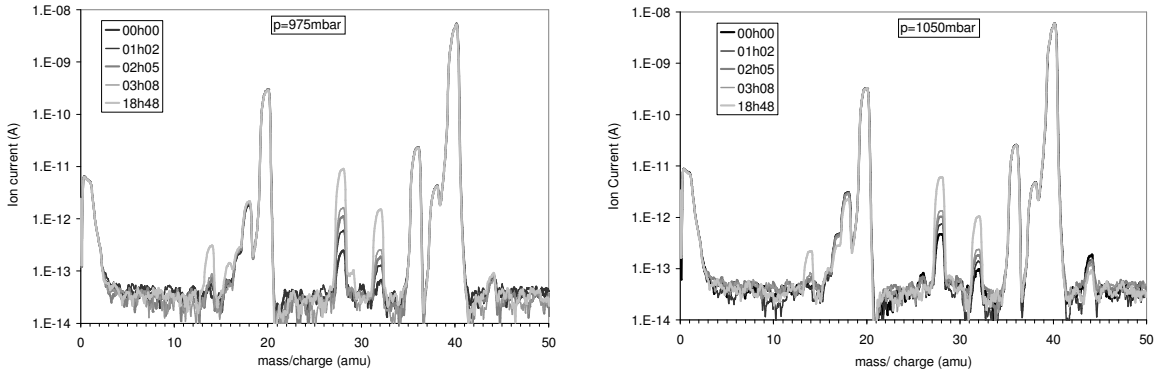

Figure 4. 1:
Mass spectra of the chamber atmosphere (100% Ar) taken over a period of almost 19 h to see the evolution of the impurity content.

To interpret the mass spectra it is important to know the main peaks of Ar which are given in Table 4. 1:

ion	$^{36}Ar^{++}$	$^{38}Ar^{++}$	$^{40}Ar^{++}$	$^{36}Ar^{+}$	$^{38}Ar^{+}$	$^{40}Ar^{+}$	$^{40}Ar_2{}^{+}$
mass/charge	18	19	20	36	38	40	80 (not shown)

Table 4. 1: Main Ar peaks observed in the mass spectra recorded from the Ar-filled reactor.

Looking at Figure 4. 1 one can see that there are some additional signals besides the main lines of Ar indicating that N_2 (14, 28 amu), O_2 (16, 32 amu) and CO_2 (44 amu) are present in the chamber (the underlined mass/ charge values are from the main peak). The presence of water is indicated by the shoulder at 17 amu (main peak 18 amu), but it is mainly obscured by the peak at 18 amu originating from $^{36}Ar^{++}$. The most significant observation is that the peaks at 14 and 28 amu (N_2) and as well as 16 and 32 amu (O_2) are increasing with time, especially after the first few measurements, indicating that there is an inward diffusion of air. The increase in signals is stronger for the lower reactor pressure, so that one can conclude that the

inward diffusion of air can be reduced by working with a chamber pressure which is higher than that of the surrounding air.

On the other hand, the signal for CO_2 (44 amu) remains stable throughout the measurement period, which means that its concentration is not influenced. No judgment can be made about how the concentration of water is affected since the peak is too much obscured by the presence of $^{36}Ar^{++}$.

As a result from these tests is was opted to continue working at pressures above the atmospheric average.

b. Stability of the test substance signal with time

A second important test was whether volatile organic test substances could be contained in the chamber and not be lost through the vacuum seals of the reactor. For this purpose, first a spectrum of the Ar-atmosphere in the chamber was recorded (at t = 00h00) before 6 µl of the organic substance (ethanol) were injected. Then spectra of the reactor atmosphere were recorded at fixed time intervals. The measurements were performed at two different pressures above standard air pressure, namely 1050 and 1099 mbar. Higher working pressures could not be used as this would compromise the working of the gas analyzer and would also exceed the range of the pressure gauge used.

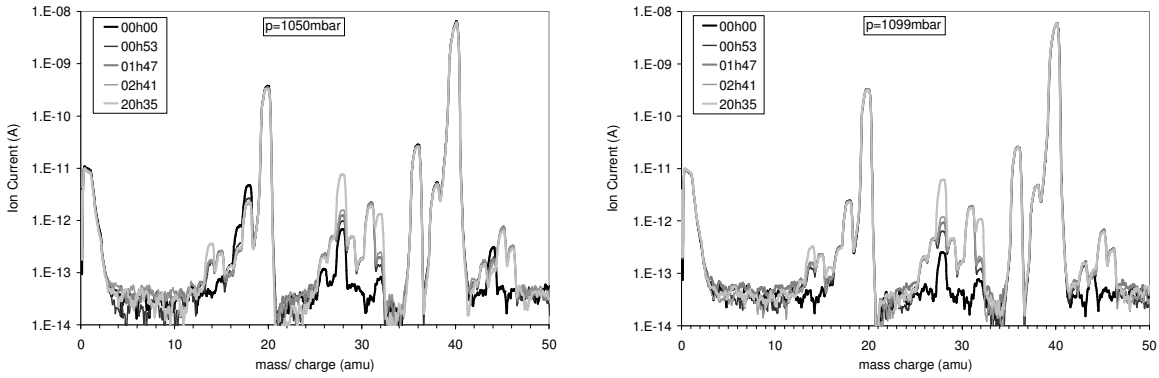

Figure 4. 2:
Stability of the ethanol signal with time for two different chamber pressures: 1050 (left) and 1099 mbar (right). The black curve shows the Ar atmosphere, the grey peaks were taken after the injection of ethanol.

The additional peaks originating from ethanol can be seen in Figure 4. 2 for spectra recorded from t = 00h53 on. These will be discussed in more detail in section 4.1.2. Since there are peaks overlapping with 14, 28 and 32 amu, which are present due to the N_2 and O_2 impurities, one can see an increase of these peaks after injection of the ethanol. When looking at the

evolution of the mass spectrum over time one can clearly see that the height of the peaks that originate primarily from ethanol do not change significantly (please refer to section 4.1.3.4). One can conclude, therefore, that this volatile organic is contained in the reactor.

Figure 4. 2 also clearly shows that using Ar instead of N_2 allows for detecting peaks around 28 amu, which would otherwise be obscured. Unfortunately, the impurity content of N_2 is still too high to allow detection of CO at 28 amu. Peaks around 32 amu (O_2) are also nicely visible here, but when switching to the Ar/ O_2 mixture (80%/ 20%) these will also be obscured.

No significant difference between the two pressures can be observed. It was opted to continue working at a chamber pressure of 1050 mbar, which is safer for the gas analyzer.

4.1.1.2 Testing in Ar/O_2

Upon switching from Ar to the Ar/O_2 gas mixture for the chamber atmosphere some adaptations in the measurement routine were made. One change was to include measurements of the peak height of selected mass/ charge points, i.e. using the multiple ion detection (MID) function of the spectrometer. Again, first the fingerprint spectrum and the stability of the chamber atmosphere were measured. Afterwards the feasibility of different volatile organic test substances was investigated.

a. Stability of reactor atmosphere with time

Adding oxygen as second component to the gas mixture complicates the mass spectrum and adds impurities as can be seen from the left side of Figure 4. 3 (next page). The right side shows the MID data collected at the same time as the mass spectra were taken. The peaks followed were 18 ($^{36}Ar^{++}$, H_2O), 28 (N_2, CO), 32 (O_2), 40 (^{40}Ar) and 44 amu (CO_2). The data collection using the MID function allows to follow the peak height of the selected mass/ charge signals more clearly than the full mass spectrum.

As can be seen from the MID measurements (Figure 4. 3, right, following page) there is a small decrease in the mass/ charge signal for all masses with exception of N_2, which can be seen to increase strongly. Latter nicely shows, qualitatively, the inward diffusion of air. No signal change of the O_2 signal is detected since now its concentrations inside and outside the chamber are close to identical.

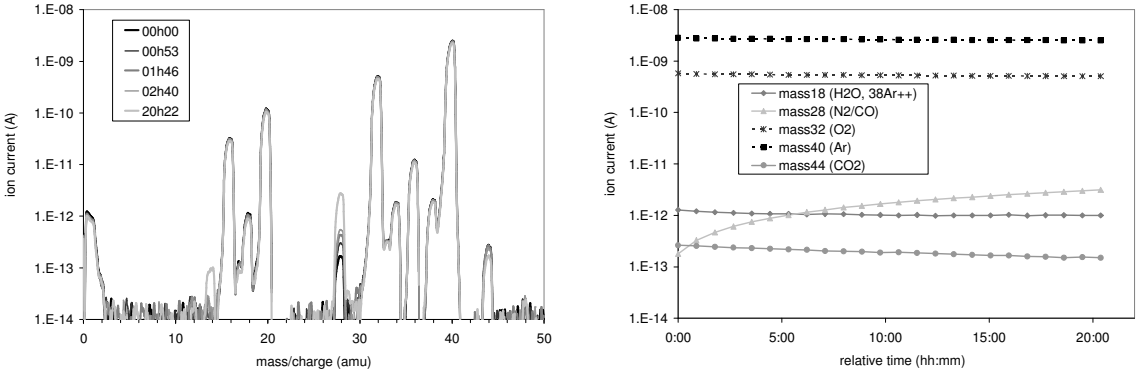

Figure 4. 3:

Mass spectrum (left) and 'multiple ion detection' (MID) graph (right) of the Ar/O_2 (80:20%) gas mixture used as air substitute in the photocatalytic test reactor.

As already mentioned, there is a small signal decay that occurs with time, especially for the low concentrations. This was found to be normal for the instrument and will be compensated for by the calibration feature when calculating concentrations from the intensity of the mass/ charge signals (section 3.1.3.3).

4.1.2 Testing of different organic test substances

Important for the choice of the test substance is that it should not have any important mass/ charge peak(s) in the range from 31 to 41 amu, since any such signal would be obscured by the strong peaks of the basic atmosphere, namely Ar and O_2. Also, the detection of water (18 amu) will be difficult, and changes could be followed qualitatively, at best. Detection of CO_2 could also pose a problem due to the high impurity content of the basic gas mixture. As a result it can also only be followed qualitatively, at best.

Several volatile organic substances (VOC's) were examined for their possible use, namely methanol, ethanol, acetone, isopropanol and propane. The materials were chosen because they represent a class of VOC's that are common in indoor air.

First, the library spectra were studied to find whether they would be compatible to the chosen chamber atmosphere and whether there was a strong molecular peak in the spectrum which allowed for measuring the photocatalytic breakdown of the compound (section 4.1.2.1). Latter is not possible using a fragment peak, since then it would not be clear whether the fragment originated from a catalytic breakdown product or fragmentation of the original molecule in the mass spectrometer.

Secondly, the remaining test substances deemed suitable were subjected to a stability test. This, together with the final choice, will be discussed in section 4.1.2.2.

4.1.2.1 Comparing library spectra to the Ar/O_2 atmosphere of the reactor

a. Methanol

Methanol is an interesting compound as it is a small molecule which can only follow a simple oxidation process as compared to longer chained alcohols.

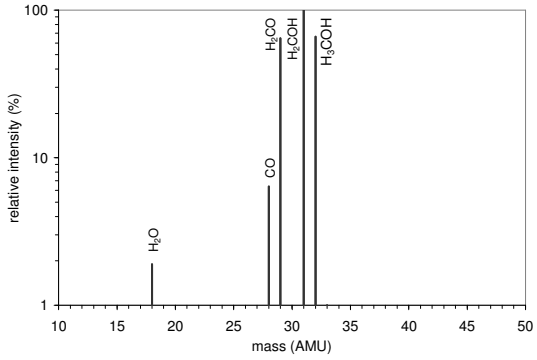

Figure 4. 4:
Library spectrum of methanol [software2].

As one can see from Figure 4. 4 above, the mass spectrum of methanol is very simple, but unfortunately the molecular peak lies at 32 amu, which will be completely obscured by oxygen from the chamber atmosphere. The peak at 31 amu could be an alternative, but it will also be partially obscured by the O_2 signal. The third strongest peak at 29 amu can easily be distinguished from the nitrogen impurity signal at 28 amu. Unfortunately it is identical to the molecular peak from formaldehyde, which is the first oxidation product of methanol. Therefore, it was decided that methanol is not a suitable candidate as organic test substance for the used reactor set up.

b. Ethanol

Ethanol is the second smallest alcohol molecule and an easy to handle organic. It also follows a rather simple photocatalytic oxidation process. The library spectrum of ethanol (Figure 4. 5, following page) shows that the molecular peak at 46 amu is not the strongest, but the peak at 45 amu, corresponding to the fragments $CH_3CH_2O^+$ or CH_3C^+HOH generated by the loss of one H, is still representative of the original molecule. There is no peak at 44 amu which could be interfering with CO_2. Possible oxidation products like acetaldehyde (CH_3CHO) and acetic acid (CH_3COOH) have molecular peaks at 43 and 60 amu, respectively, so that they are not expected to interfere with the selected peak for ethanol at 45 amu. Additionally, the 'blocked' range between 31 and 41 amu shows few peaks, so that one can conclude that ethanol is a good candidate for the organic test substance.

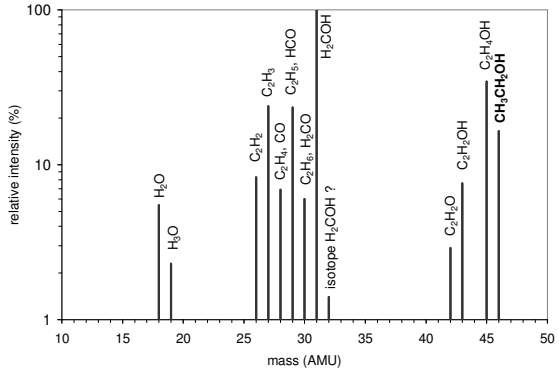

Figure 4. 5:
Library spectrum of ethanol [software2].

c. Isopropanol

Isopropanol is the most simple secondary alcohol, i.e. the alcohol function sits on the second C atom from the end of the chain.

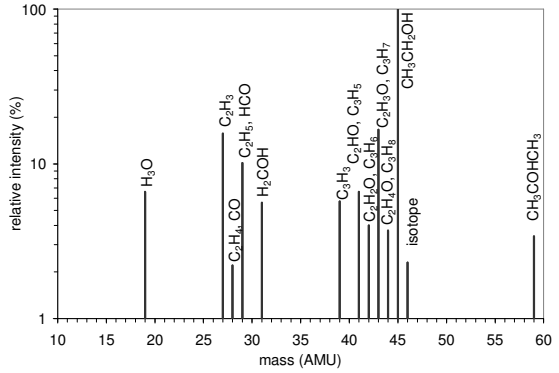

Figure 4. 6:
Library spectrum of isopropanol [software2].

When looking at Figure 4. 6, one major problem becomes immediately apparent, namely that the molecular peak at 59 amu is quite weak (only around 3.5%). The strongest peak is the one at 45 amu, which is identical to the molecular peak of ethanol, i.e. a fragment which comes from the breaking of the C-3 chain. This means that there is the possibility of interference with breakdown products during the photocatalytic reaction. On the other hand, interference with the immediate reaction product, namely acetone, is not to be expected (comparing Figure 4. 7, next page, and Figure 4. 6).

In conclusion, isopropanol is not a good choice for the organic test substance, because its molecular peak cannot be observed.

d. Acetone

Acetone is the most simple ketone, and a commonly used organic test substance.

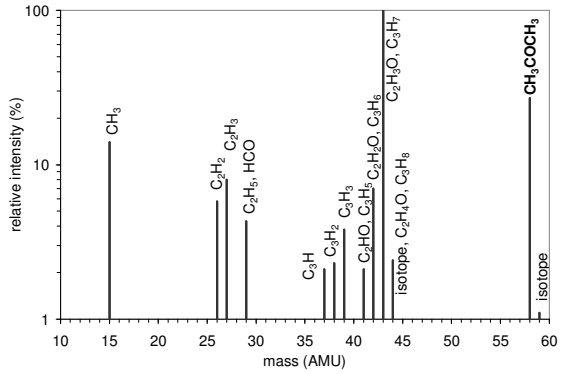

Figure 4. 7:
Library spectrum of acetone [software2].

The library spectrum of acetone (Figure 4. 7) shows that for acetone there is a strong molecular peak at 58 amu. There are some fragment peaks in the range 36-41 amu but they originate from the C_3 chain, not from oxidation products. These would contain added O in the methyl groups (e.g. $CH_2OHCOCH_3$) or fracturing of the chain (e.g. CH_3CHO^+ and CH_3OH), yielding molecules with higher or lower masses. Both should not lead to an interference with the molecular peak at 58 amu.

In conclusion, acetone looks like a good candidate for the organic test substance.

e. Propane

Propane is an interesting compound since it can be used representatively for lower chained hydrocarbons. The molecular peak from propane (44 amu) is strong enough, but unfortunately there will be interference with CO_2 which is an impurity in the Ar/O_2 gas mixture. Interference from reaction products are also possible, e.g. acetaldehyde CH_3CHO, with its molecular peak at 43 amu. Therefore, propane does not seem a good candidate for the organic test substance.

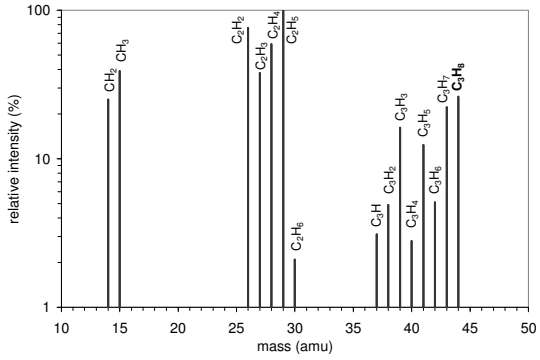

Figure 4. 8:
Library spectrum of propane [software2].

4.1.2.2 Final choice of test substance

After the selection process discussed in the previous section only acetone and ethanol remained as good choices for the organic test substance. Since ethanol had been used to perform the initial pre-testing (section 4.1.1) its signal stability with time was known. Even though acetone also passed the stability test, it was opted to use ethanol. It is the more user friendly and less toxic compound of the two and its breakdown mechanism is well known. All further experiments were, therefore, performed with ethanol.

4.1.3 Initial reaction process characterization

All previous testing had been done with the lower resolution faraday detector which had the advantage of a better signal stability but the disadvantage of a lower resolution. Therefore, spectra were also recorded with the more sensitive channeltron (SEM) detector and the two detector modes compared (section 4.1.3.1). Then the stability of ethanol as organic test substance was re-checked using the Ar/O_2 atmosphere in the reaction chamber (section 4.1.3.2). Also the calibration function of the mass spectrometer was implemented (section 4.1.3.3).

In the end two important tests, namely a blank and a dark test were performed to investigate the influences of the reaction conditions on the organic test substance ethanol which did not originate from the photocatalytic breakdown process itself (section 4.1.3.4).

4.1.3.1 Comparison of the detector mode

Figure 4. 9, next page, shows the mass spectrum of 273 ppm ethanol in the Ar/ O_2 gas mixture, recorded with the faraday (right) and the channeltron (left) detector. One can clearly see that the weaker peaks are much better resolved with the channeltron detector. Some new peaks are even seen which were not detected with the faraday detector, e.g. 22 amu (CO_2^{++}).

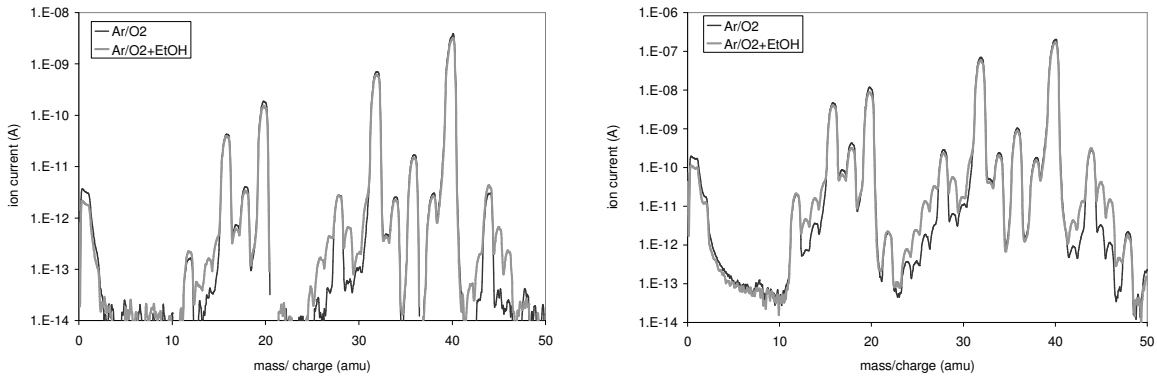

Figure 4. 9:

Comparison between faraday (left) and channeltron (right) detector for 273 ppm ethanol in the Ar/O_2 gas mixture.

A second observation is that both spectra show more peaks from ethanol than given in the QuadStar library (Figure 4. 5, p. 137), namely fragments like CH_3 (15 amu) and C_2H (25 amu). Evidently the fractioning pattern of the mass spectrum depends on the measuring conditions. As discussed before, some peaks are obscured by the Ar-peaks at 18 and 19 amu and anything in the range between 31 and 41 amu. As a result, the strongest peak at 31 amu (H_2COH), which could be seen well in pure Ar (Figure 4. 2, p. 133), is not detectable anymore in the Ar/ O_2 gas mixture. The peak at 28 amu (CO, C_2H_4) is obscured by the N_2 impurity.

It was decided to use the more sensitive channeltron detector for the photocatalysis experiments even though it was found to have a lower signal stability with time.

4.1.3.2 Stability of the test substance signal with time in the Ar/O_2 gas mixture

To test the stability of ethanol with time in the Ar/ O_2 atmosphere, 273 ppm (6 µl) ethanol were injected into the reaction chamber. Mass spectra and MID data were recorded (with the faraday detector) before and after the homogenization period following injection and then at fixed time intervals (Figure 4. 10, next page).

One can see that all signals remain quite stable with exception of the one at 28 amu, whose increase is due to the inward diffusion of N_2. The small decrease in ion current observed for the stable signals is due to the equipment (see section 4.1.1.2).

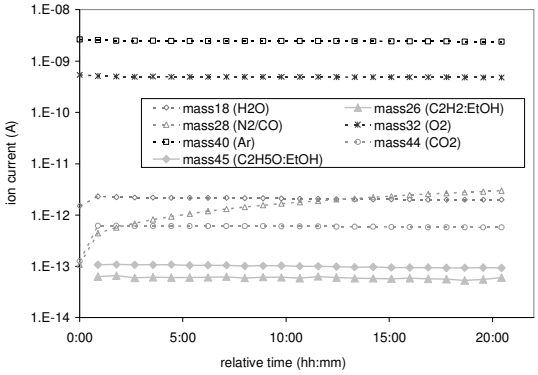

Figure 4. 10:
Stability test for ethanol in an Ar/O_2 gas mixture for 20 h, faraday detector.

4.1.3.3 Implementing the calibration function of the mass spectrometer

As a next step, the calibration function (multiple concentration detection, MCD) was implemented (section 3.1.3.3). Here, both the O_2 signal at 32 amu and the ethanol signal at 45 amu were calibrated against the Ar signal at 40 amu. No interference between mass/ charge signals originating from fraction peaks of ethanol with the two signals of Ar and O_2 is expected since the concentration of ethanol is 273 ppm (0.0273%) as compared to 80 and 20%, respectively.

The resulting data resemble the ones shown in Figure 4. 10 with addition of the data for the concentrations of Ar, O_2 and ethanol. Since the resulting MID/ MCD graphs now tend to get rather complicated, individual components were selected for pointing out the observed changes.

4.1.3.4 Blank and dark test

For the following two tests the stability of ethanol under reaction conditions needed to be examined, namely (i) under UV light without the catalyst being present (blank test) and (ii) in the dark in the presence of the catalyst (black test). These tests are needed to ensure there are no factors other than photocatalytic breakdown causing a decrease of the ethanol concentration. The results for measurement of the ethanol concentration are shown in Figure 4. 11 on the following page, with the time scale starting at the moment of turning on the UV lamp (blank test) or the equivalent point at the end of the homogenization period (black test).

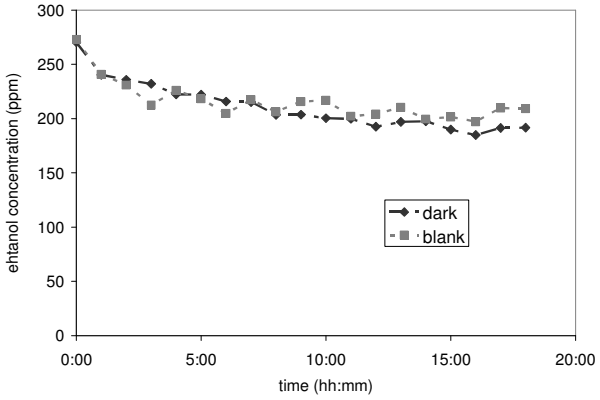

Figure 4. 11:

Blank and dark test with 6 µl ethanol. The blank test was performed illuminating a clean glass slide with a UV power of 100 W. The black test was performed by exposing a coating of P25 on glass to the chamber atmosphere in the dark.

The most important observation is that there is indeed a decrease in ethanol concentration observed, especially at the beginning of the experiment. This was found to be mostly due to the problem of the drift of the channeltron detector discussed in section 4.1.3.1, since it was not observed with the faraday detector (Figure 4. 10, previous page). The nominal 'reaction' rates of ethanol, calculated as described in section 4.1.5.1, are 0.174 and 0.152 ppm/min for the black and blank test, respectively. As we will see later (sections 4.1.6, 4.3 and 4.4) these values are substantially smaller than the photocatalytic activity observed in the P25 reference films and the sputtered TiO_2 thin films, respectively.

4.1.4 Breakdown mechanism of ethanol

For finalizing the reactor design and determining a fixed experimental procedure for testing the photocatalytic activity of different TiO_2 thin films some test experiments with P25 spin coated films were necessary. The first test, consisted of measuring the complete breakdown reaction of ethanol. The results were then compared to results from literature to determine the breakdown mechanism.

4.1.4.1 Measurement of the complete ethanol breakdown

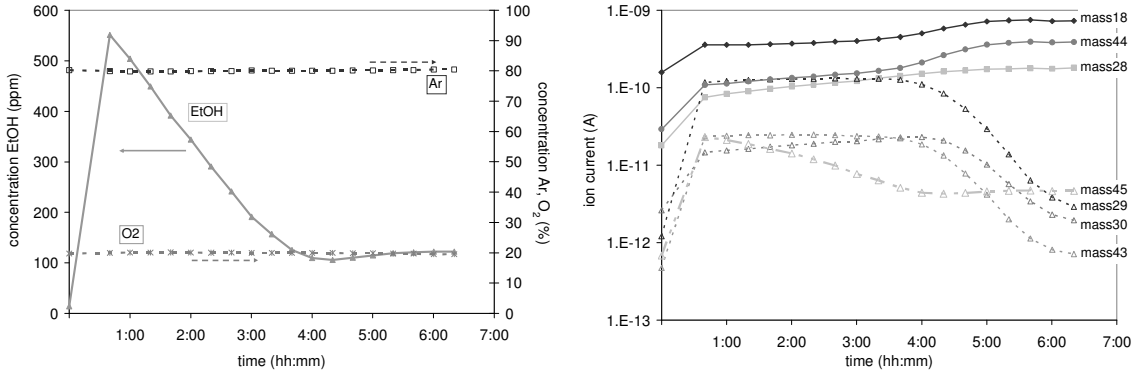

Figure 4. 12:

Multiple concentration detection (MCD, left) and multiple ion detection (MID, right) measurements during photocatalytic breakdown of 12 µl ethanol (551 ppm) with P25 (1/2 microscope glass slide).

Figure 4. 12 shows the measurement of the ethanol concentration (calibrated) and of selected mass lines. One important observation is that towards the end of the reaction the ethanol concentration seems to increase again (left graph). When looking at the right graph one can see that the final increase of the mass/ charge signal at 45 amu (used for calibration of the ethanol concentration) coincides with the strong increase of the mass/ charge signal at 44 amu, the molecular signal of CO_2. Since the difference in signal between 44 and 45 amu is two orders of magnitude this suggests that an isotope of CO_2 with 45 amu is responsible for the increased signal. There are two possibilities, namely $^{13}C^{16}O_2$, and $^{12}C^{17}O^{16}O$, with $^{13}C^{16}O_2$ being the most likely as ^{13}C has a natural abundance of 1 at% while it is only 0.038 at% for ^{17}O. As a result, it is not interesting to follow the ethanol signal further than its minimum, since it is then falsified by an increasing CO_2 concentration.

The possible ions corresponding to the observed mass/charge lines are listed in Table 4. 2:

mass/charge (amu)	18	28	29	30	43	44	45
possible ions	H2O, $^{36}Ar^{++}$	N_2, CO, C_2H_4	CHO, C_2H_5	CH_2O, C_2H_6	C_2H_3O	CO_2, C_2H_4O	C_2H_5O (ethanol), isotope CO_2

Table 4. 2: List of possible ions corresponding with the mass/ charge lines observed in Figure 4. 12.

From the different mass/ charge data (Figure 4. 12, right) one can see that the breakdown of ethanol is a two step process. First the signal at 45 amu (ethanol) decreases while the signals at 29, 30 and 43 amu increase slightly. When the signal of 45 amu has reached its minimum, the signals at 29, 30 and 43 amu decrease rapidly while the signals at 18, 44, and 28 amu increase strongly. From this one can conclude that the signals at 29, 30 and 43 amu not only originate from ethanol (Figure 4. 5, p. 137) but also from one or more intermediate

reaction product(s). As long as the intermediate is formed due to the breakdown of ethanol little change in these signals is seen due to the overlap. The second step is then the oxidation of the intermediate(s) to the final reaction products water, carbon monoxide and carbon dioxide, whose signals are seen to increase when the signals of the intermediate(s) are decreasing.

In order to see whether some oxidation products with a molecular mass higher than 50 amu were observed, mass spectra up to 80 amu were recorded (with exception of the range between 31 and 41 amu), but no lines higher than 46 amu were observed (other than those due to the measurement system). This means that acetic acid (H_3COOH, 58 amu) is not a reaction product of the photocatalytic breakdown of ethanol for the reaction setup used.

4.1.4.2 Discussion of the photocatalytic breakdown of ethanol in literature

In literature two possible mechanisms for the photocatalytic breakdown of ethanol with TiO_2 have been proposed, namely a multistep and a two step mechanism:

Multiple step mechanism:

In the multiple step mechanism the ethanol molecule is oxidized (broken down) stepwise, until the final reaction products of water, carbon monoxide and carbon dioxide are left. Possible different steps are shown in equations (4.1) to (4.5):

1) Ethanol: $CH_3CH_2OH + 0.5\ O_2 \rightarrow CH_3CHO + H_2O$ (4.1)

2) Acetaldehyde: $CH_3CHO + 0.5\ O_2 \rightarrow CH_3COOH$ (4.2)

3) Acetic acid: $CH_3COOH + O_2 \rightarrow HCHO + CO_2 + H_2O$ (4.3)

$CH_3COOH + 0.5\ O_2 \rightarrow HCHO + CO + H_2O$ (4.3)a

4) Formaldehyde: $HCHO + 0.5\ O_2 \rightarrow HCOOH$ (4.4)

5) Formic acid: $HCOOH + 0.5\ O_2 \rightarrow CO_2 + H_2O$ (4.5)

$HCOOH + \rightarrow CO + H_2O$ (4.5)a

For some equations there are two possible outcomes: if not enough oxygen is present CO instead of CO_2 can be formed (equations (4.3)a and (4.5)a).

Two step mechanism:

In the two step mechanism ethanol is first oxidized to acetaldehyde which is then broken down to the final reaction products of water, CO and CO_2.

Step 1: Oxidation of ethanol to acetaldehyde

$$CH_3CH_2OH + 0.5\ O_2 \rightarrow CH_3CHO + H_2O \quad (4.6)$$

Step 2: Mineralization of acetaldehyde

$$CH_3CHO + 2.5\ O_2 \rightarrow 2\ CO_2 + 2H_2O \quad (4.7)$$

$$CH_3CHO + 1.5\ O_2 \rightarrow 2\ CO + 2H_2O \quad (4.7)a$$

If not enough oxygen is present, CO instead of CO_2 is formed, as shown in equation (4.7)a.

In [Vorontsov04] the photocatalytic breakdown of ethanol by TiO_2 thin films in O_2 and purified air was investigated. Here the concentrations of ethanol, acetaldehyde, carbon monoxide and carbon dioxide were followed using gas chromatography. The evolution of the concentrations of these four compounds with time is shown in Figure 4. 13.

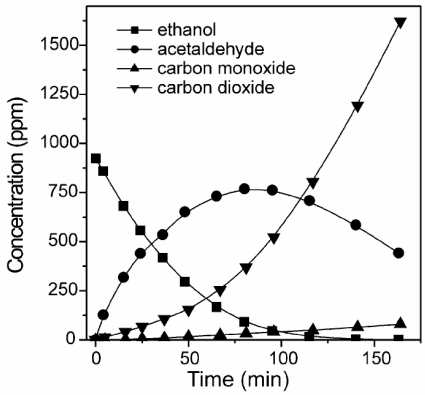

Figure 4. 13:
Photocatalytic breakdown of ethanol, taken from [Vorontsov04].

The decrease in ethanol concentration is clearly followed by the increase in acetaldehyde concentration. The carbon dioxide concentration increases little during this part of the reaction. But as soon as the acetaldehyde concentration reaches its maximum, the CO_2 concentration increases much stronger. The carbon monoxide concentration was also measured, but it was found to increase very little during the measurement.

4.1.4.3 Comparison between the experimental observations in this thesis and the discussions in literature

The observations from [Vorontsov04] match very well with the results shown in Figure 4. 12, p. 143, which leads to the conclusion that most likely acetaldehyde is the only intermediate product observed. In order to confirm this, one needs to find out whether the

observed mass/ charge lines of the intermediate(s) observed in the breakdown reaction of ethanol, namely 29, 30, 43 amu, agree with the acetaldehyde spectrum (Figure 4. 14, left).

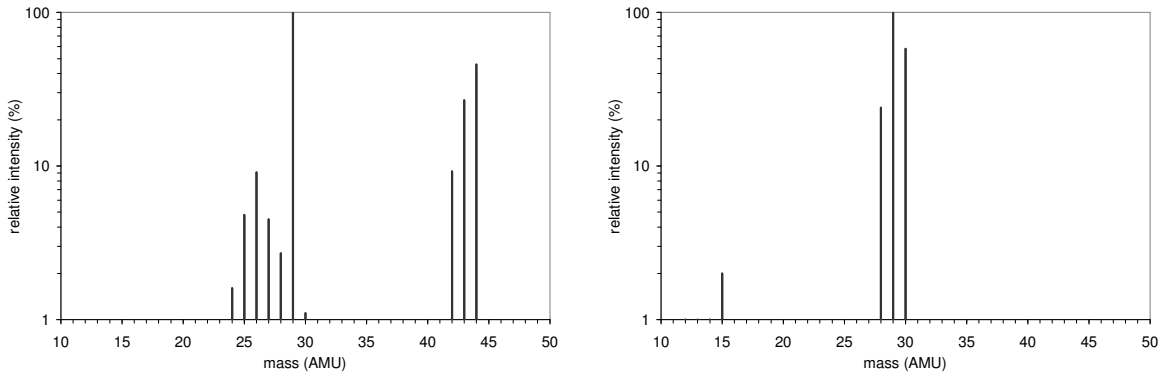

Figure 4. 14:
Reference mass spectra of acetaldehyde (left) [software2] and formaldehyde (right) [NIST].

One can see that 29 amu is the strongest mass/ charge line for acetaldehyde, followed by 43 and 44 amu. The mass/ charge line at 30 amu is very low, though. There are two possible reasons (i) the signal originates from a different molecule or (ii) the mass spectrum of acetaldehyde observed in Figure 4. 12, p. 143, is different from the literature spectrum. In order to have more information it is best to look at the recorded mass spectra from the second half of the reaction showing the breakdown of the intermediate product (Figure 4. 15, the range between 31 and 41 amu has not been recorded due to the intense peaks from O_2 and Ar).

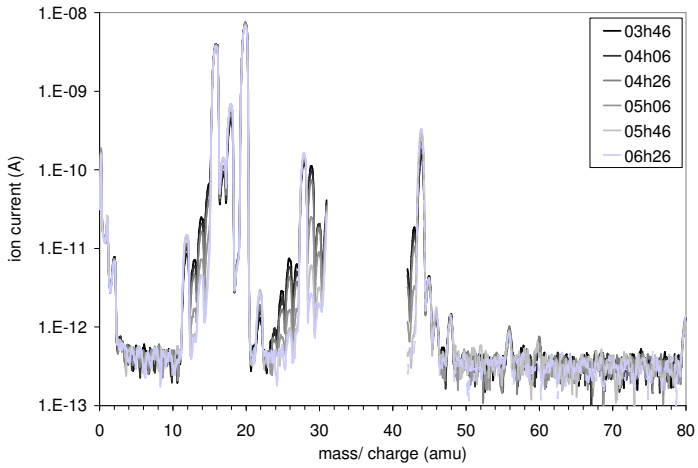

Figure 4. 15:
Mass spectra recorded during the photocatalytic breakdown of ethanol. The spectra are taken from the second half of the experiment, see discussion of Figure 4. 12.

We will first look into whether there is a good candidate for a second intermediate product. It is important to note that no significant lines above mass/ charge 46 amu are observed (48, 56 and 80 amu are system lines, the signal at 60 amu is too weak to interpret). The

mass/ charge lines at 45 and 46 amu are also very low, they should originate from isotope peaks of CO_2 (main peak at 44 amu, see discussion of Figure 4. 12, p. 143). Possible other candidates for the intermediate product are formaldehyde (H_2CO, 30 amu), formic acid (HCOOH, 46 amu) and acetic acid (H_3CCOOH, 60 amu). Since no significant lines higher than 46 amu are observed, acetic acid can be eliminated immediately. Formic acid can also be eliminated, since it should otherwise interfere with the ethanol line at 45 amu so that it would follow a pattern similar to that of the mass/ charge lines at 29, 30 and 43 amu. Formaldehyde as intermediate product remains a possibility to explain the strong line observed at the mass/ charge value of 30 amu (see Figure 4. 12, right, p. 143), since this is the second strongest line (see reference spectrum Figure 4. 14, right, p. 146). On the other hand, the strongest line in the reference spectrum of formaldehyde is 29 amu which is also the strongest line for acetaldehyde.

Secondly one needs to look at the possibility whether the mass spectrum of acetaldehyde is different from the literature spectrum due to the presence of the other components in the chamber atmosphere. Especially since there is a lot of oxygen present this could lead to a different intensity of the mass/ charge line at 30 amu. All the other mass/ charge lines that can be seen to decrease in Figure 4. 15 match otherwise very well with the acetaldehyde spectrum.

The careful analysis of the mass spectra shows that acetaldehyde is definitely an intermediate product of the photocatalytic breakdown of ethanol of a thin film of Degussa P25 in the batch reactor used in this study. Unfortunately, it cannot be excluded that also formaldehyde is an intermediate product. Here one sees the limit of a mass spectrometer, a gas chromatograph would allow for separating the components more easily.

An important conclusion is the proof of the two step mechanism for the photocatalytic breakdown of ethanol. This enables measuring the photocatalytic activity of TiO_2 thin films using the first step of the reaction, namely the breakdown of ethanol to the intermediate product(s). The measurement procedure developed and described in section 3.1.3.5 allows for determining the initial breakdown rate of ethanol, as well as to follow the complete breakdown reaction for different initial ethanol concentrations.

4.1.5 Influence of experimental parameters on the photocatalytic breakdown rate

For a better definition of the experimental test conditions, the external parameters that influence the breakdown reaction were investigated. In section 2.4.4 the most important factors

for reactions taking place in a saturated oxygen atmosphere were discussed, namely the relative humidity, the initial ethanol concentration and the UV intensity (i.e. the number of photons arriving at the TiO_2 surface).

Some experiments with P25 were performed to examine the influence of selected external parameters, namely the addition of water representing a change in humidity (section 4.1.5.1), the initial ethanol concentration (section 4.1.5.2), the power applied to the UV lamp (section 4.1.5.3) and the substrate temperature (section 4.1.5.4).

These tests, together with the method for analyzing the photocatalytic breakdown data (discussed in section 2.7.3.2), lead to the definition of the final experimental measurement procedure.

4.1.5.1 Effect of water addition

As already mentioned in section 2.4.4.5 many photocatalytic breakdown reactions are influenced by the presence of water. For ethanol it is reported that the addition of large amounts of water is detrimental [Carp04]. It was, therefore, tested whether this could be observed in our case. Note that the ethanol used for this study was exposed to the ambient air so that the azeotropic mixture of ethanol and water is established (95.6 vol% ethanol/ 4.4 vol% water).

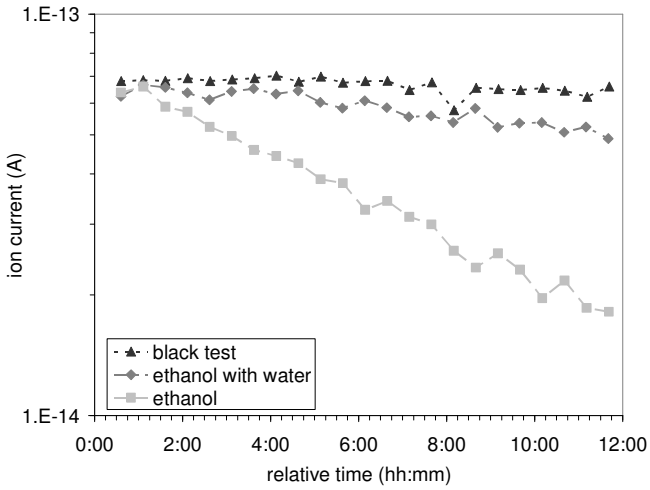

Figure 4. 16:
Influence of the water addition on the reaction rate of the photocatalytic breakdown of ethanol using a spin coated thin film of P25. The lamp power was 150 W (not focused), the ethanol concentration was 273 ppm, faraday detector.

Figure 4. 16 shows the effect of adding 12 µl water (1770 ppm, equivalent to 8% rel. hum. at 20°C) to the reaction chamber on the rate of photocatalytic breakdown of 6 µl ethanol (273 ppm). The experiments were performed at an earlier stage using only an MID measure-

ment (not calculating the ethanol concentration) and the faraday detector. A more simple UV lamp was used which had a nominal output of 150 W and could not be focused. Since the ion current of the ethanol signal can be used for qualitative comparison it allows for estimating the effect of water addition.

The highest decrease in ion current (i.e. the highest reaction rate) is seen for the case that no water is added. When 1770 ppm water are added the reaction rate drops to a value which is close to the 'black rate', i.e. the decrease of the ethanol signal in the dark. This clearly demonstrates the importance of using a controlled chamber atmosphere.

4.1.5.2 Initial ethanol concentration

The effect of the initial ethanol concentration was measured for 6 µl (273 ppm), 9 µl (410 ppm) and 12 µl (546 ppm). Both the ethanol concentration and the ion current for mass/ charge 29 amu (intermediate product) and 44 amu (CO_2) were followed. The ion currents were referenced to the ion current of Ar to eliminate the detector fluctuations.

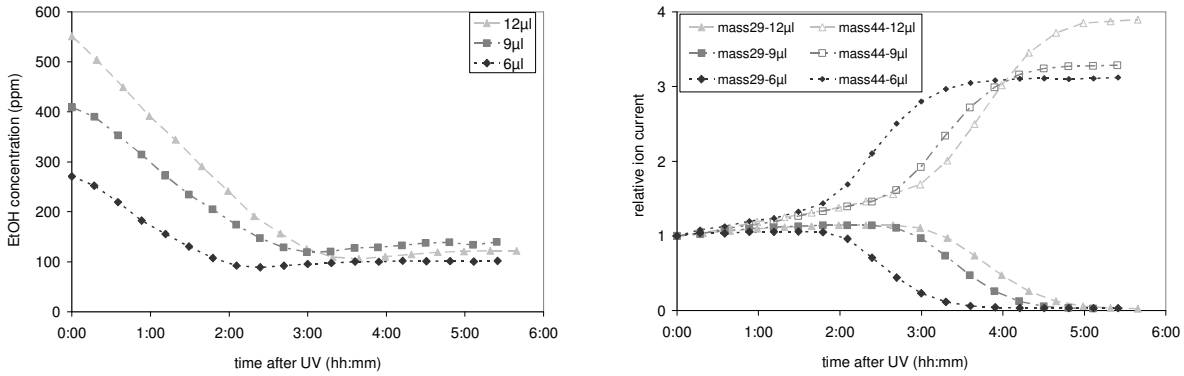

Figure 4. 17:
Effect of initial concentration on the photocatalytic breakdown of ethanol. Channeltron detector, lamp power 92 W, non-heated sample stage, P25 reference coating. Left: change in ethanol concentration, right: change in ion current of mass/ charge 29 amu (intermediate) and mass/ charge 44 amu (CO_2) with irradiation time.

When looking at the decrease of the ethanol concentration one can see that the slope of the curves increases for increasing concentration while all curves show a linear decrease of the ethanol concentration. Calculating the concentration of the ethanol in mol/dm^3 one receives 1.177, 1.766 and $2.354 \cdot 10^{-5}$ mol/dm^3 for the injected amounts of 6, 9 and 12 µl, respectively. According to section 2.4.4.4 one should expect first order kinetics for organic substance concentration below 10^{-3} mol/dm^3, i.e. for the low amounts of ethanol added here. This transition concentration of 10^{-3} mol/dm^3 is valid for suspensions of Degussa P25 in water having pow-

der concentrations of about 100 mg/dm^3 [Mills97]. This powder concentration translates to a total powder surface per unit volume of 5 m^2/dm^3 (taking into account the surface area of Degussa P25 powder being 50 m^2/g). The thin films used in this study have a surface area of 31 x 25 mm = 775 mm^2 (taking the geometrical surface area), so that the surface area per unit volume in the reaction chamber will be 775 mm^2/ 8.75 dm^3 = 8.853·10^{-5} m^2/dm^3. The difference between the two relative surface areas is 6 orders of magnitude. If taking into account that the surface area of the suspended powder might be reduced by one order of magnitude due to agglomeration and that the surface area of the film may be increased by one order of magnitude due to the film structure (see section 4.2.1.1), the difference still remains at 4 orders of magnitude. As discussed in section 2.4.4 the reaction kinetics depend also on the total surface area of the catalyst in relation to the concentration of the organic substance due to the availability of the reactive sites [Mills97]. This explains why for the photocatalytic measurement setup used in this study the transition to zero order kinetics is observed at much lower ethanol concentrations.

In conclusion, we can state that for the concentration range investigated the reaction kinetics are zero order, i.e. a linear decay of the ethanol concentration is observed at the beginning of the reaction. We will utilize this fact to calculate the initial reaction rate (see section 4.1.5.1). Since a batch reactor is used, the ethanol concentration will, after some time, fall below the critical value below which first order kinetics will be observed. Consequently, for the correct analysis only the linear part of the decay curve can be utilized.

The right side of Figure 4. 17, previous page, shows qualitatively the evolution of the intermediate product (ion current of mass/ charge 29 amu) and CO_2 (mass charge 44 amu). The initial ethanol concentration does not seem to influence the reaction mechanism. However, larger ethanol concentrations take longer to break down, leading to a time delay in the evolution of the final breakdown products and the disappearance of the intermediate.

4.1.5.3 Effect of lamp power

The effect of lamp power was examined with an ethanol concentration of 546 ppm (12 µl injected). The results were compared to a blank test using the same concentration.

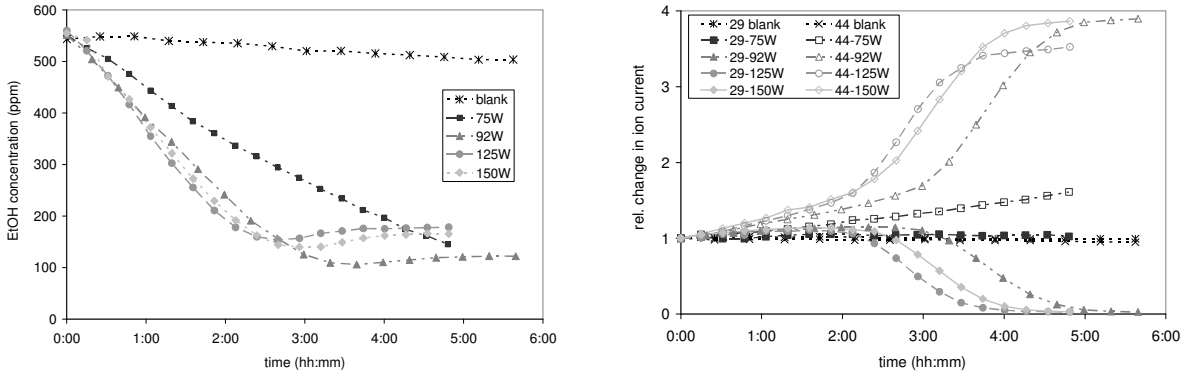

Figure 4. 18:

Effect of lamp power on the photocatalytic breakdown of ethanol. Initial ethanol concentration = 6 µl, p = 1050 mbar, non-heated sample stage, P25 reference film.

One can see from the left side of Figure 4. 18 that the slope of the ethanol decay curves increases strongly up to a lamp power of 92 W. An increase to 125 W increases the decay rate slightly, while a further increase to 150 W does not result in any further increase of the decay rate, i.e. saturation occurs. This does not correspond to what was discussed in section 2.4.4.3, where it was stated that at low light intensity the reaction rate was directly proportional to the photon flux, while at high light intensity it was proportional to the square root of the photon flux. The saturation observed here could possibly be due to overexposure. As already discussed section 4.1.5.2 most studies concerning the influence of the external parameters were performed on suspensions of P25 in water [Mills97, Salinaro99, Martra99]. Illuminating such a suspension will require a lot more (externally applied) light than the flat surface of a thin film to yield the same amount of photons per unit area. The estimated power density of active UV light reaching the films was estimated to be 0.676 W/cm^2 (section 3.1.2.1). In [Carp04] the photonflux for changing from first order to half order regime is reported to be around 25 mW/ cm^2, which is one order of magnitude lower than the photon flux used here. This means that the thin films received possibly much more light than applied in standard investigations.

Consider now the effect of lamp power on the evolution of concentration of the intermediate product (mass 29) and the final product CO_2 (mass 44). Both are shown qualitatively on the right side of Figure 4. 18. The lowest lamp power of 75 W was, within the observed time, only sufficient to complete the breakdown of ethanol but not to start breaking down the intermediate: the ion current at 29 amu (intermediate product) remained constant while the ion current of 44 amu (CO_2) increased only very little. For higher lamp powers there is no obvi-

ous change in reaction mechanism, only the reaction speed is influenced, as already seen for the decay of the ethanol concentration (Figure 4. 18, left).

From this study can be concluded that 90-100 W is the optimum lamp power, since only a small increase in reaction rate is observed for a further increase. Therefore, it was chosen to work with a lamp power of 95-100 W (there was some error in setting the exact value).

4.1.5.4 Temperature controlled heating stage

The illumination of the thin film resulted in a substantial temperature increase resulting in a final temperature of more than 35°C at the substrate. Since it is necessary to analyze the reaction rate for a constant temperature it was decided to develop a temperature controlled sample holder. Latter had a higher heat capacity compared to the old one so that temperature fluctuations were better compensated for. Also the self heating temperature was reduced. With the possibility of controlling the temperature the influence of the reaction temperature on the photocatalytic activity could be studied.

First, the necessity to pre-heat the sample holder before starting the UV illumination was examined. Secondly, different substrate temperatures were tested.

a. Effect of pre-heating the sample holder

The effect of pre-heating the sample holder was examined with a concentration of 273 ppm. When looking at the resulting decay of the ethanol concentration (Figure 4. 19), one can see that the initial slope of the curves is influenced. When the sample holder was not pre-heated there seems to occur an increase in ethanol concentration due to desorption of ethanol as a result of the temperature increase.

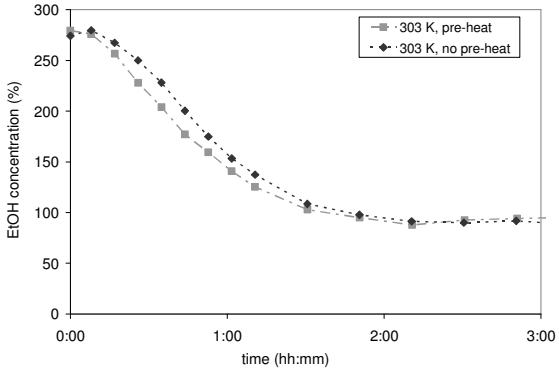

Figure 4. 19:

Effect of pre-heating the sample holder before keeping the temperature constant at 303 K (reference P25 layer), p = 1050 mbar, lamp power = 100 W, 6 µl ethanol (273 ppm).

Additionally, it took quite some time to establish the target temperature of 303 K when the sample holder was not pre-heated due to the large heat capacity of the sample holder block. Therefore it was decided to pre-heat the sample holder prior to starting the UV-illumination. As can be seen in the flow chart (Figure 3.5, p. 115) the pre-heating of the sample holder was started immediately after injecting the ethanol.

b. Effect of sample holder temperature

The aim of this study was to determine the effect of the sample holder temperature on the ethanol breakdown rate. It was assumed that the temperature measured at the sample holder is equivalent to the temperature at the thin film surface. The possible error due to the glass substrate being a poor thermal insulator is minimized by its small thickness (1 mm).

Three different temperatures were tested: 293 (room temperature), 303 and 313 K. The lowest temperature was maintained by cooling the sample holder internally by flowing air through it. The other two temperatures were maintained by heating the sample stage.

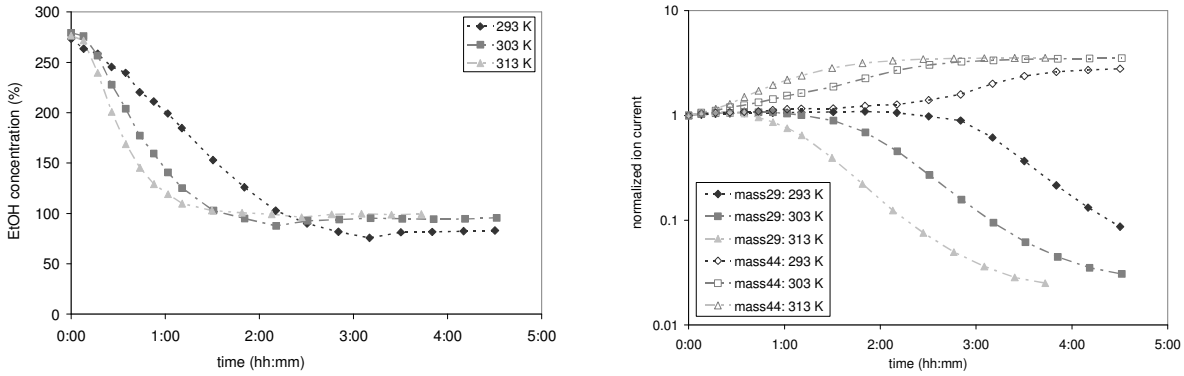

Figure 4. 20:

Effect of sample holder temperature on the photocatalytic breakdown of ethanol (left: ethanol concentration, right: relative ion current of intermediate and final products), using a spin coated Degussa P25 film, lamp power = 100 W, 6 µl ethanol (273 ppm).

The left side of Figure 4. 20 shows the increase in decay rate of ethanol with increasing sample holder temperature. Between 293 and 303 K the increase is substantial, it is small when going from 303 to 313 K.

The intensity of the mass/ charge lines at 30 (intermediate product) and 44 amu (final product CO_2) indicate that the elevated temperature of the sample holder does not influence the reaction process much (Figure 4. 20, right). It seems, though, that the breakdown of the intermediate product occurs faster, so that the evolution of CO_2 is observed almost from the beginning of the reaction on.

Since the reaction rate was the fastest for 313 K and this was a temperature which could be easily maintained, it was chosen to continue working with this temperature.

4.1.6 Final experiment design for testing photocatalytic activity of sputtered thin films

4.1.6.1 Analysis of the photocatalytic breakdown data

Since the photocatalytic breakdown of ethanol occurs in two steps (section 4.1.4) and the first step is almost completed before the second step becomes dominant, it is possible to use the breakdown reaction of ethanol for characterizing the photocatalytic activity of TiO_2 thin films. The experiments performed with Degussa P25 films showed that with the chosen reaction conditions, namely a lamp power of 100 W, a starting concentration of 273 ppm and a sample temperature of 313 K zero order reaction kinetics are observed for the chosen sample and reactor dimensions. This means that the decay of the ethanol concentration is expected to follow a linear relationship at the beginning of the reaction.

For analyzing these decay curves it was, therefore, necessary to determine the initial linear part which allowed to calculate the reaction rate from its slope. It was chosen to report the reaction rate for the ethanol breakdown in *ppm/min*. Finding the linear portion of the curve was done semi-manual, by applying the linear fitting function in Microsoft Excel to a decreasing number of initial data points until a constant slope was obtained. The slope was defined as constant when the results for the slope started to show scatter. This scatter was then taken to define the error margin of the method. The slopes calculated for these linear fits are in ppm/day and negative. The finally reported reaction rates are given as the positive value, recalculated to ppm/min.

To minimize the error with determining the reaction rate it became important to take as many data points as possible in the beginning of the breakdown reaction. This meant that data spacing had to be reduced to 2-3 min which was done by reducing the number of mass/ charge points followed during the MID measurement and by reducing the measurement time for the mass spectra. It was also no longer necessary to follow the complete breakdown reaction, so that the measurement was stopped as soon as the minimum in ethanol concentration was reached.

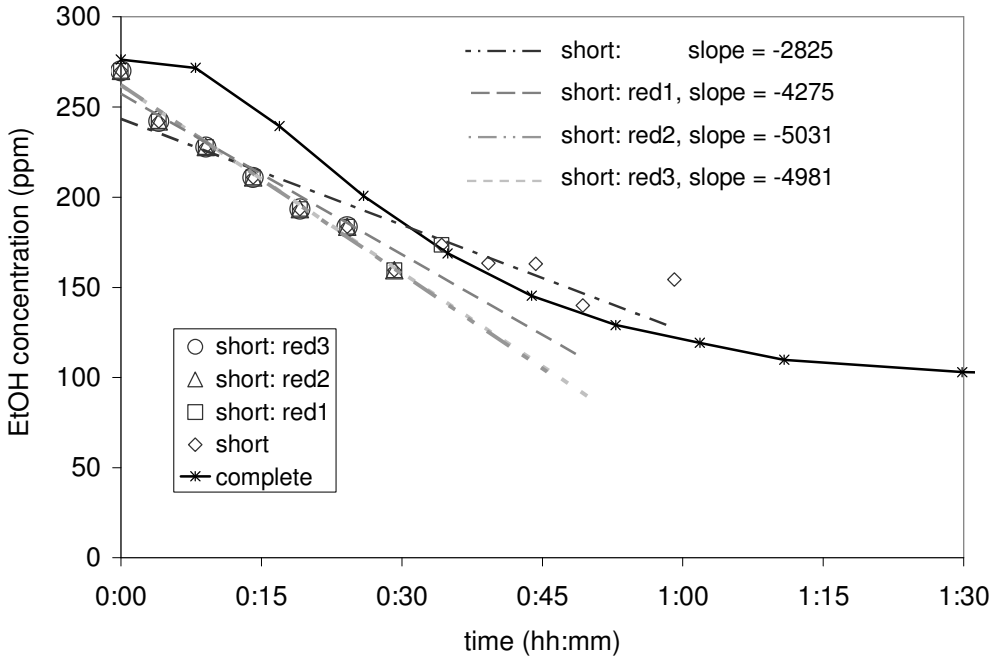

Figure 4. 21:

Linear fits to different initial parts of the breakdown curve of ethanol. The curve 'complete' shows a measurement of the complete breakdown reaction. 'Short' refers to a measurement with closer data spacing, 'red' refers to a reduced number of data points used from this measurement. The numbers 1 through 3 refer to a decreasing number of data points used in the reduced curve (P25 reference layer, 273 ppm ethanol, lamp power = 100 W).

Figure 4. 21 shows an example on how the reaction rate was determined for a spin coated layer of Degussa P25 powder. Two different measurements are shown, the first taken with a larger data spacing covering the complete breakdown reaction (*) and the second recorded with a shorter data spacing ('short') until the concentration started to reach a constant level (◇). Here a linear fit is clearly not possible ( ), the value of the slope is too low. For the short curve three consecutively shorter data ranges were linearly fitted, labeled 'short: red1' (□), 'short: red2' (Δ) and 'short: red3' (○), respectively. The fit to 'short: red1' ( ) is already better but still yields a too low value for the slope. The fits to 'short: red2' ( ) and 'short: red3' ( ) can be said to be identical: both can be rounded to 5000 ppm/day, which corresponds to about 3.5 ppm/min.

4.1.6.2 Reference photocatalyst: P25

As already discussed in section 2.7.1.3 the choice of a thin film reference catalyst is not so straightforward. For this study it was decided to follow a recipe given in [Mills02] to deposit spin coated layers of P25 onto glass. There were some problems with the reproducibility of these layers. When depositing a series of coatings from the same batch, no significant differ-

ence in photocatalytic activity was found. When comparing the photocatalytic activity of coatings from different batches, strong differences could be observed. The visual appearance of the coatings was also different: the least active layer also looked thinner. Therefore, it was investigated how the concentration of the P25 slurry and/ or the number of coatings deposited onto one slide influenced the photocatalytic activity of the thin films (Figure 4. 22). Unfortunately the thickness of the coatings could not be determined with the profilometer due to their weak adhesion to the substrate and large inhomogeneity (Figure 4. 23, next page). When all prepared layers using the first slurry (hereafter referred to as '*slurry 1*') were used up, a second slurry ('*slurry 2*') was prepared and new films deposited from it. After receiving rather thin coatings with this second slurry a third ('*slurry 3*') was prepared with the double P25 concentration. It was found that depositing a double coating using first *slurry 2* and then *slurry 3* yielded P25 films having a photocatalytic activity similar to that of the most active TiO_2 thin films prepared by sputtering and subsequent annealing (compare to section 4.2).

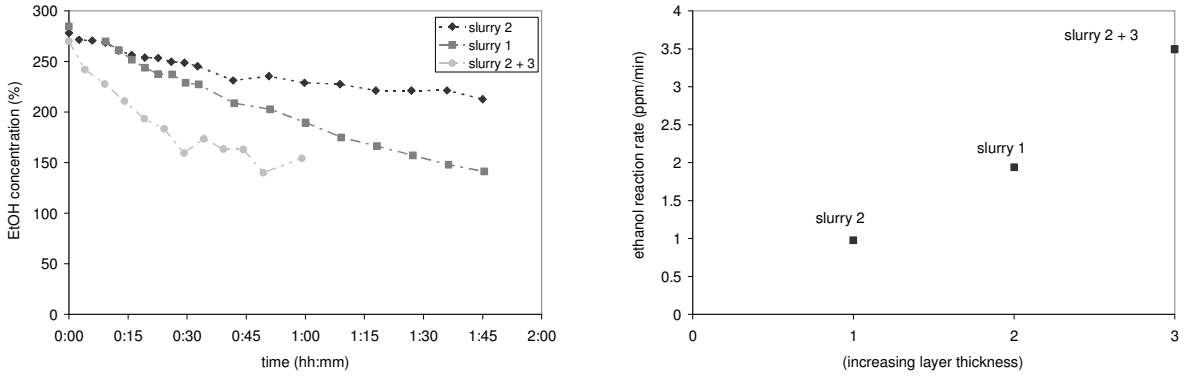

Figure 4. 22:

Different reaction rates for spin coated thin films of Degussa P25 powder (please refer to text); lamp power = 100 W, T = 313 K, ethanol concentration = 273 ppm.

Some spin coated P25 films were subjected to the photocatalytic breakdown reaction several times, without showing any sign of catalyst poisoning. This was only valid when the reaction was allowed to be completed. When stopping after the breakdown of ethanol was complete, but not the breakdown of the intermediate product(s), it was found that the reactivity of the films deteriorated after a few applications. Therefore, it was decided to preferably use a fresh P25 layer for catalytic testing.

The spin coated P25 thin films were investigated by SEM (Figure 4. 23). For the thinnest films (prepared from *slurry 2*) the glass surface was not completely covered by powder. This means that the active surface area of the powder is smaller than the actual surface area of the

glass slide. For the thickest films (prepared from *slurry 2* and *3*) complete coverage of the glass substrate was achieved. Here one can see the open structure of the powder very well.

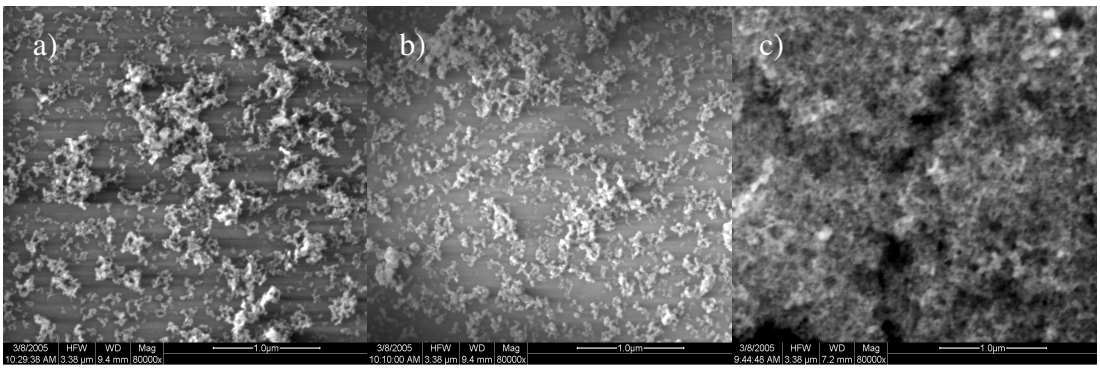

Figure 4. 23:
SEM images of the surfaces of spin coated P25 thin films onto glass substrates.
a) P25 single coat, slurry 2, b) P25 single coat slurry 1, c) P25 double coat, slurry 2 and 3.
See text and section 3.2.1 for further explanations.

4.1.6.3 Summary: Experimental design of the photocatalytic thin film testing

a. Reference catalyst layer

It was chosen to use the thickest layer of P25 (double coated with *slurry 2* and *3*) for a reference catalyst. This could be used to perform regular checkups of the chamber and conduct any further tests if necessary.

b. Amount of ethanol

The standard amount of the test substrate ethanol was chosen to be 273 ppm (6 µl), which allowed for reasonable testing times using catalysts with lower reactivity compared to the reference coatings of Degussa P25.

c. Lamp power

As lamp power 95-100 W was chosen. Here no saturation effects and a reasonable reaction rate were observed (see section 4.1.5.3).

d. Temperature of sample holder

The temperature of the sample holder was chosen to be 313 K. This temperature shows an increased reaction rate against room temperature and allows for good temperature control of the sample holder. 313 K also seems to be an interesting temperature with respect to device applications.

e. Data spacing

The data spacing during the initial period of the experiment should be as close as possible (section 4.1.6.1). Since the measurement procedure includes several calibration steps for each data point (section 3.1.3) the minimal data interval ended up being about 3 min. To achieve this small data spacing it was opted to only follow mass/ charge lines during the MID measurement which were relevant for measuring the ethanol concentration and for monitoring the behavior of the OmniStar. The time for collecting the mass spectra was also reduced compared to the initial studies.

f. Data analysis

The method for data analysis as described in section 4.1.6.1 was found to be applicable for all photocatalytic tests performed when using close data spacing. The slope values, reported in ppm/min, are the equivalent of the initial reaction rate of the photocatalytic breakdown reaction of ethanol and were used to compare the photocatalytic activities of the thin films.

4.2 TiO_2 thin film deposition: Characterization of the sputter process

In this part the behavior of the sputter process when depositing (doped) TiO_2 thin films was studied. In section 4.2.1 the characteristics of the different target materials used is discussed, including the sputtering behavior of metallic Ti and ceramic TiO_{2-x} targets. The use of the latter targets was preferred as they led to a more stable process. The factors influencing the thin film deposition using these targets were, therefore, investigated in more detail (section 4.2.2), by looking at the sputter gas pressure, the applied d.c. power and the film uniformity. In the end the influence of the additives (Fe_2O_3, Nd_2O_3 and V_2O_3) on the sputtering behavior of the TiO_{2-x} targets is discussed (section 4.2.3).

4.2.1 Target characteristics

In this section the three different target types used for the preliminary studies will be discussed, namely metallic Ti (section 4.2.1.1), plasma sprayed ceramic TiO_{2-x} (section 4.2.1.2) and sintered ceramic TiO_{2-x} (section 4.2.1.3). The sputtering behavior of the metallic and ceramic targets is compared and the final material choice discussed (section 4.2.1.4).

4.2.1.1 Metallic Ti target

The metallic Ti-targets were cut from a 5 mm thick Ti-sheet and machined to a thickness of 3 mm. No further structural or electrical characterization of these targets was performed.

4.2.1.2 Plasma sprayed ceramic TiO_{2-x} target

One type of ceramic TiO_{2-x} targets was prepared by plasma spraying rutile onto a Cu-plate of 1 mm thickness that was covered with a bonding layer. The preparation of the target was performed as to yield sub-stoichiometric TiO_{2-x} layer of 3 mm thickness. As a result these targets have a total thickness of 4 mm. No structural or electrical characterization of these targets was performed. These targets were used for some initial studies before the sintered targets were available. No significant differences in sputtering behavior, other than the higher discharge voltage due to the larger thickness were observed between the two types of ceramic targets.

4.2.1.3 Sintered ceramic TiO_{2-x} target

The ceramic TiO_{2-x} targets were sintered in an inert atmosphere to obtain reduced rutile of the approximate composition $TiO_{1.75}$ (measured at ITME with Rutherford Backscattering, RBS). A finer starting powder allowed to sinter the targets at lower temperatures which influenced the grain size of the final ceramics. For the fine grain size precursor, which allowed a sintering temperature of 1623 K, a final grain size of about 5-10 µm was observed. The large grain size precursor required a sintering temperature of 1973 K and the resulting grain size in the target was about 50-100 µm. These differences in structure did not influence the sputtering behavior of the TiO_{2-x} targets [Tomaszewski04]. The resistivity of these targets was less than 1 Ω cm.

4.2.1.4 Comparison of sputtering behavior between Ti and TiO_{2-x} targets

As discussed in section 2.8.4 TiO_2 thin films can be deposited by reactive sputtering from metallic Ti targets or sub-stoichiometric rutile TiO_{2-x} ceramic targets. In order to verify the differences in behavior under metallic and reactive sputtering conditions, the dependence of voltage, pressure and deposition speed on the oxygen flow were determined for both a metallic Ti and a plasma sprayed ceramic TiO_{2-x} target. Sputtering was performed at 180 W. Note that reducing the target thickness as well as increasing the depth of the erosion groove (equivalent to reducing the target thickness) results in a lower discharge voltage in constant power mode.

Figure 4. 24 shows the voltage hysteresis for the two different targets (top), as well as the dependence of the deposition rate on the oxygen flow (bottom). One can see the strong changes in discharge voltage and the hysteresis behavior for the metallic target while the ceramic target shows a much lower variation of the discharge voltage and almost no hysteresis. The deposition rates of films deposited with a ceramic target in pure Ar are roughly half of those of the metallic target at the highest oxygen flow still in metallic sputtering mode. At higher oxygen flows, when both targets are in the reactive mode, they have the same deposition rate, which is expected from the discussion in section 2.8.4.

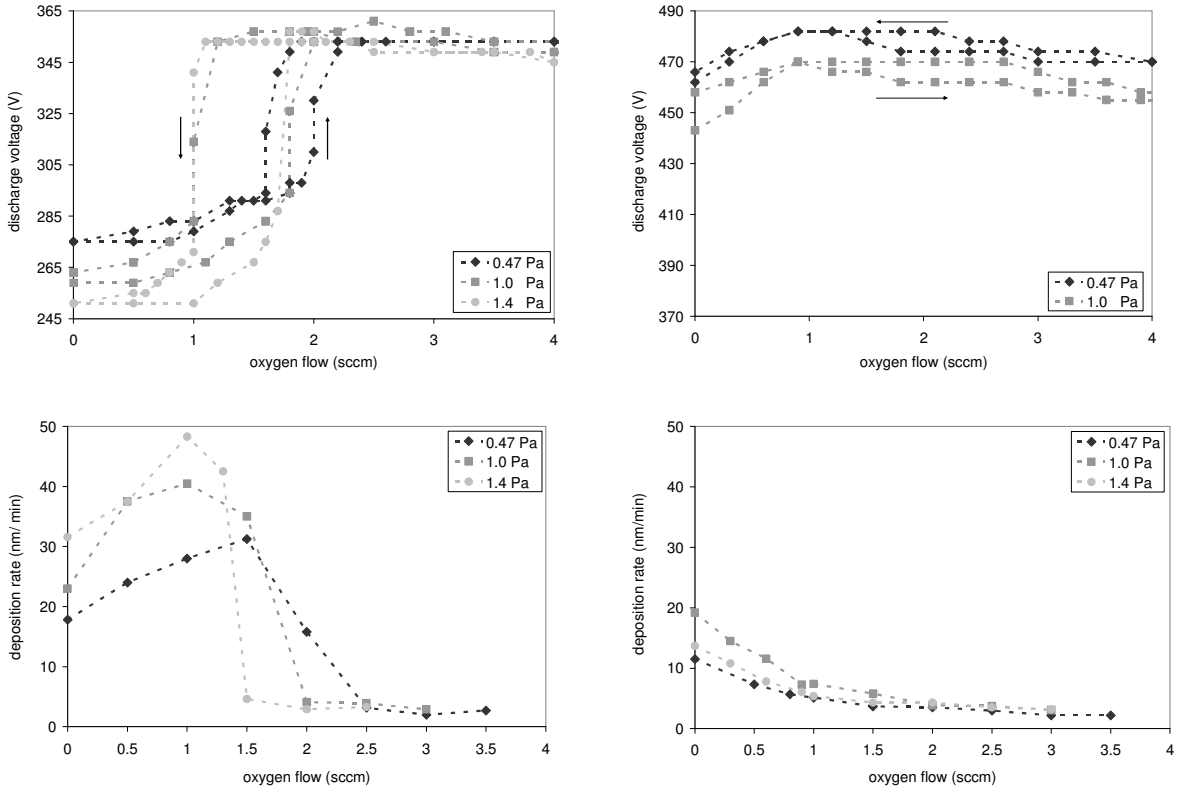

Figure 4. 24:

Dependence of the discharge voltage (top) and deposition rate (bottom) of a Ti (left) and a TiO_{2-x} (right) target on the O_2-flow during sputtering in Ar/ O_2 gas mixtures for different Ar-pressures. As the discharge voltage was different between the two different targets it was necessary to choose a different absolute range but the size of the interval is identical. The applied d.c. power was 180 W.

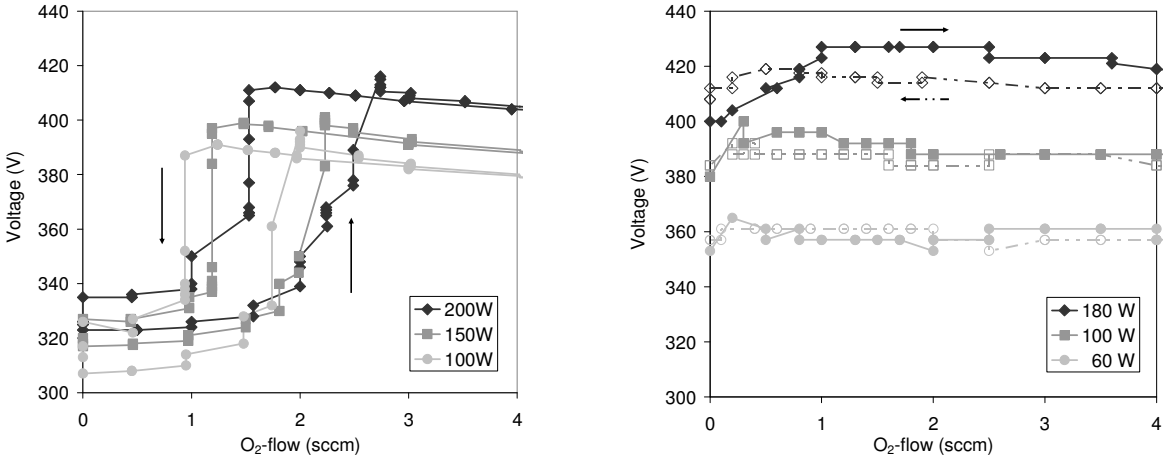

Figure 4. 25:

Dependence of the discharge voltage on the oxygen flow for different d.c. powers: (left) a metallic Ti target, sputtered at 1.0 Pa, (right) ceramic TiO_{2-x} target, sputtered at 1.4 Pa [Janssen05]. Note that the ceramic TiO_{2-x} target has a lower discharge voltage than the plasma sprayed target due to its lower thickness.

Figure 4. 25 shows the effect of power on the hysteresis behavior of the discharge voltage. Here a sintered ceramic target of 3 mm thickness was used. The Ar-pressures were 1.0 and 1.4 Pa for the Ti and the ceramic target, respectively.

For both targets the maximum discharge voltage is shifted to lower flows with lower applied power. The reason is the reduced getter effect as the sputter rate decreases with power (see also below). Especially for the ceramic target the voltage peak is less pronounced with decreasing applied power so that at 60 W it is almost gone.

Figure 4. 25 also shows that approximately the same discharge voltage is reached in the poisoned mode for both the metallic and the ceramic target. This is due to the target surface reaching the same degree of oxidation [Depla06a]. The reason why this is not observed in Figure 4. 24, top is due to the difference in target thickness.

4.2.2 Factors influencing the thin film deposition using TiO_{2-x} targets

For investigating the TiO_2 films the dependence of the deposition rate on the different process parameters is needed. The effect of these parameters was investigated for pure Ar. We will discuss the applied d.c. power (section 4.2.2.1) and the Ar-pressure (section 4.2.2.2). The uniformity of the thin films on the substrate is also discussed (section 4.2.2.3).

4.2.2.1 Dependence of deposition rate on the applied d.c. power

The dependence of the deposition rate on the applied d.c. power (Figure 4. 26, left) shows the typical linear behavior. The offset from zero is due to the fact that there is a minimum applied d.c. power necessary to maintain the discharge [Westwood03].

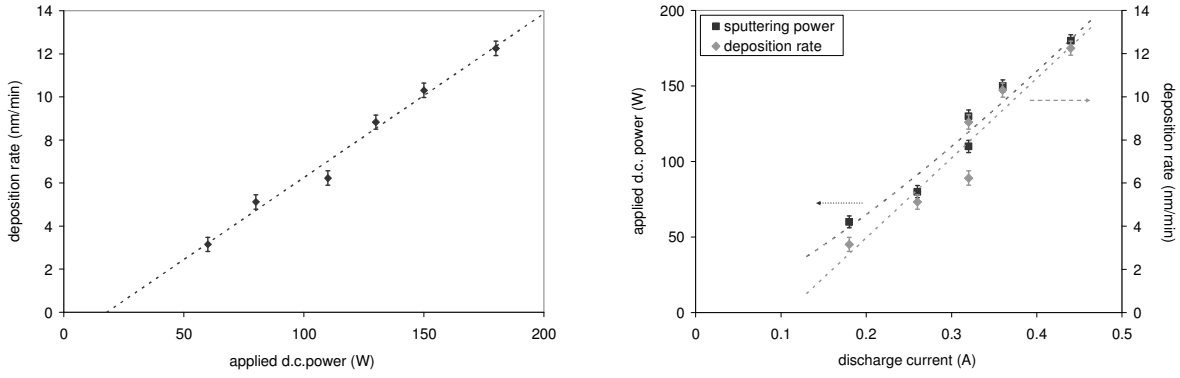

Figure 4. 26:
Dependence of deposition rate on applied d.c. power (left), and sputtering power/ deposition rate on the discharge current (right). The dashed lines are linear fits to the deposition rate and a power fit to the sputtering power.

For some powers several depositions were performed to see the spread in resulting film thickness when choosing the same deposition time; in Figure 4. 26 the averages are shown, together with the error bars. The reasons for this spread lie in the stability of the process and measurement errors when determining the film thickness. Even though the process is quite stable, the amount of arcing occurring during deposition can vary, with a higher arc rate leading to a decreased deposition rate (the power supply will shut down briefly to extinguish arcs). Arcing can occur from oxide deposits next to the race track on the target [Segers03] or oxide build up on the magnetron device itself (i.e. the target holder and the anode).

The linear behavior observed for the deposition rate as a function of the power may seem straightforward: The deposition rate is proportional to the sputter rate, which again is proportional to the power [Westwood03]. With increasing power we observe a strong increase in discharge current and a weak increase in discharge voltage, according to the I-V characteristic of the magnetron discharge, equation (4.8):

$$I = k\,V^{n} \tag{4.8}$$

The sputter rate is dependent on the discharge current and on the discharge voltage. The discharge current determines the amount of Ar-ions in the discharge gas (section 2.8.2.1) and therefore, their number impinging on the target. The discharge voltage, on the other hand, determines the energy of the Ar-ions when reaching the target (section 2.8.2.1) and therefore, the number of sputtered particles released per impinging Ar-ion. The increase in discharge current plays the dominating role, so that the linear increase observed for the dependence of the deposition rate on the discharge current (Figure 4. 26, right) is reflected in its dependence on the discharge power (Figure 4. 26, left).

The targets show poor heat conductivity, which results in a thermal gradient over the target during sputtering. When increasing the applied d.c. power, the chance for cracking of the target increases. Therefore, it was chosen to work with targets of 3 mm thickness which will show a lower temperature difference between the two target surfaces compared to thicker targets.

4.2.2.2 Dependence of the deposition rate on the Ar-pressure

Figure 4. 27 shows the dependence of the deposition rate on the Ar-pressure for three different applied d.c. powers.

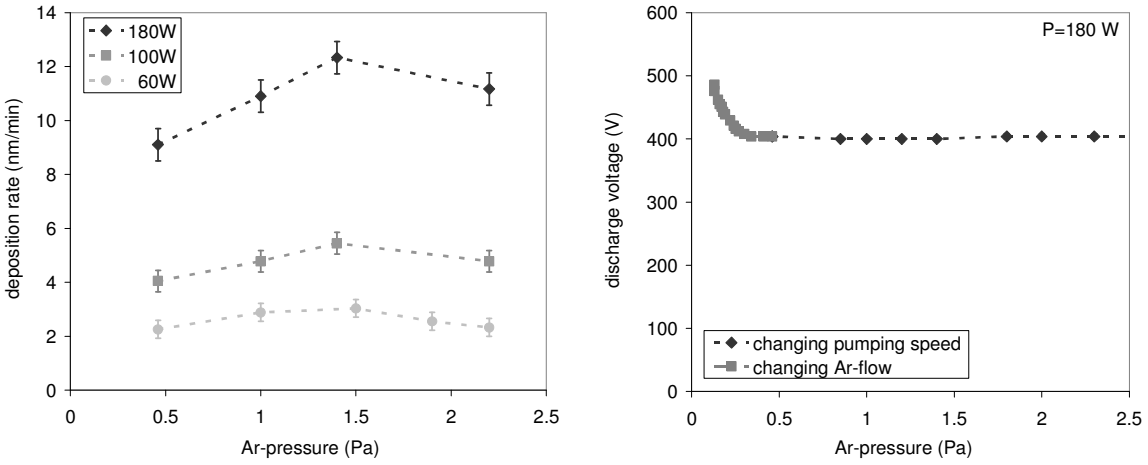

Figure 4. 27:

Left: Dependence of the deposition rate on the Ar-pressure for different discharge powers. Right: Dependence of the discharge voltage on the Ar-pressur at a power of 180 W. It was necessary to decrease the Ar-flow to obtain pressures below 0.5 Pa, while for higher pressures always the pumping speed was changed.

One can see that the deposition rate goes through a maximum at ca. 1.4 Pa. The occurrence of a maximum is generally observed in magnetron and glow discharges [Chapman80]. Normally this is explained by the following: At low pressures the discharge current increases due to a decrease in discharge voltage (at constant power) for increasing gas pressure [Buyle04]. The increase of the current will increase the sputter rate and, hence, the deposition rate, while the decrease in voltage (due to the constant power regime) will decrease the deposition rate. The effect of the current increase is stronger than that of the discharge voltage. At higher pressures the discharge current and voltage are influenced little by the increasing pressures and the decrease in the deposition rate results from an increased scattering of the sputtered particles.

Unfortunately, this reasoning does not apply here, since the discharge voltage is almost independent of the Ar-pressure above 0.5 Pa, where the measurements of the deposition speed occurred (Figure 4. 27, left). One reason for the increase in deposition rate with increasing Ar-pressure lies with the increase in the thin film density, which will be discussed in section 4.3.4.1. At 1.4 Pa a point is reached where the particles scattering is stronger than latter effect. If a thin film has a given porosity (in %), its thickness will be increased by this percentage. This means that the deposition rate will also increase by the same percentage. At 0.47 Pa and 1.4 Pa (60 W) the porosity was found to be 5 and 22.5 %, respectively. The corresponding deposition rates are 2.25 and 3.0 nm/ min. For 0 % porosity one would calculate a deposition rate of 2.15 nm/ min, so that a porosity of 25 % result in an observed deposition

rate of 2.6 nm/ min. For 180 W the porosities at 0.47 and 1.4 Pa are 0 and 12%, respectively. The corresponding deposition rates are 9.1 and 12.33 nm/ min, respectively. Calculations would result in deposition rates of 8.7 and 9.75 nm/ min for 0 and 12% porosity, respectively. For both powers the deposition rates calculated from the porosity increase are lower than the measured ones for the thin films deposited at 1.4 Pa, so that other effects must be playing a role, too.

4.2.2.3 Uniformity of the film thickness

In order to know the thickness distribution over the length of the sample, the film thickness was measured at different points on the long side of the sample. The reference point was the free end of the sample which was positioned at one edge of the magnetron. The other end of the substrate was clamped to the sample holder (Figure 4. 28, right). The sample was mounted so that the position of the target center lies at ca. 25 mm.

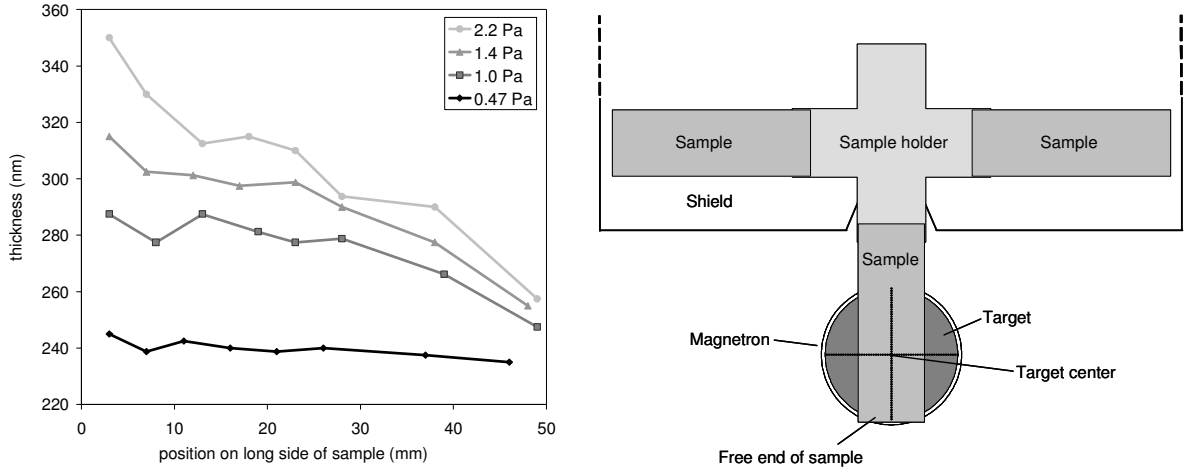

Figure 4. 28:
Left: Thickness distribution along the long side of the substrate measured with the profilometer. The thin films were deposited at a power of 180 W [Janssen05].
Right: sketch of the sample holder, magnetron and shield. The target center lies at 25 mm, the free end of the sample marks the zero point.

As can be seen from Figure 4. 28 (left) the thickness distribution is dependent on the Ar-pressure. For the lowest pressure the distribution is quite homogeneous, but one observes a decrease in thickness with increasing distance from the free end, especially for the distances of more than 30 mm. This non-uniformity becomes stronger with increasing pressure. Such behavior is contradictory to the standard observation in thin film deposition that the thickness inhomogeneity should decrease with increasing pressure. Latter is due to the increased scattering of the sputtered atoms so that a less directional flux of atoms occurs [Westwood03,

Mahieu06a]. Normally also a Gaussian thickness profile is observed: the thickness should decrease on both sides away from the center of the magnetron [Westwood03, Mahieu06a], which clearly is not the case here.

To explain the observed thickness distribution one needs to look at the manner the substrate is mounted (Figure 3.6, p 116, Figure 4. 28, previous page). On the side where the sample is mounted there is a large metal plate at the height of the sample. This prevents the free movement of the sputtered particles, i.e. acts as a trap for them, so that they can no longer reach the substrate. As a result the film thickness decreases towards the shield, distorting the deposition profile. The effect will be stronger with increasing pressure since the trapping of the shield increases with increasing amount of particle scattering.

A second reason could be the fact that an insulating layer of TiO_2 forms on the shield, which influences the plasma potential during sputtering. Since the plasma potential is positive compared to the anode potential, the composition of the plasma close to such a surface will be different from the plasma in contact with a wall at anode potential. Insulator covered chamber parts (also referred to as 'dirty anodes') usually result in a lowering of the deposition speed [Belkind98, Schiller97]. They can also lead to other effects like the ignition of secondary plasmas [Belkind98]. Latter effects could be observed in the experiments here. There was always sufficient chamber surface available as anode to not visibly disturb the magnetron discharge. Therefore, this effect is expected to be small, but it cannot be excluded.

As can be seen in Figure 4. 28 the film homogeneity decreases rapidly for positions further than 30 mm from the free sample edge. Therefore it was decided that only the first half of the glass slide (i.e. 0-38 mm) would be used for photocatalytic analysis. The following 10-15 mm of the second half (up to 48 mm from the free edge, Figure 4. 28) were deemed suitable for all other analysis techniques since they require only a small sample area.

4.2.3 Effect of additives on the characteristics of the TiO_{2-x} targets

Three different dopants for TiO_2 thin films were investigated, namely Fe, Nd and V. To deposit these films mixed oxide targets of TiO_{2-x} with Fe_2O_3, Nd_2O_3 and V_2O_3 were sintered under the same conditions as the pure TiO_{2-x} targets. Only the sintering temperature had to be varied according to the additive due to processing requirements (section 3.2.2.1). The amount of additive (Table 4. 3) was rather high to allow for studying the sputtering behavior of the targets and to be able to detect the amount of additive in the film.

Additive	1.0 wt%	1.8 wt%	2.3 wt%	5 wt%	10 wt%
Fe_2O_3	x	-	-	x	x
Nd_2O_3	-	-	x	x	x
V_2O_3	-	x	-	x	x

Table 4. 3: Overview of the concentrations of the additives used for the TiO_{2-x} mixed oxide targets.

The targets with 1.8 and 10 wt% V_2O_3 could not be used for sputtering due to a too high target resistivity. On the other hand, one target containing 5 wt% V_2O_3 was suitable for d.c. sputtering. There were also some reproducibility problems for the mixed oxide targets using Fe_2O_3, occasionally the target resistivity was too high to use the target for sputtering (> 100 kΩ cm). This could be related to the color of the target, which was grayish instead of the dark blue of semiconducting TiO_{2-x}. The reasons for this must lie in the target manufacturing process and indicate an interaction of the dopant with the structural and electronic properties of TiO_2.

4.2.3.1 Target structure

The structure of the pure TiO_{2-x} and mixed oxide targets was investigated by SEM of thermally etched target surfaces. Both Fe_2O_3 and Nd_2O_3 addition influences the grain growth of the target. Nd acts as grain growth inhibitor, so that a decrease in grain size with increasing Nd_2O_3 content is observed (with the exception of 1 wt% which shows the same grain size as the pure TiO_{2-x}). In addition an increase in inner grain porosity is observed with increasing grain size. On the other hand, for the addition of Fe_2O_3 there is first an increase in grain size for lower concentrations, while the highest concentration shows again the same grain size as the pure TiO_{2-x}. Small amounts of Fe promote grain growth while large amounts show no influence. Especially for Fe addition the formation of a second phase at the grain boundaries could be observed. The targets with V_2O_3 addition were not studied with SEM.

XRD analysis of targets with 10 wt% Fe_2O_3 and Nd_2O_3 additive (Figure 4. 29) confirmed the formation of the second phase.

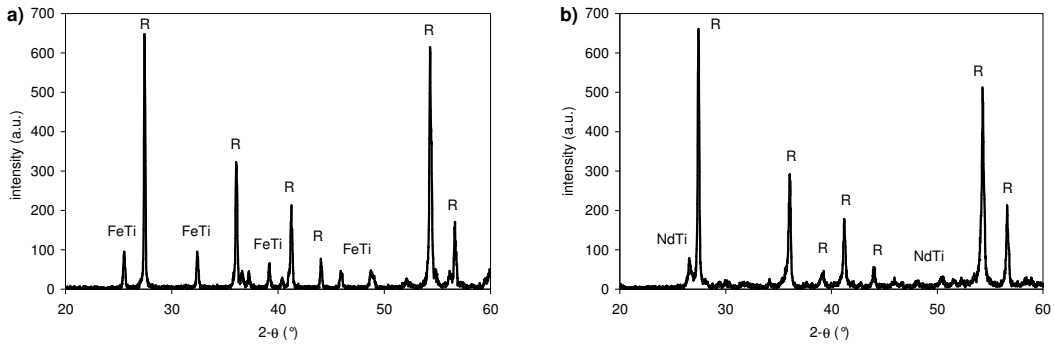

Figure 4. 29:

XRD of targets with a) 10 wt% Fe_2O_3 and b) 10 wt% Nd_2O_3. 'R' indicates peaks from the rutile TiO_2 phase while FeTi and NdTi indicate peaks from one or more iron rich FeTi-oxides and $Nd_4Ti_9O_{24}$, respectively.

In contrast to this, V_2O_3 addition was found not to result in the formation of a crystalline second phase, only rutile was detected.

4.2.3.2 Target resistivity and discharge voltage

To understand the discharge behavior of the sub-stoichiometric ceramic targets the effect of the additive on the target resistivity was studied (Figure 4. 30). A low target resistivity (around 1 Ω cm) will not influence the sputtering behavior of the target [Depla06a]. If the target resistivity is high, but remains below 100 kΩ cm, d.c. magnetron sputtering is still possible. The impedance of the system target-plasma is influenced strongly, though, and consequently, also the discharge voltage.

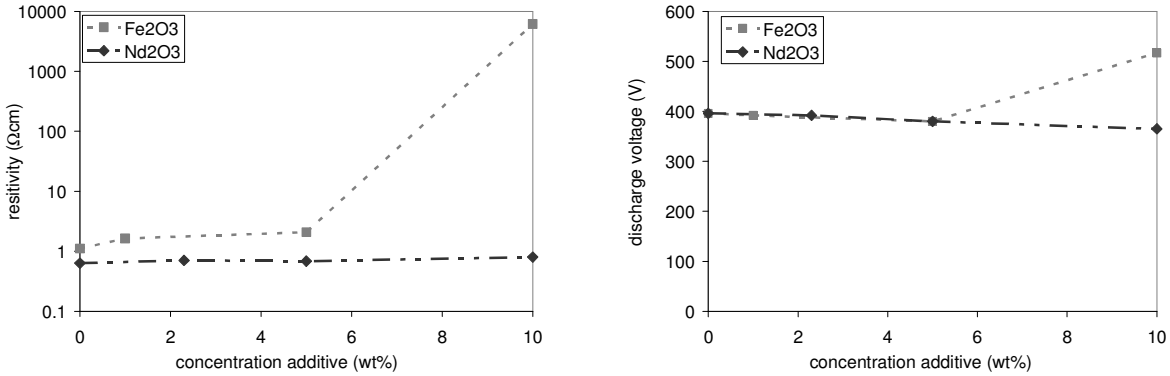

Figure 4. 30:

Dependence of the target resistivity (left) and the discharge voltage (right), sputtered in pure Ar at 1.4 Pa, on the dopant concentration for Nd_2O_3 (black) and Fe_2O_3 (grey) addition to TiO_{2-x} targets.

As one can see from Figure 4. 30 the target resistivity does not change significantly for dopant additions between 0 and 5 wt% (a very small increase is seen). For the highest dopant

concentration Fe and Nd behave differently. While for 10 wt% Nd_2O_3 the resistivity remains low, a strong increase is seen in the case of 10 wt% Fe_2O_3. As a results one sees a strong increase of the discharge voltage in the latter case. For the other dopant levels and 10 wt% Nd_2O_3 actually a decrease in discharge voltage is observed which cannot be linked to the small change in target resistivity.

This behavior of the discharge voltage can be understood when looking at the sputtering behavior of the mixed oxide targets. One major factor influencing the discharge voltage of a given target material is its secondary electron emission coefficient under ion bombardment during sputtering [Buyle04]. As discussed in section 2.8.2.2 non-reduced insulating oxides (e.g. Al_2O_3) show a very high value for the secondary electron emission coefficient while metal surfaces and reduced oxides show a lower value [Depla06c]. While TiO_2 is known to show reduction under ion bombardment, this is not the case for Fe_2O_3 and Nd_2O_3. Therefore, one can expect that TiO_2 will have a lower secondary electron emission coefficient than Fe_2O_3 or Nd_2O_3. As a result one would expect a mixed oxide target of TiO_2 with added Fe_2O_3 or Nd_2O_3 to show an increase in secondary electron emission with increasing amount of additive. An increase in secondary electron coefficient results in an increase in discharge current, which translates to an decrease in discharge voltage under constant power d.c. sputtering. This explains most likely the small decrease in discharge voltage observed in Figure 4. 30 right.

4.2.3.3 Influence on voltage hysteresis and deposition speed

The influence of the additives on the sputtering behavior of the mixed oxide targets in Ar/ O_2 gas mixtures was also investigated. Both the voltage hysteresis and the dependence of the deposition speed on the oxygen flow were measured, for increasing concentrations of Fe_2O_3 and Nd_2O_3.

As one can see from Figure 4. 31 (a and b) the curves for the voltage hysteresis are similar to that of pure TiO_2. For both Fe_2O_3 and Nd_2O_3 the decrease in discharge voltage is independent of the O_2 flow for the lower two concentrations. The discharge voltage change occurring upon transition to the poisoned state seems slightly more pronounced for the mixed oxide target but occurs at about the same O_2 flow. The exceptions are those with 10 wt% additive. For 10 wt% Fe_2O_3 the discharge voltage is higher due to the high target resistivity as discussed earlier. Also the discharge voltage increases with increasing oxygen flow in the poisoned state showing a behavior different from the lower dopant levels. This behavior during

poisoning is even more pronounced for 10 wt% Nd_2O_3. For the moment this behavior is not understood.

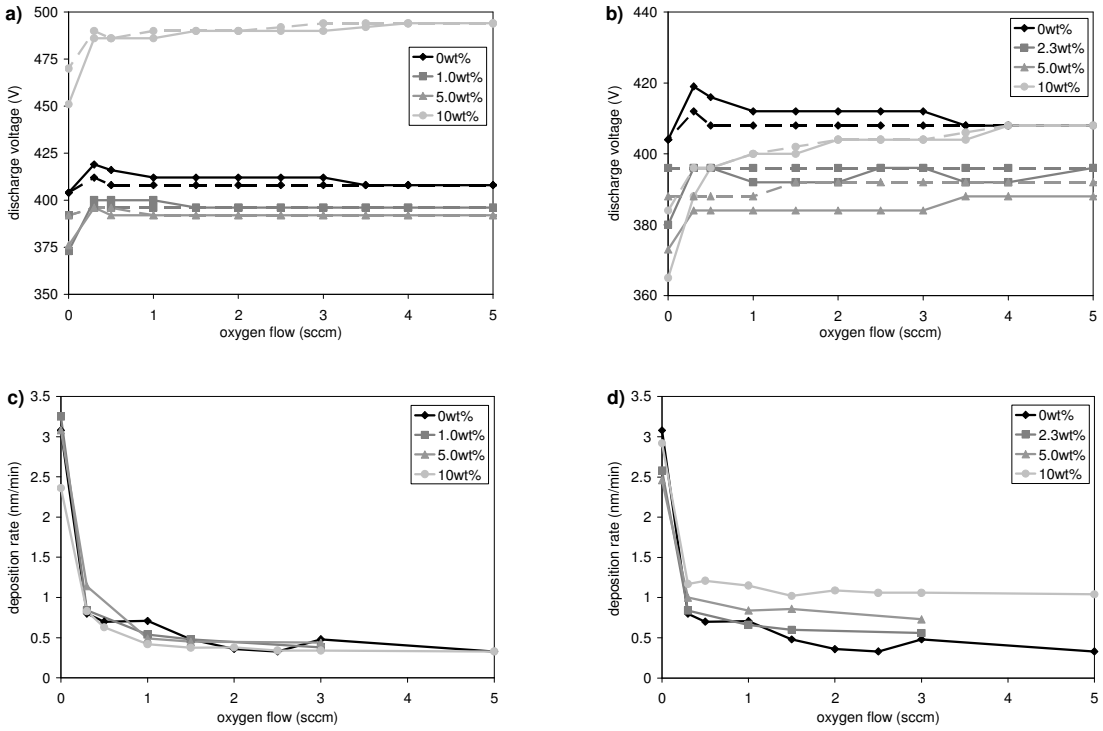

Figure 4. 31:

Dependence of the discharge voltage (top) deposition rate (bottom) on the O_2-flow for different dopant levels of a) and c) Fe_2O_3, b) and d) Nd_2O_3 in the targets. All results were obtained at an Ar-pressure of 1.4 Pa and applied d.c. power of 60 W.

When looking at the deposition rate in the completely poisoned mode one sees that the addition of Fe_2O_3 has no influence, even not in the highest concentration. On the other hand, for the Nd_2O_3 addition the deposition rate increases with increasing amount of additive. To understand the behavior of the deposition rate the following hypothesis was proposed. When looking at the mixed oxide target one can divide the target area into two parts in analogy to the Berg model developed for reactive sputtering [Berg05]. The first part is the additive and the second part is the TiO_{2-x} matrix. When the surface area of the two parts changes, their relative contribution to the erosion rate will change. The change of deposition rate of an oxide with increasing oxygen flow is related to its oxygen affinity during the sputtering process: the higher the affinity, the stronger the decrease of the erosion rate [Depla01]. Since both TiO_{2-x} and Fe_2O_3 have the ability to absorb a certain amount of oxygen (TiO_{2-x} by increasing the amount of Ti^{4+}, Fe_2O_3 by partial oxidation to +4), we would expect both TiO_{2-x} and Fe_2O_3 to show a decrease in erosion rate. If this decrease is similar for both oxides, we would expect no difference between pure and mixed oxides, which is observed in Figure 4. 31 c.

On the other hand, Nd_2O_3 is stoichiometric and not capable of further increasing its oxidation state, meaning it will have a low oxygen affinity. As a result, we expect that its erosion rate will not depend on the amount of oxygen present in the sputter gas. A target containing both Nd_2O_3 and TiO_{2-x} will, therefore, have on its surface one part with high oxygen affinity (TiO_{2-x}) and one part with low oxygen affinity (Nd_2O_3). Both parts contribute to the erosion rate of the total target. If the erosion rate of Nd_2O_3 is higher than that of TiO_{2-x}, we expect that the deposition rate from a target with higher Nd_2O_3 content will be higher, as observed in Figure 4. 31 d.

4.3 Influence of the deposition parameters on the properties of TiO_2 thin films

Since there is a variety of parameters influencing the structure of thin films (sections 2.8.3 and 2.8.4), a selection had to be made. It was chosen to change the morphology of the sputtered films by changing the Ar-pressure and the applied d.c. power during deposition. It was found that the sputtering system yielded transparent, XRD amorphous layers over a wide range of sputtering conditions when using a non-heated substrate (the maximum temperature reached during deposition was approximately 323 K). It was opted not to try to deposit crystalline films in situ but to use post deposition annealing.

The crystallization of the thin films was studied by changing the anneal temperature and time. Since the photocatalytic activity depends on the film thickness (section 2.5.4) the point at which the photocatalytic activity levels out needed to be determined. From these parameters an optimum combination (sputter pressure, d.c. power, anneal temperature and time, film thickness) was determined. Using these optimum parameters films were then deposited using M_2O_3/ TiO_{2-x} mixed oxide targets (M = Fe, Nd, V). Some films deposited under optimum conditions with a TiO_{2-x} target were also ion implanted with Fe and Nd. The effect of introducing dopants on the film characteristics was studied for these two methods and will be discussed in section 4.4.

In this section the study of the pure TiO_2 films will be discussed. The goal was to understand the influence of the chosen deposition and crystallization parameters on the thin film characteristics: morphology (section 4.3.1), stoichiometry (section 4.3.2), crystallization behavior (section 4.3.3) and optical properties (section 4.3.4). The relationship between structural and optical properties will be discussed in section 4.3.5. Then follows a presentation of the photocatalytic properties (4.3.6), with the results being discussed in the light of their structural and optical characteristics in section 4.3.7. In the end there will be a summary of the study of the pure TiO_2 thin films (section 4.3.8).

4.3.1 Morphology

4.3.1.1 General morphology

The morphology of the thin films was studied by looking at their top surface and cross sections obtained by fracturing the glass substrate they were deposited on. SEM cross sections of the thin films reveal a column-grain structure, where the grains extend through the thick-

ness of the film. The thickness of these column-grains does not seem to vary throughout its length, but it is difficult to see the bottom of the film properly due to the low resolution. This is caused by the low vacuum technique needed for viewing these highly insulating films on a highly insulating substrate.

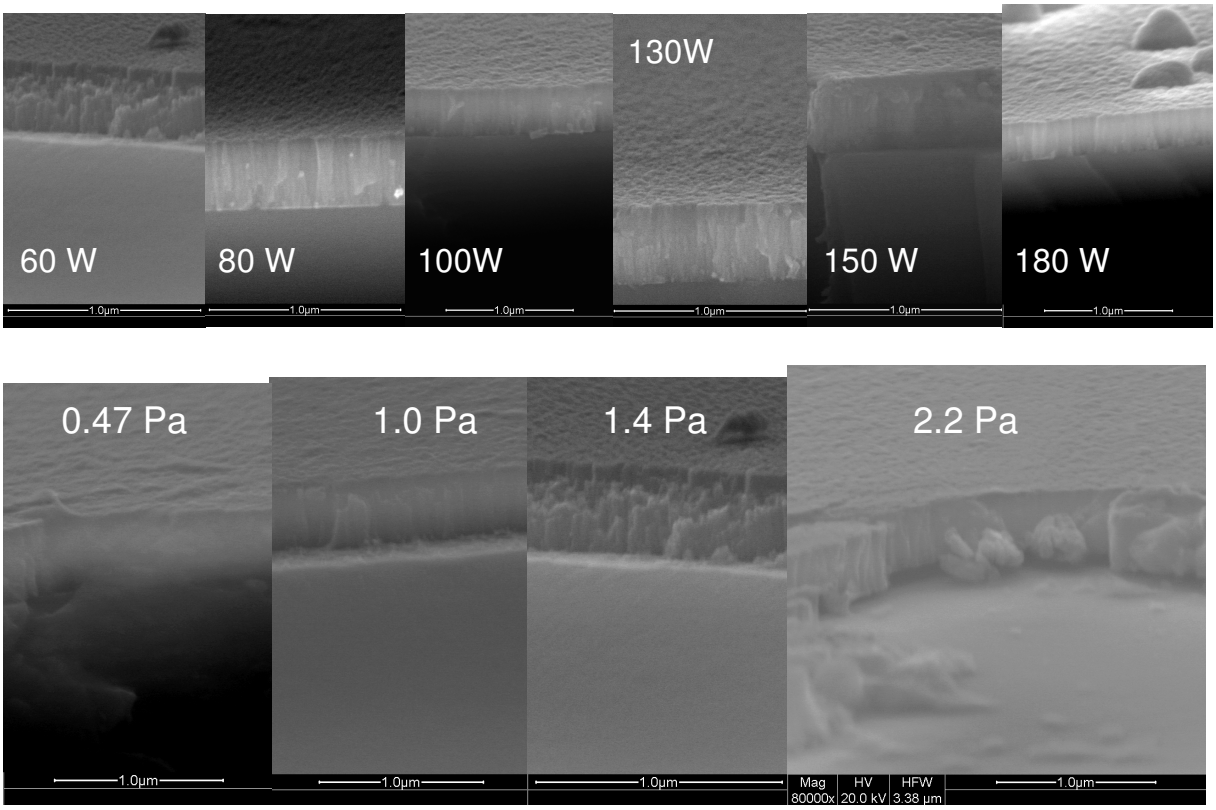

Figure 4. 32:
SEM cross sectional views of thin films deposited at 1.4 Pa for different applied sputtering powers (top) and at 60 W for different Ar-pressures (bottom).

The columns are not densely stacked, indicating a low film density. The packing density seems to become denser with increasing applied d.c. power and decreasing Ar-pressure. This is confirmed by the optical measurements (section 4.3.4).

As the column-grains are rather not densely stacked and also XRD amorphous (section 4.3.3), the growth mechanism follows a Zone 1a growth (section 2.8.3), which is expected given the low substrate temperatures. The high irregularity of the columns depicted in Figure 2.13, p. 99 is not really observed here, as the columns look rather regular. But, as already discussed above, the resolution of the images does not allow to study the exact structure of the columns.

SEM top views of the films reveals a cauliflower-like structure which is typical for amorphous films. Clearly, the apparent density of the films decreases with decreasing sputtering power and increasing Ar-pressure, confirming the results from the cross sections.

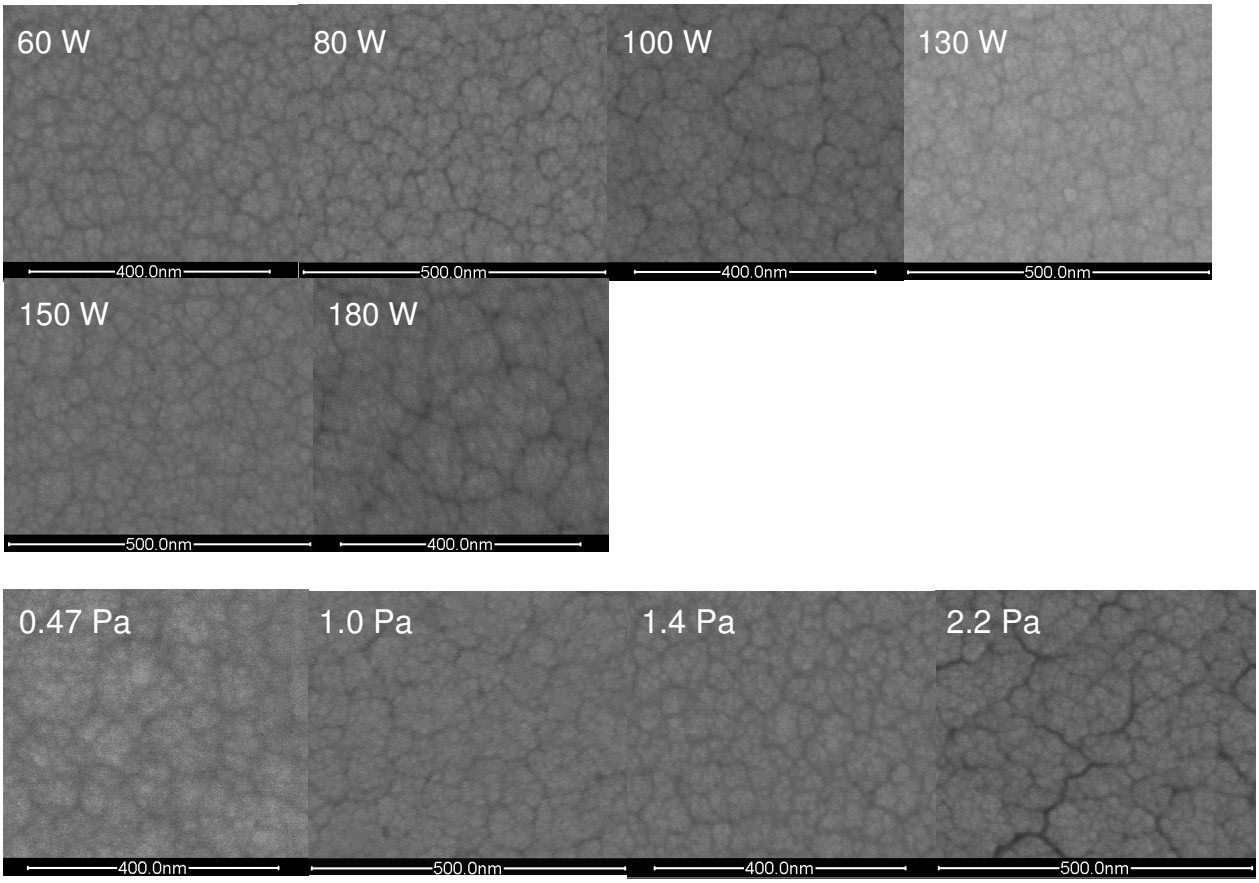

Figure 4. 33:
SEM top views of thin films deposited at 1.4 Pa for different applied sputtering powers (top) and at 60 W for different Ar-pressures (bottom).

When looking at the 'cauliflower-' type nodules in more detail (Figure 4. 34) one can see that they consist of smaller grains which are closely spaced together. If we compare the size of these smaller grains and the larger nodules to the columns seen in the cross sectional images it becomes clear that the columns have the size of the nodules. This means that, the columns should consist of different grains. However, the resolution of the cross sectional images did not allow to verify this. It would be interesting to see whether these small grains also extend throughout the film thickness, or whether they are shorter.

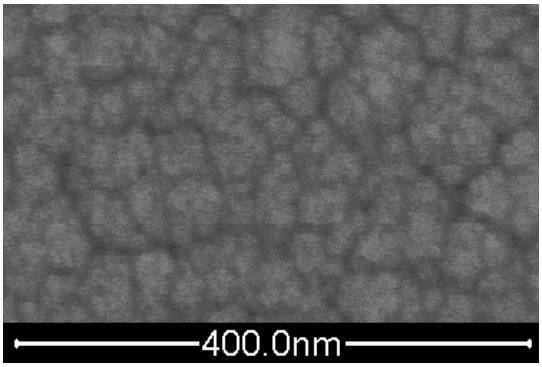

Figure 4. 34:
Detail from the SEM top view of the thin film deposited at 1.4 Pa and 60 W.

From the top view images one can estimate the width of the larger nodules and the smaller grains they consist of. For films sputtered at 60 W one obtains for the widths of the nodules and the smaller grains values around 35 and 10 nm, respectively. For films sputtered at 180 W one obtains ca. 45 and 10 nm, respectively. This means that the nodule size reduces slightly with decreasing sputtering power. Both results were obtained at an Ar-pressure of 1.4 Pa. Both the grain and nodule size of the films deposited at 60 W and 0.47 Pa are comparable to those deposited at 180 W and 1.4 Pa, so that there is a decrease of nodule size with increasing deposition pressure.

Estimate of the surface area of the column-grain structured films

One can calculate the change in surface area due to the nodular structure if assuming that the top of a nodule can be represented by a semi-sphere and that these semi-spheres are packed in a two-dimensional close-packed fashion. In Figure 4. 35 the layout of the arrangement of the circular bases of these semi-spheres is sketched.

To calculate the surface area occupied by the circular bases of the semi-spheres one can divide the area into rectangles, defined by the sides a and b. The side a shall be defined as a row of n circles, i.e. is equal to $2\,n\,r$, with r the radius of a circle. This means that the complete area is filled by $n\,(n+1)$ circles. From Figure 4. 35 one can see that the side b is defined as $(n+1)\,r\,\sqrt{3}$.

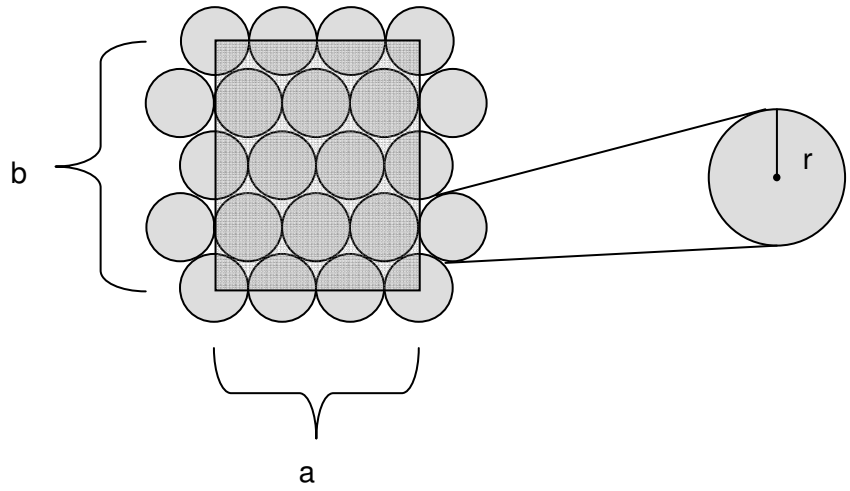

Figure 4. 35:

Close packing of circles on a surface. The area defined by the sides *a* and *b* is filled with a certain number of circles, namely (*n*+1) rows of *n* circles, in total *n* (*n*+1). The side *a* is defined by the diameters of *n* circles or 2 *n r*, with *r* the radius of one circle. The side *b* is defined by (*n+1) r* √3.

The flat area occupied by an array of semi-spheres (i.e. the sum of their flat circular base) is $\pi n\,(n+1)\,r^2$, while the total area over which these semi-spheres are distributed will be $2\sqrt{3}\,n\,(n+1)\,r^2$. Since the area of a semi-sphere is twice that of its flat circular base, the total area of the semi-spheres will be $2\pi n\,(n+1)\,r^2$. This means that the ratio of the total area of the semi-spheres to the total area over which they are distributed is $\pi/\sqrt{3} = 1.81$. In conclusion, the top surface area of the thin films is close to twice that of the flat glass substrate.

The available surface area for catalytic activity could be further increased if the spacing between the column grains is large enough to allow gas-exchange on their side surface. It is difficult to estimate whether the complete side-surface area of the column-grains will be available for all deposition conditions since it is not clear if the column-grains are well separated. If we take the columns to be cylinders separated over the complete length, the increase in total surface area would be the ratio between the cylinder surface (without the bottom surface) and the top surface of the cylinder, namely:

$$\frac{\textit{surface cylinder side and top}}{\textit{top surface columns}} = \frac{\pi \cdot d \cdot h + \pi \cdot r^2}{\pi \cdot r^2} = \frac{2 \cdot h}{r} + 1 \qquad (4.9)$$

with *d* the diameter of the cylinder and *h* its height.

If we take a column-grain diameter of 50 nm and a film thickness of 400 nm, then the surface area would increase by a factor of 33. This would be a much larger effect than the roundness of the column tops (nodules).

4.3.1.2 Effect of annealing

Figure 4. 36 (cross section) and Figure 4. 37 (top view) show the effect of anneal temperature and time on the morphology of thin films deposited at 1.4 Pa and 60 W. SEM cross sections of the annealed films show no difference to non-annealed films. For comparison also the as deposited film is shown.

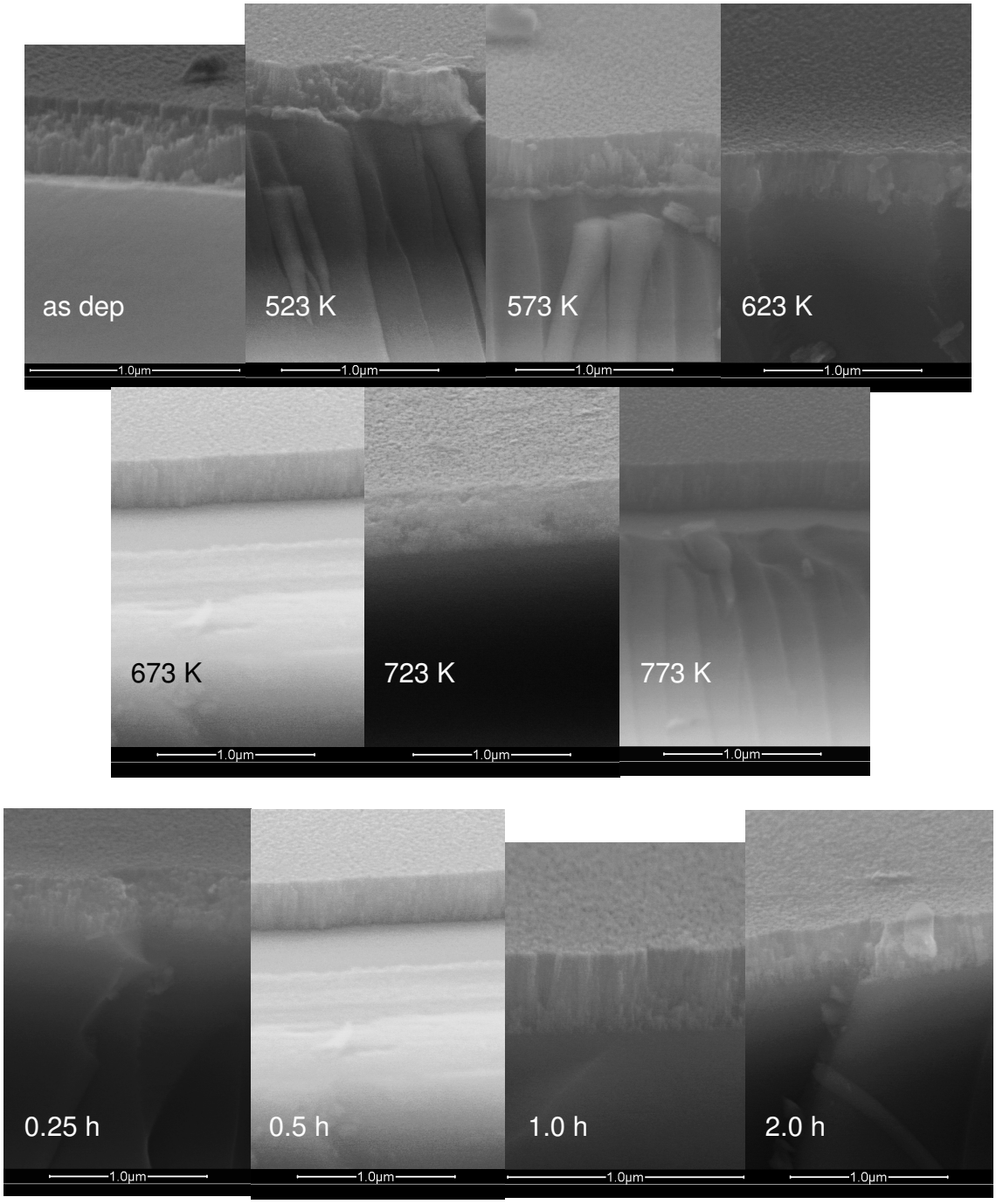

Figure 4. 36:
SEM cross sections of thin films deposited at 60 W and 1.4 Pa, annealed at different temperatures for 0.5 h (top) and annealed at 673 K for different times (bottom).

The structure of the column grains remains practically unchanged as a function of anneal temperature. The same is valid for different anneal times at 673 K.

SEM top views of the films (Figure 4. 37) reveal a gradual increase in spacing between the nodules up to a temperature of about 673 K. Cracks appear between the nodules (indicated in Figure 4. 38)

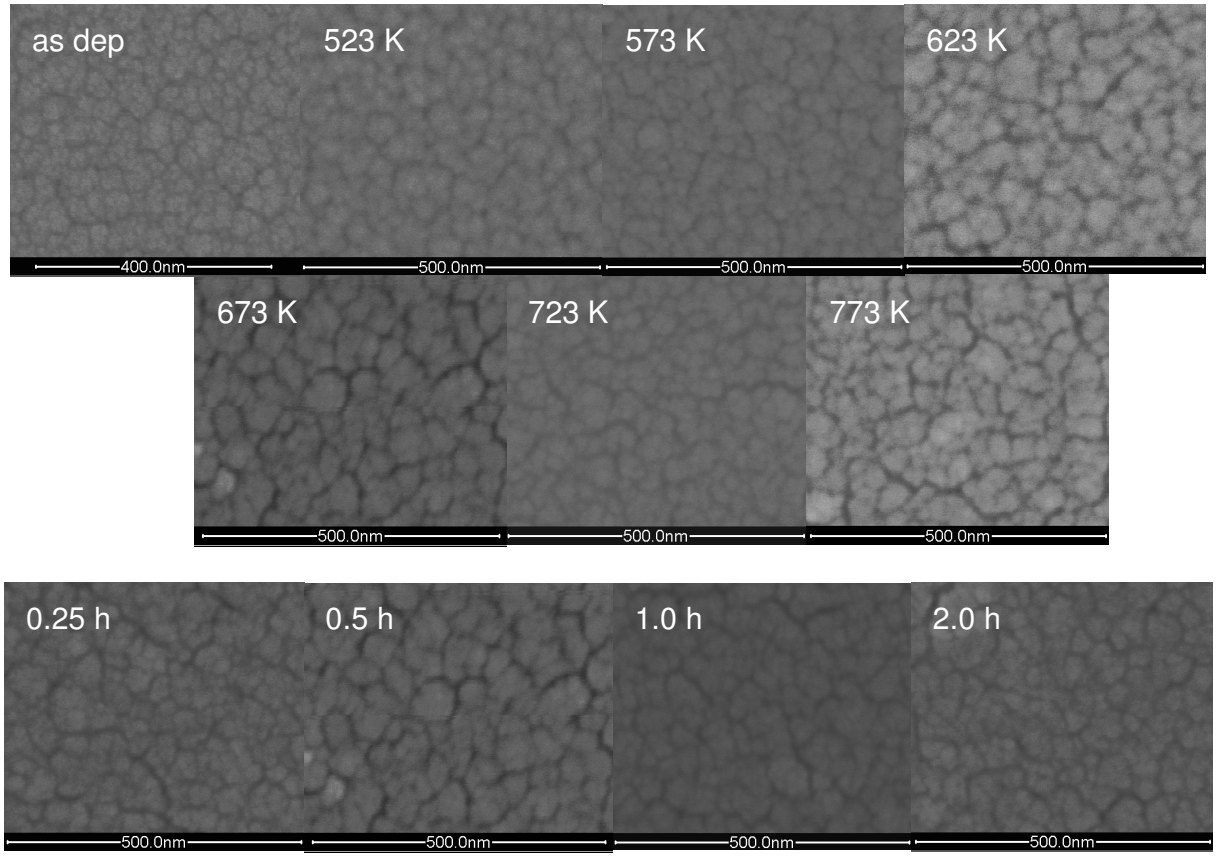

Figure 4. 37:
SEM top views of TiO_2 thin films deposited at 60 W and 1.4 Pa, annealed at different temperatures for 0.5 h (top) and annealed at 673 K for different times (bottom).

There are two possible reasons for this crack formation. The first is thermal mismatch upon heating and cooling, the second is densification of the column grains leaving voids between them. The origin of these cracks is stress relief: Thermal expansion mismatch between the thin films and the substrate will generate stress in the film. Heating will cause either compression or tension in the film, depending on the difference in thermal expansion coefficient. During cooling the opposite occurs: If the nodules are shrinking more due to crystallization than would be caused by thermal expansion, the film shrinks as compared to the substrate, generating a tension in the film. Latter can, theoretically, be relieved by two means, namely delaminating of the film from the substrate or delaminating of the columns from each other.

Compressive stress will more likely cause delamination of the film. This process can result in macroscopic blistering of the film, in cross sectional view one may see areas where the film has detached from the substrate (latter must be interpreted with care, though, since it can happen also during the breaking of the substrate). Column delamination will manifest itself as increased inter-column spacing and crack formation in the film. Blistering or film delamination was never observed in annealed thin films. Instead the crack formation seen in Figure 4. 37 and Figure 4. 38 indicates that the mechanism of inter-column delamination is active for stress relief in the thin films.

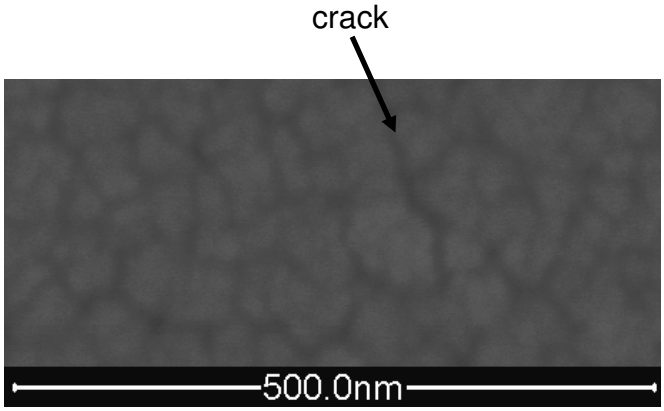

Figure 4. 38:
Detail of the SEM top view of a TiO_2 thin film deposited at 60 W and 1.4 Pa, annealed 673 K/ 1 h.

At anneal temperatures higher than 673 K the film structure remains rather unchanged. For thin films annealed at 673 K for different lengths of time, the typical cracked structure can already be seen after 0.25 h but is only fully developed after 0.5 h. From the SEM top views it seems that no changes to the surface other than the cracking occur. On first sight the cauliflower structure of the as deposited material is not changed, i.e. the size of the nodules remains the same. But when looking closer at the nodules (Figure 4. 38), it seems that the fine grain structure which could be seen in the as deposited sample is no longer visible in the annealed specimen. This could be due to the loss of focus observed for the annealed samples. A loss of focus can, on the other hand, be due to a more smooth surface. Therefore, it is possible that the small grains observed within a nodule in the as deposited sample have sintered together. This could be the reason for the volume loss causing the crack formation between the nodules. We will come back to this in section 4.3.3 when discussing the crystallite sizes obtained from XRD analysis.

A temperature of 673 K may seem a rather low for sintering of TiO_2, but one has to remember the very small particle size, being around 10 nm, involved here. Normally TiO_2 pow-

der compacts (with powder grain sizes in the range of tens of µm) need to be sintered at temperatures close to 2000 K, i.e. a temperature close to the melting temperature of 2115 K, to yield dense (rutile) ceramics (section 4.2.2). Using a finer powder (range of 1 µm) allowed reducing the sintering temperature to 1623 K. The reason is, that smaller particles have a higher surface energy. This enhances processes like sintering, grain growth and crystallization. Lowering the particle size into the sub-micrometer range is one of the reasons why nano-grain sized materials are interesting for materials science. When estimating the surface area of the annealed films this would result in a decrease of surface area due to the smoother surface of the nodules which should be more than compensated, though, by an increase in surface area due to the crack formation. We shall come back to this issue when discussing the density of the thin films as estimated from the refractive index (sections 4.3.4.3 and 4.3.4.4).

The dependencies on power and Ar-pressure during deposition discussed above remain unchanged. No indications of grain growth can be seen. Therefore, these images will not be shown here.

4.3.1.3 Effect of sodium in the substrate

In section 2.6.6 the influence of sodium in the glass substrate on the properties of heat treated TiO_2 thin films was discussed. In our study some initial heat treating experiments were performed with thin films deposited onto soda-lime microscope slide glass.

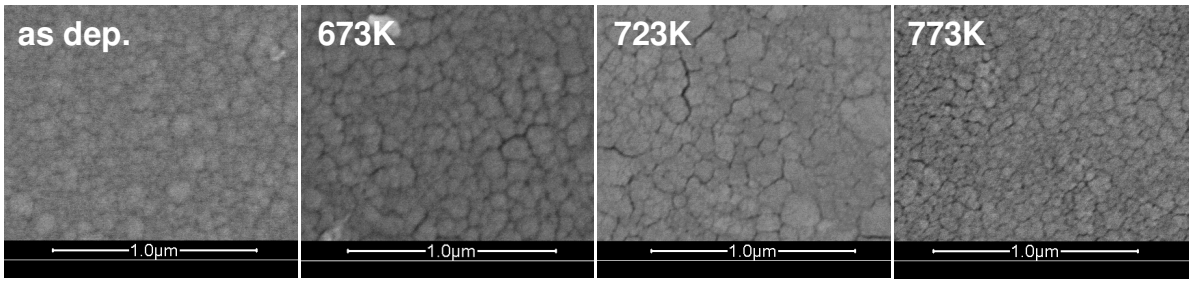

Figure 4. 39:
Effect of Na^+ diffusion on the crystallization of thin films deposited at 180 W onto soda-lime glass, heat treated at different temperatures for 0.5 h.

When comparing Figure 4. 39 (films deposited onto soda-lime glass) to Figure 4. 37 (films deposited onto sodium-free glass) one sees the same trends. The microstructure of the films does not change with annealing other than crack formation. Unfortunately, the lower resolution does not allow for resolving the (fine) structure of the nodules. The nodule size is comparable, when taking into account that the films from Figure 4. 39 were deposited at 180 W. Therefore, the presence of sodium in the substrate does not seem to influence the col-

umn structure. It is not surprising that the column structure was not affected by the anneal process other than crack formation (section 4.3.1.2). The sintering of the smaller grains could not be verified here due to the low resolution of the SEM images. Other studies (section 2.6.6) have reported that Na diffusion into a TiO_2 film results in retarding the crystal growth, so one might expect that the fine grain structure of the nodules is retained somewhat more in this case than for sodium free glass. Crystal sizes will be discussed in section 4.3.3.

4.3.2 Stoichiometry

Thin films deposited at 180 W in pure Ar were subjected to ESCA analysis. The thin film surface was studied without sputter cleaning, because this results in preferential removal of O (i.e. reduction of the surface) so that the true stoichiometry is no longer measurable [Hashimoto02]. At the film surface, ambient oxygen is absorbed, leading to an abnormally high O-content as measured by ESCA. The stoichiometry of the sample can, therefore, not be determined by measuring the Ti/O ratio but by a peak fit to the Ti2p signal to determine the contributions of different oxidation states of Ti. The measurements revealed that the thin films were stoichiometric, i.e. the Ti2p line shape could be fitted by only the contribution of Ti^{4+}, independent of the Ar-pressure during deposition. The influence of sputter power was not measured since normally the stoichiometry improves with decreasing power, i.e. decreasing deposition rate. The reason for this is that at lower deposition rate a lower oxygen content in the atmosphere is necessary to achieve the same stoichiometry in the thin film. There are two sources of oxygen in the sputtering chamber, namely rest gas (on the order of 0.5 to $1 \cdot 10^{-5}$ Pa, mostly water desorbing from the walls) and oxygen sputtered from the TiO_{2-x} target. Since sputtered Ti has a high affinity to oxygen these two sources obviously provide enough oxygen to yield stoichiometric films. It was, therefore, not necessary to add oxygen to the sputter gas.

A second way to estimate the stoichiometry of the thin films is to look at the optical transmission of the TiO_2 thin films. These films show a high optical transmission in the visible light range when being fully stoichiometric. The presence of Ti^{3+} generates a dark blue coloring of the film, i.e. it will show absorption in the yellow part of the visible light spectrum. Since all TiO_2 thin films showed a high optical transmission and no absorption in the visible range it was concluded that the chosen deposition conditions yielded stoichiometric films. This was not changed by subsequent annealing.

4.3.3 Crystallization

All as deposited layers were found to be XRD amorphous. When the sputtered TiO_2 thin films were heat treated, crystallization occurred above a certain temperature. The dependence of the crystallization behavior on the film deposition parameters will be discussed in section 4.3.3.1. One important goal of the crystallization study was to find the best temperature and time for annealing (sections 4.3.3.2 and 4.3.3.3, respectively). The effect of sodium in the substrate will be treated in section 4.3.3.4. A discussion of the crystallization behavior and the comparison with the microstructural observations follows in section 4.3.3.5.

Processing of the XRD spectra

Before looking at all this, we first consider the reproducibility of the measurements. From the measured XRD spectra we deduced the (004)/ (101) peak height ratio (to estimate the preferred (004) orientation) as well as for estimating the crystallite size and the strain on the a- and c-axis (section 3.3.1). In order to determine the error of the method, the same thin film (deposited at 1.4 Pa, 60 W, annealed at 673 K/ 0.5 h) was measured several times and each measurement was interpreted individually.

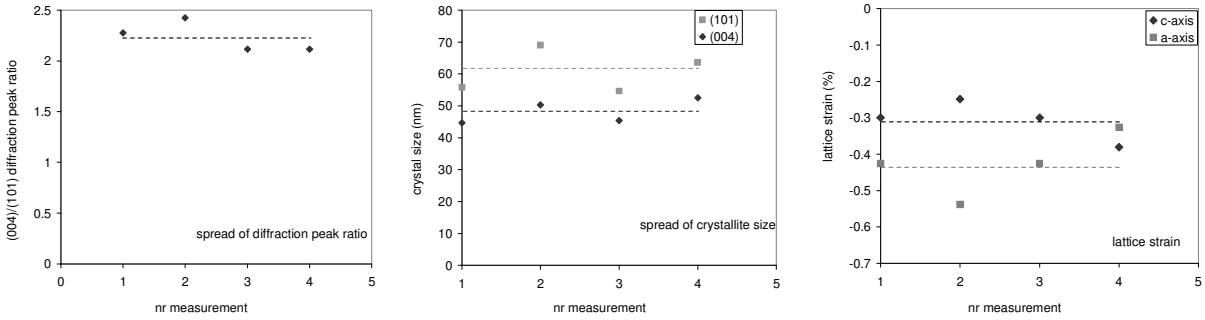

Figure 4. 40:
Spread of (004)/ (101) diffraction peak ratio, crystallize size and lattice strain determined from different measurements of a thin film deposited at 1.4 Pa, 60 W, annealed at 673 K/ 0.5 h.

The average value of the four measurements is indicated by the dashed line. The spread in diffraction peak ratio is from 2.21 to 2.42, in crystallite size from 44.7 to 52.5 nm (004) and 54.7 to 69.2 (101), and in strain from -0.326 to -0.539 (a-axis) and -0.249 to -0.380 (c-axis). In conclusion, using the stronger peak, here (004), naturally gives the least spread on the crystallite size calculation. The data for the strain have a rather large error and must be interpreted with care.

4.3.3.1 Dependence on the sputter conditions

a. Ar-pressure

The dependence of the crystallization of the TiO_2 thin films on the Ar pressure during deposition yielded some striking results. When comparing the spectra to the NIST powder spectrum also given in Figure 4. 41 one can see that all films show a different ratio in the (004) and (101) peak height. This means that there is some degree of crystalline orientation in the thin films, which is related to the Ar-pressure.

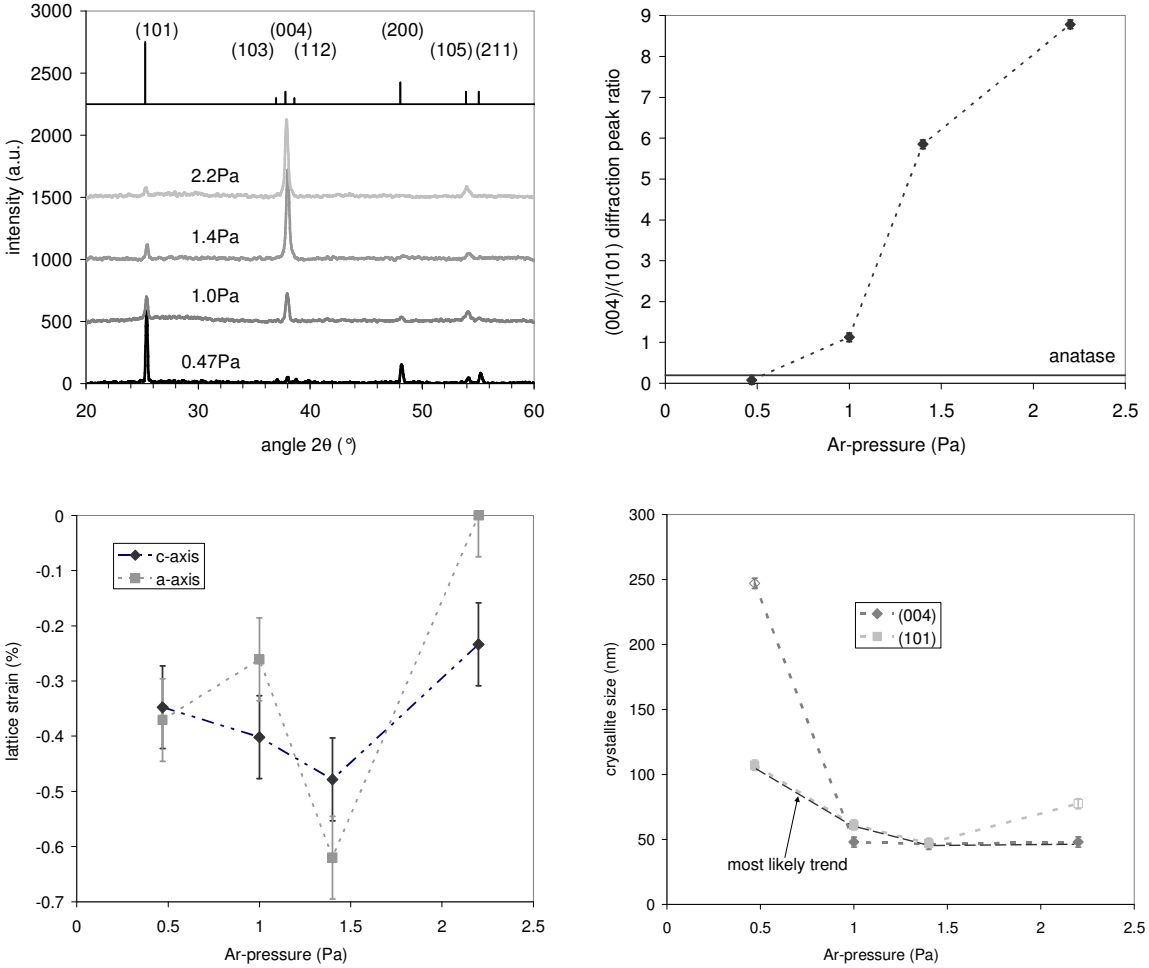

Figure 4. 41:

Dependence of the crystallization of the TiO_2 thin films on the Ar-pressure during deposition (60 W, annealed 673 K/ 1 h): Top: θ-2θ scans (left), (004)/ (101) peak ratio (right).

Bottom: lattice strain (left), crystallite sizes calculated from the (101) and (004) diffraction peak (right). Given that the measurement points with open symbols are not accurate (see text) the most likely trend is the one indicated.

On the top right hand side of Figure 4. 41 the (004)/ (101) peak height ratios for the thin films (dots) and the NIST powder spectrum (line) are shown. The film deposited at 0.47 Pa

shows a (004)/ (101) peak ratio of 0.08 as compared to 0.2 observed for the NIST powder spectrum. This seems to indicate a (101) preferential out of plane orientation. But the fact, that all reflection peaks of the reference spectrum are visible in its XRD spectrum indicates that this thin film does not show any preferential orientation. The measured (004) peak is very weak, so that the uncertainty of its height is the reason for the deviation of the measured (004)/ (101) peak height ratio to the NIST standard. From 1.0 Pa on a (004) preferred orientation is clearly visible which becomes increasingly stronger for increasing Ar-pressure.

The lattice strain (bottom left of Figure 4. 41) is negative for both the a-and c-axis. While the trend is not quite the same for the two lattice constants, they have in common that the strain is the highest for the film deposited at an Ar-pressure of 1.4 Pa and is the lowest at 2.2 Pa. A negative strain means that the lattice constant has decreased, i.e. the strain is compressive. Since there is a strong degree of (004) orientation in the columns at 1.4 Pa there is a certain compressive strain through the length of the columns. This strain increases with increasing (004) preferential orientation, with exception of the film deposited at 2.2 Pa. Why the strain decreases at the highest pressure is not clear for the moment. Perhaps there is some strain relief due to the large inter-column spacing in this film (see sections 4.3.1.1 and 4.3.1.2).

The grain sizes were estimated from the peak broadening of the (101) and (004) diffraction peaks (bottom right Figure 4. 41). Here the grain size for the (004) peak has a similar value of slightly lower than 50 nm for films deposited at pressures of 1.0 Pa and higher. The value for the film deposited at 0.47 Pa must be taken with care as its (004) peak intensity is very low. The grain size calculated from the (101) diffraction peak decreases from slightly above 100 nm to slightly below 50 nm for decreasing pressure until 1.4 Pa. At 2.2 Pa the grain size increases to around 80 nm, but again this value must be taken with care as the (101) diffraction signal is rather low at this pressure.

When combining the above information one can say that annealing films deposited at 0.47 Pa at a temperature of 673 K yields (101) randomly oriented grains with a size of ca. 110 nm. Films deposited at 1.0 Pa result in a somewhat (004) preferred orientation and a grain size of 50-60 nm. Films deposited at 1.4 and 2.2 Pa result in a stronger (004) preferred orientation and a grain size of slightly below 50 nm.

Films deposited at 180 W, annealed at 673 K/ 1 h, show the same tendencies as for the films deposited at 60 W. At the lowest pressure of 0.47 Pa a random orientation (Figure 4. 42, top) is observed and with increasing Ar-pressure an increasing (004) preferred orientation

develops, but it is weaker than observed for 60 W. For the two highest pressures of 1.4 and 2.2 Pa no further change in preferred orientation is observed. The maximum (004)/ (101) peak height ratio is 1.5, which is much less than the value of almost 9 reached at 60 W, 2.2 Pa.

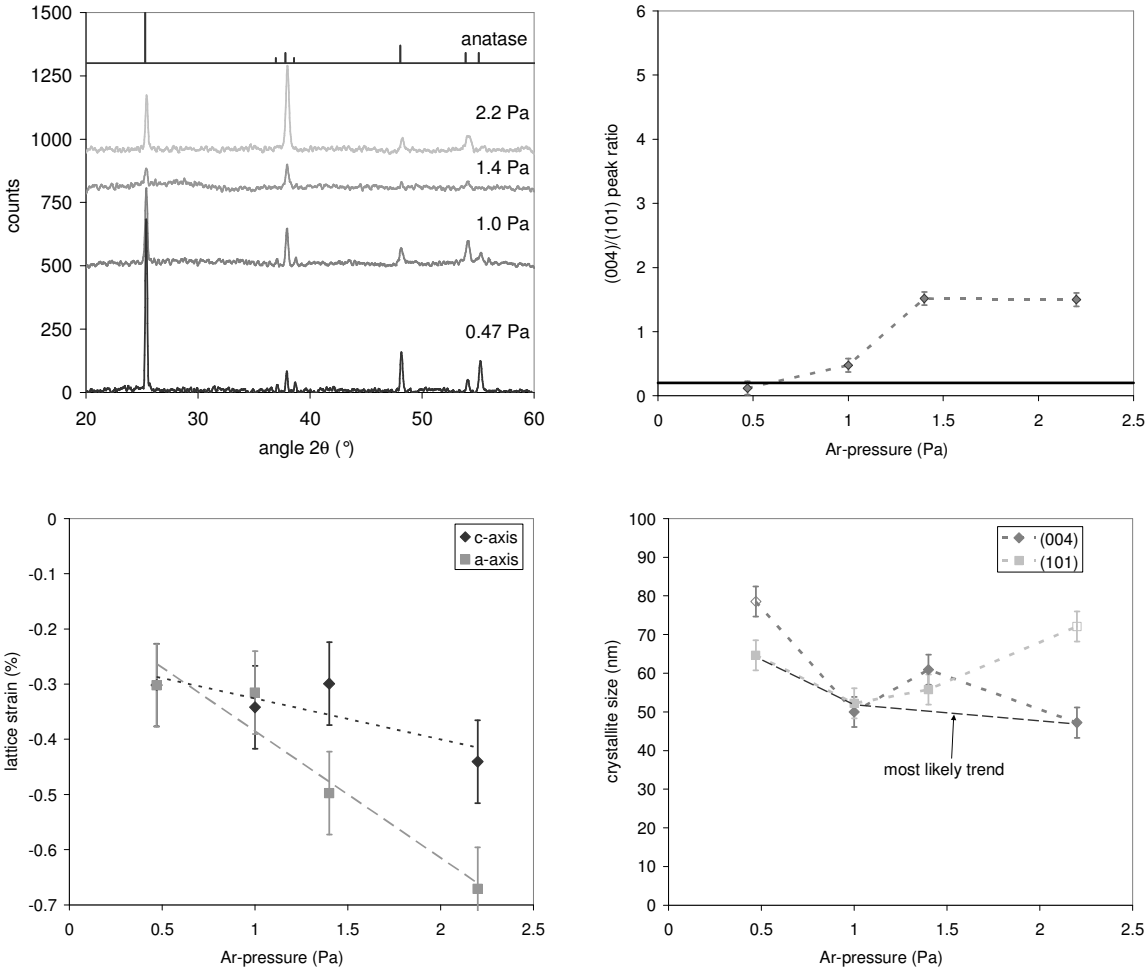

Figure 4. 42:

Dependence of the crystallization of TiO_2 thin films on the Ar-pressure during deposition (180 W, 673 K/ 1 h). Top: left θ-2θ scans, right (004)/ (101) peak ratio.

Bottom: left c-axis lattice strain, right crystallite sizes calculated from the (101) and (004) diffraction peak.

The lattice strain (Figure 4. 42) is also negative for thin films deposited at 180 W but follows a trend different from that at 60 W. The lowest strain is observed for the lowest Ar-pressure and it increases, on average, for both the a and the c-axis, so that the film deposited at 2.2 Pa shows the highest strain. The increase is much stronger for the a-axis. Possibly the strain is not relieved by the microstructure for these films. These films also show a higher density as seen in SEM (section 4.3.1.1) and calculated from the refractive index (section 4.3.4.1).

The crystallite size follows a trend similar to the films deposited at 60 W. For the highest pressures the calculated crystallite sizes are similar to those for 60 W. Compared to the corresponding film deposited at 60 W a smaller crystallite size of 65 to 80 nm is observed at 0.47 Pa for 180 W.

b. Sputter power

As was already obvious from Figure 4. 41 and Figure 4. 42 above, the TiO_2 thin films deposited at 1.4 Pa at different applied d.c. power show a preferred (004) orientation. Figure 4. 43, top left shows the effect of power more clearly. The (004) orientation is the strongest for 60 W but less pronounced for higher d.c. powers.

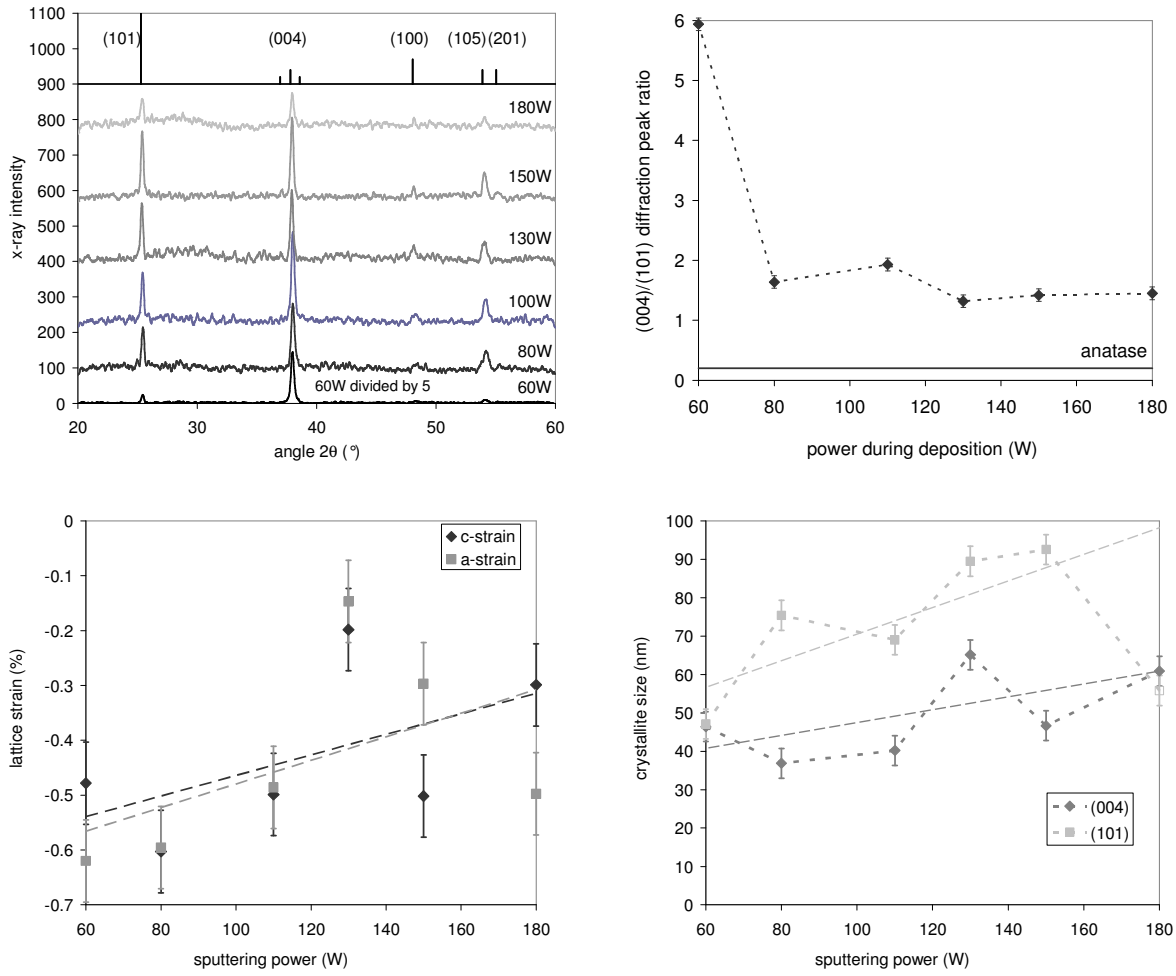

Figure 4. 43:

Effect of sputtering power on the crystallinity of thin films deposited at 1.4 Pa in pure Ar, annealed at 673 K/ 1 h. Top: left θ-2θ scans, right (004)/ (101) peak height ratio.

Bottom: left lattice strain, right crystallite sizes calculated from the (101) and (004) diffraction peak. Given that the measurement points with open symbols are not accurate (see text) the most likely trend is the one indicated.

The (004)/ (101) peak height ratio slightly decreases with increasing sputtering power for powers of 80 W and higher (Figure 4. 43, top right). Apparently the sputtering power (from 80 W on) has a much smaller influence on the crystallization behavior than the Ar-pressure during deposition.

The lattice strain (Figure 4. 43, bottom left) shows quite some scatter on the data but the general tendency is a decrease in the absolute value of the lattice strain (for both a- and c-axis) for increasing d.c. power. Neglecting the grain size calculated from the (101) reflection at 180 W (low signal intensity of the XRD peak) one can conclude from Figure 4. 43 bottom right that the crystallite sizes calculated from the (101) and (004) reflections both increase with increasing sputtering power. The calculated grain sizes are larger for the (101) reflection, which could have two reasons: The first is, that the instrumental broadening corrections chosen for the (101) and (004) reflections are not correct (section 3.3.1), meaning that the correction factor for the (101) reflection was chosen too large or the one for the (004) reflection too small. The second reason could be that the crystallite size vertical to the surface is indeed different for the two different orientations.

Note that the increase in crystallite size with increasing sputtering power does not correspond to the observed decrease in nodule size that was deduced from the SEM images. The relationship between crystallite and column-grain size will be discussed further in section 4.3.3.5.

4.3.3.2 Dependence on anneal temperature

An important study was to find the lowest temperature at which crystalline films could be obtained and whether increasing the anneal temperature would influence their crystallization behavior.

From the left hand side of Figure 4. 44 one can see that films deposited at 60 W and 1.4 Pa annealed at lower temperatures up to 623 K are XRD amorphous while the films annealed at 673 K or higher are well crystallized anatase. Note that even at the highest temperature no reflections of rutile are observed. As was already discussed in section 4.3.3.1 there is a strong (004) preferred orientation. The right hand side of Figure 4. 44 shows the (004)/ (101) peak height ratio for the crystalline films (dots) and the anatase powder spectrum (line), latter having a value of 0.2. The peak ratio observed for the thin films lies between 2 and 2.5, indicating a strong (004) orientation. The degree of orientation does not seem to be influenced significantly by the annealing temperature for the range investigated.

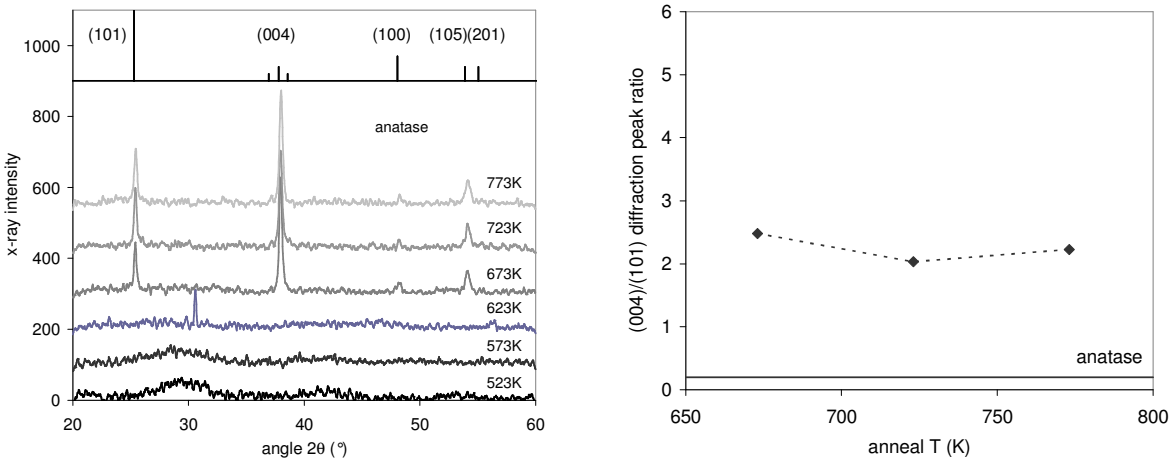

Figure 4. 44:

Effect of anneal temperature on the crystallinity of thin films deposited at 1.4 Pa and 60 W. Anneal time was 0.5 h. Left: θ-2θ scans; the peak observed at 623 K is an artifact. Right: (004)/(101) peak height ratio.

For thin films deposited at 180 W and 1.4 Pa crystallization was observed from a temperature of 573 K on (anneal time 1 h, Figure 4. 45). The degree of (004) orientation was not significantly affected by the anneal temperature so that the (101)/ (004) peak height ratio was not calculated. As already discussed in section 4.3.3.1 the preferred (004) orientation is lower compared to the films deposited at 60 W.

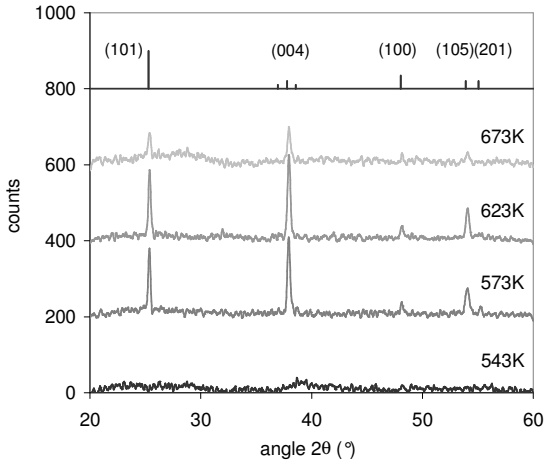

Figure 4. 45:

Effect of anneal temperature on the crystallinity of the thin films deposited at 1.4 Pa and 180 W. Anneal time was 1 h.

An important conclusion of this study is that the crystallization temperature of the thin films depends on the sputter power during deposition. A reason for this could be a smaller primary particle size (the grains observed inside the nodule in the SEM images is discussed in section 4.3.1.1). Even though the primary grain size does not seem to be different between films

deposited at 60 W and 180 W, the resolution of the images may not be good enough to measure the grain size exactly. A second reason may be the intrinsic energy in the thin films. For higher deposition powers the amount of energetic particles arriving per unit time is much higher due to the increase in deposition rate (see Figure 4. 26, p. 162), even though the energy per incoming particle is not much different. In section 2.8.4.3 studies are discussed that found an increased crystallinity with applied d.c. power; in [Kim02c] it was also argued that the total amount of energy delivered by the arriving particles increased with sputtering power. This issue will be discussed further in section 4.3.3.5.

The dependence of the c-axis strain and crystallite size of the (crystalline) thin films on the annealing temperature was also determined (Figure 4. 46). Note that the films deposited at 60 W only crystallize from 673 K on. There seems to be an obvious relationship between the c-axis lattice strain and the crystallite size, especially for thin films deposited at 60 W. For the latter power an increase in the negative value of the lattice strain together with a decrease in crystallite size is observed with increasing anneal temperature. The a-axis strain, on the other hand seems to remain constant with increasing anneal temperature. The intensity of the diffraction peaks does not change with increasing anneal temperature indicating that there is no increase in the number of crystallites.

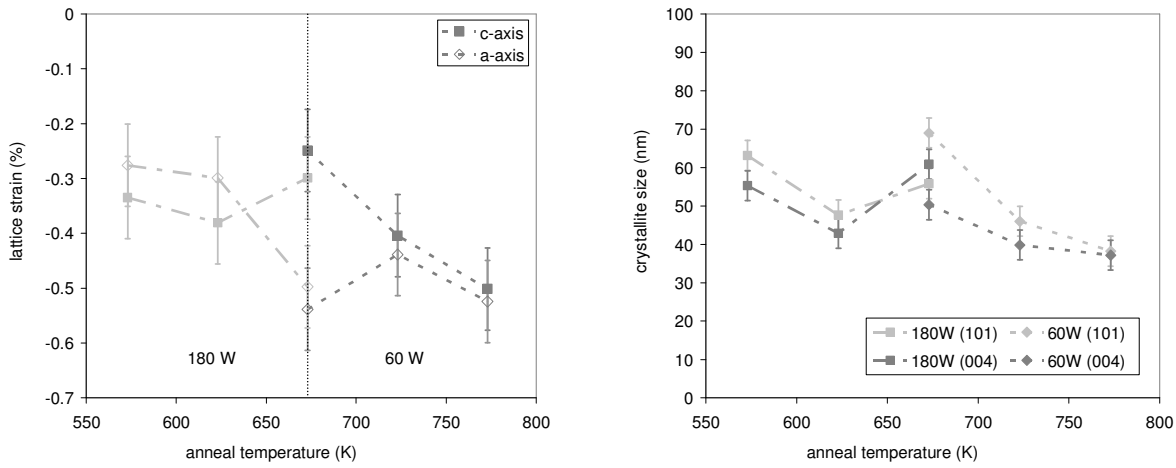

Figure 4. 46:
Lattice strain and crystallite size calculated from the XRD spectra for thin films deposited at 60 W and 180 W at a pressure of 1.4 Pa, annealed at different temperatures. Note that the films deposited at 60 W only crystallize from 673 K on.

For the films deposited at 180 W there is a decrease of the a-axis and little change of the c-axis strain for the different anneal temperatures investigated. All films show a considerable

lattice strain. There is also little change of the crystallite size, following the trend of the c-axis strain.

In conclusion, the crystalline structure of the thin films is already fully developed at the lowest temperature showing film crystallization, namely 673 K for films deposited at 60 W and 573 K for films deposited at 180 W (both for a pressure of 1.4 Pa). Therefore, it is not necessary to anneal the films at a higher temperature. For the comparative studies in this thesis it was chosen to use 673 K as the standard anneal temperature.

4.3.3.3 Dependence on anneal time

When looking at the dependence of the crystallization on anneal time (Figure 4. 47) it seems that the film annealed at 1 h shows a much stronger (004)/(101) peak height ratio than the other films. This result seems to be 'out of spec' not only when considering the anneal time but also the power dependence (Figure 4. 43 top right, p. 186). A possible reason could be that there was some difference in sample holder geometry during the measurement. XRD spectra of preferentially oriented films are sensitive to the alignment of the diffractometer. When extrapolating (linearly) the results from Figure 4. 43 and Figure 4. 47 one should rather expect a value between 1.8 and 2.6 for the (004)/ (101) peak height ratio for the film deposited at 1.4 Pa, 60 W and annealed at 673K / 1 h. Since the points in Figure 4. 47, except the one for 1 h, lie nicely on a straight line it seems one could use the value of 2.6 for the (004)/ (101) peak ratio. This would not change the general interpretation of the other figures, though, since it would not change the trends observed in Figure 4. 41 p. 183, and Figure 4. 43.

The negative value of the c-axis lattice strain seems to increase slightly with increasing anneal time, while the a-axis strain seems to show the opposite behavior. There is no difference for annealing times of 1 h or 2 h for the c-axis strain. The grain size remains rather stable, perhaps showing a slight increase with increasing anneal time when looking at the values calculated from the (004) diffraction peak. The values calculated from the (101) diffraction peak will have a larger error due to the smaller peak size. The data suggest, though, that the crystallite size for the (101) oriented crystals decreases with increasing annealing time until it stabilizes at 1 h. One possible conclusion is that the (101) oriented grains grow faster initially but then are consumed or outnumbered by (004) oriented grains.

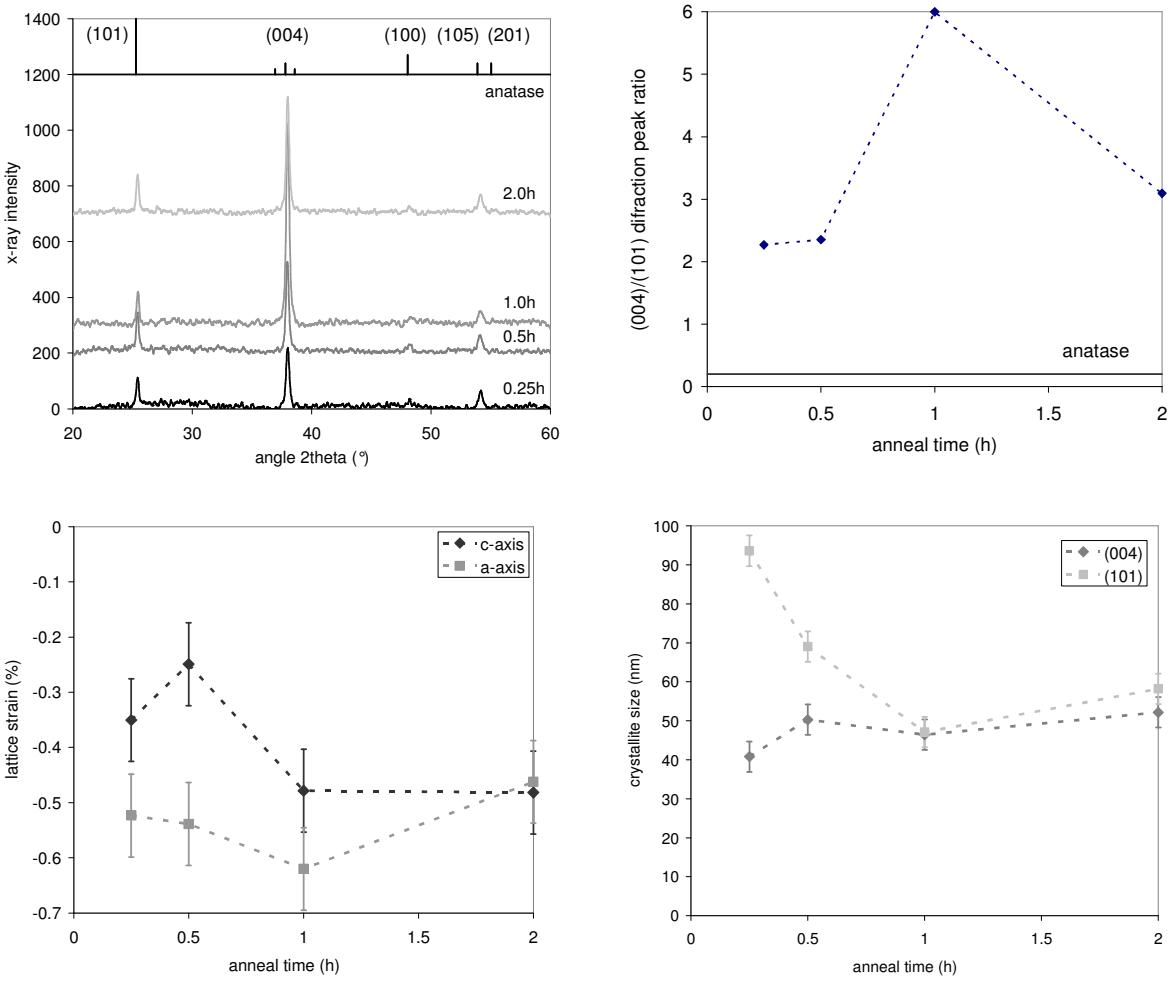

Figure 4. 47:

Dependence of film crystallization of TiO_2 thin films sputtered at 60 W, 1.4 Pa, annealed at 673 K on the anneal time. Top: θ-2θ scans (left), (004)/(101) peak ratio (right). Bottom: lattice strain (left), crystallite size (right).

The intensity of the diffraction peaks in general increases up to an anneal time of 1 h, possibly indicating an increase in the number of (large) crystallites. But there is no change from 1 h to 2 h. It was, therefore, chosen that the standard anneal time would be 1 h.

4.3.3.4 Effect of substrate (Na^+ content)

Some initial heat treatment experiments were performed with thin films deposited at 180 W onto standard microscope slide glass, which contains sodium. In Figure 4. 48 the influence of the anneal temperature and the Ar-pressure during deposition are shown. Due to the weak XRD reflections it was not trusted to calculate the c-axis strain and the (004)/ (001) peak height ratio.

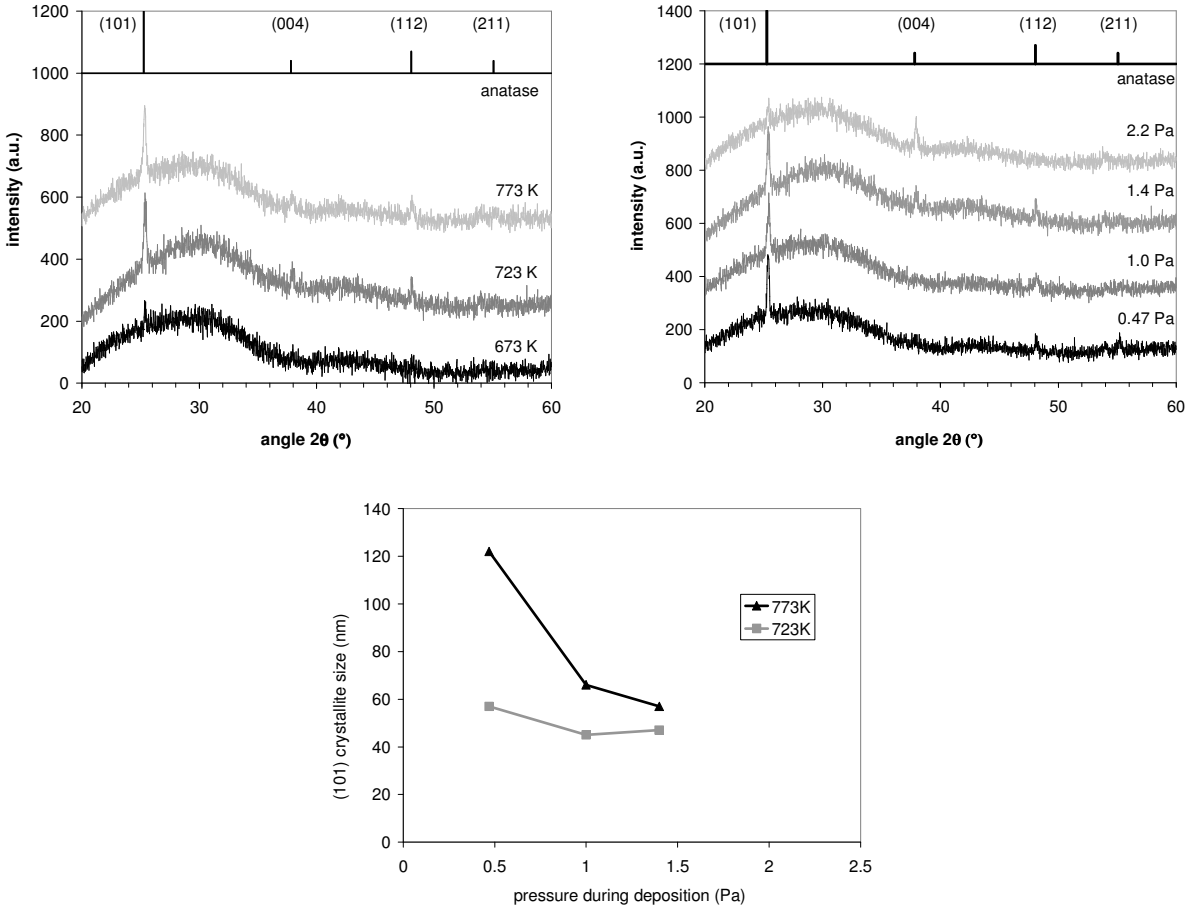

Figure 4. 48:

TiO_2 thin films deposited at and 180 W onto soda-lime glass and heat treated for 0.5 h.

Top: XRD spectra of films deposited at 1.4 Pa and heat treated at different temperatures (left); films deposited at different Ar-pressures and heat treated at 723 K (right).

Bottom: Dependence of the crystallite size, calculated from the (101) reflection, on the Ar-pressure and the anneal temperature.

The most striking difference with the results presented in the previous sections is the low degree of crystallization observed in these films, which is reflected by the low signal-to-noise ratio. The second difference is the crystallization temperature which has increased from 573 K (for the equivalent films on alkali-free glass, see section 4.3.3.2) to 723 K, i.e. 150 K higher. The conclusion is, that the soda-lime glass retards the crystallization of TiO_2 thin films, which was also found in [Nam04].

When comparing the dependence of crystallization on the Ar-pressure during deposition for thin films deposited on sodium free and soda-lime glass (Figure 4. 42 p. 185, and Figure 4. 48, respectively) one can see that the development of the preferred (004) orientation is also influenced by Na diffusion into the film. For soda-lime glass no preferred orientation is

observed with exception of the film deposited at 2.2 Pa, which shows the (004) preferred orientation observed for the films deposited on sodium free glass.

It was not possible to calculate the grain size from the (004) reflection due to the low XRD signals observed. For the film deposited at 2.2 Pa the (001) reflection was also too weak. Therefore, only the crystallite sizes for the lowest three pressures using the (101) signal were calculated. This was done for the two anneal times yielding crystalline films. When looking at the crystallite sizes of the films annealed at 723 K on soda-lime glass and 673 K on sodium-free glass one can see that the films on soda-lime glass have a somewhat smaller grain size. This does not correspond to [Nam04] where an increased particle size for films on soda-lime glass was observed. Looking at the evolution of the crystallite size with increasing temperature one can see that there is a small increase for 1.4 Pa and that the increase becomes larger with decreasing pressure. In contrast, for the films deposited onto sodium free glass (180 W) there was no influence of the crystallization temperature on the crystallite size. As a result the grain size of thin films annealed at higher temperatures will be higher for films on soda-lime glass.

Together with the discussion in section 2.6.6 one has to conclude that the influence of sodium in the substrate is more complex than thought. It stands without discussion, though, that the presence of sodium in the substrate has a profound influence on the crystallization behavior of the sputtered TiO_2 thin films. Especially the weak crystallinity should have some further consequences towards their photocatalytic activity. This confirms the importance to use alkali-free glass when heat treating the films to avoid Na-contamination and investigate the intrinsic properties of the TiO_2 thin films.

4.3.3.5 Discussion of the crystallinity of the sputter deposited TiO_2 thin films

a. Crystallization behavior

The most interesting finding regarding the crystallization of the sputter deposited TiO_2 thin films is that they develop a preferred orientation while starting from an XRD amorphous structure. In this section an attempt will be made to explain this behavior.

All as deposited layers were found to be XRD amorphous. The amorphous structure is normally taken to be random. How can such a random structure develop directional crystal growth?

Crystallization is a nucleation and growth process. Small nuclei of the crystalline phase form and grow at the expense of the amorphous phase around them and later possibly at the expense of neighboring crystallites. The kinetics of this process are controlled by the nucleation and the crystal growth steps of the process. Usually some activation energy is needed to form the nuclei, which then proceed to grow at a specific rate. Both steps are temperature dependent. The final crystallite size will depend on the growth speed, but there can be limiting factors, e.g. if the crystallites are being restricted by others, i.e. cannot grow by consuming each other. In the case of the crystallization of anatase from the XRD amorphous, as deposited films we must see this process strictly as a phase transformation process. The temperatures of 673 K are rather low and prevent large scale sintering to grain/crystallite sizes of µm. There is, therefore, a structural limitation on the crystallite sizes, namely the dimensions of the column-grains.

How is this process influenced by the deposition conditions? These must result in a somewhat different structure of the as deposited thin films. From the discussion in the previous sections it has become clear that the column size is affected rather little, but the most obvious change is the film density. The lower the film density, the higher the degree of preferred orientation.

On the other hand, the same factors favoring a higher film density (lower Ar-pressure and higher sputtering power) also favor a lower oxygen content in the film, while higher Ar-pressure and lower sputtering power favor a higher oxygen content (as discussed in 4.3.2). Even though ESCA results showed that the films were stoichiometric, the measurement error does not allow exact determination of the stoichiometry. It is, therefore, possible that the films with random orientation are slightly sub-stoichiometric while the films with increasing (004) preferred orientation are increasingly more oxidized. Since only Ar is used as sputter gas it is not expected to obtain over-oxidized films.

How can we understand preferential crystal growth from an amorphous matrix? It seems difficult to explain this without assuming that the as deposited films already have some kind of (preferential) local ordering, which then serves as nucleation sites for crystal growth during anneal treatment. This means, that small areas of defined crystal structure exist. There are two possible reasons why these crystalline areas do not yield an XRD signal, namely (i) their size is too small, (ii) their number is too low. Former would result in an extreme peak broadening so that no longer a peak is visible. Latter would result in a too low intensity of the diffraction peak so that it is not distinguishable from the noise level. In order to estimate the size of these

crystalline areas one needs to know the minimum grain size for which an XRD signal can be observed. In e.g. [Liu06, de Almeida Filho06] a grain size of 5 nm and higher yields a well defined diffraction pattern, which becomes very broadened at grain sizes estimated to be between 3 and 4 nm. This means that estimated grain sizes of 3 nm still yield a distinguishable, albeit broadened, diffraction signal. It was tried to find any indication of small crystallites in these 'amorphous' films using a more sensitive XRD technique, which implemented a linear detector and longer measurement times, but no sign of crystallinity could be detected. Very small domains of crystallization can only be detected by high resolution TEM which is not a straightforward technique for ceramic thin films, especially if the presumed crystalline areas are not numerous. In Table 4. 4 the number of unit cells for small grains ≤ 5 nm is listed:

Grain diameter (nm)	1.0	1.2	1.4	1.6	1.8	2.0	3.0	4.0	5.0
# unit cells in grain	3.8	6.6	10.5	15.7	22.4	30.7	103.7	245.9	480.3
# TiO_2 units in grain	15	27	42	63	90	123	415	984	1921

Table 4. 4:

Number of anatase unit cells in small grains ≤ 5 nm.

In a 5 nm grain there are close to 500 unit cells, in a 3.0 nm large grain close to 100. Latter seems to be the limit that can be detected in XRD for anatase. We must, therefore, conclude that the as deposited samples from this thesis have a grain size corresponding to less than 100 unit cells.

How can we understand the effect of Ar-pressure and sputtering power on the preferred orientation of the nuclei/nucleation sites? For this we need to look into the theory of thin film growth, bearing in mind that this normally discusses the growth of a completely crystalline film while we are supposedly dealing with the growth of very small crystalline islands inside an amorphous matrix. In section 2.8.4.3 the influence of the deposition parameters on thin film crystallization was discussed. It was not mentioned then, but usually an increasing preferential orientation was observed with increasing crystallinity, i.e. with decreasing deposition pressure and increasing sputtering power. This is the complete opposite of the behavior during crystallization observed in the study presented in this thesis, namely the preferred orientation increases with increasing sputtering pressure and decreasing sputtering power. In both cases the pressure has a stronger influence than the power. The forming of the nuclei/ nucleation sites must therefore follow a different mechanism than crystalline thin film growth.

A last question is why an increase in sputtering power results in a lower crystallization temperature. Measurable crystallization occurs when the transformation reaction can proceed at a fast enough speed to be detected. From the results on the effect of anneal time (section 4.3.3.3) it seems that once the material begins to crystallize it does so rather quickly, so that the temperature effect must be due to a change in activation energy needed to start the process. It is difficult to judge what will cause this lowering of the activation energy. The thin films deposited at higher power show a higher density, possibly a lower oxygen content and a more random crystalline orientation. Looking at the thermodynamic formula defining the stable nucleus size r_c:

$$r_c=-2\sigma/(\Delta G/V_m(\beta)) \qquad (4.10)$$

with σ the surface tension, $V_m(\beta)$ the molar volume of the nucleus phase and the change in Gibbs free energy of the reaction, ΔG, defined as:

$$\Delta G=\Delta H-T\Delta S \qquad (4.11)$$

with ΔH and ΔS the change in enthalpy and entropy of the reaction, respectively. From equations (4.10) and (4.11) one can see that with increasing temperature the critical nucleus size decreases. In opposite reasoning, a smaller nucleus size means that a higher crystallization temperature is needed for the nucleus to grow. As a result one can conclude that, since the films deposited at 180 W have a lower crystallization temperature as compared to the films deposited at 60 W, former should have a larger nucleus size. This means that, in a way, they have a higher degree of crystallinity, which follows the observations discussed in section 2.8.4.3.

A final point is the relationship between the crystallite and the column-grain size. The column-grains have a diameter of approximately 50 nm and extend throughout the film thickness (i.e. between 350 and 400 nm). The crystallite size calculated using the Scherrer formula reflects their extension perpendicular to the thin film surface. The Scherrer formula does not yield any information on their size parallel to the surface of the film. Since the crystallites are usually around 50 nm, this means that they do not extend through the complete column. Since no re-crystallization occurs due to the low anneal temperatures (i.e. the boundaries of the column-grains are not changed) the maximum horizontal extension of the crystallites is bound to the structure of the column-grains. As discussed in sections 4.3.1.1 and 4.3.1.2 the column-grains (referred to as ‘nodules’) seem to consist of smaller grains which can only be resolved for the as-deposited films in the SEM images. Possibly this was due to the limited resolution

of the SEM or due to sintering of these very small grains of ca. 10 nm size. In conclusion, one can state that the extension of the crystallites parallel to the film surface will be limited by the width of the column-grains, i.e. a maximum of 35-45 nm.

b. Lattice strain

In all thin films a negative lattice strain was found for both the a- and the c-axis, which means that the unit cell volume is smaller compared to unstrained anatase, i.e. the unit cell is under compressive strain. There was no clear link between the lattice strain and the crystallization of the layers.

4.3.4 Optical properties

As already discussed in detail in section 3.3.5 the refractive index and optical band gap were determined from two different transmission measurements.

Determining the refractive index using the envelope method (Swanepoel) was rather straightforward. There was some error in the transmission measurements, though, probably due to the films being inhomogeneous over their thickness. The reference values for the refractive index n were determined at 550 nm, where the fit of the envelopes was rather well. The film thickness could also be determined using the envelop method, provided that sufficient interference fringes were recorded. This was the case for films thicker than ca. 300 nm. Here, good agreement between the film thickness measured with the profilometer and by optical analysis was seen. It was chosen to use the film thickness resulting from the optical measurement for calculating the optical absorption since both were determined using the same area on the film.

From the optical transmission spectra the absorption coefficient α of the films was determined according to equation (2.6)b, p. 12, taking into account transmission losses from the substrate as well as the film thickness. Normally the absorption coefficient is a material constant and independent of the film thickness. The validity of this approach can be seen when looking at the absorption calculated for thin films deposited under the same conditions but with different sputtering times (i.e. thicknesses), shown in Figure 4. 49.

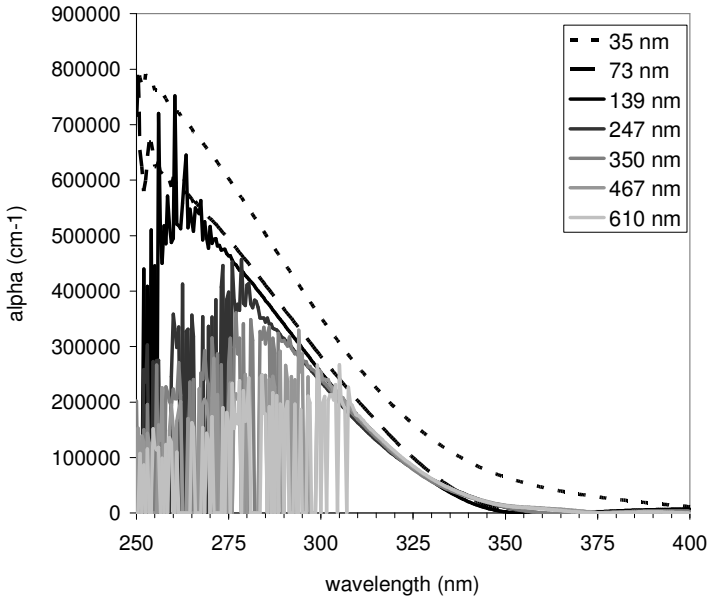

Figure 4. 49:

Influence of the film thickness on the spectral dependence of the optical absorption coefficient α for TiO_2 thin films deposited at 1.4 Pa and 60 W.

For all film thickness but the lowest two the dependence of the absorption coefficient on the wavelength is the same (disregarding the regions of strong absorption at low wavelengths). The deviation of the two thinnest films is most likely due to an error in determining the film thickness with the profilometer. For these films it was, additionally, not possible to use the envelope method for determining the film thickness (section 3.3.2).

To determine the transition mode of the optical band gap the method discussed in section 2.2.4.5 was used. For the four different *m* values listed in table 2.2, p. 17, the plot according to equation (2.12), p. 17 was made (Figure 4. 50). The thin film with a thickness of 350 nm (Figure 4. 49) was used.

No linearity could be obtained for the direct allowed transition ($m = 1/2$). For the direct forbidden ($m = 3/2$), indirect allowed ($m = 2$) and, to a less extent, the indirect forbidden ($m = 3$) transition, a well defined linear range was found.

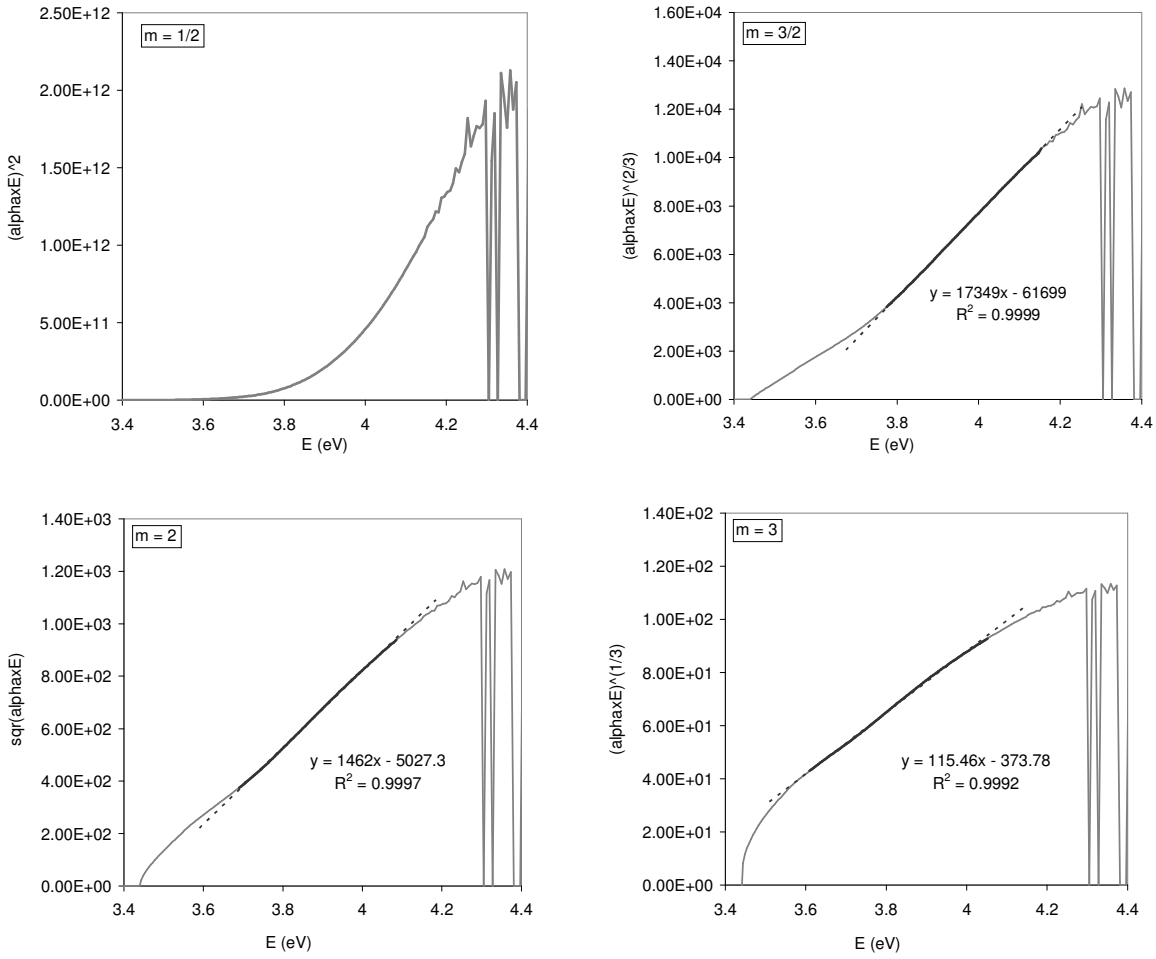

Figure 4. 50:

Results for equation (2.12), p. 17 for values of *m* = 1/2, 3/2, 2 and 3, representing the direct allowed, direct forbidden, indirect allowed and indirect forbidden transition.

There are three reasons why this range of linearity is limited: (i) one observes interference fringes at lower incident light energy, which limits the accuracy of the determination of α, (ii) there is noise due to the strong absorption at higher incident light energy and (iii) simplifications were needed to formulate equations (2.6) through (2.8), p. 13. The band gap energy can be determined from the linear range when dividing the y-axis intercept by the slope, both given by the linear relationship given of the trend line fit. This corresponds to the intercept of the fitting line with the x-axis. For the three different transition modes that yield a linear relationship, one receives three different values for the band gap, namely 3.56, 3.44 and 3.24 eV for the *direct forbidden*, *indirect allowed* and *indirect forbidden* transition, respectively. The linear fit seems to be well for all three curves, making it impossible to select the correct one using this method. One has to keep in mind that for the indirect transitions the phonon contribution to the measured transition energy is neglected for this analysis, meaning that the band gap energy is only an estimate.

It was also tried to directly fit equation (2.11), p. 16 within the same linear region shown in Figure 4. 50, but no reasonable result for *m* could be obtained.

In literature almost exclusively the *indirect allowed* transition is used to determine E_{bg} of anatase. In the case of amorphous and nano-crystalline TiO_2 there was some discussion on whether the transition should be *direct forbidden*, instead (section 2.5.1.2). Therefore, the band gap values for both the *indirect allowed* ($m = 2$) and the *direct forbidden* transition ($m = 3/2$) will be presented and discussed. For some doped TiO_2 thin films the *indirect forbidden* transition ($m = 3$) yielded the best fit; the effect of doping will be discussed in section 4.4.

In the following sections first the dependence of the optical properties of the thin films on the deposition and annealing conditions will be discussed (sections 4.3.4.1 to 4.3.4.4). In section 4.3.4.5 the effect of sodium will be described briefly and in section 4.3.5 the optical properties will be compared to the microstructure and crystallinity of the thin films.

4.3.4.1 Dependence on Ar-pressure

a. Refractive index

The refractive index (at 550 nm) of as deposited films shows a very strong decrease with increasing pressure during deposition for both 60 and 180 W. As can be seen from Figure 4. 51 the decrease is stronger for 60 W. The value of the refractive index for the film deposited at 180 W and 0.47 Pa is close to that of dense anatase (2.5). On the other hand, the lowest refractive index is observed for the film deposited at 2.2 Pa and 60 W. These tendencies are observed for as deposited as well as annealed thin films.

For films deposited at 60 W the refractive index increases with annealing for the films deposited at low pressures, but at high pressures there is hardly any change. For the films deposited at 180 W the refractive index increases for all pressures with exception of the film deposited at 1.4 Pa. The different behavior at this pressure is possibly due to an artifact yielding a higher refractive index for the as deposited film. Overall the difference between the annealed and as deposited films decreases with increasing pressure, following the trend observed for 60 W.

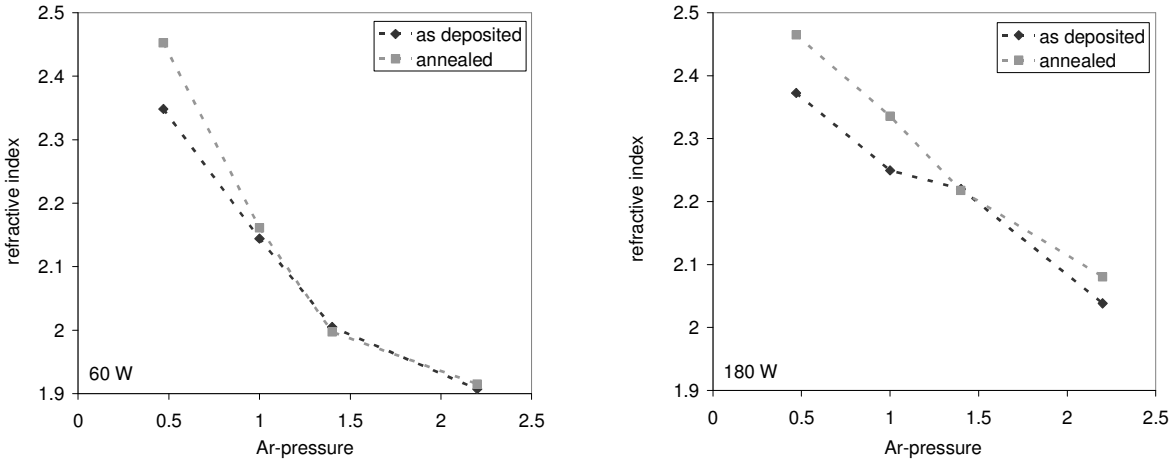

Figure 4. 51:

Dependence of the refractive index of as deposited and annealed (673 K/ 1 h) thin films on the Ar-pressure during deposition; 60 W (left), 180 W (right).

It is interesting to note that there is not much change of the refractive index upon crystallization. This will be discussed in more detail in sections 4.3.4.3 and 4.3.4.4.

Since the SEM images (section 4.3.1.1) already indicated that the film porosity increases with increasing pressure during deposition, it seemed a reasonable conclusion that the porosity is the reason for the decrease in refractive index. As discussed in section 2.2.2.3 the porosity can be estimated from the refractive index according to equation (2.5), p. 12. The obtained results are shown in Figure 4. 52.

One can see that the porosity of films deposited at 2.2 Pa and 60 W reaches a value of about 25%.

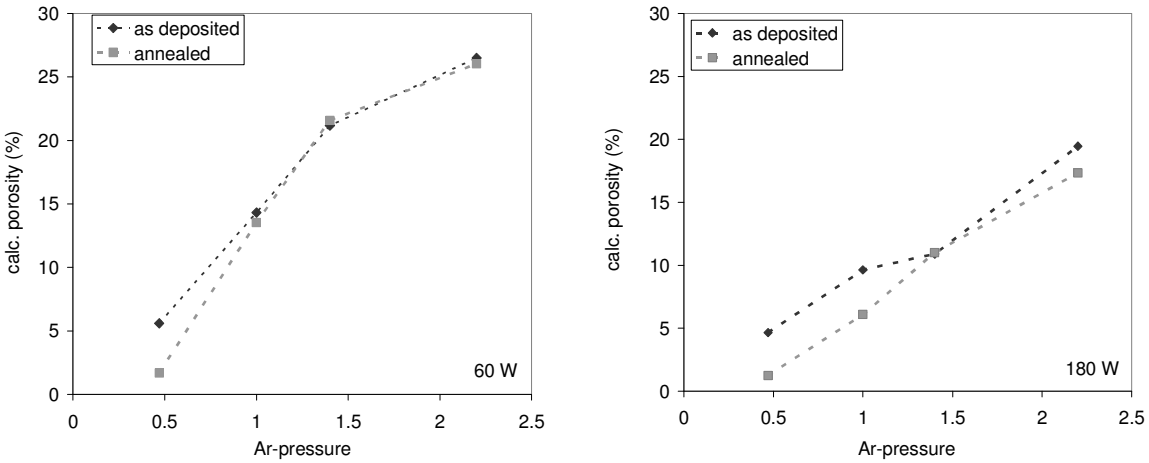

Figure 4. 52:

Dependence of porosity of as deposited and annealed (673 K/ 1 h) thin films on the Ar-pressure during deposition; 60 W (left), 180 W (right); calculated from the refractive index.

The annealed film deposited at 0.47 Pa shows a very low porosity of about 1.5%, i.e. its density is close to the theoretical value of anatase. Annealing the thin films deposited at high pressures at 60 W does not influence their density, even though SEM images show crack formation. As already discussed in section 4.3.1 there is evidence, that there is some compaction within the columns, i.e. sintering of the fine grain structure. This could compensate for the looser packing of the columns that manifest itself as cracking. The increased porosity of the thin films deposited at 0.47 Pa can very well be the result of cracking: the as deposited films are almost fully dense so that the density of the column-grains cannot increase. Crack formation would then automatically lead to a decrease in density.

b. Optical band gap

For the as deposited films the band gap energy E_{bg} increased with increasing Ar-pressure during deposition up to 1.4 Pa, after which it remained constant (Figure 4. 53). The values for E_{bg} determined by assuming a *direct forbidden* or an *indirect allowed* transition were both higher than the literature value of 3.20 eV for anatase. Taking a *direct forbidden* (*indirect allowed*) transition the E_{bg} increased from 3.43 (3.33) to 3.55 (3.44) eV.

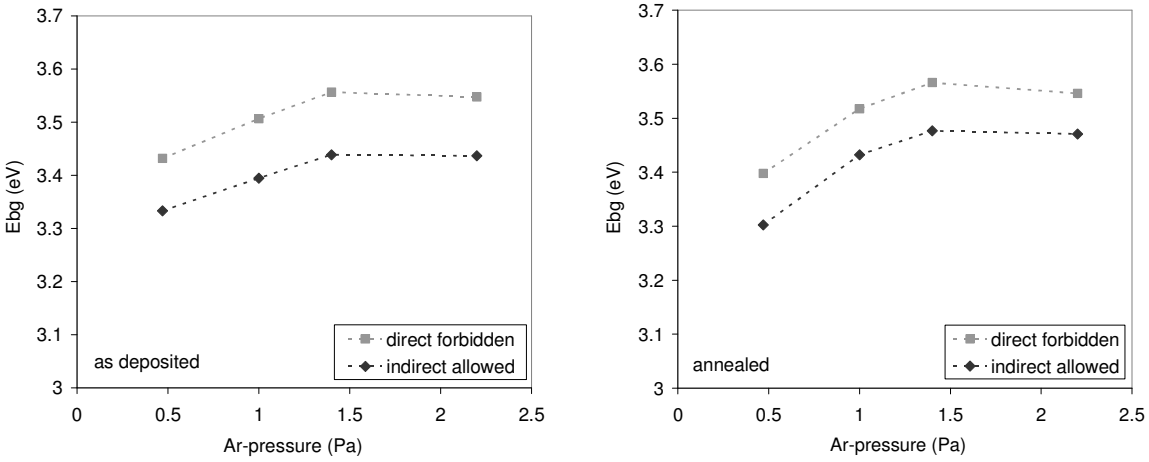

Figure 4. 53:
Dependence of the band gap energy E_{bg} on the Ar-pressure during deposition for TiO_2 thin films deposited at 60 W; as deposited (left), annealed 673 K/ 1 h (right).

The annealed films express the same general trend as observed for the as deposited films, but the pressure dependence is stronger. Here, the band gap energies at the lowest pressure are 3.30 and 3.40 eV and the highest values at a pressure of 1.4 Pa are 3.48 and 3.57 eV, for the *indirect allowed* and the *direct forbidden* transition, respectively. When comparing the results one can see that annealing has decreased the value of the band gap for the lowest pressure while it has increased the value for the highest pressures.

Thin films deposited at 180 W show the same trends as films deposited at 60 W (Figure 4. 54). The band gap increases for increasing sputtering pressure, but to a less extent than for 60 W. Annealing also increases this trend, again as a result of a decrease of the band gap energy at low pressures together with a small increase at high pressures.

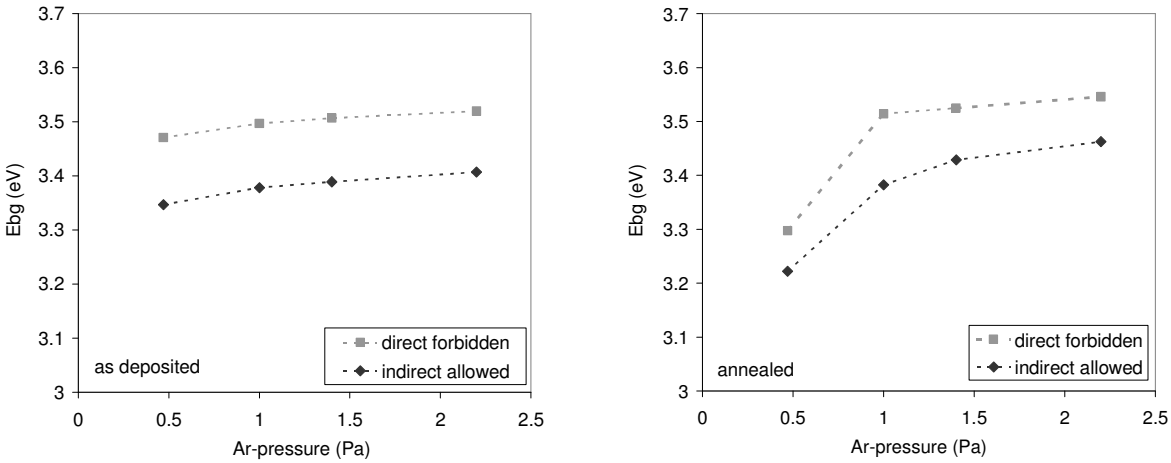

Figure 4. 54:

Dependence of the band gap energy E_{bg} on the Ar-pressure during deposition for TiO_2 thin films deposited at 180 W; as deposited (left), annealed 673 K/ 1 h (right).

The band gap (for the *indirect* band gap transition) of the thin films deposited at 180 W and 0.47 Pa is close to the literature value of 3.2 eV for anatase. These films also show a refractive index of 2.46, which is close to the literature value of 2.5 for anatase (Figure 4. 51).

4.3.4.2 Dependence on sputtering power

a. Refractive index

For samples deposited at 1.4 Pa the refractive index shows a linear increase with increasing sputtering power (Figure 4. 55, left). The scatter of the data points does not allow for a reliable conclusion on the effect of annealing other than that it is rather small.

The porosity (Figure 4. 55, right), as calculated from the refractive index, shows a decrease from ca. 22.5% (60 W) to ca. 11% (180 W). This confirms the increased column packing density observed in SEM which was discussed in section 4.3.1.1.

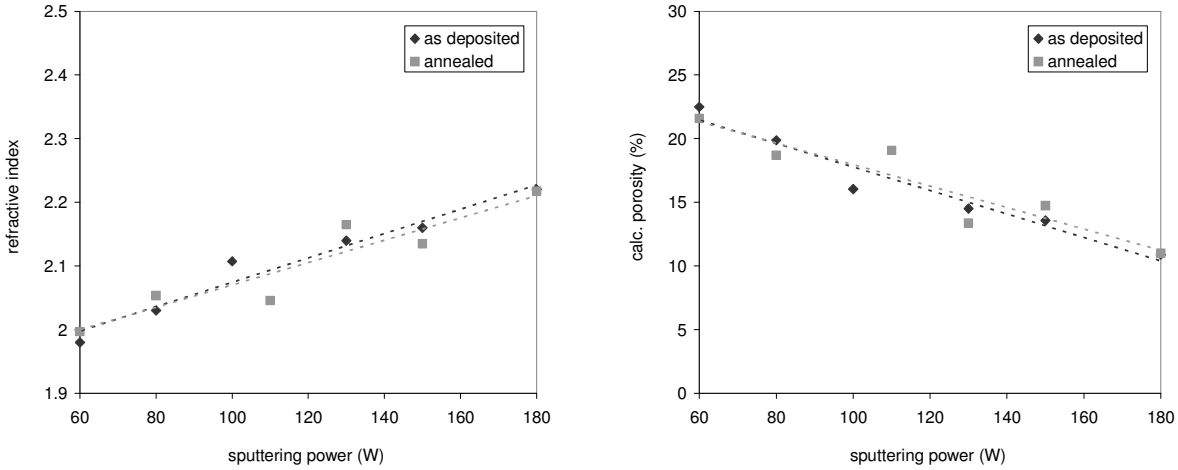

Figure 4. 55:

Dependence of refractive index (left) and porosity (right, calculated from refractive index) of as deposited and annealed (673K/ 1 h) thin films on the sputtering power (Ar-pressure = 1.4 Pa). The dotted lines indicate the linear trend.

b. Optical band gap

Figure 4. 56 shows that there is a small decrease of the band gap energy with increasing sputtering power for as deposited (left) as well as annealed films (right). As already discussed in section 4.3.4.1 the band gap energy increases slightly upon annealing, which can be observed for all powers. The exception is the film deposited at 130 W, here the value for the band gap determined for the annealed film seems too low. For this film it was also difficult to obtain a linear relationship for any of the tested band gap relations, perhaps due to the unlucky position of an interference fringe.

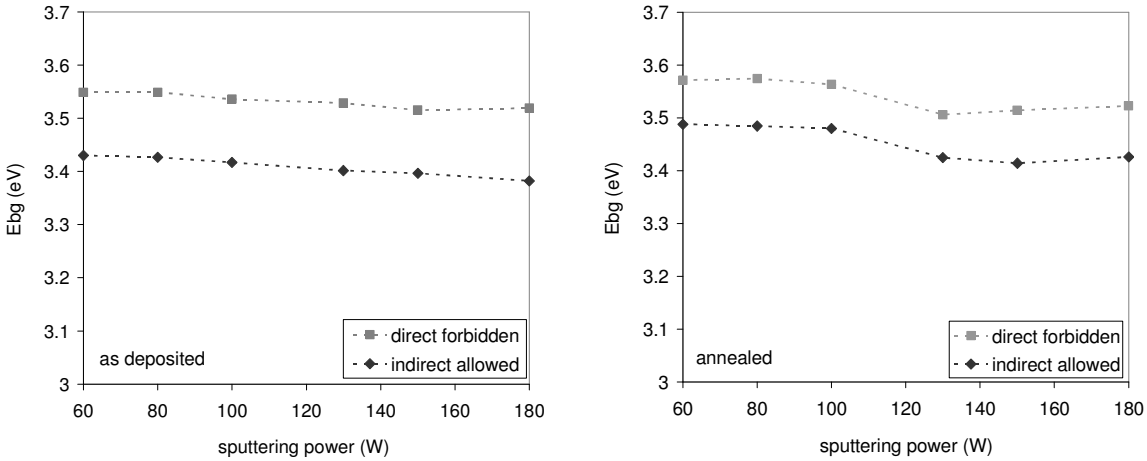

Figure 4. 56:

Dependence of the band gap energy on the sputtering power during deposition for TiO_2 thin films deposited at 1.4 Pa; as deposited (left), annealed 673 K/ 1h (right).

For the amorphous films the variation of the band gap energy when going from 60 to 180 W is 3.43 (3.55) to 3.38 (3.52) eV when assuming an *indirect* (*direct*) band gap transition. For the annealed films one obtains 3.49 (3.57) to 3.42 (3.52) eV for the *indirect* (*direct*) transition, respectively. One can see that the effect of annealing on the band gap decreases with increasing sputtering power.

4.3.4.3 Dependence on anneal temperature

a. Refractive index

The effect of anneal temperature on the refractive index is shown in Figure 4. 57 (left) for TiO_2 thin films deposited at 1.4 Pa and 60 and 180 W. For both powers the refractive index is not significantly influenced by the anneal treatment. This was already reflected in Figure 4. 51, p. 201 and Figure 4. 55, showing the pressure and power dependence of the as deposited and annealed thin films. Note that the difference in anneal time does not influence the crystallization of the thin films (section 4.3.3.3).

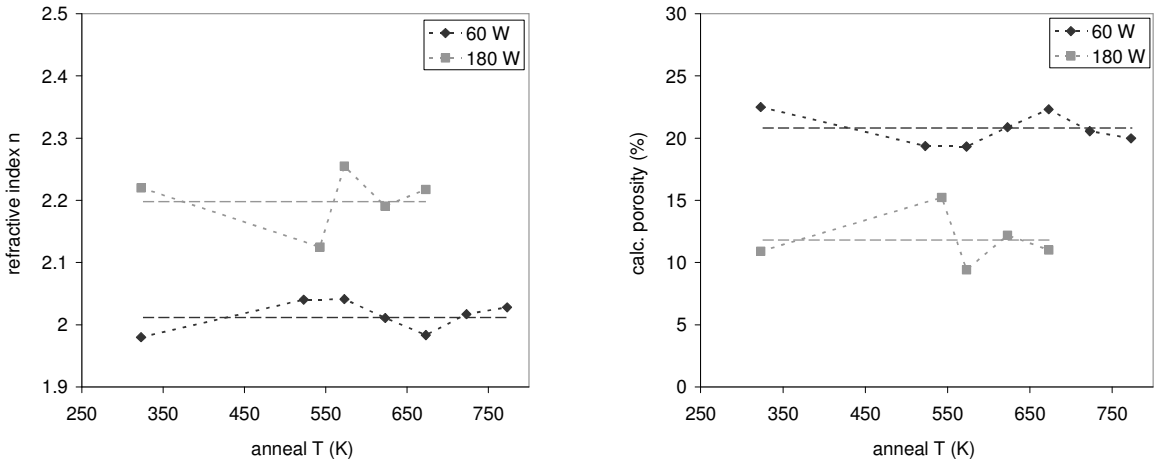

Figure 4. 57:
Dependence of refractive index (left) and porosity (right, calculated from the refractive index) of thin films deposited at 60 and 180 W on the anneal temperature, annealed for 0.5 h (60 W) and 1 h (180 W) (Ar-pressure = 1.4 Pa).

The porosity of films deposited at 60 W (Figure 4. 57, right), calculated from the refractive index, remains around 20 to 23% for all temperatures. For the films deposited at 180 W the porosity remains between 10 and 15%. This is to be expected as the anneal temperatures are too low to facilitate compaction due to sintering.

b. Optical band gap

As one can see in Figure 4. 58, the crystallization is reflected in the evolution of the band gap energy, with the effect being stronger for thin films deposited at 60 W. The most interesting point is that there is an increase in band gap energy upon crystallization when assuming that no change in the band gap transition mode occurs upon crystallization.

For films deposited at 60 W the band gap energy first decreases with increasing T, shows a jump at the crystallization temperature and proceeds to decrease again with increasing temperature. For films deposited at 180 W the band gap energy increases less drastic with crystallization: only when assuming an *indirect transition* one can see a small jump in the band gap energy; when assuming a *direct transition* the band gap energy increases smoothly. This seems surprising since according to the quantum size effect theory (section 2.5.3.2) it is expected that E_{bg} should decrease with increasing crystallite (grain) size. This is clearly not the case here. Since little is reported about the band gap of amorphous TiO_2 it is difficult to compare the obtained band gap values. One reference [Nakamura00b] reported the band gap of r.f. sputtered amorphous TiO_2 thin films to be on the order of 3.6 eV, without stating whether the *indirect allowed* or the *direct forbidden* transition mode was assumed for the calculation. In the same study the thin films were also annealed to obtain crystalline anatase but the band gap of the annealed films is not reported.

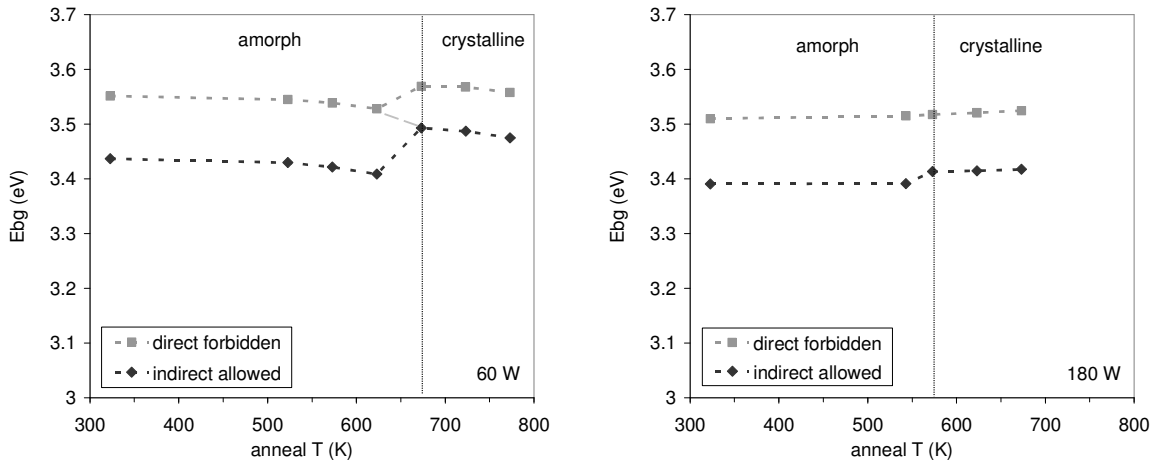

Figure 4. 58:
Dependence of the band gap energy on the anneal temperature for TiO_2 thin films deposited at 1.4 Pa; 60 W annealed for 0.5 h (left), 180 W annealed for 1 h (right).

In literature the hypothesis was phrased (section 2.5.1.2) that the band gap transition for nanocrystalline films may be *direct forbidden* instead of *indirect allowed*, and if one assumes that the same would be valid for amorphous films, then a continuously decreasing band gap

energy with increasing anneal temperature (dotted line left hand side Figure 4. 58) would be observed for the films deposited at 60 W. On the other hand, for films deposited at 180 W there would be a sudden drop in band gap energy, so that it seems unlikely that the above stated hypothesis is true.

4.3.4.4 Dependence on anneal time

a. Refractive index

There is little dependence of the refractive index on the anneal time for thin films annealed at 673 K between 0.25 and 2 h (deposited at 60 W, 1.4 Pa), showing a slight maximum at 1 h (Figure 4. 59). Accordingly, the porosity shows a small dip at 1 h, but values remain roughly between 22 and 25%. A possible reason could be the interplay between sintering of the fine grain structure within the columns and the cracking, i.e. the separation between the column-grains as discussed in section 4.3.1.2.

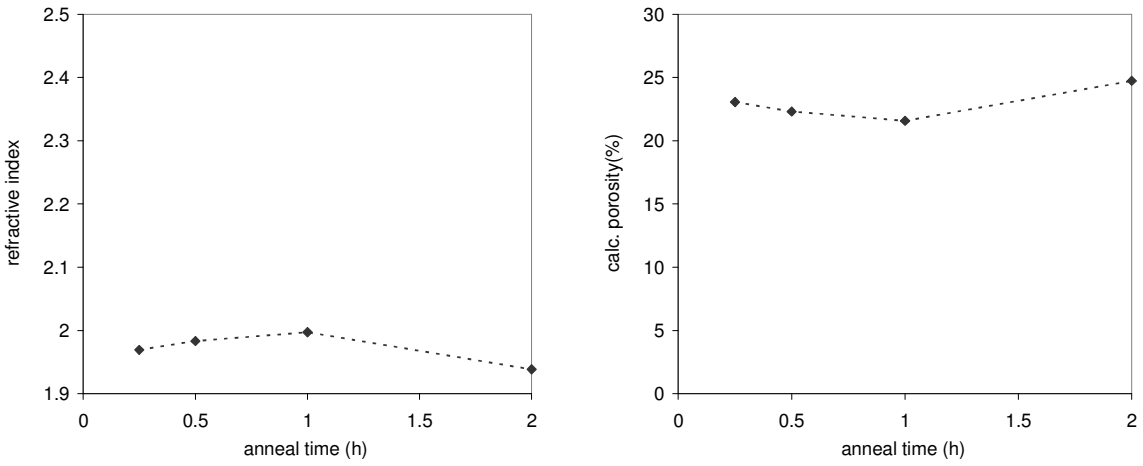

Figure 4. 59:
Dependence of refractive index (left) and porosity (right, calculated from refractive index) on the anneal time for thin films deposited at 60 W and 1.4 Pa, annealed at 673 K. The scale of the vertical axes is chosen to match the other figures.

b. Optical band gap

There is little dependence of the band gap energy on the anneal time. The most obvious feature in Figure 4. 60 is the increase in band gap energy due to crystallization (the film annealed for 0.25 h was already crystalline, see Figure 4. 47, p. 191). This effect is stronger for the *indirect allowed* than for the *direct forbidden* transition (Figure 4. 60). Increasing the anneal time above 0.25 h obviously does not result in any changes in the sample structure which would influence the band gap energy.

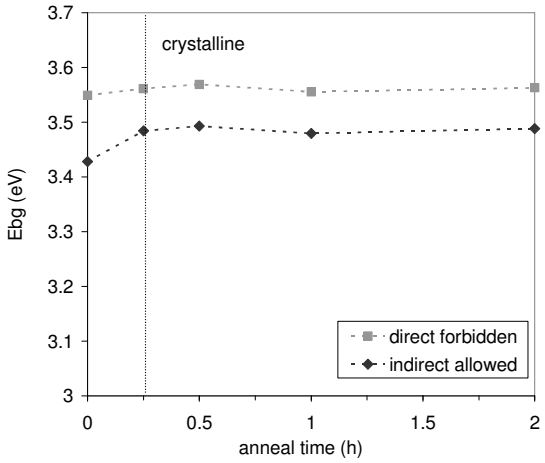

Figure 4. 60:
Dependence of the band gap energy on the anneal time for TiO_2 thin films deposited at 1.4 Pa and 60 W, annealed at 673 K.

4.3.4.5 Effect of sodium content

Refractive index

The presence of sodium in the substrate does not influence the general dependence of the refractive index on the Ar-pressure during deposition (Figure 4. 61). The refractive indices of the films annealed on the soda-lime substrate show a slightly reduced refractive index compared to the films annealed on sodium free glass, i.e. they are more similar to the non-annealed values.

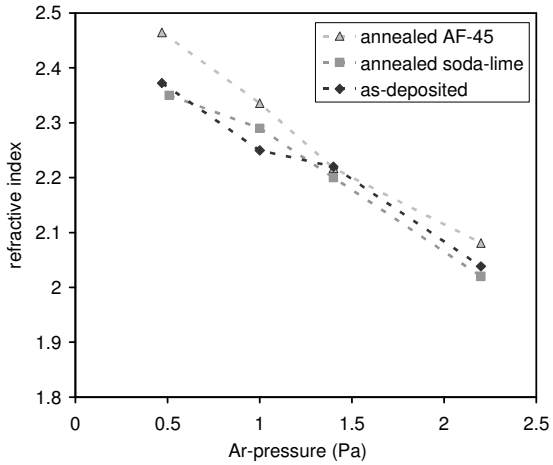

Figure 4. 61:
Effect of sodium content in the substrate on the pressure dependence of the refractive index of TiO_2 thin films sputtered at 180 W. The films were annealed at their crystallization temperature (soda-lime glass: 773 K/ 0.5 h, sodium free AF-45 glass: 673 K/ 1 h)

4.3.5 Relationship between structural and optical properties of the TiO_2 thin films

In this section we will consider the relationship between the morphology and crystallinity of the TiO_2 thin films and their optical properties (refractive index and band gap). In the previous sections the link between the refractive index, the calculated porosity and the morphology as visualized by SEM was discussed. In this section the main focus will lie on the possible influences of the thin film structure on the band gap energy.

4.3.5.1 Refractive index

The refractive index was found to be influenced by the deposition conditions: decreasing with increasing Ar-pressure and decreasing sputtering power. Annealing had no significant influence on the refractive index. The decrease in refractive index can be explained by an increase in film porosity (section 2.2.2.3), so that an increase in film porosity with increasing Ar-pressure and decreasing sputtering power is observed. This follows the trend observed for the thin film microstructure and crystallization behavior. Obviously, the cracking of the films observed upon annealing does not change the total calculated film porosity. As was already discussed in section 4.3.1.2 the compaction of the column-grains due to crystallization is compensated by inter-grain cracking.

4.3.5.2 Band gap

The first interesting observation was the effect of crystallization on the band gap energy, namely that it increased even though a decrease was expected due to the presence of larger crystallites. According to the confinement theory (section 2.5.3.2) there should be a blue shift in the band gap energy for particle sizes smaller than 10 nm which decreases with increasing particle size. For particles larger than 20 nm there should be no confinement and, therefore, no blue shift. Since crystallization occurs abruptly and immediately results in crystallites which extend ca. 50 nm into the depth of the column, the high band gap energy observed upon crystallization does not fit with the confinement theory (section 2.5.3.2). The reason for the increase in band gap energy upon crystallization and the fact that the crystalline layers have such a high band gap has to be a different one.

As discussed in section 2.5.1.5 a second possible factor influencing the band gap energy is lattice strain. The XRD amorphous films were found to have no measurable crystallites, but it was argued in section 4.3.3 that some crystal nuclei should be present. In general, it is diffi-

cult to define what the band gap of this 'amorphous' TiO_2 should be. The lattice strain of the amorphous films cannot be determined from the XRD measurements since they revealed no crystalline structure. The lattice strain in the crystalline films was determined in section 4.3.3. In all films a decrease of the a- and c-axis was seen, i.e. the volume of the unit cell was decreased. According to [Wunderlich04a, Wunderlich04b] an increase in the band gap energy should be observed for a decrease in a-axis length in anatase, namely according to $\Delta E_g / \varepsilon$ = -1.6eV / 0.177 = -9.040 eV, with ΔE_g the change in band gap energy and ε the a-axis strain.

Using this expression for the variation of the band gap with the a-axis lattice strain we can calculate the change in band gap for the (annealed) thin films. In Figure 4. 62 the results are shown for the dependence of the band gap on the Ar-pressure during deposition (for both 60 and 180 W, top left and right, respectively), on the sputtering power (center) and on the anneal temperature and time (bottom left and right, respectively).

The results presented in Figure 4. 62 show as most important result that the increase in band gap energy observed for most films cannot be caused by the a-axis strain developed in the thin films. The calculated band gap energies are only very slightly increased, but the increase does not match the measured one by far. The second observation is the calculated changes in band gap energy do not necessarily reflect the measured changes in band gap energy. The most obvious case is the influence of the Ar-pressure on the a-axis lattice strain. Here the nature of the dependence of the measured band gap is by far not reflected by the calculated one. Especially for the thin films deposited at 60 W the trend in the calculated band gap is the opposite, showing a decrease instead of the measured increase with increasing pressure. The anneal time and temperature had no significant influence on the band gap, measured or calculated. Very striking is the result for the dependence on the sputtering power: here the kink in the curve seen for the measured band gap is reproduced by the calculated one. Especially the trend for the measured values assuming a direct forbidden transition are very well reproduced, even though the absolute value of the calculated band gap is substantially lower. This latter would indicate that the a-axis lattice strain does influence the band gap energy. On the other hand it does not explain the generally high band gap energies observed in the thin films. For the simulations in [Wunderlich04a, Wunderlich04b] it was assumed that the unit cell volume remains constant, i.e. a negative a-axis strain would result in a positive c-axis strain. In the sputtered thin films a decrease in unit cell volume was observed, and it is not known whether this could play a secondary role. No direct link to the dependence of the band

gap could be found. The conclusion is that there is a different reason for the elevated band gap energies observed in the thin films.

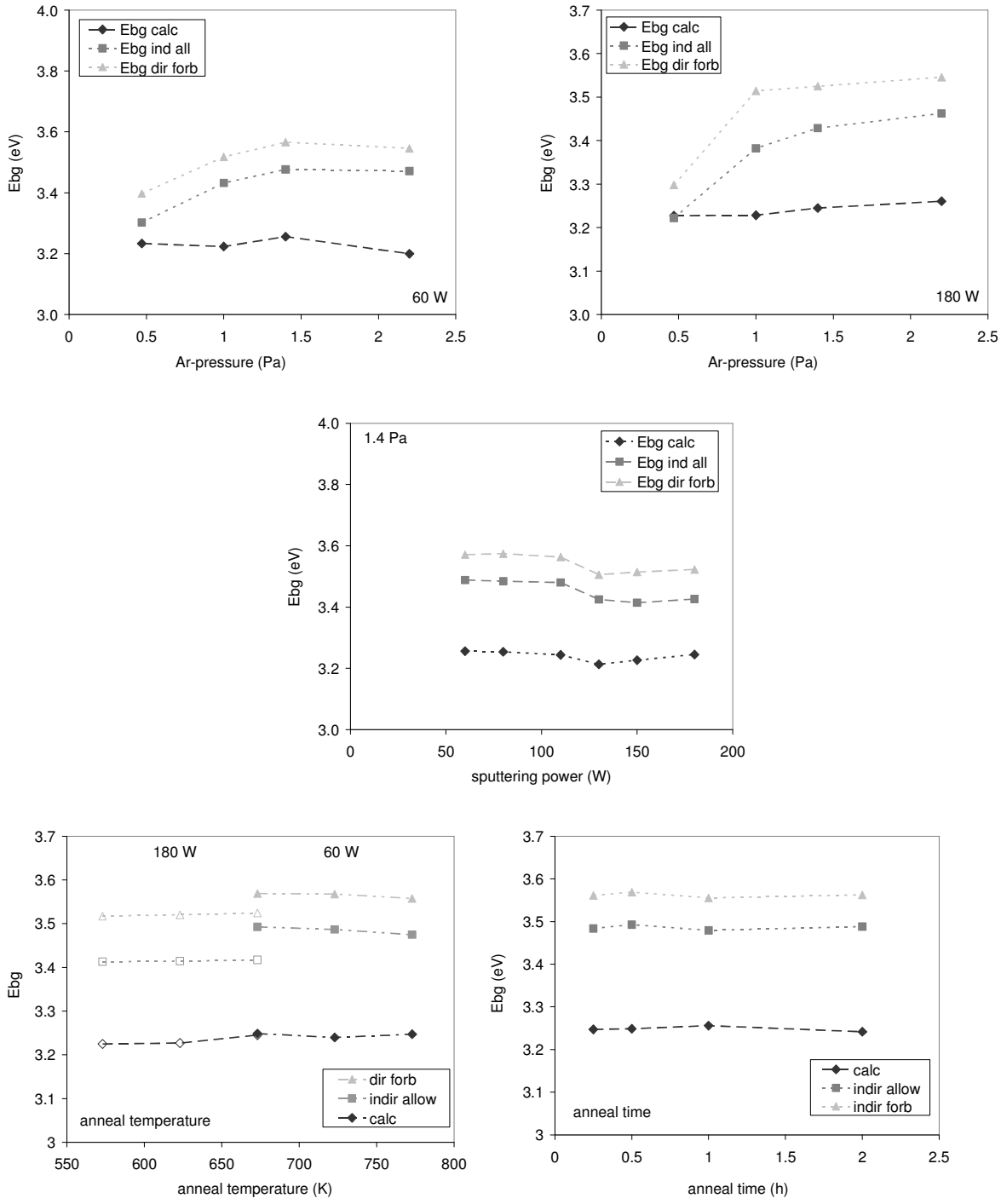

Figure 4. 62:

Calculated band gap energy E_{bg} from the a-axis lattice strain for the thin films deposited at 1.4 Pa, 60 W, annealed at 673 K for 1 h unless specified otherwise:

Top: Ar-pressure for 60 W (left) and 180 W (right), Center: sputtering power.

Bottom: anneal temperature for 60 (0.5 h) and 180 W (1 h) (left), anneal time at 673 K (right).

The next striking observation was the preferred orientation developed after crystallization in the thin films. For the thin films deposited at 0.47 Pa a random orientation was observed, while a preferred (004) out of plane orientation was found to develop and increase with increasing Ar-pressure and decreasing sputtering power, with the sputtering power having only a small influence. The same tendency is found for the band gap, namely an increase with increasing Ar-pressure (up to 1.4 Pa) and slight decrease with increasing sputtering power. Films deposited at 180 W and 0.47 Pa, which are expected to have the most randomized structure show a band gap close to that reported in literature for bulk anatase. These results seem to indicate that the higher band gap is related to an increased (004) orientation in the films. No information could be found on the influence of the crystallographic orientation on the band gap in literature other than a statement in [Pankove71]: “Since the interatomic distance in a crystal is not isotropic but rather varies with the crystallographic direction, one would expect this directional variation to affect the banding states. Thus, although the energy gap which characterizes a semiconductor has the same minimum value in each unit cell, its topography within each unit cell can be extremely complex”. The increase in (004) orientation was also found to be linked to a more negative a- and c-axis strain for the pressure dependence of films deposited at 180 W and the dependence on sputtering power, Figure 4. 42, p. 185 and Figure 4. 43, p. 186, respectively. On the other hand, this is not the case for the pressure dependence of the films deposited at 60 W (Figure 4. 41, p. 183).

There is little influence of the anneal temperature and time on the degree of (004) orientation (Figure 4. 44, Figure 4. 45 and Figure 4. 47 on pages 188 and 191, respectively).The c-axis strain, although it remains unchanged with increasing anneal time for films deposited at 60 W, becomes more negative for films deposited at 180 W, the change in a-axis strain showing the opposite behavior (Figure 4. 46, p. 189). There is little influence of the anneal time on both the a- and c-axis strain (Figure 4. 47, p. 191). When comparing these results with the measured band gap energies one sees that there is a small decrease in band gap energy with anneal temperature for thin films deposited at 60 W, 1.4 Pa, while films deposited at 180 W, 1.4 Pa show a slight increase (Figure 4. 58, p. 206). There is no influence of anneal time on the band gap (Figure 4. 60, p. 208). As a result there is no clear link between preferred orientation, strain and band gap energy.

From this discussion it becomes clear that for the pressure dependence of the thin films deposited at 60 W a deviating behavior is observed. What distinguishes this series from the others is the strong change in porosity. The porosity (calculated from the refractive index,

Figure 4. 52, left, p. 201) and the band gap (Figure 4. 53, p. 202) seem to be correlated for these films. There is less good correlation for the pressure dependence at 180 W and no clear correlation for the pressure dependence at 60 W as well as the dependence on anneal time or temperature for both powers. No information concerning the influence of porosity on the band gap was found in literature, but the results presented here indicate that it may not be neglected.

4.3.6 Photocatalytic activity

As discussed in section 2.5.4 the photocatalytic activity increases strongly with film thickness until a certain saturation value is reached, after which there is a small or no further increase. Tests were performed to find this saturation thickness. It is desirable to work with films thicker than this saturation value to ensure variations in the photocatalytic activity are not caused by (small) variations in the film thickness between samples. The measured dependence of the photocatalytic activity on the film thickness is presented in section 4.3.6.1, together with a comparison to the reference coatings Degussa P25 and Pilkington Active™. In section 4.3.6.2 the dependence of the photocatalytic activity on the film thickness will be discussed. After these preliminary studies the effect of the deposition parameters (4.3.6.3) and annealing conditions (4.3.6.4 and 4.3.6.5) are presented. Also the effect of sodium uptake from the substrate will be discussed briefly (section 4.3.6.6).

4.3.6.1 Effect of film thickness

a. Sputter deposited thin films

As can be seen from Figure 4. 63 the photocatalytic activity increases strongly with film thickness up to about 300-350 nm. For thicker films the dependence becomes small, so that the influence of film thickness can be neglected when the changes remain in an interval of about 50 nm. Tentatively a linear relationship can be proposed for the dependence of the photocatalytic activity on the film thickness, resulting in two different slopes above and below the saturation value. Whether this relationship actually is true will be discussed in the following sections. The observed saturation thickness corresponds rather well with the values discussed in section 2.5.4, were a value of 400 nm was reported by [Nam04].

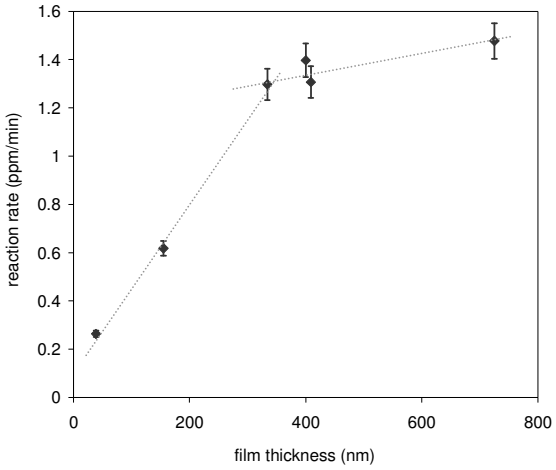

Figure 4. 63:
Dependence of photocatalytic activity on film thickness, as deposited at 60 W and 1.4 Pa.

It was decided to work with a film thickness of 350-400 nm to remain above this saturation level. Deposition of thicker films does not improve the photocatalytic activity much and only requires longer deposition times. This thickness was also above the minimum requirement for optical analysis (section 4.3.4).

In [Tada97] this saturation thickness was attributed to the diffusion length of the charge carriers, but from our side there was some doubt whether the experimental setup used by these authors was able to prove this (see section 2.5.4). The second possibility for the saturation thickness is that at a certain thickness the absorption of UV light has become too low to generate a measurable number of charge carriers. In this latter case an exponential dependence of the film thickness on the photocatalytic activity is expected. This issue will be discussed further in section 4.3.6.2.

b. Reference coating P25

In order to study the dependence of the photocatalytic activity on film thickness for P25 films, four different layer thicknesses were prepared by spin coating the substrate 1 to 4 times with the same suspension. The dependence of the photocatalytic activity of these films on the number of layers applied is shown in Figure 4. 64. Here a linear as well as an exponential fit following the expression for the dependence of the absorption on the film thickness (equation (4.12), p. 218) were applied to the data points. For latter a layer thickness of 100 nm per spin coated layer and an absorption coefficient of $2.0 \cdot 10^4$ cm^{-1} were assumed; these values may not reflect actual values as neither were determined, but they are on the order of the film thickness reported in [Mills03] and the absorption coefficients found in the sputtered thin films (section 4.3.6.2).

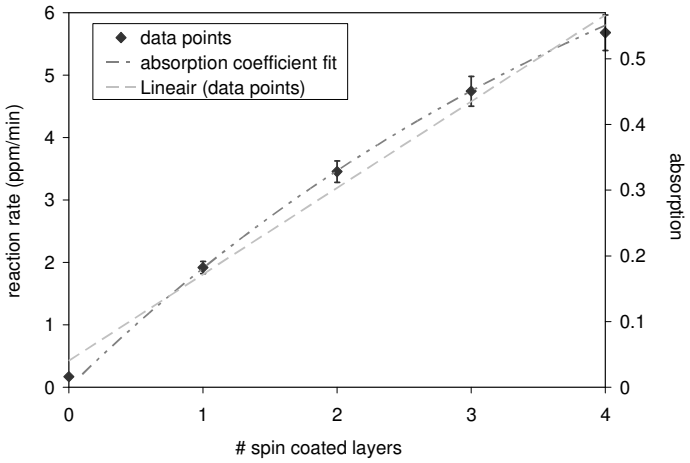

Figure 4. 64:

Dependence of photocatalytic activity on the number of P25 layers spin coated onto a glass substrate. Both a linear fit and one using equation (4.12), p. 218 have been applied.

On first sight Figure 4. 64 shows that for the spin coated P25 layers, the fit following the expression for the optical absorption yields a much better result than the linear fit, as was used for the sputter deposited thin films below 350-400 nm (Figure 4. 63). One has to keep in mind, though, that the thickness of the spin coated layers is not known. It is, therefore, also not known whether the film thickness increases linearly with the number of spin coated layers, even though it is usually assumed that this is the case. One cannot conclude, therefore, whether a linear or an exponential fit is correct.

The structure of the spin coated films (Figure 4. 23, p. 157) is rather different from that of the sputter deposited thin films (section 4.3.1). The spin coated layers consist of a fine grained powder that adheres due to electrostatic forces. The powder is loosely packed, generating a large surface area. Unless there is a crystallographic relationship between two adjacent grains, the grain boundaries represent some kind of barrier to migrating charge carriers. The height of this barrier will depend on the closeness of the contact between the two grain boundaries. With increasing packing density of the grains a polycrystalline material will have more closely connected grain boundaries and will allow conduction of charge carries across them more easily. A loosely packed powder, on the other hand, will most likely not allow migration of the charge carriers between different grains unless they form strong aggregates. This situation we find in the P25 powder, where charge carriers generated in the depth of the material cannot migrate to the surface but must react at the surface of the grain (or agglomerate) they were generated in. Therefore, one can expect that the penetration depth of the UV light is the controlling factor in the spin coated films.

c. Reference coating Pilkington Active™

Coatings of Pilkington Active™ on glass were obtained from Prof. Mills, the author of the study reported in [Mills03]. This reference catalyst is a thin coating (15 nm) of anatase TiO_2 on a SiO_2 buffer layer on glass, deposited by CVD deposition at 615°C (888 K). It is reported to have a good mechanical stability, but due to its low thickness it has a rather low photocatalytic activity. A reaction rate of 0.34 ppm/min was determined for this film in the photocatalytic test reactor developed in this thesis. To compare this material with the sputtered films one needs to extrapolate the results obtained for the standard sputtered thin films (deposited at 1.4 Pa and 60 W, annealed at 673 K), which have a thickness of 400 nm, down to a thickness of 15 nm. This can be done by taking into account the following results:

1) The reaction rate determined for the standard sputtered thin film (400 nm) is about 1.5 ppm/min

2) The reaction rate of a standard sputtered film decreases with thickness according to the linear equation of $y = 0.0035\ x + 0.1051$, with x the film thickness in nm and y the reaction rate in ppm/min (from Figure 4. 63).

3) The reaction rate determined for the standard sputtered thin films, annealed at 673 K is about 3.5 ppm/ min (Figure 4. 70, p. 225), so that the ratio in photocatalytic activity between annealed and as deposited films is about 3.5/ 1.5.

From statement 1) and 2) one can estimate the photocatalytic activity of an as deposited thin film of 15 nm thickness, namely 0.16 ppm/min. From point 3) one can estimate the photocatalytic activity if this film were annealed. As a result one obtains a photocatalytic activity of 0.37 ppm/min as an estimate for a thin film deposited using the standard sputtering conditions, annealed at 673 K and having a thickness of 15 nm. This value is quite comparable to the photocatalytic activity measured for the Pilkington Active™ coating.

If one looks at the SEM image reported for this coating in [Mills03], shown in Figure 4. 65, one can see that its microstructure is quite similar to the sputtered thin films discussed in this thesis (section 4.3.1).

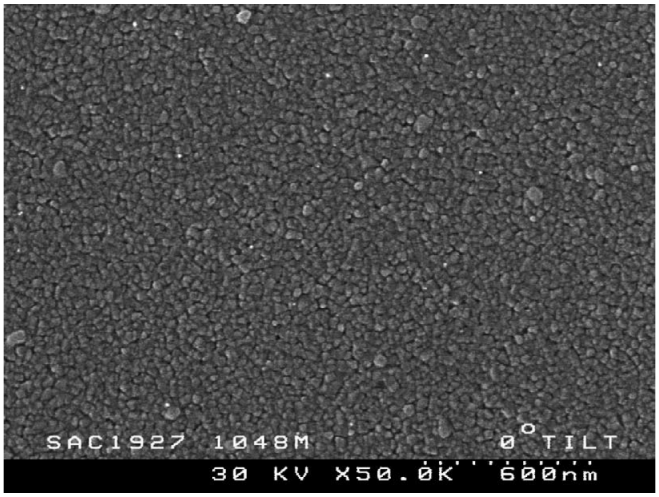

Figure 4. 65:
SEM image of Pilkington Active™ anatase TiO_2 coating on glass (from [Mills03]).

In [Mills03] nothing was reported about the optical properties of these thin films.

4.3.6.2 Discussion of the thickness dependence of the photocatalytic activity in the sputtered thin films

In order to determine whether the diffusion of the charge carriers or the UV absorption were the limiting factors for increasing the photocatalytic activity with film thickness two different methods were used. The first was to see whether the optical film absorption could be matched to the trend of the photocatalytic activity. The second was to use UV cut-off filters and determine whether there was a different photocatalytic activity for different UV light wavelengths. First the two methods and the obtained results will be described, followed by a discussion.

a. Relationship of photocatalytic activity and optical absorption with film thickness

As discussed in section 3.1.2.1 and repeated in Figure 4. 66 the wavelengths of the UV-lamp active for photocatalysis are the ones between 300 and 387 nm (equivalent to the cut-off of the water filter and the band gap of 3.2 eV for anatase, respectively).

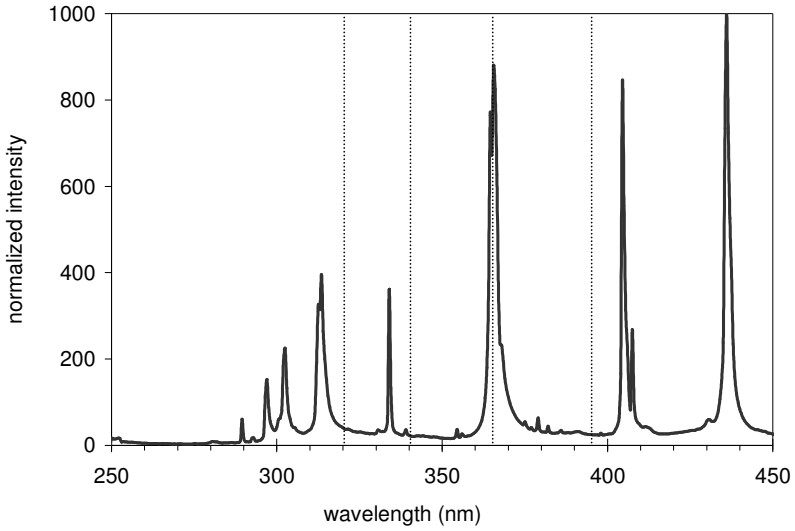

Figure 4. 66:
Emission spectrum of the mercury high pressure short arc lamp used for the photocatalysis experiments, after passing through the IR filter and the chamber window.

There are several emission peaks below 320 nm and a strong one at 365 nm, for former the absorption of UV light can be estimated using the absorption coefficient α of the TiO_2 thin films at 320 nm as a lower limit (Figure 4. 49, p. 198). The dependence of the optical absorption *A* on the film thickness *d* is then calculated using the relation:

$$A = 1 - e^{-\alpha d} \qquad (4.12)$$

For the wavelength of 320 nm an average absorption coefficient of $1.08 \cdot 10^5$ cm^{-1} could be determined from the films with a thickness of 139 nm and higher from the absorption data presented in Figure 4. 49, p. 198.

The absorption coefficient at 365 nm could not be determined from the absorption data because at this wavelength the interference fringes have too large an influence. Therefore, the absorption coefficient was determined from the extinction coefficient *k* using the relation:

$$\alpha = 4 \pi k / \lambda \qquad (4.13)$$

with *k* obtained from fitting the optical transmission around the absorption edge using a linear oscillator relationship [Poelman03]. A value of $9.296 \cdot 10^3$ cm^{-1} was determined for α.

The resulting dependencies of the absorption on the film thickness are shown in Figure 4. 67. Here also the results from the photocatalysis measurements have been included (diamonds), together with a fit following equation (4.12), p. 218 using an absorption coeffi-

cient of $\alpha = 4.6 \cdot 10^{-4}$ cm^{-1} (pale grey dotted curve). This absorption coefficient corresponds to a wavelength of ca. 335 nm (Figure 4. 49, p. 198) in the TiO_2 thin films.

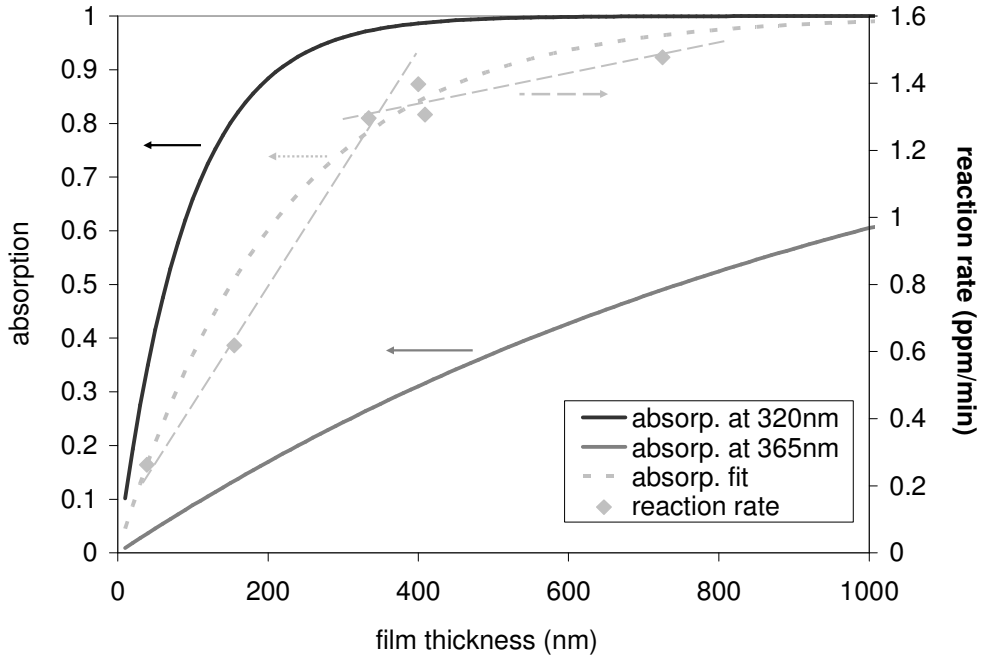

Figure 4. 67:

Dependence of optical absorption on film thickness for TiO_2 thin films deposited at 1.4 Pa, 60 W using the absorption coefficient for 320 and 365 nm, obtained from data shown in Figure 4. 49, p. 198. The pale grey dashed line is a tentative fit to the photocatalytic data by using an adsorption coefficient of $4.6 \cdot 10^4$ cm^{-1} in equation (4.12), p. 218.

Using the absorption coefficient determined at 365 nm the optical absorption approaches unity only at a film thickness of 10 000 nm, i.e. 10 µm (not shown). Additionally, for a film thickness of 400 nm the optical absorption is only about 31%, which means that the film is still rather transparent. Absorption at this wavelength cannot explain the dependence of the photocatalytic activity on the film thickness.

Using the absorption coefficient at 320 nm the optical absorption saturates at about 400 nm, but the increase in absorption at low thickness is too strong so that the photocatalytic data are not well reproduced.

It was also tried to fit the photocatalytic data with an expression derived from equation (4.12), p. 218. This function also results in a satisfying fit to the data, compared to using two straight lines. From the results alone it cannot be concluded whether the limited charge carrier diffusion of the optical absorption is causing the saturation behavior. An important point is why no complete saturation is observed, but that the photocatalytic activity continues

to increase slowly with film thickness. This can be explained by the microstructure of the material. Not only the top surface but also, to some extent, the sides of the column-grains can be surfaces active for photocatalysis, which will be discussed in more detail in section 4.3.7.3. Since the porosity between the column-grains extends more or less completely over their length and the column width is around 50 nm, an electron/ hole pair created there can easily reach an active surface. This means that in any case the absorption of the light is the determining factor. In order to determine the escape depth/ diffusion length of the charge carriers by measuring the photocatalytic activity it will be necessary to use a very dense structure to ensure that only the top surface is active. Unfortunately such a film has a very low photocatalytic activity as will be shown in section 4.3.6.3. When determining the escape depth one will also have to account for absorption losses of light with increasing depth and the statistical distribution of the charge carrier lifetime.

b. Dependence of the photocatalytic activity on the UV light wavelength

In order to further examine the dependence of the photocatalytic activity on the optical absorption, light of different wavelength ranges was admitted to the chamber. As discussed in section 3.1.2.1 the spectrum of the lamp could be changed by using UV-VIS cut-off filters. For three different films the photocatalytic activity was tested without, with a 345 nm and with a 395 nm filter inserted between the water filter and the chamber window. The tested films were a 400 nm and a 1000 nm thick film deposited at 1.4 Pa, 60 W and annealed at 673 K/ 1 h, and a spin coated layer of Degussa P25 (2 layers, Figure 4. 64, p. 215, denoted P25-2x). For the thicker sputter deposited film, no measurement using the 395 nm filter was performed.

The relative photocatalytic activity was determined in % by referring the absolute activity to the value obtained without cut-off filter. The activity per % absorbed photons was calculated taking into account the percentage of incoming photons absorbed in the film. All results are summarized in Table 4. 5. The black measurement obtained with P25 (section 4.1.3.4) is included for comparison purposes.

		sputtered film 400 nm				sputtered film 1000 nm				P25-2x	
cut-off filter	**entering photons > 3.2 eV**	**photons absorbed > 3.2 eV**	**abs re-action rate**	**rel. re-action rate**	**activity per % absorbed**	**photons absorbed > 3.2 eV**	**abs re-action rate**	**rel. re-action rate**	**activity per % absorbed**	**abs re-action rate**	**rel. re-action rate**
	(%)	(%)	(ppm/ min)	(%)	(ppm/ min/%)	(%)	(ppm/ min)	(%)	(ppm/ min/%)	(ppm/ min)	(%)
none	100	58.0	3.67	100	0.0632	78.9	6.06	100	0.074	3.34	100
345 nm	41.0	13.0	1.08	29.4	0.0831	25.0	2.51	41.4	0.119	1.44	43.1
395 nm	1.40	N.A.	(0.139)	3.78	N.A	N.A.	-	-	-	(0.107)	(3.21)
no lamp	0	N.A.	-	-	N.A.	N.A.	N.A.	N.A.	N.A.	0.174	(5.21)

Table 4. 5:

Dependence of the reaction rate on the cut-off filter used. Thin films deposited at 1.4 Pa, 60 W, annealed 673 K/ 1 h, thickness 400 and 1000 nm, Degussa P25 layer with 2 depositions. Photocatalytic activities in brackets are below the black level.

Using the cut-off filter of 345 nm reduces the reaction rate to ca. 30, 41 and 43% of the unfiltered value for the sputter deposited films of 400 and 1000 nm and the P25 thin film, respectively. The number of photons having an energy above 3.2 eV was calculated to be reduced to ca. 41% of the unfiltered value.

We can understand the higher relative activity of the film of 1000 nm thickness when taking into account the microstructure of the thin films. Lower wavelength light (320 nm) will be completely absorbed at a thickness of 400 nm, so that one expects little difference in the effectiveness of light of this wavelength. On the other hand, light of 335 nm (365 nm) will be absorbed for 84% (31%) at a depth of 400 nm and 99% (61%) at a depth of 1000 nm, respectively. As a result, more light of higher wavelengths is absorbed in the thicker film. Table 4. 5 shows that the activity per absorbed photon does not decrease with increasing film thickness, but rather shows a small increase. Together with the fact, that long wavelength light creates electron/ hole pairs deeper in the film, this shows that these electrons are (to some extent) available for photocatalysis. The conclusion is, that there is no limiting film depth for charge carrier diffusion. There are two possible reasons for this, namely (i) the charge carrier diffusion length is larger than the film thickness, or (ii) the column sides are available surfaces for photocatalysis so that the charge carriers do not need to diffuse to the top surface of the film. It was already discussed in part *a* of this section that the latter case is most likely the reason why the absorption of light with increasing film depth is the reason for the dependence of the photocatalytic activity on the film thickness. The issue of the activity of the side walls of the column-grains will be discussed in more detail in section 4.3.7.3, where it will be shown, that indeed these surfaces are available for photocatalysis.

When the 395 nm cut-off filter is used, both thin films no longer show any photocatalytic activity. This is not surprising since the number of photons having an energy of > 3.2 eV is reduced to less than 1% with this filter. Obviously the small amount of photons with an energy > 3.0 eV is not sufficient to activate the Degussa P25 film or the rutile in the powder is not photocatalytically active.

c. Concluding remarks

From determining the thickness dependence of the photocatalytic activity it was not possible to solve the issue on whether UV-absorption or charge carrier transport is the factor determining the thickness dependence of the photocatalytic activity. On the other hand, the experiments using light of different wavelengths showed that higher wavelength light, which is absorbed deeper in the film, shows a higher photocatalytic activity. This result shows that the

absorption of light is the determining factor, not the charge carrier diffusion length. The reason is most likely, that the columnar and porous film microstructure enable the photocatalytic breakdown reaction to take place at the column sides deeper inside the material. In order to determine the charge carrier diffusion length a dense film will have to be used. As will be discussed in the next section such a thin film has a very low photocatalytic activity, so that the cut-off experiments as performed here will not be useful.

4.3.6.3 Dependence on the sputter conditions

a. Ar-pressure

The photocatalytic activity was found to be strongly dependent on the Ar-pressure during deposition, as shown in Figure 4. 68. The films deposited at 0.47 Pa show a very low to no activity, namely 0.31 and 0.07 ppm/ min for films deposited at 60 and 180 W, respectively, compared to the blanco value of 0.17 ppm/ min (section 4.1.3.4). For films deposited at 60 W the photocatalytic activity increases strongly with increasing Ar-pressure, but levels out at 1.4 Pa. For thin films deposited at 180 W a linear increase with increasing pressure is observed.

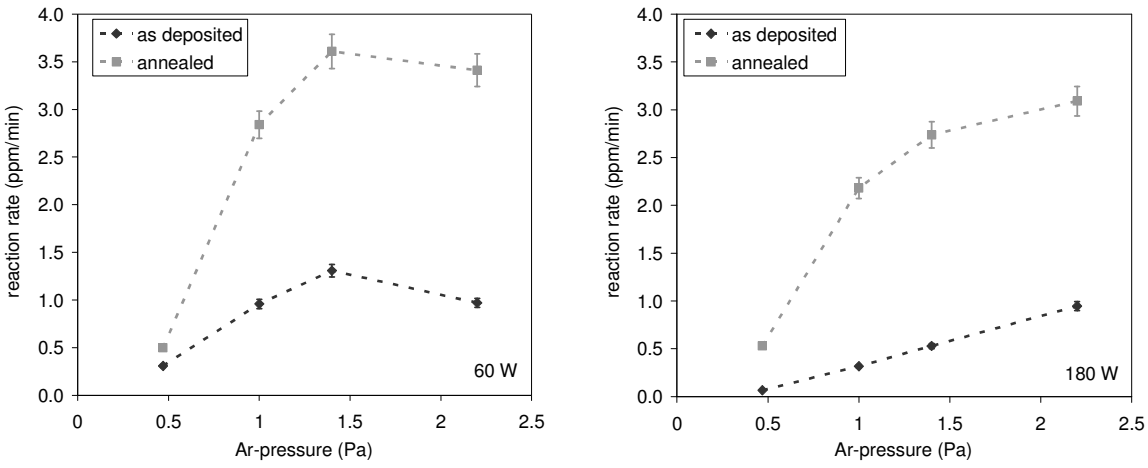

Figure 4. 68:
Photocatalytic activity of as deposited and annealed (673 K/ 1 h) thin films deposited at 60 W (left) and 180 W (right) at different Ar-pressures. The annealed films were crystalline anatase.

All films show a strong increase in photocatalytic activity with crystallization. For films deposited at 60 W and 1.4 Pa the reaction rate of the ethanol breakdown increases from 1.4 to 3.6 ppm/ min, which is more than 2.5 times higher. For the films deposited at 60 W crystallization does not change the pressure dependence of the photocatalytic activity. On the other

hand, the films deposited at 180 W show, after annealing, a deviation of the linear dependence on the Ar-pressure.

b. Sputtering power

Figure 4. 69 shows the dependence of the photocatalytic activity on the applied d.c. power. Interestingly, there is a linear decrease in photocatalytic activity with increasing sputtering power for the as deposited films. For the annealed films the power dependence is less clear, but a linear fit similar to the one for the as deposited films is possible. The slope of the two curves is rather similar so that they are almost parallel. This means that the effect of applied d.c. power on the photocatalytic activity is not influenced by the anneal treatment, but an offset is created due to crystallization.

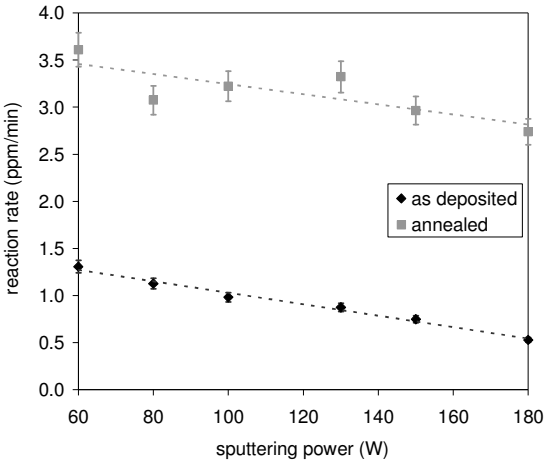

Figure 4. 69:
Dependence of the photocatalytic activity of the as deposited and annealed (673 K/ 1 h) thin films on the sputtering power. The Ar-pressure was 1.4 Pa.

For the as deposited films the activity at 180 W is less than half of that of films deposited at 60 W. For the annealed films the reaction rate for the ethanol breakdown drops from 3.6 to 2.8 ppm/min. Since the highest photocatalytic activity is observed for thin films deposited at 60 W it was opted to continue working at this sputtering power.

4.3.6.4 Effect of anneal temperature

For the thin films deposited at 60 W there is a very sharp transition from low to high photocatalytic activity at the crystallization temperature of 673 K (Figure 4. 70). All films annealed below this temperature have a photocatalytic activity in the range of the as deposited film, while all films annealed above this temperature have the same activity as the film an-

nealed at 673 K. The conclusion is that annealing does not influence the photocatalytic activity of these films as long as no change in phase occurs.

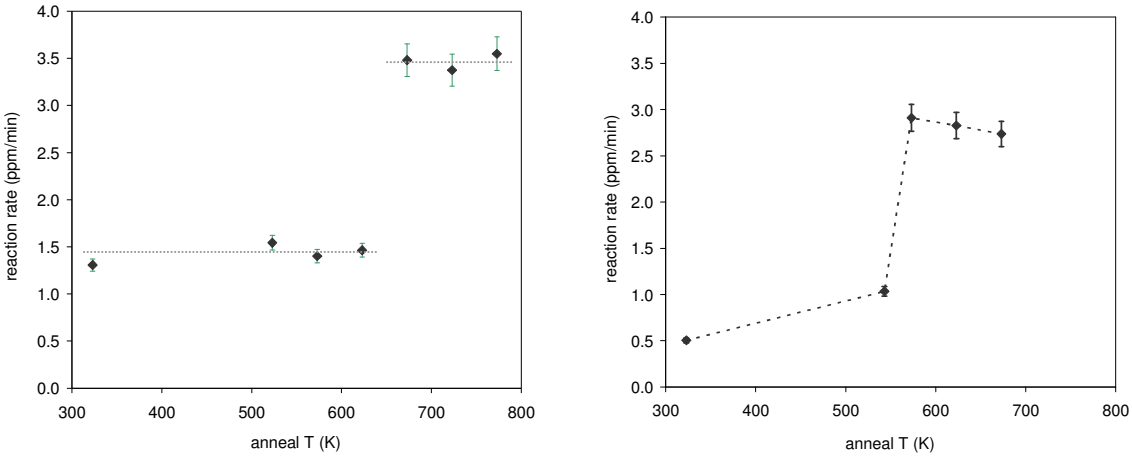

Figure 4. 70:
Dependence of the photocatalytic activity on the anneal temperature for thin films deposited at 60 W, annealed for 0.5 h (left) and 180 W, annealed for 1 h (right). The Ar-pressure was 1.4 Pa.

The films deposited at 180 W show the same basic behavior, but the transition is less abrupt. Here the photocatalytic activity increases with anneal temperature for the film annealed below the crystallization temperature of 573 K. At crystallization there is a strong increase in photocatalytic activity (by about a factor of 3). For increasing anneal temperature above the point of crystallization the photocatalytic activity decreases slightly but taking into account the error bars, it is also possible to fit a horizontal line indicating that there is no effect of the anneal temperature on the photocatalytic activity.

4.3.6.5 Effect of anneal time

When looking at the effect of anneal time on the photocatalytic activity one can see that all films show the high activity observed for crystalline films (Figure 4. 71).

This is not surprising since all films showed a well defined crystallinity (section 4.3.3.3). It seems, though, that the photocatalytic activity is the highest for the film annealed at 1 h and the lowest for the film annealed for 0.25 h, but taking into account the error bars it is also possible to fit a horizontal line for anneal times from 0.5 h on, indicating no further change.

The discussion of the photocatalytic activity in view of the optical and structural properties of the thin films will follow in section 4.3.7.

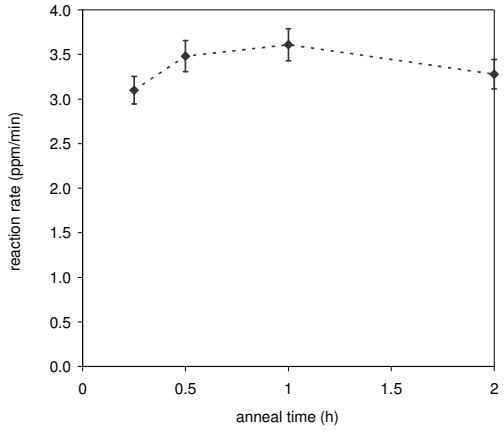

Figure 4. 71:
Effect of anneal time on the photocatalytic activity for thin films deposited at 1.4 Pa and 60 W, annealed at 673 K.

4.3.6.6 Effect of Na^+

For the as deposited samples the type of glass substrate used did not influence the photocatalytic activity. Even though a negative influence was reported in literature, some initial tests for heat treatments were performed on soda-lime glass. The results for the photocatalytic activity, shown in Figure 4. 72, confirmed the findings discussed in section 2.6.6, namely that using soda-lime glass as substrate had a detrimental effect on the annealed films.

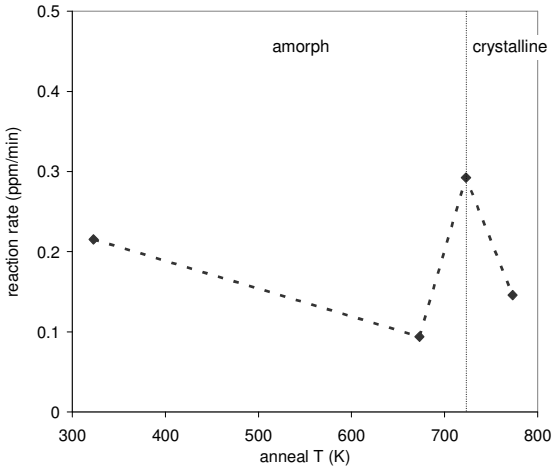

Figure 4. 72:
Effect of using a soda-lime substrate on the photocatalytic activity of TiO_2 thin films annealed at different temperatures for 0.5 h, deposited at 1.4 Pa and 180 W.

Note that the photocatalytic activity of the films shown in Figure 4. 72 appears lower compared to the other measurements, because it was measured with a decreased illumination intensity (the water in the IR-filter had become cloudy due to corrosion). This was noticed

only after the experiments were performed. Even though the absolute values do not compare the general trends are valid.

The photocatalytic activity decreases with increasing temperature as long as no change in phase occurs. At the crystallization temperature of 723 K (section 4.3.3.4) the photocatalytic activity increases by a factor of about 2, which is lower than observed in thin films annealed on sodium free glass (section 4.3.6.4). When annealing at the higher temperature of 773 K the photocatalytic activity decreases again. This behavior is easily explained by increasing Na^+ diffusion into the thin films with increasing anneal temperature.

It was, therefore, concluded that standard microscope glass (soda-lime) could be used for samples that were analyzed as deposited, while sodium free glass was needed for samples that were annealed.

4.3.7 Relationship between the photocatalytic activity and the structural and optical properties of the TiO_2 thin films

4.3.7.1 Structural properties – as deposited thin films

The as deposited, XRD amorphous, TiO_2 thin films showed quite some photocatalytic activity. According to literature (section 2.5.1.2), this should not be the case for amorphous TiO_2. The photocatalytic activity of these films was found to be strongly affected by the Ar-pressure during sputtering, with the films deposited at the lowest Ar-pressure (0.47 Pa) showing almost no photocatalytic activity and the maximum observed at 1.4 to 2.2 Pa. The photocatalytic activity decreased with increasing sputtering power, so that the most active film was the one deposited at 60 W and 1.4 Pa. The most obvious link between the deposition conditions and the photocatalytic activity of the as deposited thin films is their density/ porosity. The same conditions increasing the photocatalytic activity decrease/ increase the density/ porosity of the thin films (sections 4.3.1 and 4.3.4). In conclusion, for amorphous thin films the structural changes caused by the Ar-pressure and the sputtering power determine the photocatalytic activity by influencing the porosity of the structure. This shows that there is a strong micro-structural component determining the photocatalytic activity of TiO_2 thin films. This issue will be discussed in more detail in section 4.3.7.3.

4.3.7.2 Structural properties – annealed thin films

A first important result is the effect of thin film crystallization. The statement that anatase has a higher photocatalytic activity than ‘amorphous’ TiO_2 is confirmed. But the sample den-

sity, as determined by the microstructure, remains a very strong influence. Even though crystallization increases the photocatalytic activity substantially, a *crystalline* thin film deposited at 0.47 Pa shows a lower photocatalytic activity (0.5 ppm/ min) than an *XRD amorphous as deposited* thin film at 1.4 Pa (1.4 ppm/ min). The effect of density will be discussed in more detail in section 4.3.7.3.

With the annealed films the question arises, whether the preferred crystallographic orientation plays a role. The films with the lowest photocatalytic activity (lowest Ar-pressure) show no preferential orientation while the films with the highest photocatalytic activity show a (004) preferential orientation. The degree of orientation was found to increase with increasing Ar-pressure and decreasing sputtering power, the same trend that is followed by the photocatalytic activity, but also by the film density (porosity). To separate the two effects it would be necessary to split the evolution of the film density from the development of the (004) preferred orientation – if this was possible.

Another factor to look into is the crystallite size. But when comparing the dependence of the estimated crystallite sizes on the Ar-pressure with the observed dependence of the photocatalytic activity there is no clear correlation. The films deposited at 0.47 Pa have a larger crystallite size, but for the other three pressures it remains more or less constant around 50 nm. These numbers are not affected significantly by the sputtering power.

The dependence of the photocatalytic activity on the anneal time is small and runs contrary to the dependence of the film porosity: while the photocatalytic activity shows a maximum at 1 h, the porosity shows a minimum. Probably one should interpret this in the sense that for both factors the variation lies within the experimental error.

The results obtained for the dependence of the photocatalytic activity on the annealing temperature for films deposited at 60 W and 180 W showed small differences. While at 60 W there was no change other than the transition between XRD amorphous and crystalline anatase phase, the thin films deposited at 180 W showed possibly an influence of the anneal temperature. The increase in photocatalytic activity observed for the film annealed below the crystallization temperature could be due to an increase in crystallinity which is not yet detectable by XRD. The decrease in photocatalytic activity observed for temperatures above the crystallization temperature is less clear. The only property related to the decrease in photocatalytic activity is the observed decrease in the crystallite size for the films deposited at 180 W (Figure 4. 46, right, p. 189), which is not observed for the films deposited at 60 W.

The role of the crystallite size is less clear, but it has been reported that for decreasing crystallite size below 35 nm the photocatalytic activity of TiO_2 thin films decreases [Jung02].

In conclusion, also for the annealed thin films the microstructure has the strongest influence on the photocatalytic activity, which increases with increasing film porosity. Preferential out of plane orientation or crystallite size play a subordinate role, if any.

4.3.7.3 Film density/ porosity

In catalysis the available surface area is important for the catalytic activity of a given volume of catalyst. In dense thin films the geometrical surface area is taken to be the available one. Since the most active sputtered TiO_2 thin films discussed in this thesis show a rather high porosity, as calculated from the refractive index (section 4.3.4), and as it was found that this factor had the most significant influence on their photocatalytic activity, it is interesting to look at this issue in more detail. The increase in surface area, if the columns were completely separated from each other, was estimated to be roughly a factor of 30 (section 4.3.1.1). For this surface area to be available, there has to be sufficient spacing between the column-grains to allow reactants and reaction products to enter and exit the inter-column space. The distance between the columns can be estimated in a simple manner, depicted in Figure 4. 73. Here it is assumed that the column grains themselves are 100% dense. Here we describe the columns as square based cuboids, which is more suitable to calculate the inter-grain porosity in the films.

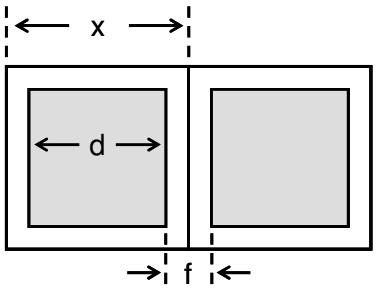

Figure 4. 73:
Calculation of the free space between the column-grains which are taken as cuboids defined by the side length *d* of their square base. *x* is the outer length of the square based tube of empty space, *f* is the spacing between two adjacent grains.

We take the column-grain as a square based cuboid with base length d and height h, and the porosity as a rectangular tube surrounding this cylinder having outer diameter of x. The volume of the outer cuboid described by the diameter x is $x^2 h$ and the volume of the grain is $d^2 h$. The volume of the free space is equal to (i) the subtraction of the inner from the outer

cuboid and (ii) the product of porosity *P* times the outer cuboid (here the porosity may not be taken in % but as a fraction of 1):

$$x^2 h - d^2 h = P \cdot x^2 h \qquad (4.14)$$

which simplifies to:

$$x^2 - d^2 = P \cdot x^2 \qquad (4.14)a$$

and after resolving for *x*:

$$x = \frac{d}{\sqrt{(1-P)}} \qquad (4.14)b$$

And with $f = x - d$ one receives:

$$f = d\left(\frac{1}{\sqrt{(1-P)}} - 1\right) \qquad (4.15)$$

The calculated spacing *f* between two column grains for a given porosity *P* is listed in Table 4. 6.

Porosity *P* (%)	1.0	2.5	5.0	7.5	10.0	12.5	15.0	17.5	20.0	22.5	25.0
Inter-grain spacing *f* (nm)	0.25	0.64	1.3	2.0	2.7	3.5	4.2	5.1	5.9	6.8	7.74

Table 4. 6:
Calculation of the inter-grain spacing *f* from the porosity according to Figure 4. 73.

The spacing between the column-grains listed in Table 4. 6 are only an estimate, but they give an idea of the pore size that can be formed between the column grains. Note that the above values were calculated taking the column-grains as 100% dense. Since this is most likely not the case, especially for the as deposited films, the true inter-column spacing will be smaller.

According to the UPAC definition one distinguishes the following different pore sizes according to their diameter *d* [wikipedia2]:

macropores: $d > 50$ nm

mesopores: $2 \leq d \leq 50$ nm

micropores: $d < 2$ nm

From Table 4. 6 one can see that from a porosity of about 7.5% on the TiO_2 thin films are mesoporous. In order for the surface of a pore to be catalytically active its size needs to be

large enough to allow for transport of the reactants and products. The molecules involved in the breakdown reaction of ethanol are all rather small, with ethanol being the largest. Mesopores are known to increase the active surface area of a catalyst, while micropores are usually too small. The active pore size depends on several factors, including the diffusion coefficient of the reactants into and products out of the pores, their concentration in the atmosphere surrounding the catalyst and the flow rate of the air stream passing over the catalyst bed. Latter does not play a role in a batch reactor where no forced flow is present.

The dependence of the photocatalytic activity on the Ar-pressure during deposition was linked to the film porosity (section 4.3.6.3), showing a strong increase with increasing Ar-pressure. For the thin films deposited at 60 W the photocatalytic activity increased by about a factor of 4 (7) for as deposited (annealed), when increasing the Ar-pressure from 0.47 to 1.4 Pa. While upon annealing the porosity remained constant (ca. 22%) for the films deposited at 1.4 Pa, it decreased from about 5 to 2% for the films deposited at 0.47 Pa. This should explain the lower effect of crystallization for the thin films deposited at the lowest Ar-pressure. The influence of the pressure also becomes clear from the inter-column spacing (which we take as estimate for the pore size) on the thin film porosity (Table 4. 6). For a porosity of 7.5% we reach the limit of the mesopore range (2.0 nm), i.e. the pore size in these films is rather low, so that it becomes less likely for the reaction to take place inside the pores. With increasing porosity we reach a pore size of 6.8 nm for 22% and 7.7 nm for 25% porosity. Both pore sizes should be large enough for the breakdown reaction of ethanol to take place inside them, so that the two films do not show a strong difference in photocatalytic activity, which was indeed observed (Figure 4. 68, p. 223). The experiments discussed in 4.3.6.2 showed that light of higher wavelengths, which enters deeper into the thin film, is more active for the thicker film. This could be explained when assuming that the reaction could take place at the side walls of the column grains, i.e. in the inter-grain pores, confirming the hypothesis that the inter-grain pores are accessible during the photocatalytic breakdown reaction.

One has to remember, that annealing changed the microstructure, introducing cracking and column densification, without changing the calculated porosity. Possibly there is a further increase in inter-column spacing increasing the pore size and, therefore, the photocatalytic activity, although, as discussed earlier, most likely a saturation point has already been reached for the as deposited films.

4.3.7.4 Optical properties

In all studies the importance of the band gap on the photocatalytic activity is stressed, especially the increase of the band gap due to the quantum size effect is often claimed to be beneficial. In this study the increase in band gap energy with Ar-pressure seemed to follow the increase in photocatalytic activity. In contrast to this, the dependence of the band gap energy on the anneal temperature (Figure 4. 58, p. 206) could not be correlated with the photocatalytic activity. There also seemed to be an influence of the orientation on the band gap energy, and the effect of porosity was also not clear (section 4.3.5). For all films a band gap higher than the literature value for anatase was found. The lowest band gap was observed for the least active films, i.e. deposited at the lowest Ar-pressure. In conclusion, the results in this study show that there is no clear correlation between the band gap of the thin films and their photocatalytic activity. With the light source used one would not expect the measured band gaps of the thin films to have a significant effect on the absorption of the incoming light as they lie at wavelengths higher than the peak at 365 nm (assuming the *indirect allowed* band gap transition). No indication of the quantum size effect could be found.

4.3.7.5 Effect of sodium diffusion from the substrate

The question why the uptake of sodium from the substrate was detrimental to the photocatalytic activity was discussed in section 2.6.6. The reasons reported there ranged from the effect of Na^+ on the electronic states in TiO_2 to crystallographic changes. In Figure 4. 48, p. 192, one can see that the presence of Na^+ leads to a strong decrease in the degree of crystallization while the crystallization temperature was increased substantially (from 573 to 723 K). It is not surprising that the lower degree of crystallization results in a lower photocatalytic activity. The grain size was found to be decreased slightly by the presence of Na in the substrate. This contradicts the findings of [Nam04] where an increase in crystallite size was reported. Since the presence of Na was found to deteriorate the photocatalytic activity even when no structural or optical changes were found (i.e. in the heat treated, amorphous films annealed at 673 K), it must be concluded that the presence of Na in itself must be causing some changes to the material which are deteriorating its photocatalytic activity. In sections 4.4.8 and 4.4.9 the general changes due to doping are discussed.

4.3.8 Discussion of the influence of the deposition parameters on the properties of the sputter deposited TiO_2 thin films

One goal of this study was to determine the influence of the deposition parameters on the photocatalytic activity of sputter deposited TiO_2 thin films and relate the results back to the optical and microstructural properties. The conclusion of the study was that the strongest effect on the photocatalytic activity was the thin film porosity: with increasing porosity the photocatalytic activity increased strongly. The band gap and crystal size were also influenced by the deposition parameters, but to a much less extent and their influence on the photocatalytic activity was much less clear, so that one can conclude that they play a subordinate role, if any.

A very important result of the study was that the amorphous, as deposited films showed a noticeable photocatalytic activity if sputter deposited under the right conditions (i.e. yielding a high porosity). When comparing thin films with low and with high porosity it was found that an annealed film with low sample porosity had a much lower photocatalytic activity than an as deposited film having a high porosity. This is not surprising, as it is known that for a catalyst the active surface area is of strong importance.

Another important result was the confirmation of the importance of the film thickness. For thin films up to a thickness of 350-400 nm a steep increase in photocatalytic activity was observed, which became shallow for thicker films. Two possible reasons were proposed, namely (i) the limited diffusion length of the charge carriers and (ii) the increased absorption of the incoming light with increasing film thickness. Since the porous film structure could allow the photocatalytic reaction to take place at the column sides, the charge carriers need not diffuse to the film surface. This means that the film thickness only plays a role as to determine the amount of light (by absorption) that can reach the bottom of the film. As a result it is not possible to determine which mechanism is active.

Besides the main goal followed in this study some very interesting results were obtained on the side:

- A seemingly amorphous film can show a preferential out-of plane crystallization upon post-deposition heat treatment, with the degree of orientation depending on the deposition conditions but not on the anneal treatment conditions. It was proposed, that small nuclei are formed in the film which show a preferential orientation but are too small to be de-

tected in the XRD. These nuclei then grow during the crystallization process, yielding measurable crystallites.

- Almost all thin films showed a negative lattice strain in a- and c-direction, i.e. a decrease of the unit cell. Since in literature a shrinkage of the a-axis was found to increase the band gap energy, this change was calculated from the measured a-axis lattice strain. The resulting increase of the band gap energy was found to be too small to explain the high band gap energy observed for most of the thin films. The calculations did not reproduce the dependence of the band gap energy on the Ar-pressure, but seemed to reproduce a 'kink' observed in the dependence of the band gap on the sputtering power. As a result the high band gap energy observed in the thin films could not be explained.
- The band gap energy increased rather than decreased upon crystallization of the thin films. According to the quantum size effect a material with a very small crystallite size should show an increased band gap. As already discussed, it is suspected that in the as deposited thin films (very) small nuclei are present, which should show the quantum size effect due to their small size. In the crystalline films crystallite sizes around 40-50 nm are detected, which should no longer show any quantum size effect, i.e. the band gap should be the same as for bulk anatase. In general, the quantum size effect does not seem to be applicable to TiO_2 thin films because the requirement of insulated particles, as is the case for a colloidal suspension of TiO_2 particles, is not fulfilled.

4.4 Effect of doping on the TiO_2 thin film properties

In the previous section (4.3) the optimum photocatalytic activity was observed for thin films deposited at 1.4 Pa and 60 W, so that these were chosen as the standard sputtering conditions for investigating the effect of doping. It was chosen to use the lowest crystallization temperature of 673 K and a time of 1 h for annealing the doped films.

As discussed in chapter 3 the dopants were added by two methods, (i) d.c. magnetron sputtering from mixed oxide targets and (ii) ion implantation. The dopant concentration differed between the two techniques, being low for ion implantation and high for mixed oxide sputtering, with an overlap at 1 at% (equivalent to 1 wt% Fe_2O_3 and 2.3 wt% Nd_2O_3). When comparing the results between the two techniques one has to keep the different range of concentrations in mind. The concentrations given for the mixed oxide sputtered films refer to the oxide concentration in the target while the concentrations given for the ion implanted samples refer to the concentration implanted into the topmost 40 nm (section 3.2.3).

The doped TiO_2 thin films were studied with the same techniques as the pure TiO_2 thin films. First the morphology was investigated by SEM (section 4.4.1), the stoichiometry (section 4.4.2) and dopant distribution (section 4.4.3) were checked, and crystallization behavior examined (section 4.4.4). In section 4.4.5 the photoluminescence of Nd doped thin films is discussed. The optical and photocatalytic properties of the thin films will be described in sections 4.4.6 and 4.4.7. In the end the results obtained for the doped TiO_2 thin films are summarized (section 4.4.8).

In sections 4.4.1 to 4.4.4 first the doping by mixed oxide target sputtering is discussed, differentiating between the dopants; the same follows then for ion implantation. In sections 4.4.6 and 4.4.7 both doping methods will be treated together. The effect of annealing will not be treated as a separate section but discussed together with the as deposited samples.

4.4.1 Morphology

4.4.1.1 Effect of dopant introduction by mixed oxide target sputtering

a. Fe-addition

SEM cross sections (Figure 4. 74) show no effect of iron addition on the column-grain structure of the films for the as deposited as well as the annealed films.

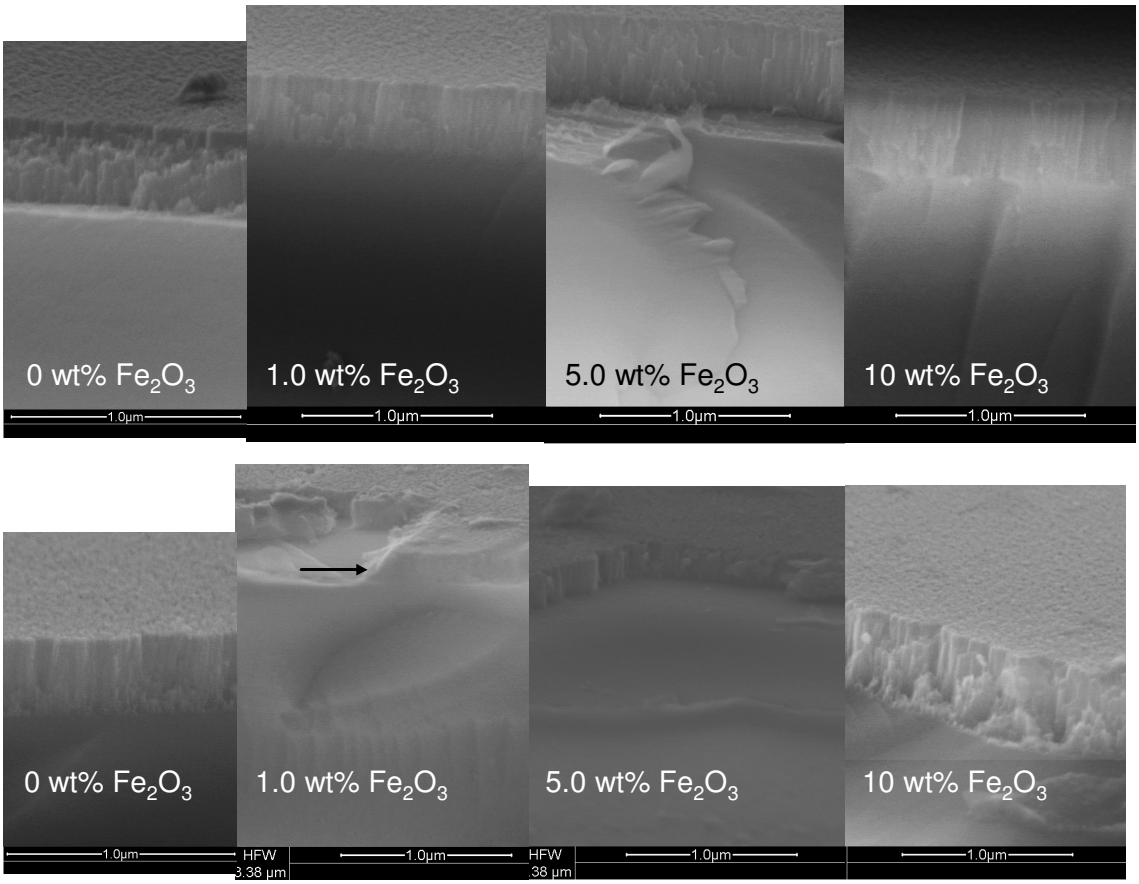

Figure 4. 74:

SEM cross sectional views of thin films deposited from Fe_2O_3/ TiO_{2-x} mixed oxide targets (1.4 Pa, 60 W), as deposited (top) and annealed 673 K/ 1 h (bottom).

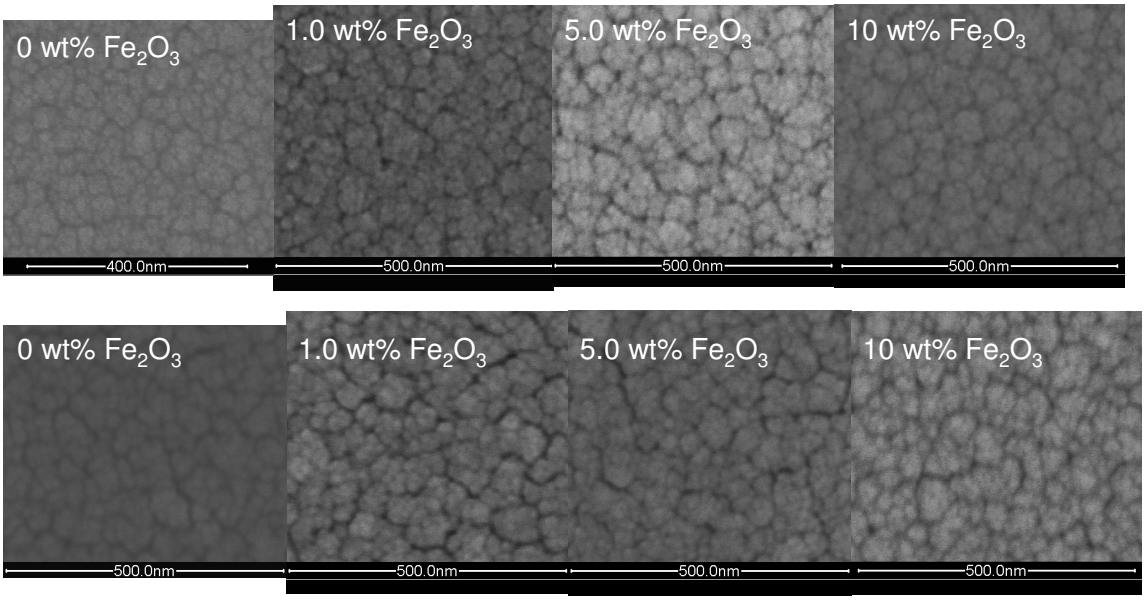

Figure 4. 75:

SEM top views of thin films deposited from Fe_2O_3/ TiO_{2-x} mixed oxide targets (1.4 Pa, 60 W), as deposited (top) and annealed 673 K/ 1 h (bottom).

The same is valid for SEM top views (Figure 4. 75). No significant change in grain size or of the structure of the column-grain tops can be seen.

The addition of Fe by sputtering from Fe_2O_3/ TiO_{2-x} mixed oxide targets thus does not affect the morphology of the thin films. The sputtering behavior of the Fe_2O_3/ TiO_{2-x} targets showed that the discharge voltage (Figure 4.31, top left) and deposition rate (Figure 4.31, bottom left) (p. 170) were changed little up to a Fe_2O_3 content of 5 wt%. Only the target with 10 wt% showed a deviating behavior due to its high resistivity. It does not seem surprising, therefore, that the lower amounts of Fe_2O_3 do not cause a difference in film structure. The higher discharge voltage and lower deposition speed observed for the highest Fe_2O_3 amount would suggest, that the particles arrive at the substrate with a higher energy which should influence the thin film structure. Clearly this is not the case here; probably the high Ar-pressure causes too much energy loss due to scattering effects, eliminating the effect of the increased voltage.

b. Nd-addition

SEM cross sectional views of thin films deposited from Nd_2O_3/ TiO_{2-x} mixed oxide targets (Figure 4. 76, top) show no effect of Nd-addition up to a concentration of 5.0 wt% Nd_2O_3. For the highest concentration of 10 wt% Nd_2O_3 no column-grains could be distinguished. The sputtering conditions were not significantly influenced by the amount of dopant (section 4.2.3.3) so that no difference in growth conditions is expected with the different dopant levels. Therefore, one should still observe zone 1a growth (section 2.8.3), i.e. columnar grain growth. The reasons for not seeing the column-grains in the cross sections for the films deposited from the targets containing 10 wt% Nd_2O_3 could be that (i) the columns have become rather irregular (closer to what is depicted in Figure 2. 13, p. 99) or (ii) the column-grains are densely packed. Both can result in the film not breaking along the grain boundaries but through the grains so that no structure is observed in the film cross section. Heat treatment at 673 K did not affect the structure of the thin films (Figure 4. 76, bottom).

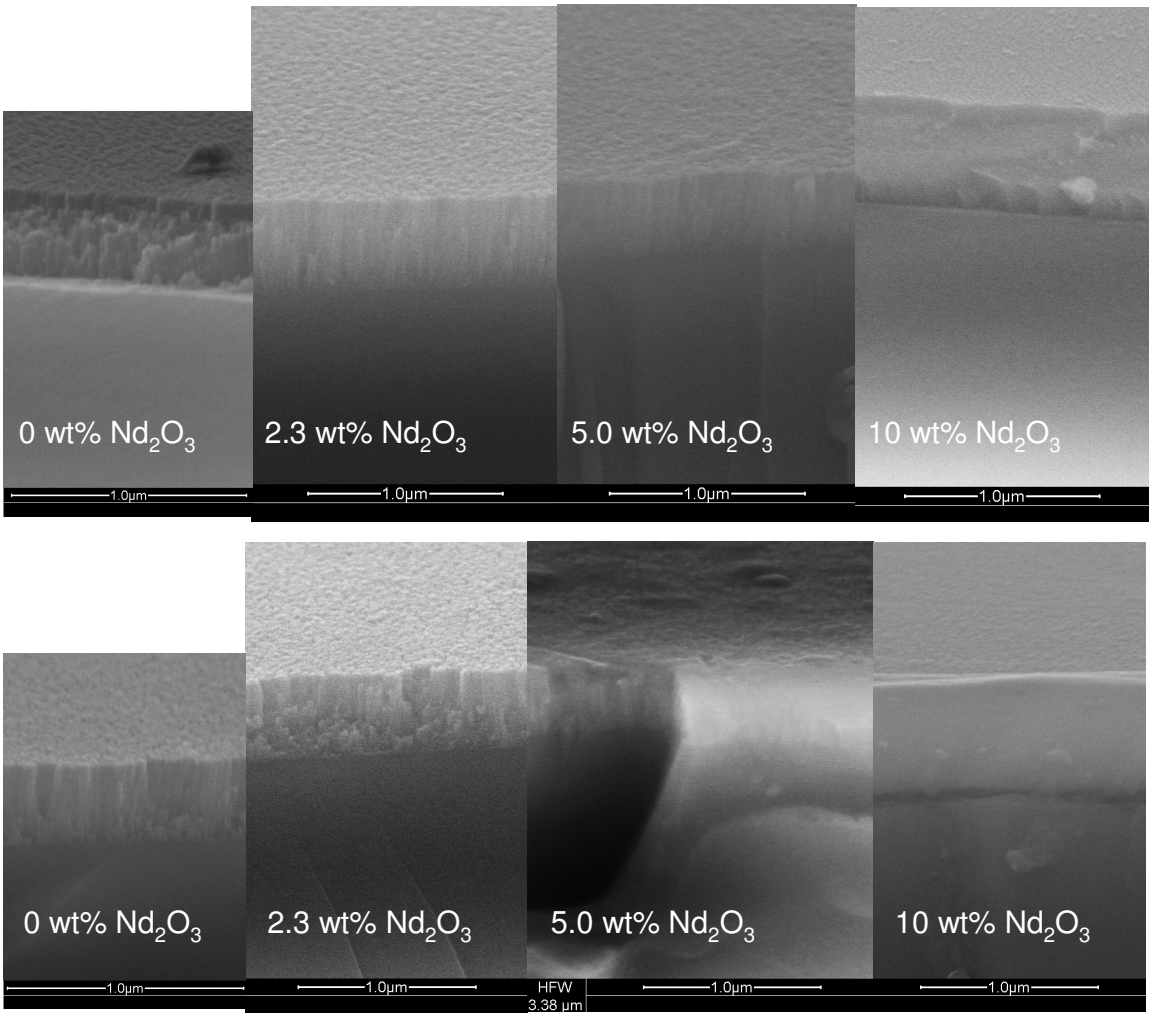

Figure 4. 76:
SEM cross sectional views of thin films deposited from Nd_2O_3/ TiO_{2-x} mixed oxide targets (1.4 Pa, 60 W), as deposited (top) and annealed 673 K/ 1 h (bottom).

The SEM top views of the as deposited thin films (Figure 4. 77, top) show a different surface structure depending on the amount of Nd in the film. For concentrations of 2.3 and 5.0 wt% Nd_2O_3 the surface of the column-grains looks rougher, i.e. the borders of the nodules (column tops) are not well defined. The total diameter of the column top remains unchanged. In contrast to this, the surface structure for a thin film deposited from a target containing 10 wt% N_2O_3 looks very smooth. The surface seems to consist of rounded grains instead of the cauliflower structured nodules usually observed. The grain size, on the other hand, is not affected. Overall, the packing density of the column-grains looks quite high for these films.

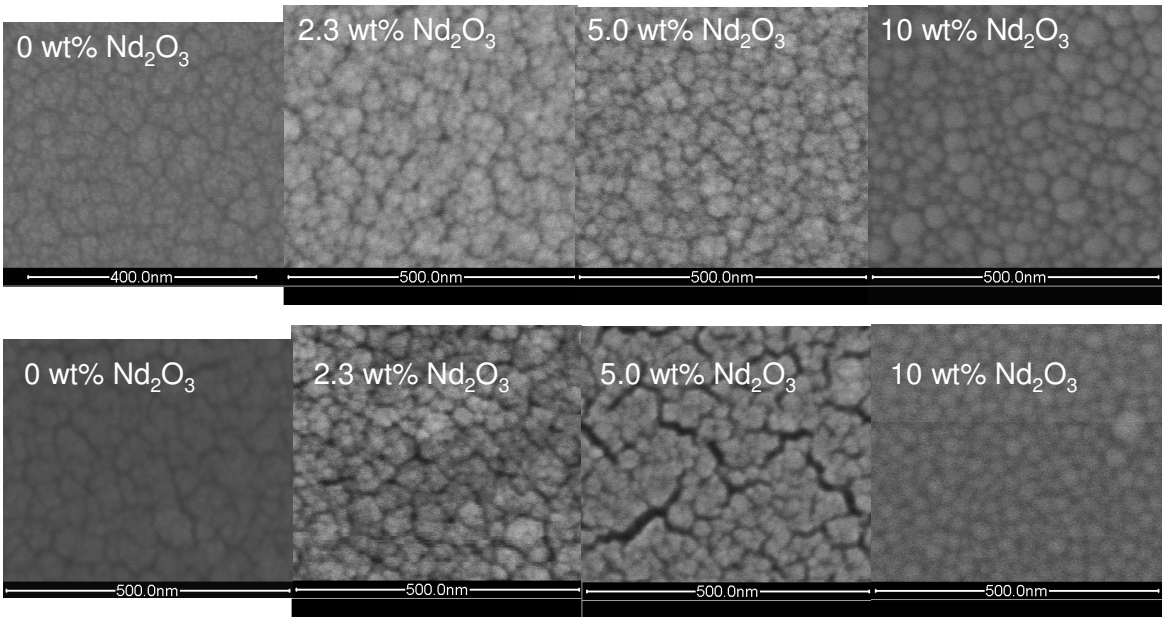

Figure 4. 77:

SEM top views of thin films deposited from Nd_2O_3/ TiO_{2-x} mixed oxide targets (1.4 Pa, 60 W), as deposited (top) and annealed 673 K/ 1 h (bottom).

The film structure after annealing at 673 K/ 1 h (Figure 4. 77, bottom) also depends strongly on the Nd_2O_3 content in the target. For the intermediate concentrations of 2.3 and 5.0 wt% Nd_2O_3 the crack formation increases with Nd_2O_3 content and is very strong for 5 wt%. As with the pure TiO_2 thin films the fine structure of the nodules seems to have disappeared; additionally the grain boundaries seem better defined compared to the as deposited films. This indicates that the column-grains densify more with increasing Nd_2O_3 content upon annealing. For the highest concentration of 10 wt% Nd_2O_3 no cracking is observed in the annealed films; the grain surface has retained its very round shape. This confirms that the density of the as deposited films indeed is rather high, so that no further densification can occur upon annealing.

It is difficult to explain this difference in film structure from the sputtering behavior of the mixed oxide targets. The discharge voltage was not affected by the Nd_2O_3 content in the target (Figure 4.31, top right). The deposition speed was somewhat higher for the pure TiO_2 and 10 wt% Nd_2O_3 target as compared to the targets with 2.3 and 5 wt% Nd_2O_3 (Figure 4.31, bottom right) (p. 170). Possibly the difference in size and weight of Nd as compared to Ti plays a role. Due to its large weight Nd looses less energy due to collisions in the gas phase, arriving at the substrate with a higher energy than Ti. Even though the differences in energy are small they could aid in densification.

c. V-addition

SEM cross sectional views (Figure 4. 78) reveal no change in the column-grain structure upon addition of V_2O_3 for the as deposited (left) as well as the annealed films (right).

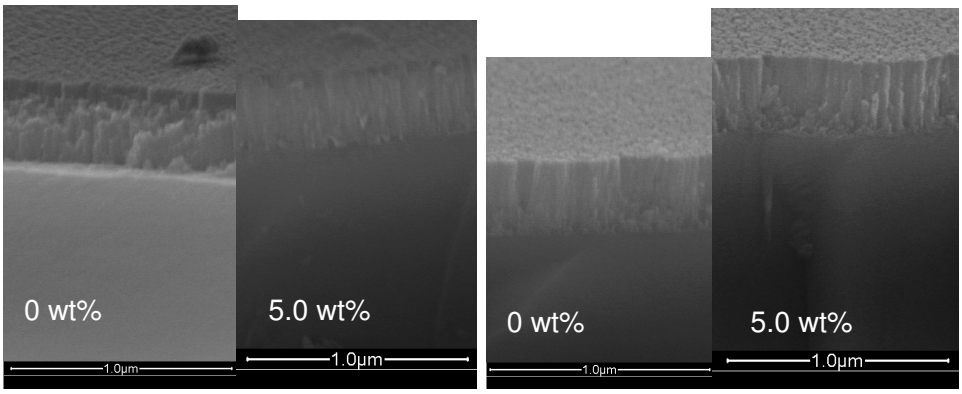

Figure 4. 78:
SEM cross sectional views of thin films deposited from a V_2O_3/ TiO_{2-x} mixed oxide target (1.4 Pa, 60 W), as deposited (left) and annealed 673 K/ 1 h (right).

The SEM top views (Figure 4. 79, left) show that the structure of the film sputtered from a 5 wt% V_2O_3 containing target is somewhat different from a pure TiO_2 film. The top of the column-grains looks rather flat and their circumfence is less round. Overall the boundaries of the column-grains are less clearly defined. After annealing at 673 K/ 1 h the grain boundaries become more pronounced, indicating that the fine grain structure disappears with annealing, following the generally observed trend. The overall shape of the grain tops seems not affected, though. The opening between the column-grains is similar to that of the pure TiO_2 films.

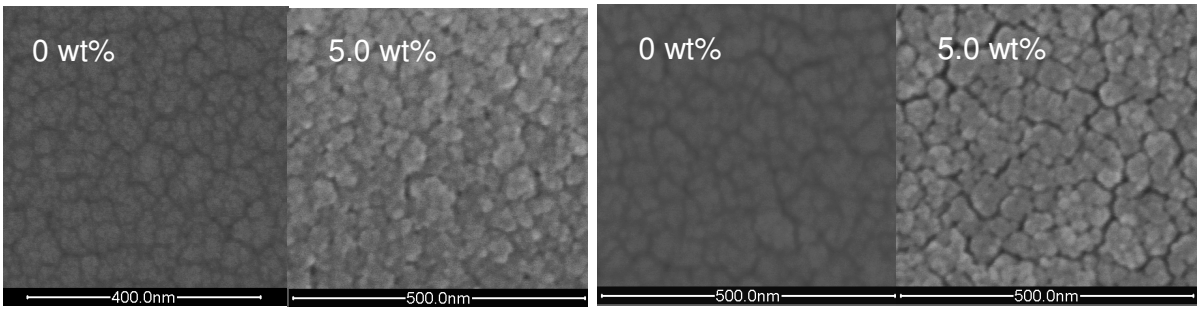

Figure 4. 79:
SEM top views of thin films deposited from a V_2O_3/ TiO_{2-x} mixed oxide target (1.4 Pa, 60 W), as deposited (left) and annealed 673 K/ 1 h (right).

For the 5 wt% V_2O_3 target a lower deposition speed (2.5 nm/min) and a higher discharge voltage (466 V) were observed. Both result in the sputtered particles to leave the target with a

higher energy. As already argued before, most of this energy is lost due to scattering with the gas atoms at the high sputtering pressure used. As a result there is little influence of V on the structure of the thin films.

4.4.1.2 Effect of dopant addition by ion implantation

In general the ion implanted films were difficult to image with SEM. Both the cross sectional as well as the top views revealed very little features so that focusing was problematic. This fact on its own is an indication that the film structure has changed as to show less features, i.e. that it has been smoothened (see comment section 4.3.1.2).

Fe-implantation

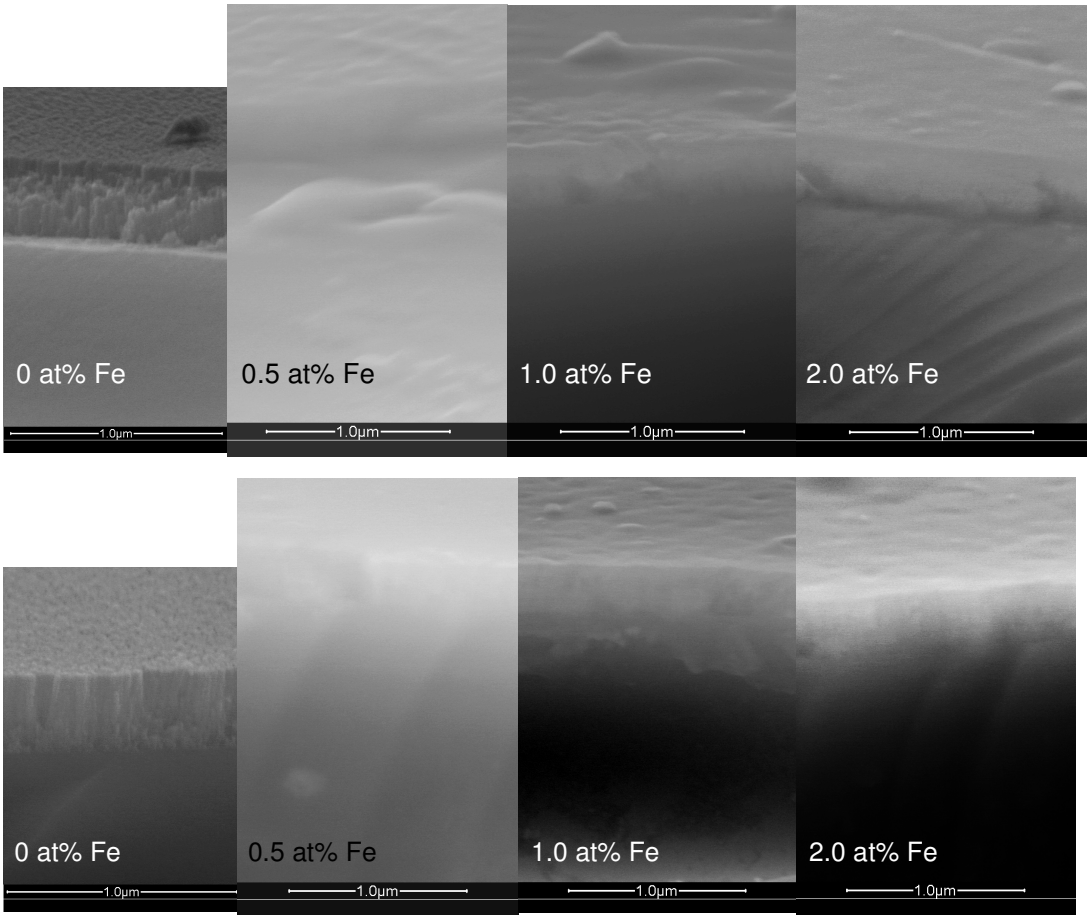

Figure 4. 80:
SEM cross sectional views of Fe ion implanted TiO_2 thin films (deposited at 1.4 Pa, 60 W), as implanted (top) and annealed 673 K/ 1 h (bottom).

Figure 4. 80 shows the ion implanted TiO_2 thin films, both before and after annealing. The only film that shows some structure is the one implanted with 2.0 at% Fe and annealed, where the column-grains can be identified. In all implanted films the surface has become very

smooth (see in more detail in Figure 4. 81), which is most likely the reason for the focusing problems. A careful conclusion is, that the column-grain structure of the films is not destroyed by ion implantation but that the changes to the sample surface make it more difficult to focus the SEM.

The SEM top views (Figure 4. 81) reveal that the surface structure of the as implanted films is completely destroyed. As could be seen from the cross sections the focusing problems with the microscope are due to the loss of surface roughness, i.e. that the film surface appears to have been polished by the ion implantation process. In the images one can still see the, albeit blurred, outlines of the original column-grain tops, but no detail is left. In these images the true size of the column-grains is possibly not shown due to the image distortion (out of focus).

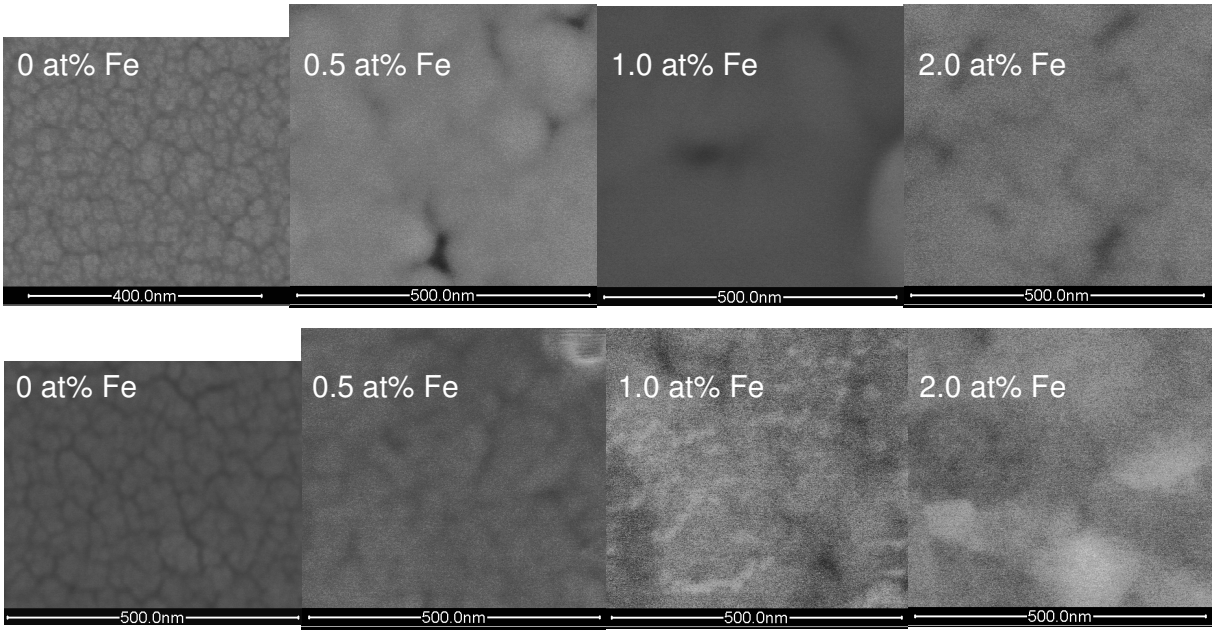

Figure 4. 81:
SEM top views of Fe ion implanted TiO_2 thin films (deposited at 1.4 Pa, 60 W), as implanted (top) and annealed 673 K/ 1 h (bottom).

After annealing the film surface remains featureless but some kind of surface roughening, which is not related to the original column-grain structure seems to have developed, especially for the films with 1 and 2 at% Fe implanted.

b. Nd implantation

SEM cross sectional views (Figure 4. 82) of Nd implanted films showed more detail than their Fe counterparts. In all cases the column-grain structure could be resolved, but again the smooth film surface prevents good focusing of the SEM. For the as implanted films with 1.0

and 2.0 at% implanted Nd one can visually distinguish two zones in the thin films (Figure 4. 82, top). This is no longer the case in the annealed films (Figure 4. 82, bottom).

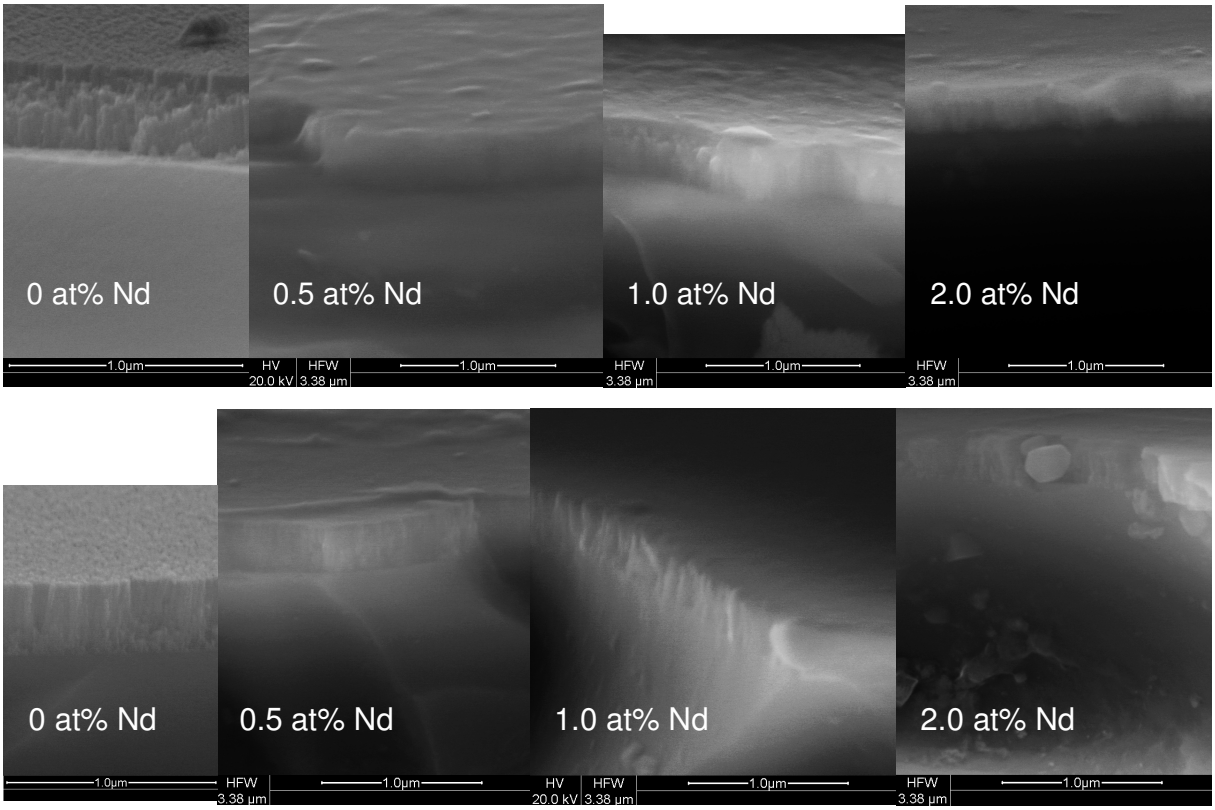

Figure 4. 82:
SEM cross sectional views of Nd ion implanted TiO_2 thin films (deposited at 1.4 Pa, 60 W), as implanted (top) and annealed 673 K/ 1 h (bottom).

A detail of the as implanted film (1.0 at%) is shown in Figure 4. 83. One can clearly see that the top layer has a different structure, the column-grains are no longer visible. Latter have either been destroyed or the mechanical properties of this part of the film have changed so that the fracturing properties are different from the rest. The total film thickness is about 400 nm so that the thickness of the altered layer is about 100 nm.

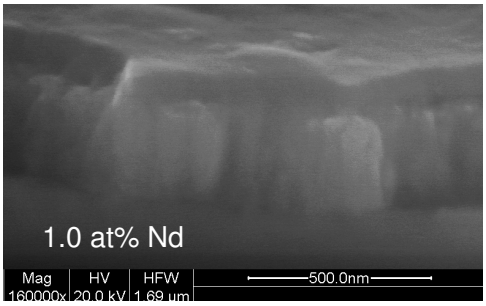

Figure 4. 83:
Detail from the SEM cross sectional view of an Nd ion implanted TiO_2 thin film (deposited at 1.4 Pa, 60 W, as implanted, 1.0 at% Nd).

As described in section 3.2.3 the desired implantation depth was 40 nm with a homogeneous distribution up to the surface. This should correspond to ca. $1/10^{th}$ of the total film thickness of 400 nm. Obviously the film structure was disturbed deeper than the intended implantation depth. This confirms the warning in section 2.9, that it is difficult to predict exact implantation profiles in mixed covalent/ionic materials as TiO_2.

SEM top views of the Nd-implanted films (Figure 4. 84) show in more detail that the surface contrast is almost completely lost. The original shape of the column-grains can still be resolved, but only weakly. Obviously the polishing effect is less with Nd than with Fe. Since different ion energies were used for the two dopants and they have a different mass, it is not surprising that their effect on the film surface is different.

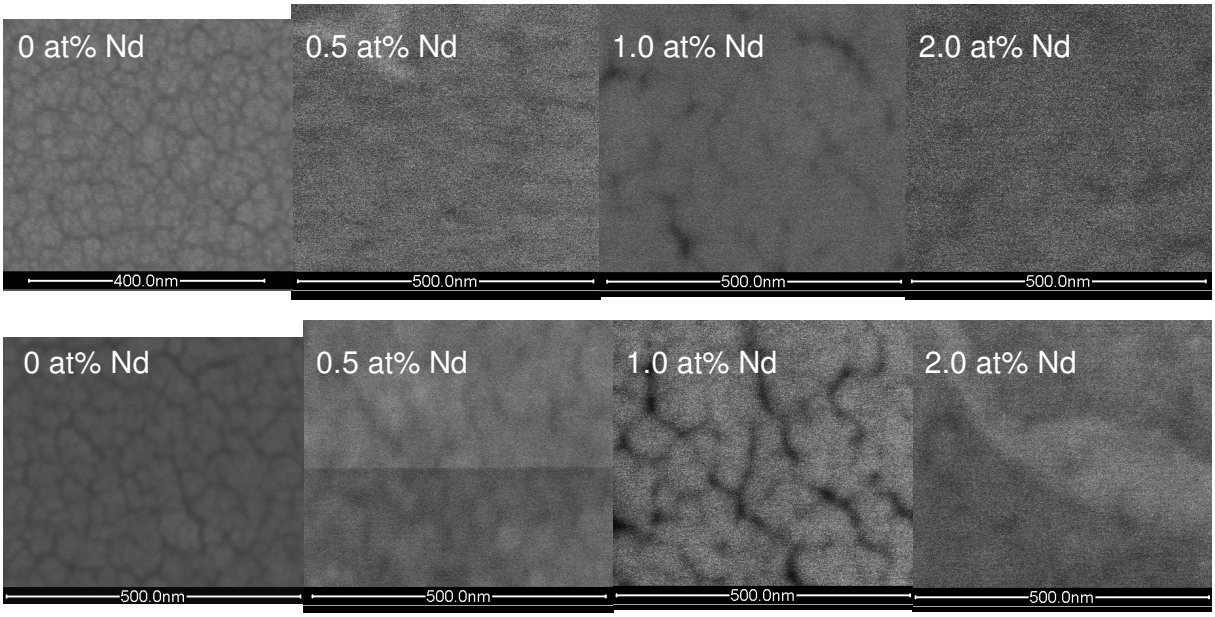

Figure 4. 84:
SEM top views of Nd ion implanted TiO_2 thin films (1.4 Pa, 60 W), as implanted (top) and annealed 673 K/ 1 h (bottom).

For 0.5 at% Nd implanted films patches of not altered surface were found, probably they were masked by debris on the surface. Figure 4. 85 shows the border area between a masked and an implanted area.

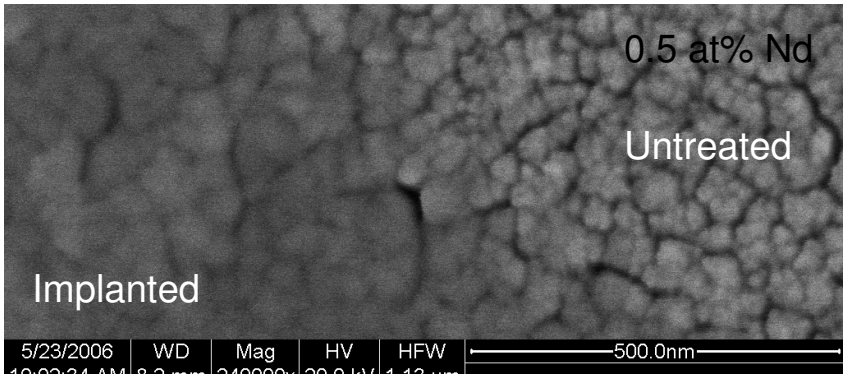

Figure 4. 85:
SEM top view image showing the difference between an implanted and a masked area on a thin film implanted with 0.5 at% Nd (as implanted).

Figure 4. 85 confirms that the diffuse image of the implanted area is due to a lack of image contrast, caused by 'polishing', i.e. smoothening due to the ion implantation process. On first thought it may not be clear how this can happen. It is known that treating a surface with a high-energy ion beam results in etching. Usually 'etching' is taken synonym with 'surface roughening'. On the other hand, the technique of ion beam etching, also called 'ion milling' is used for polishing down samples for TEM analysis. This effectively is a polishing technique as the sample is ablated carefully with the ion beam as to result in a central hole with an as low as possible inclining edge. Latter then yields an area large and thin enough (some nm at maximum) to be analyzed with TEM. So it seems not surprising that also ion implantation can lead to polishing of the sample surface. The question why Fe is causing a stronger surface modification than Nd cannot be answered straightforwardly: Fe is a much lighter element, and was implanted at different conditions to yield the same implantation profile (section 3.2.3).

4.4.2 Stoichiometry

The stoichiometry of the thin films was assed by ESCA measurements. Since TiO_2 looses preferentially oxygen in high vacuum when sputtered with Ar, it is not possible to clean the contaminated surface and determine the stoichiometry from the Ti/ O ratio. It is, therefore, necessary to look at the shape of the Ti2p peak (section 4.3.2).

4.4.2.1 Effect of dopant addition by sputtering from mixed oxide targets

The shape of the Ti2p peak in the doped thin films was very symmetric and not different from the peak form observed for the pure TiO_2 thin films. No sign of reduction of the Ti^{4+} could be detected.

4.4.2.2 Effect of ion implantation

As received ion implanted films showed a bluish-grey discoloration which is an indicator that the films are sub-stoichiometric TiO_{2-x}. Apparently the implantation process caused a loss of oxygen in parts of the film. Since the film surface was polished during implantation this means that material was removed from the film surface by the process. As oxygen is preferentially removed by ion beam etching (section 4.3.2) the result is a sub-stoichiometric surface layer. Figure 4. 83, p. 243, shows that this altered layer was ca. 100 nm deep. Possibly only this altered layer shows sub-stoichiometric TiO_{2-x}. Unfortunately, the depth of the reduced layer cannot be investigated by ESCA depth sputtering as this alters the oxygen concentration of the layer for the same reason (section 4.3.2).

The ESCA spectra of the as received samples show that the Ti2p peak is asymmetric, broadened and shifted to lower energies. This confirms that the surface of the layers is reduced. After annealing in air the ion implanted thin films were returned to the colorless state, indicating that they were stoichiometric, which is confirmed by their symmetric Ti2p peak shape.

4.4.3 Dopant concentration and distribution

Before discussing the results from the ESCA analysis, there are some general remarks on determining the dopant distribution in the TiO_2 thin films. The first concerns the intensity of the ESCA signals for the Fe and Nd energy windows. It was already mentioned in section 2.6.5.1 that it is difficult to obtain a good Fe3d signal, which was confirmed in this thesis. For determining the Nd concentration it was necessary to use the Nd4d instead of the more intense Nd3d signal, because latter is obscured by O-Auger signals occurring at a very similar energy.

The second comment refers to the accuracy of the calculation of the dopant content. Since the oxygen atomic concentration on the surface deviates from the bulk, there is no means of determining this value. Therefore, the concentration of the dopant is determined as % cation, defined as atomic percent cation divided by the total cation concentration (Ti + dopant) as given by the ESCA analysis. The general rule for ESCA analysis is that the relative error increases with decreasing concentration of the element analyzed. Values below 1 at% become semi-quantitative.

As already mentioned in section 4.3.2, normally the untreated surface of the thin films was analyzed by ESCA, i.e. no sputter cleaning was performed. For selected samples also a depth profile was measured to determine the dopant distribution in the depth of the film.

It would also be very interesting to investigate the lateral dopant distribution after annealing, i.e. whether the dopants are distributed homogeneously within the column-grains or segregate to the grain boundaries. While for as deposited and as received implanted films a randomized dopant distribution is expected, this is likely to change after the anneal treatment. Unfortunately both available analysis techniques, namely ESCA and the energy dispersive x-ray analysis (EDX) system of the SEM have a lateral resolution on the order of 100 and 1-2 µm, respectively, more than two orders of magnitude larger than the width of the column-grains. A third option would be using the backscattering detector of the SEM which shows an element dependent contrast.

4.4.3.1 Dopant concentration in the thin films sputter deposited from mixed oxide targets

a. Surface measurement

Figure 4. 86 shows the relationship between the atomic concentration of Fe and Nd at the surface of the thin films sputtered at 1.4 Pa an 60 W, as determined by ESCA, and the respective Fe_2O_3 and Nd_2O_3 concentrations used for preparing the mixed oxide targets. The results for the 5 wt% V_2O_3/ TiO_2 target are listed in Table 4. 7, below.

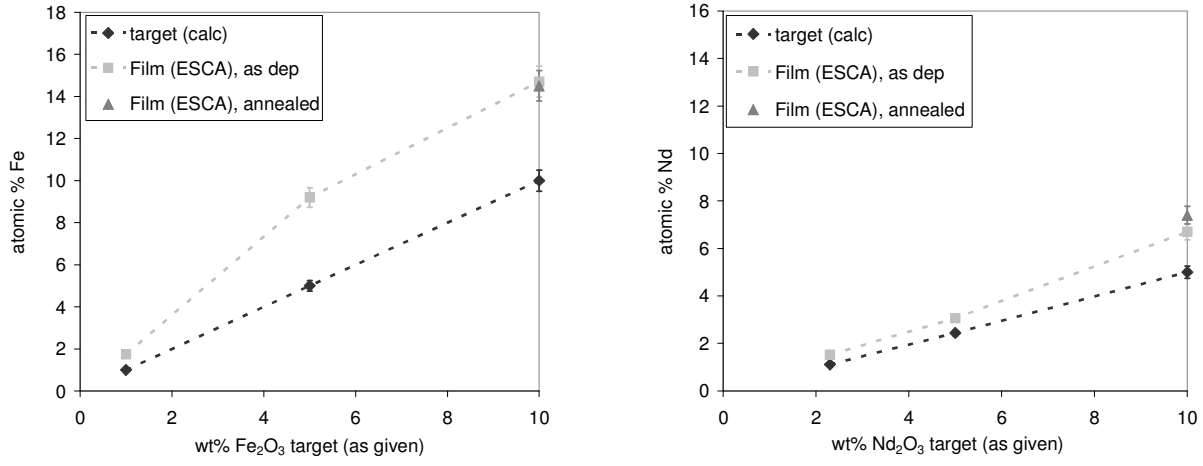

Figure 4. 86:

Dependence of the cation concentration (at%) of the dopant in the thin film, as determined by ESCA, on the metal-oxide additive (wt%) to the target for thin films sputtered from Fe_2O_3- and Nd_2O_3-TiO_2 mixed oxide targets. The at% calculated from the wt% in the target is also shown.

Sample	Target (calc.)	As deposited	Annealed
V-concentration (at%)	5.3	3.14	4.44

Table 4. 7: Vanadium concentration in the thin films and the target, for the 5 wt% V_2O_3/TiO_2 target.

The dark grey curves in Figure 4. 86 give the at% as calculated from the wt% of dopant used to prepare the mixed oxide target. The light grey curves shows the at% measured by ESCA. The annealed samples sputtered from the 10 wt% targets are indicated as grey triangles. Since these results do not differ significantly from the as deposited ones no further measurements were performed on the annealed samples.

As one can see from Figure 4. 86, the concentration of 10 wt% of Nd_2O_3 in TiO_2 is calculated to be about 5 at%, while the concentration of 10 wt% Fe_2O_3 actually is equivalent to 10 at%. Table 4. 7 shows that the concentration of 5 wt% V_2O_3 in TiO_2 is calculated to be 5.3 at%. It will be important to keep this in mind when comparing the effect of dopant concentration on the film properties for the different dopants used in this study. When reporting the results the concentrations as given for the target concentration and implantation depth of 40 nm are used. The scale for the concentration in the figures is chosen to be close or identical to 10 at% of the dopant cation.

Figure 4. 86 also shows that the measured cation concentration is higher than the calculated one. This could indicate that (i) there is preferential sputtering of the dopant cation or (ii) the cation concentration in the target is higher after sintering than in the initially mixed powders. It was not trusted to perform ESCA analysis of the target surface. The targets are sintered on ceramic setters and afterwards polished to the required dimensions. The different processing steps do not guarantee that the outer surface layer is clean enough to give accurate analysis results, even after cleaning. Some ESCA analysis of the surface of TiO_{2-x} targets was performed which showed high Si-concentrations on the target surface that could not be found back in the thin films after sputtering. This confirms the above suspicion that process related contaminants polluted the target surface. It would be safer to use a less surface sensitive technique like quantitative EDX or EPMA (electron probe micro-analysis), which was not implemented in this study.

b. Depth Profile

For the as deposited sample sputtered from a mixed oxide target containing 10 wt% Nd_2O_3 a depth profile was measured down to ca. 240 nm. No change in concentration could be observed throughout the investigated depth. This confirms that the race-track of the

target reaches an equilibrium concentration during pre-sputtering which does not change in the course of the deposition process. The equilibrium is reached when the discharge voltage, which has a different start-up value, remains constant [Depla01].

4.4.3.2 Dopant concentration in the ion implanted thin films

a. Surface measurement

At the surface of the ion implanted thin films no signal could be detected for the implanted cation using ESCA. The only exceptions were the films implanted with 2 at% Nd, where concentrations of 1.17 (as received) and 1.21 at% (annealed) were detected. These are both lower than the intended implanted concentration of 2 at%. Since the values are rather similar, it would seem that the distribution of Nd in the TiO_2 thin film was not influenced by the anneal treatment. If this was the case one could either observe an inward (homogenization) or an outward (segregation) diffusion of the implanted Nd, which would result in the surface concentration either decreasing or increasing, respectively. There are several reasons why this concentration is so low: (i) the error at these concentrations is large, (ii) the implantation depth is deeper than intended so that the same number of implanted ions is distributed over a larger range, (iii) the surface concentration is lower than the subsurface concentration. Both the second and third point can be checked when determining a depth profile of the Nd concentration.

b. Depth Profile

A depth profile was taken for the as received and annealed sample implanted with 2 at% Nd (Figure 4. 87). Due to the long measurement time needed to obtain an acceptable resolution of the Nd signal (3-4 h) and the necessity to do the depth sputtering manually, it was chosen to take only 5 different measurements per sample, including one measurement at the surface. As a result, the depth profile can only be indicative.

Figure 4. 87 shows three important things: (i) the concentration is not homogeneous throughout the measured depth interval, (ii) the implantation depth is probably more than twice the intended depth and (iii) the dopant distribution is not altered by the heat treatment. In the SEM cross sections (Figure 4. 83, p. 243) an altered layer of ca. 100 nm was seen, confirming the larger implantation depth. The reason for the inhomogeneous dopant distribution, i.e. that two peaks in the Nd-concentration are observed, most likely due to the use of two implantation energies that were not matched well as to give only a small overlap. It is not surprising that the actual dopant distribution deviates strongly from the intended one.

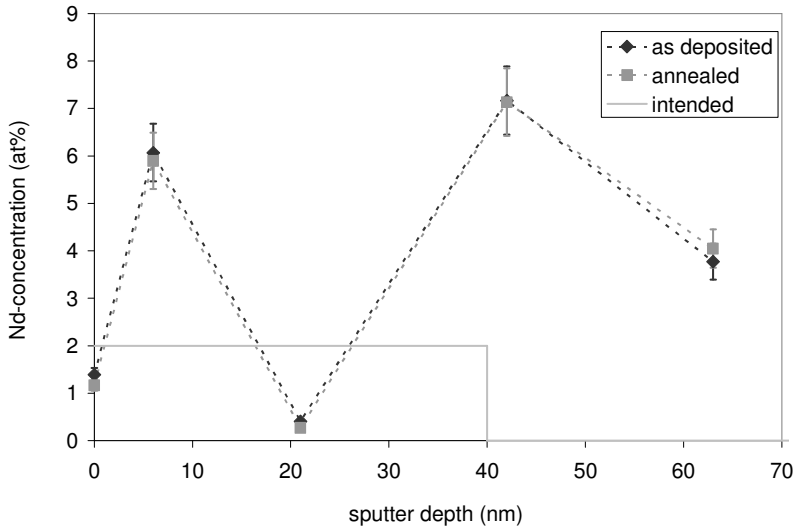

Figure 4. 87:

Depth profile of TiO_2 thin films implanted with 2 at % Nd, as received and annealed at 673 K/ 1 h.

Obviously, this also resulted in the surface concentration to be quite lower than the peak concentration. In section 2.9 the warning was reported that for partially ionic solids the nature of the bonding is not clearly defined and simulated implantation profiles can be quite wrong. Clearly this is the case for the implanted films of this study.

Additionally, the implanted ion dose must also have been higher than intended.

4.4.4 Crystallization

All as deposited or as implanted doped films were XRD amorphous. Annealing was performed at the temperature (673 K) and time (1 h) that was found to be most ideal for annealing the pure TiO_2 thin films sputtered using the same conditions (1.4 Pa, 60 W). The aim of this study was to investigate the effect of dopant type and concentration on the crystallization behavior of the thin films.

In sections 4.4.4.1 and 4.4.4.2 the effect of dopant addition by sputtering from mixed oxide targets and ion implantation will be discussed, respectively. In section 4.4.4.3 a comparison between the two methods and the different types of dopant will be given. In the graphs the range of the dopant concentration was chosen to be the equivalent of 10 at% to allow for better comparison (please refer to section 4.4.3).

4.4.4.1 Dopant addition by mixed oxide target sputtering

a. Effect of Fe addition

The addition of Fe_2O_3 has only a small influence on the crystallization behavior of the thin films (Figure 4. 88, top left) for Fe concentrations up to 5 wt%. The preferred (004) orientation is still present but becomes less pronounced with increasing Fe content (Figure 4. 88, top left). In contrast, the film sputtered from the target containing 10 wt% Fe_2O_3 does not crystallize at the chosen conditions.

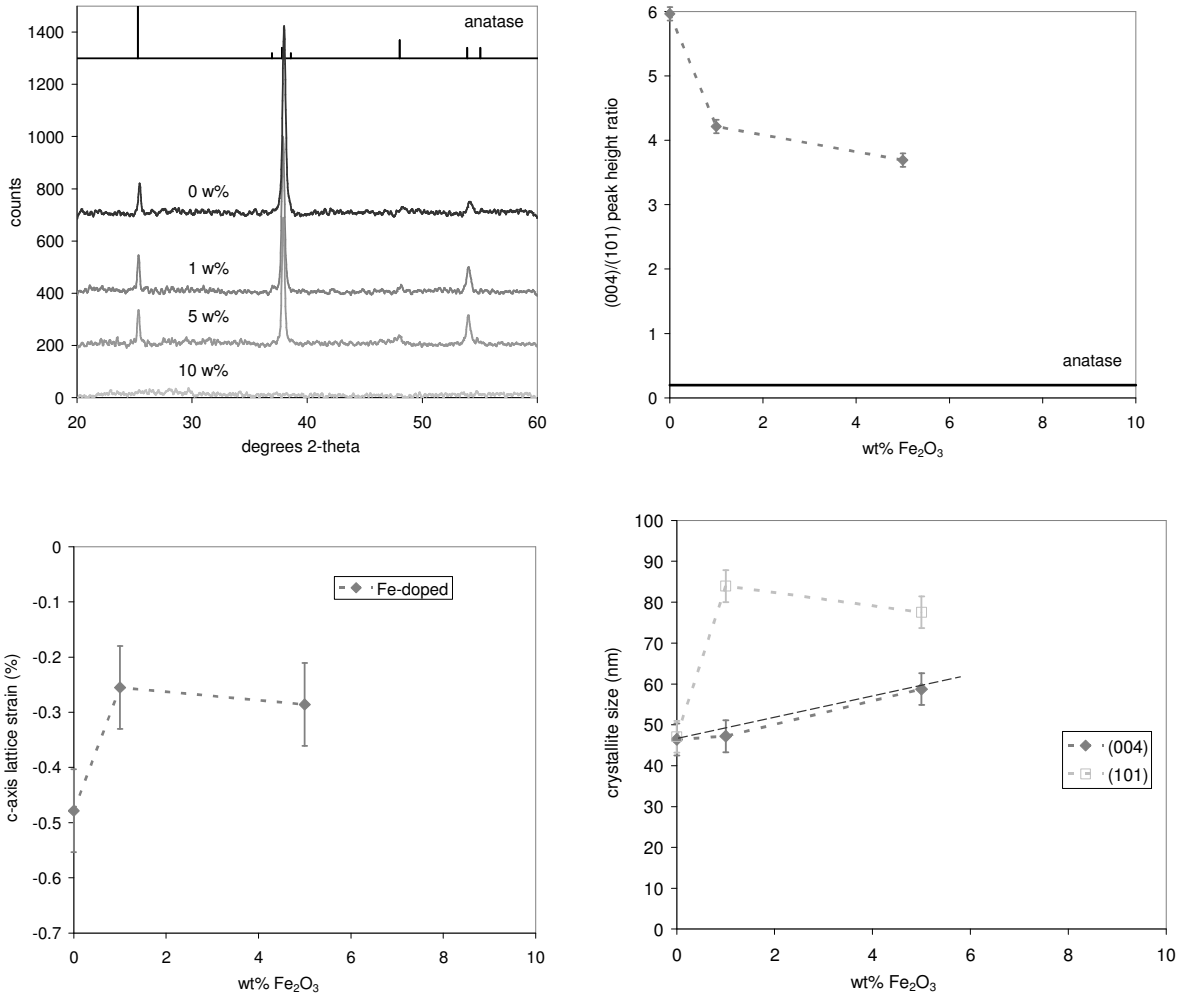

Figure 4. 88:

Dependence of crystallization on Fe_2O_3 content for thin films deposited from Fe_2O_3/ TiO_{2-x} mixed oxide targets (1.4 Pa, 60 W, annealed 673K / 1 h): XRD θ/ 2θ spectra (top left), (004)/ (101) peak height ratio (top right), c-axis strain (bottom left), crystallite size calculated from the (004) and the (101) diffraction peaks (bottom right). Since the calculation from the (101) peak is less reliable the respective square symbols are left open. The most likely trend is indicated with the darker dashed line.

The value of the negative c-axis strain decreases with increasing Fe-content in the films (Figure 4. 88, bottom left). The crystallite size follows the same trend (Figure 4. 88, bottom right). Here, the calculation from the (004) diffraction peak is more accurate due its stronger intensity. It is, therefore, better to use the trend indicated by the dashed line. This indicates that concentrations of 5 wt% Fe_2O_3 and below promote crystal growth. This tendency was also observed for the sintering of the targets (section 4.2.3.1): for the same amounts of added Fe_2O_3 the grain size increased, while it decreased again for the highest concentration (10 wt%). Note that in the targets the individual grains are single crystals due to the sintering process.

Comparing the observed crystallization behavior of these films with the crystallization behavior reported in literature (section 2.6.5.1.) is difficult, because there only films crystallized (i) during deposition or (ii) after annealing to higher temperatures are discussed. It was also mentioned that the rutile content in TiO_2 thin films increased with increasing Fe content for as deposited crystalline films, and that the anatase-to-rutile transformation temperature decreased. In our case the rather low anneal temperature of 673 K did not yield any rutile crystallization and crystallization was prevented for the highest content of Fe.

b. Effect of Nd addition

The XRD spectra of annealed thin films deposited from Nd_2O_3/ TiO_{2-x} mixed oxide targets (Figure 4. 89, top left) show that the film deposited from a 2.3 wt% Nd_2O_3 target crystallizes similar to a pure TiO_2 film. Films sputtered from 5.0 and 10 wt% Nd_2O_3 targets show a completely different XRD spectrum: only a single diffraction peak is present, which is not from anatase. When comparing to the rutile and brookite NIST spectrum (also shown in Figure 4. 89) it seems rather unlikely that one of the two crystal structures has been formed. The spectrum could also not be related to any known Nd-Ti-mixed oxide phase. As a result the crystalline phase formed in these two thin films could not be identified.

Since thin films with the highest two Nd_2O_3 concentrations did not crystallize in the anatase phase, the (004)/ (101) peak height ratio and c-axis strain could not be calculated. The crystallite size calculation is independent of the crystal phase, so it was calculated from the single measured diffraction peak. Figure 4. 89 (top right) shows that the (004)/ (101) peak height ratio decreases for the addition of 2.3 wt% Nd_2O_3 to the target, but the films are still strongly (004) preferentially oriented. The value of the negative c-axis lattice strain decreases by the addition of 2.3 wt% Nd_2O_3 to the target.

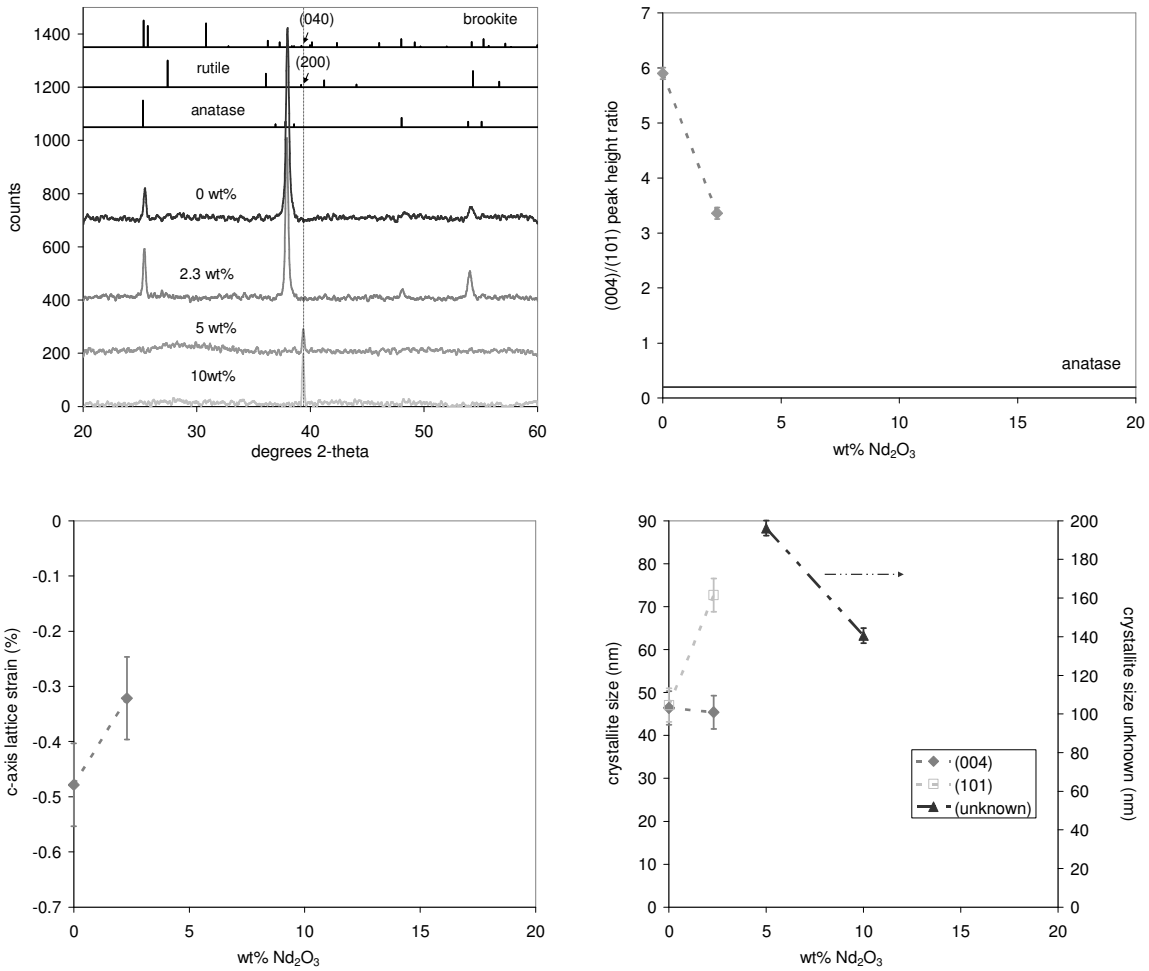

Figure 4. 89:

Dependence of crystallization on Nd_2O_3 content for thin films deposited from Nd_2O_3/ TiO_{2-x} mixed oxide targets (1.4 Pa, 60 W, annealed 673 K/ 1 h): θ/ 2θ spectra (top left), (004)/ (101) peak height ratio (top right), c-axis strain (bottom left), crystallite size calculated from the (004) and the (101) diffraction peaks (bottom right). Since the calculation from the (101) peak is less reliable the respective square symbols are left open. The most likely trend is indicated by the (004) reflection.

The crystallite size calculated from the (004) reflection decreases slightly, which is more reliable than the calculation using the (101) reflection. In conclusion, there is no significant change in crystallite size with the addition of this small amount of Nd_2O_3. The crystallite sizes calculated for the two highest Nd_2O_3 concentrations (Figure 4. 89, bottom right, right vertical axis) are substantially higher, being close to 200 nm for 5 wt% and 140 nm for 10 wt%, respectively. The crystallite size seems to first increase when the new phase is formed but then decreases again with increasing dopant concentration. These findings reflect the observed influence of Nd_2O_3 addition on the grain size of the sintered rutile target material (section 4.2.3.1).

c. Effect of V addition

The addition of 5 wt% V_2O_3 decreases the degree of (004) out of plane orientation compared to the pure TiO_2 film, but the preferential orientation still remains strong (Figure 4. 90, top). The c-axis strain is not influenced by the addition of 5 wt% V_2O_3. The crystal size, as calculated from the more intense (004) peak, shows a small decrease with the addition of V_2O_3 to the target.

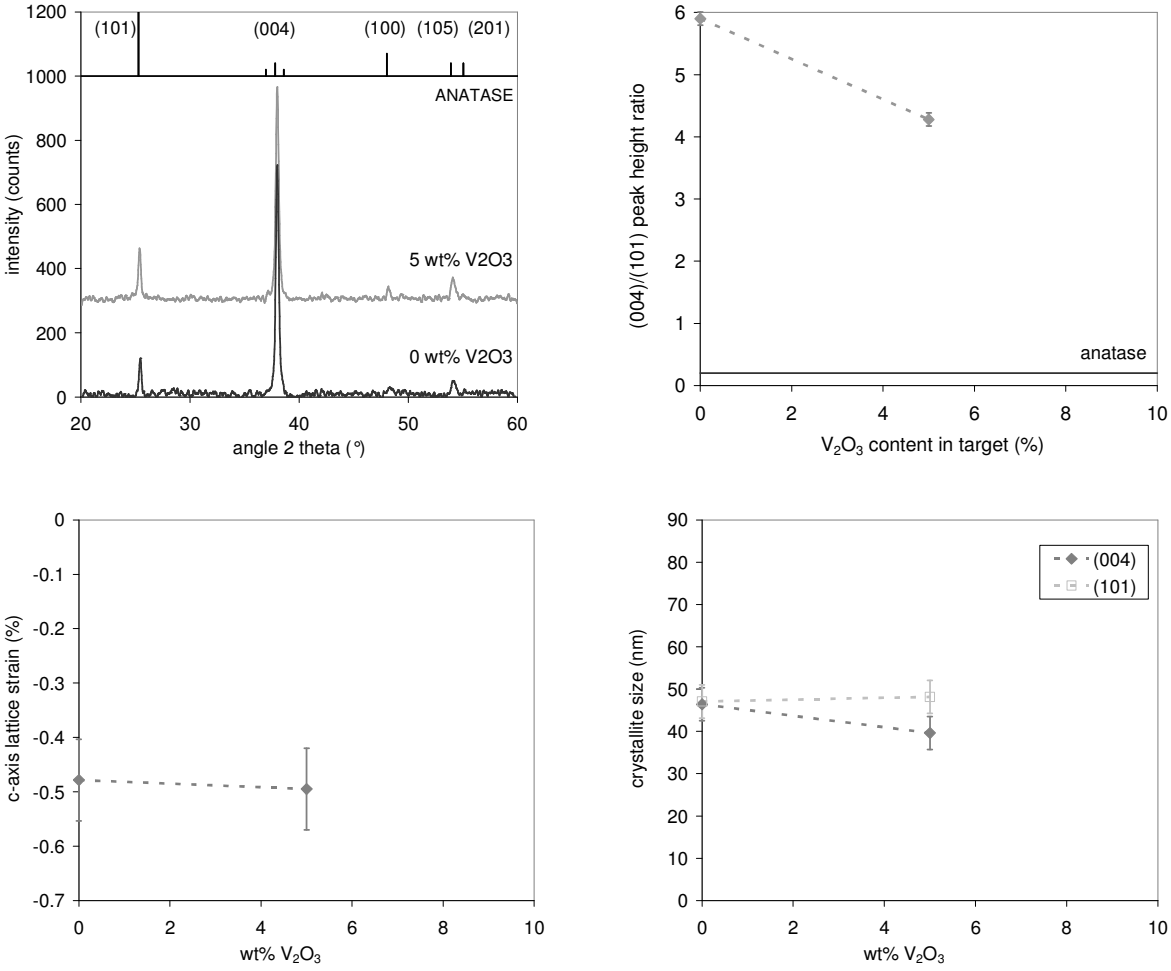

Figure 4. 90:

Dependence of crystallization on V_2O_3 content for thin films deposited from V_2O_3/ TiO_{2-x} mixed oxide targets (1.4 Pa, 60 W, annealed 673 K/ 1 h): XRD θ/ 2θ spectra (top left), (004)/ (101) peak height ratio (top right), c-axis strain (bottom left), crystallite size calculated from the (004) and the (101) diffraction peaks (bottom right). Since the calculation from the (101) peak is less reliable the respective square symbols are left open. The most likely trend is indicated by the (004) reflection.

In conclusion, the addition of V does not influence the crystallinity of the TiO_2 thin film other than decreasing the preferential orientation and crystallite size slightly. Since only one

dopant concentration could be tested due to problems with a too high target resistance, which did not allow d.c. sputtering (section 3.2.2.1), these results must be interpreted with care.

4.4.4.2 Dopant addition by ion implantation

a. Fe implantation

The implantation of Fe in the top layer of TiO_2 thin films shows a strong influence on their crystallization behavior. The very strong (004) out of plane orientation observed in the pure TiO_2 film is changed to an almost random orientation for all implanted concentrations of Fe (Figure 4. 91, top). The XRD spectra for the ion implanted films were measured for a longer time, therefore the signal of the pure TiO_2 thin film was rescaled.

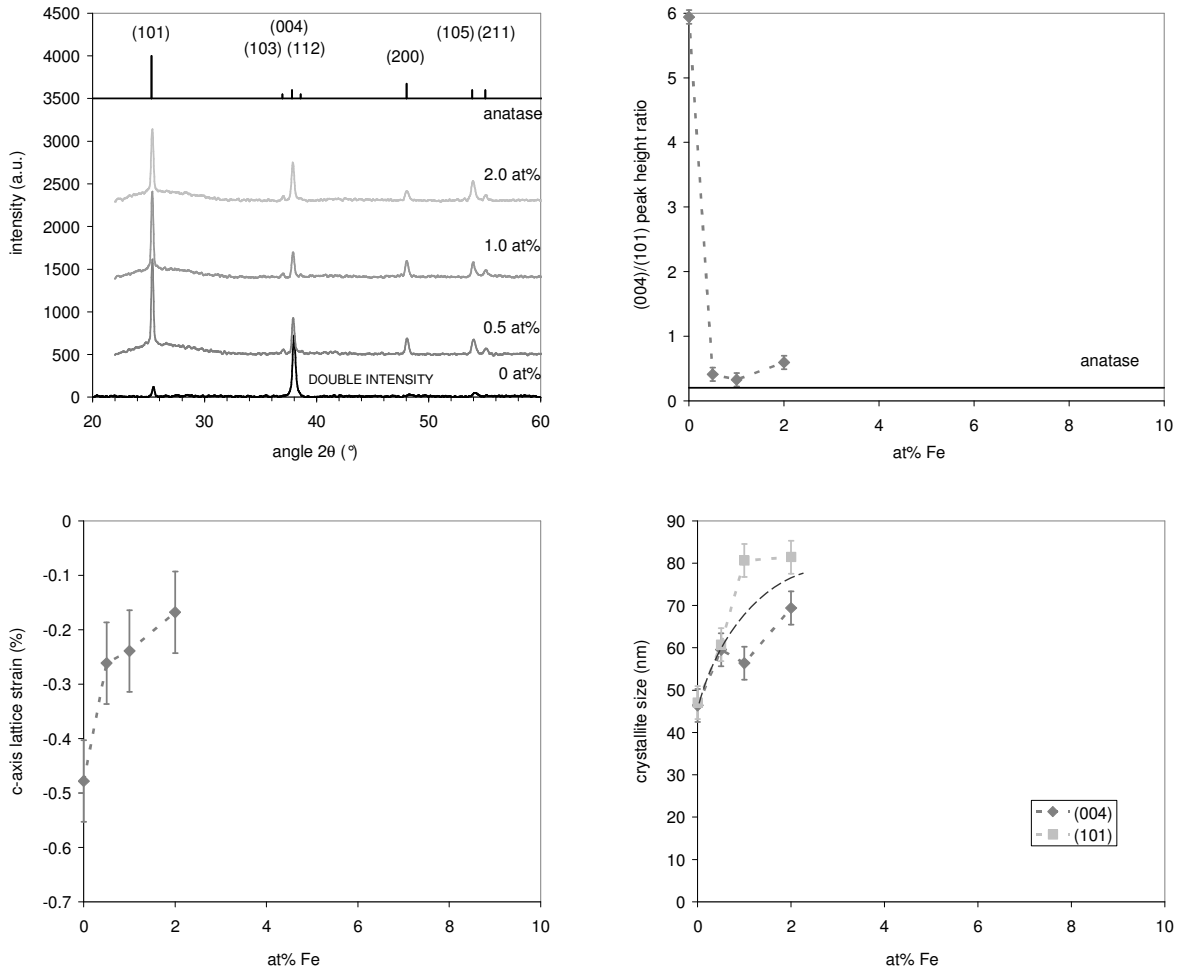

Figure 4. 91:

Effect of Fe-ion implantation on the crystallization behavior of TiO_2 thin films deposited at 60 W, 1.4 Pa, heat treated at 673 K/ 1 h: XRD spectra (top left), (004)/(101) peak height ratio (top right), c-axis strain (bottom left) and crystallite size (bottom right).

The value of the negative c-axis strain decreases with Fe implantation, but the strongest effect is seen between the films with and without Fe. The crystallite size increases with increasing amount of implanted Fe.

When comparing the crystallization behavior of the films deposited from Fe_2O_3/ TiO_2 mixed oxide targets and the Fe-ion implanted films one can see that the trends observed for the c-axis strain and the crystallite size are the same, but that the out of plane orientation of the crystallites is completely different for the two films. While the (004) preferential orientation was only slightly decreased for the films doped during sputtering, it is almost completely lost for the ion implanted films. Possibly, the ion implantation process has disrupted the local ordering that was established upon sputtering. This disruption must be almost throughout the complete film thickness. If it would only take place in the intended depth of 40 nm (section 3.2.3) the XRD spectrum should show an overlap of the random oriented top 40 nm and strongly (004) oriented remaining 360 nm, which should show a somewhat less intense (004) orientation but not an almost complete random orientation. Since it was not possible to detect the Fe concentration at the surface of the implanted film using ESCA, a depth profile was not taken. A second possibility is, that the implantation procedure has not completely randomized the local ordering in the film.

b. Nd implantation

The implantation of the much heavier Nd has a small effect on the crystallization behavior of thin films for concentrations up to 1.0 at%. As one can see from the top right of Figure 4. 92 the preferential (004) out of plane orientation is even higher for the two lowest implantation concentrations. Only the film with the highest Nd-concentration shows almost complete randomization. Evidently, the implantation of Nd influences the crystallization of the TiO_2 films only at higher implantation doses, which is different from Fe implantation.

For the implantation concentration of 2 at% the ESCA depth profiles showed that Nd was implanted at least 60 nm deep into the film. A top layer of different characteristics having a thickness of about 100 nm was observed in SEM. From these two observations it is clear that the implantation most likely does not affect the complete film but only about the top quarter of the thickness. If only this layer would show random crystallization one should expect only a weakened (004) out of plane preferred orientation. As this is not the case, the perturbation in the upper ¼ of the film must cause random crystallization throughout the film, but only when the concentration of Nd is above a certain level. Even though the concentration profile of the lower two implantation concentrations could not be measured, for 1 at% the same perturbed

layer as for 2 at% was observed, indicating it is independent of concentration. In section 2.9, Figure 2.15 (p. 107) confirms this, showing only a weak dependence of the implantation depth on the implanted concentration. Obviously, the amount of Nd ions implanted causes a more or less strong perturbation of the top layer.

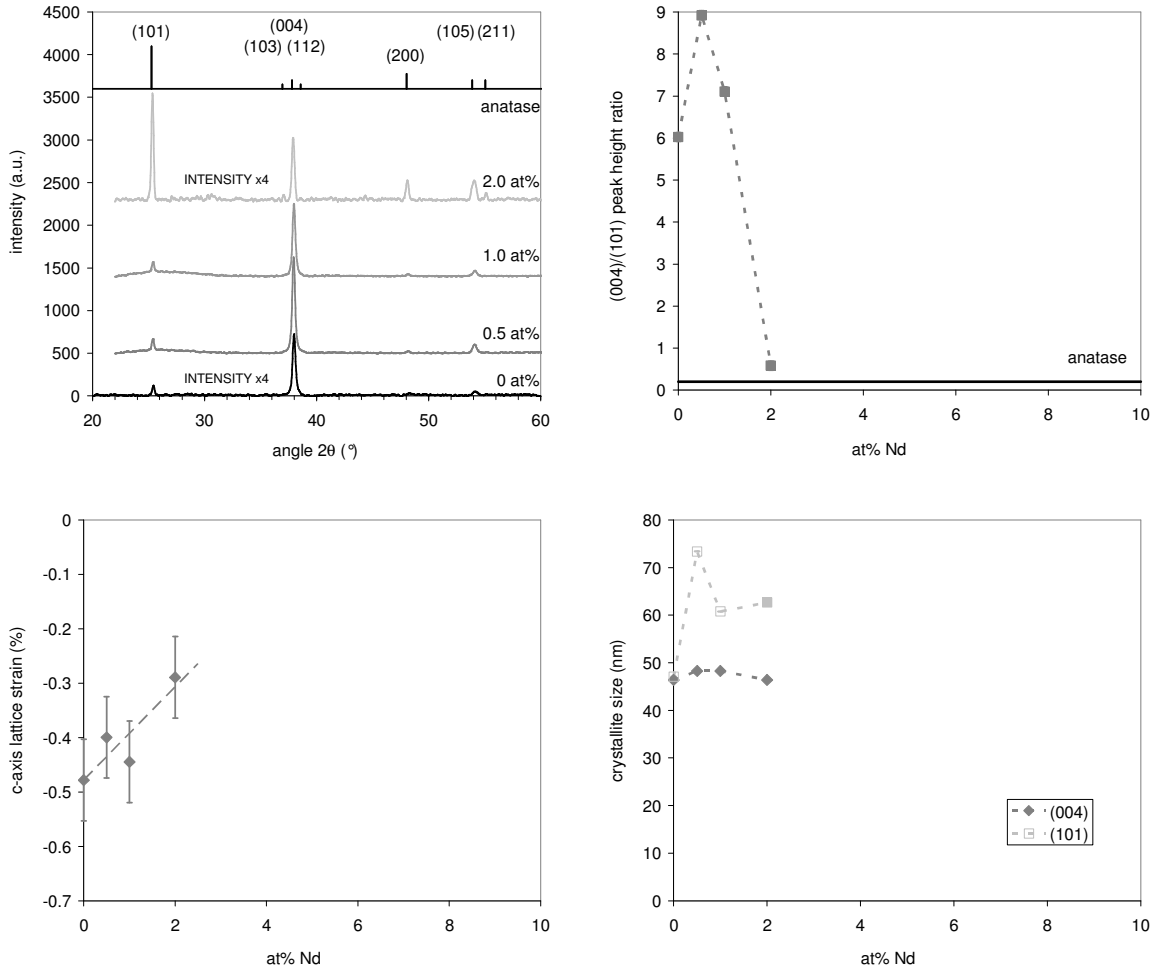

Figure 4. 92:

Effect of Nd-ion implantation on the crystallization behavior of TiO_2 thin films deposited at 60 W, 1.4 Pa, heat treated at 673 K/ 1 h: XRD spectra (top left), (004)/ (101) peak height ratio (top right), c-axis strain (bottom left) and crystallite size (bottom right). The open symbols indicate less reliable data.

The value of the negative c-axis strain decreases and the crystallite size remains constant with increasing implanted Nd concentration (Figure 4. 92, bottom). Former trend is similar to the one observed for Fe-implantation.

The crystallization behavior of the films deposited from Nd_2O_3/ TiO_2 mixed oxide targets and the Nd-ion implanted films exhibit the same tendencies when comparing the film deposited from a 2.3 wt% Nd_2O_3 mixed oxide target with a 1.0 at% Nd implanted film. At this concentration no randomization during implantation was observed. The high (004) orientation is

even better preserved for the ion implanted films. The trends for c-axis lattice strain and crystallite size are also similar between the two doping techniques.

4.4.4.3 Discussion of the effect of dopant addition on the crystallinity of the thin films

Doping with V had no significant influence on the crystallization behavior of the TiO_2 thin films. This is not surprising as the incorporation of especially V^{4+} into anatase is known to be favorable (section 2.6.5.1 b). Fe and Nd doping, on the other hand had a strong influence on the crystallization behavior and their influences were different, depending on the doping method as well as the dopant concentration. The only common influence was a decrease of the negative c-axis strain which was observed for both Nd and Fe addition, independent of the technique.

During annealing we observed the formation of anatase at low concentrations of Nd and an unknown phase for concentrations of 5 wt% and higher. On the other hand, the Fe doped films crystallize in the anatase phase, with exception of the film deposited from the 10 wt% Fe_2O_3/ TiO_2 mixed oxide target where no crystalline phase is formed. Obviously, the anatase phase is the most stable for Fe-addition (with exception of the highest concentration), while for Nd-addition the anatase phase is favored for lower concentrations but at higher concentrations some unknown phase is more stable.

The crystallite size was seen to increase with Fe-addition, independent of the doping technique. For Nd-addition the behavior was more complex. At low concentrations, where the anatase phase was formed, the crystallite size was seen to remain more or less constant. On the other hand, at higher concentrations (above the level used for implantation), where the unknown crystal phase was formed, the crystallite size decreased with increasing Nd-addition. This behavior reflected the influences on grain growth observed for the sintered targets (both Fe_2O_3 and Nd_2O_3/ TiO_2 mixed oxide targets). One can conclude, that Fe and low concentrations of Nd act as crystallite/ grain growth promoters while in high concentrations Nd acts as crystallite/ grain growth inhibitor in TiO_2 (for both thin films and targets). In sintering (of the target) grain growth is promoted by the formation of a liquid phase at the grain boundaries, while grain growth is inhibited by an insoluble second phase present at the grain boundaries. Possibly for the addition of Fe and a small amount of Nd a liquid phase is formed at the grain boundaries, while this is not the case for high concentrations of Nd. What happens during crystallization of the thin films is less clear, since no real sintering process occurs due to the low anneal temperatures. Even though no change in the column-grain size occurs upon an-

nealing (sections 4.3.1 and 4.4.1) it is possible that the inner structure of the column-grains is changed, as discussed in section 4.3.2.1.

For the films doped during sputtering little influence of the dopant addition on the preferred (004) out of plane orientation was observed for those compositions crystallizing in the anatase structure. For the ion implanted films, on the other hand, randomization of the crystallographic orientation was found for the Fe-implantation and the highest concentration of Nd-implantation. The films with lower implanted Nd concentrations showed even an increase in preferential orientation. The reason for latter influence of Nd is not understood. Obviously low concentrations of Nd do not cause strong enough changes to influence the local ordering in the thin films leading to the preferential orientation.

For Fe no two-layered structure could be seen in SEM (section 4.4.1.2), which could indicate the presence of a perturbed layer. This means that (i) the two layers cannot be distinguished or (ii) there is only one layer present, i.e. the complete thin film has been perturbed. Since the films show randomization at all implantation concentrations any separate perturbed layer should be large enough to influence the complete crystallization behavior of the thin film.

4.4.5 Photoluminescence measurements on Nd-doped thin films

Nd is known to form centers for photoluminescence in a variety of materials. The emission spectrum is known to depend on the (local) ordering around the Nd-centers. Only two films showed a measurable photoluminescent response, namely the annealed films deposited from the target containing 2.3 wt% Nd_2O_3 and implanted with 2 at% Nd_2O_3 (Figure 4. 93).

The two spectra are not identical, indicating that there is some difference in the (local) ordering around the Nd-centers. This is not surprising since both films showed a different crystallization behavior: the film sputtered from the mixed oxide target had a strong preferential (004) out of plane orientation, while the ion implanted film showed an almost random orientation. It was already discussed in section 4.4.4 that the process of ion implantation changes the structure of the as deposited TiO_2 resulting randomization. The film sputtered from the target containing 2.3 wt% Nd_2O_3 followed the crystallization behavior of the as deposited TiO_2 thin film.

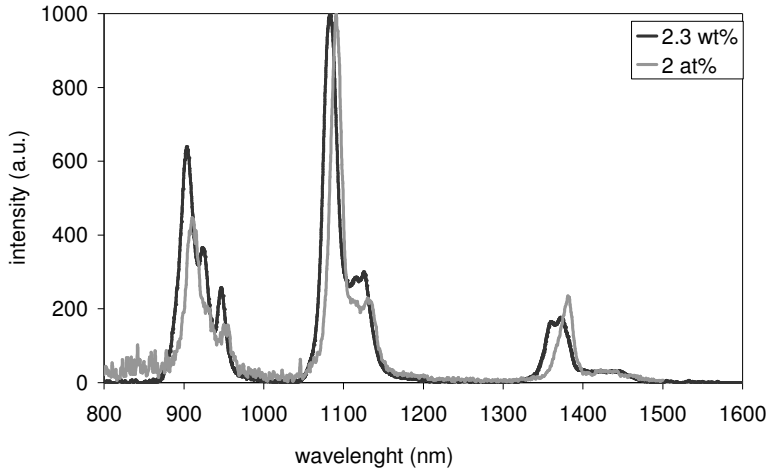

Figure 4. 93:

Photoluminescence spectra measured for a thin film deposited from a target containing 2.3 wt% Nd_2O_3 and a TiO_2 thin film implanted with 2 at% Nd. Both films were deposited at 1.4 Pa, 60 W and annealed at 673 K/ 1 h. The excitation wavelength was 330 nm.

Unfortunately the as deposited and as implanted films did not show any photoluminescent response. If this had been the case, possible differences in signal could have been used to identify structural differences: the Nd-ions could have been used as markers for investigating the as deposited thin films deposited at different Ar-pressures and powers. Obviously crystallinity and a sufficient Nd concentration is needed for a measurable photoluminescent response. For the highest concentrations of Nd there are two reasons why no photoluminescence was measured: (i) the concentrations were too high, resulting in quenching or (ii) the crystal structure formed (not anatase) was not favorable.

4.4.6 Optical properties

For the optical properties it is more suitable to present the results per additive as it allows to directly compare the results obtained for sputtering from mixed oxide targets and ion implantation. The effect of the addition of Fe, Nd and V on the refractive index and band gap are discussed in sections 4.4.6.1, 4.4.6.2 and 4.4.6.3, respectively. The different additives are compared and possible links to the film structure are discussed in section 4.4.6.4.

In the case of doped TiO_2 thin films the refractive index is no longer dependent on the film porosity alone but also on the type and amount of dopant. If the refractive index of the doped thin film at 100% density was known or could be calculated, the porosity could be calculated using equation (2.3), p; 12 with this reference value. An estimate of the refractive index of a mixed oxide can be made also by using equation (2.3), but only if the mixed oxide

consists of two different phases and the refractive index is known for both phases. Unfortunately these two conditions are not fulfilled in our cases, so that it will not be possible to determine the porosity of the doped thin films.

4.4.6.1 Dependence on Fe addition

a. Refractive index

When doping Fe into the TiO_2 thin films deposited at 1.4 Pa and 60 W the refractive index increases from 2 to about 2.2 (Figure 4. 94), independent of the doping technique. For the addition of Fe by sputtering from mixed oxide targets the refractive index is independent of the Fe-content and closer to 2.15. For the addition of Fe by ion implantation the results seem somewhat scattered but can be interpreted to show the same tendency, with the average refractive index being slightly higher. There is little effect of annealing on the refractive index, which is consistent with the findings for pure TiO_2.

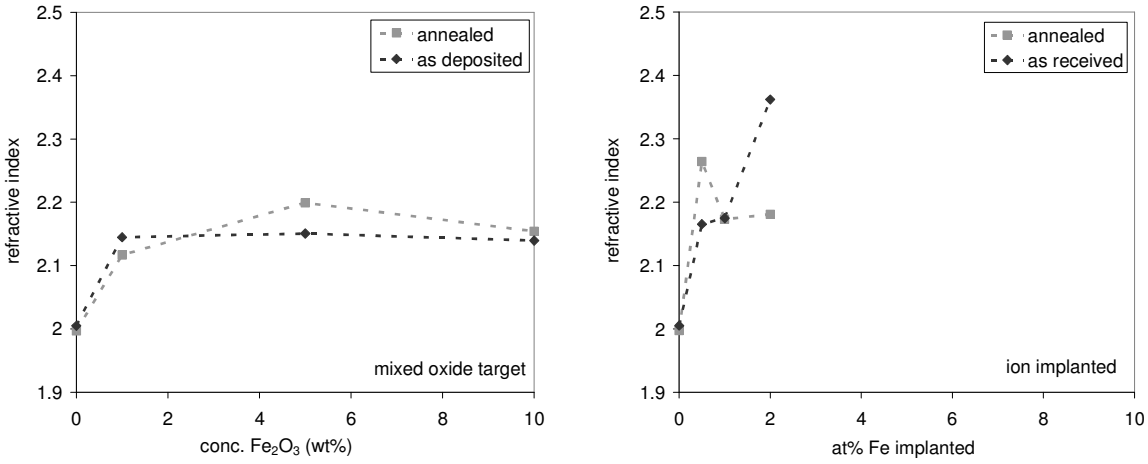

Figure 4. 94:
Dependence of refractive index on the Fe_2O_3 content in the Fe_2O_3-TiO_2 mixed oxide targets (left) and the implanted ion concentration (right) of the thin films deposited at 60 W and 1.4 Pa; as deposited/ received and annealed at 673 K/ 1 h.

The conclusion is, that here the method of Fe doping does not influence the effect of the dopant on the refractive index.

b. Optical band gap

When determining the band gap energy the value of $m = 3$ for the *indirect forbidden* transition yielded the same quality of fit for the as deposited thin films as for the other two values for m used, namely $m = 3/2$ for the *direct forbidden* and $m = 2$ for the *indirect allowed* transition. For the annealed films no linear fit could be obtained using $m = 3/2$ (*direct forbidden*

transition). The pure TiO_2 thin films showed a fit for the *direct forbidden* and the *indirect allowed* transition. The results for the Fe-doped films possibly indicate a change in band gap mode when annealing the Fe-doped TiO_2 thin films. The obtained results are shown in Figure 4. 95 for the films sputtered from mixed oxide targets (top) and ion implanted films (bottom).

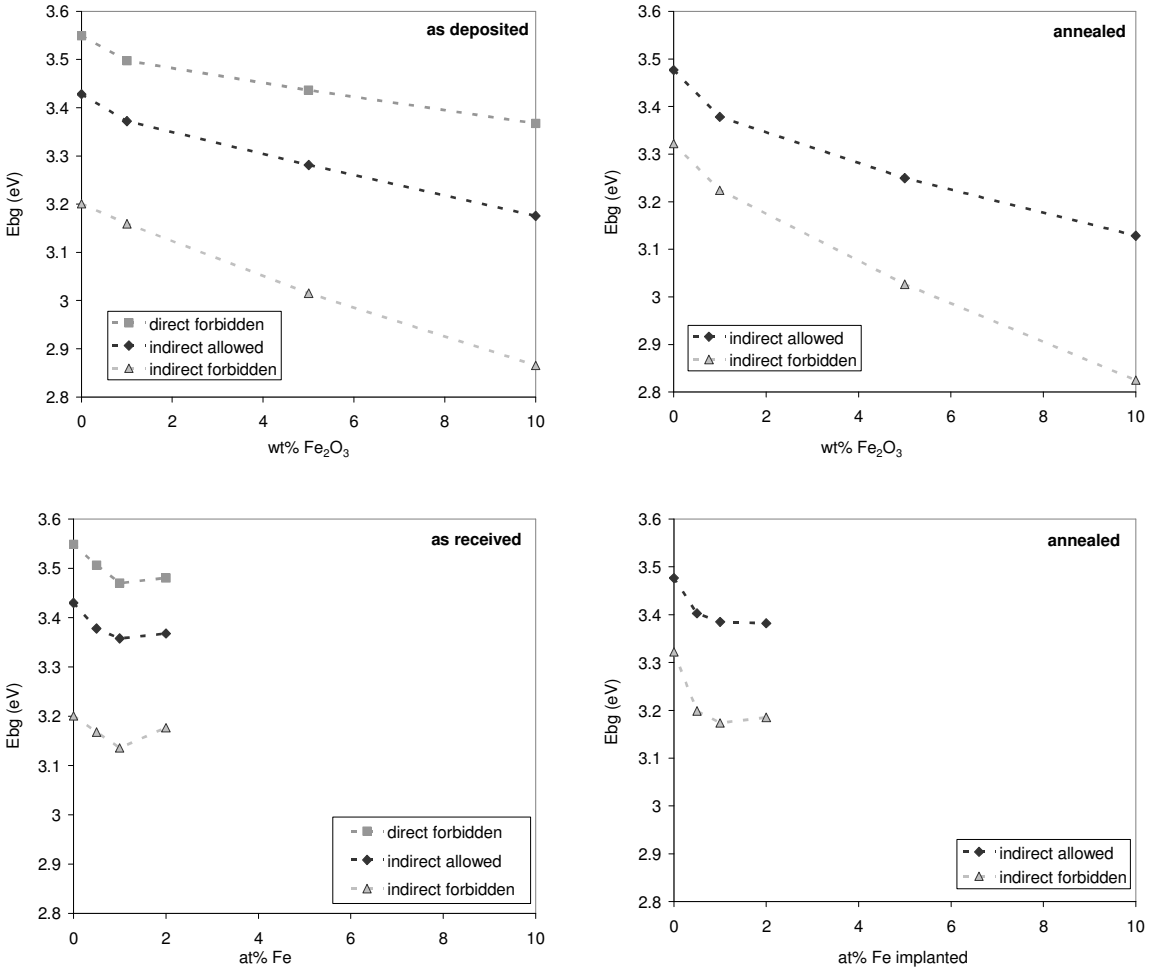

Figure 4. 95:

Dependence of the band gap energy on the Fe_2O_3 content in the Fe_2O_3-TiO_2 mixed oxide targets (top) and implanted Fe content (bottom) of thin films sputtered at 60 W and 1.4 Pa; as deposited (left) and annealed at 673 K/ 1 h (right).

For both dopant methods there is a strong decrease of band gap energy with increasing dopant level up to 1 at% (1 wt%). For higher concentrations the band gap energy seems to level out at 1 at% for the implanted films, while there is a steady decrease in band gap energy with increasing amount of dopant for the thin films deposited from the mixed oxide targets. Looking more closely at the results and taking into account the range of the measurement er-

ror, one sees that the results for the ion implanted films fall into the same range as observed for the comparable concentration in the thin films deposited from the mixed oxide targets.

Films sputtered from the 5 wt% Fe_2O_3/ TiO_2 mixed oxide target showed a yellow color, which intensified for the films deposited from the 10 wt% Fe_2O_3/ TiO_2 mixed oxide target. The color was not affected by annealing. This indicates that the films absorb in the blue part of the visible light spectrum. The band gap values for the films deposited from the 10wt% mixed oxide targets calculated assuming an indirect forbidden transition are close to 2.85 eV. The corresponding wavelength is 443 nm, which agrees with the observed film color. The band gap energy calculated assuming an indirect allowed transition would yield a band gap energy of 3.2 eV, which corresponds to light absorption in the UV part of the spectrum. Unfortunately the color of a thin film is determined not only by its band gap but also other factors like roughness and the thickness itself, so that we cannot draw any conclusions from it.

4.4.6.2 Dependence on Nd addition

a. Refractive index

Figure 4. 96 shows the influence of Nd addition on the refractive index of the doped TiO_2 thin films. On first sight a different behavior is observed for films deposited from mixed oxide targets compared to ion implanted films. Former leads to a steady increase of the refractive index with increasing dopant level, reaching almost 2.4 for films sputtered from the target containing 10 wt% Nd_2O_3.

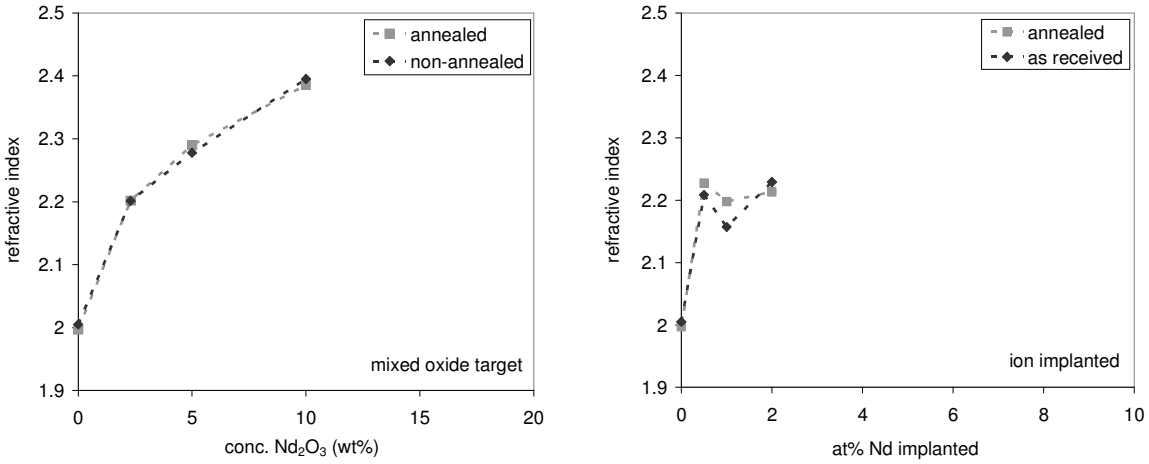

Figure 4. 96:

Dependence of the refractive index on the Nd_2O_3 content in the Nd_2O_3-TiO_2 mixed oxide targets (left) and the implanted ion concentration (right) of the thin films sputtered at 60 W and 1.4 Pa; as deposited/ received and annealed at 673 K/ 1 h.

Ion implantation on the other hand results in an increase of the refractive index to slightly above 2.2; for higher concentrations the refractive index does not change much. This value is close to the one observed for thin films sputtered from a 2.3 wt% Nd_2O_3/ TiO_2 target, which have a concentration of close to 1 at% Nd. Looking more closely one sees that the small range of concentrations for the ion implanted films still falls within the curve observed for the sputtered thin films. The conclusion is, that the method of Nd-addition likely does not influence the refractive index for similar dopant concentrations.

As with the pure TiO_2 films there is no effect of annealing on the refractive index.

b. Optical band gap

In the case of Nd addition to TiO_2 no change in band gap mode is observed. In general there is only a small effect of Nd addition on the band gap energy for thin films deposited from Nd_2O_3/ TiO_2 mixed oxide targets (Figure 4. 97, top): With the addition of a small amount of Nd_2O_3 the band gap energy decreases slightly, leveling out and increasing again for the highest concentration. The initial decrease is stronger after annealing due to the fact that the band gap energy of the pure TiO_2 film is influenced stronger than the one of the doped thin films. Note that the thin films deposited from the mixed oxide targets containing 5 and 10 wt% did not crystallize in the anatase structure.

For the ion implanted films it is also observed that the band gap energy decreases somewhat with increasing dopant level for the lower concentrations and then levels out for higher concentrations. Upon annealing a higher band gap is observed for all concentrations of Nd, which is opposite to the result obtained for the films deposited from the mixed oxide targets.

Independent of the doping technique and the amount of dopant added the observed band gaps remain in the UV, which is reflected by the absence of color in the doped thin films (the blue color of the as received implanted films was due to sub-stoichiometry, section 4.4.2.2).

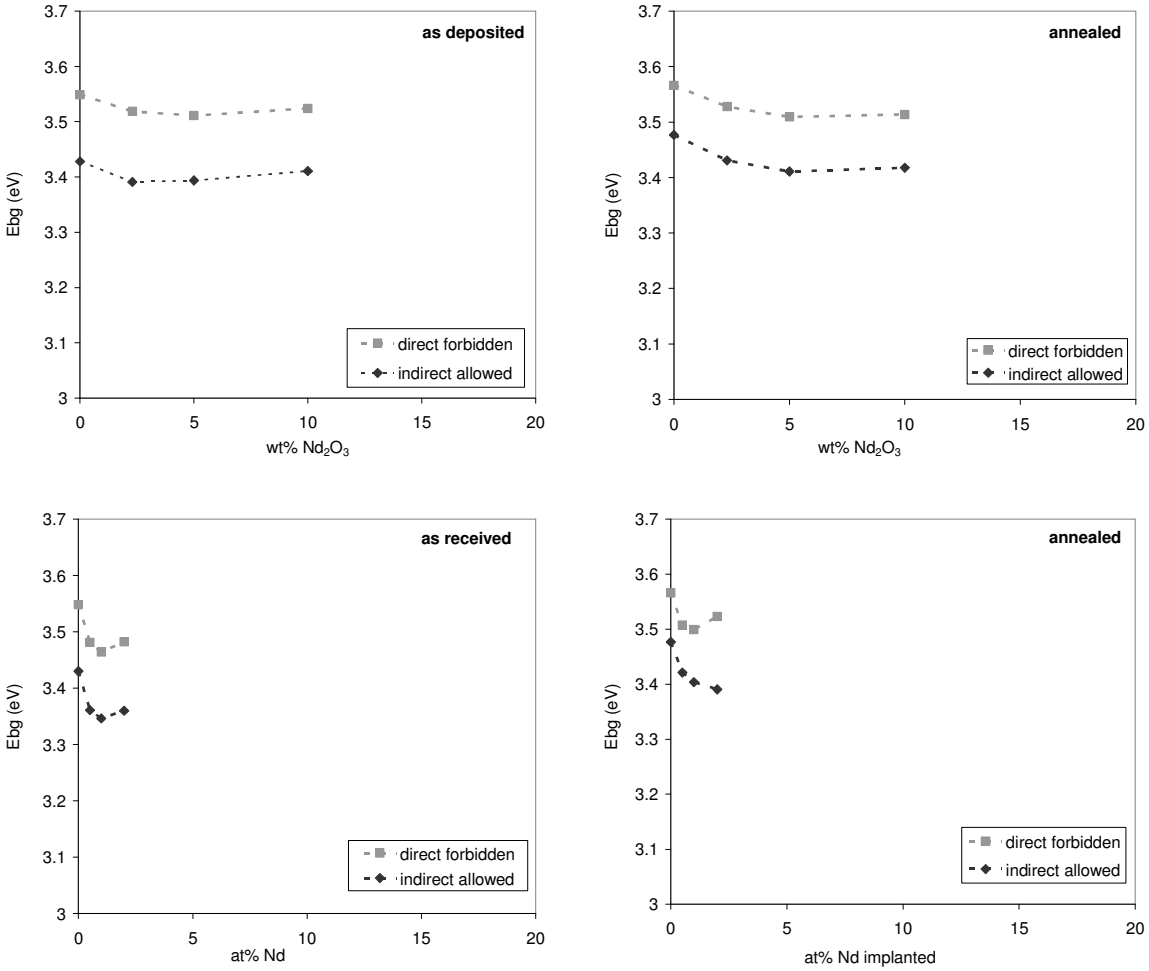

Figure 4. 97:
Dependence of the band gap energy on the Nd_2O_3 content in the Nd_2O_3-TiO_2 mixed oxide targets (top) and implanted Nd content (Bottom) of thin films sputtered at 60 W and 1.4 Pa; as deposited/ received (left) and annealed at 673 K/ 1 h (right).

4.4.6.3 Dependence on V addition

a. Refractive index

As can be seen in Figure 4. 98 the refractive index of the thin films sputtered from the mixed oxide target containing 5 wt% V_2O_3 is similar to that of the pure TiO_2 thin film. Upon annealing the refractive index decreases slightly for the V-doped film.

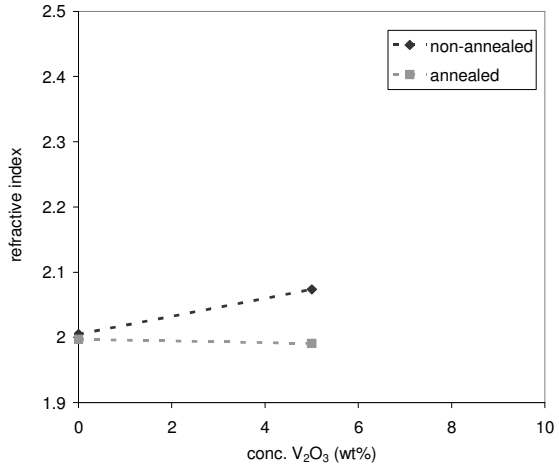

Figure 4. 98:

Dependence of the refractive index on the V_2O_3 content in the V_2O_3-TiO_2 mixed oxide targets of thin films sputtered at 60 W and 1.4 Pa; as deposited and annealed at 673 K/ 1 h.

b. Optical band gap

For the films deposited from the mixed oxide target containing 5 wt% V_2O_3 it was again found that for the annealed films a linear fit could only be obtained assuming an *indirect allowed* or an *indirect forbidden* transition (compare to Fe-doped films, section 4.4.6.1). For the non-annealed films a linear fit could be obtained also for the *direct forbidden* transition. It was already suggested that this indicates a transition in band gap mode upon addition of V, especially for the annealed thin films. The results for the band gap calculations for the film sputtered from the 5 wt% V_2O_3/ TiO_2 mixed oxide target are shown in Figure 4. 99.

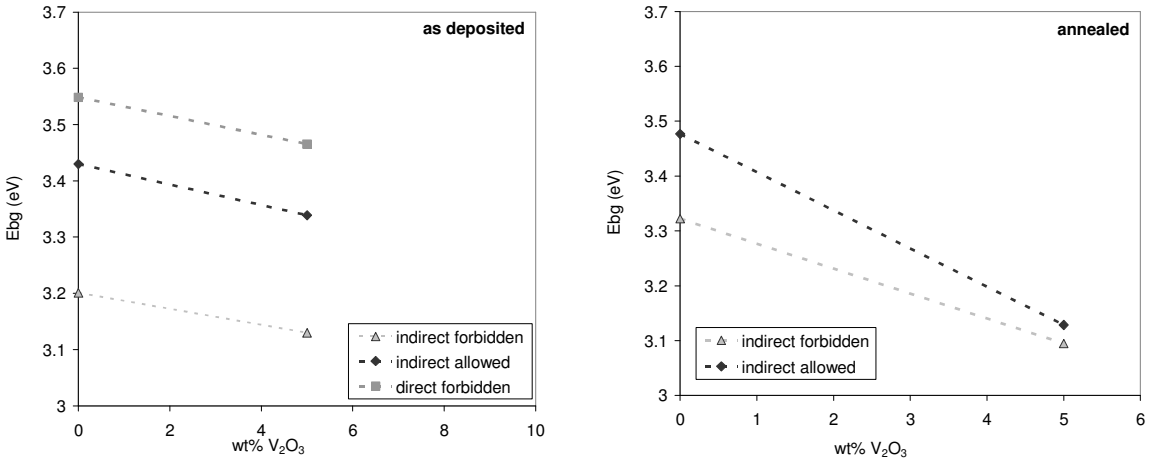

Figure 4. 99:

Dependence of the band gap energy on the V_2O_3 content in the V_2O_3-TiO_2 mixed oxide targets of thin films sputtered at 60 W and 1.4 Pa; as deposited (left) and annealed at 673 K/ 1 h (right).

No change in color was observed for these films, which can be understood when looking at the band gap values: These are close to 3.1 eV when calculated assuming the *indirect forbidden* transition mode and 3.35 (3.15) eV when assuming the *indirect allowed* transition mode for the as deposited (annealed) films. These band gap energies correspond to light in the UV range of the spectrum.

While for the pure TiO_2 films there is an increase in band gap energy after annealing, there is a slight decrease observed for the V-doped thin films.

4.4.6.4 Discussion of the effect of dopant addition on the optical properties

The decrease (red-shift) of the band gap energy for Fe and V doped TiO_2 was reported in literature (section 2.6.5.1) and is confirmed here. A strong red shift was observed for the thin films sputtered from the mixed oxide targets, especially for the thin films deposited from targets containing 10 wt% Fe_2O_3. The transition of the band gap mode observed for the Fe and V doped films indicates, though, that the nature of the effective band gap was changed. The *intrinsic* band gap transition mode of anatase TiO_2 cannot change since it is determined by the crystal lattice. But there are reasons why the *apparent* transition mode can be different. One possibility is that defect states introduced into the anatase band gap distort the optical absorption of the material making it difficult to obtain the correct transition mode. The second possibility is that the thin films consist of anatase embedded into an amorphous matrix (not detected in XRD) which has a lower band gap energy and an *indirect forbidden* band gap transition. Since its band gap is lower than anatase the measured effective band gap would have the properties of this phase. This second phase should be a Fe/ Ti compound since the solubility of Fe in anatase is rather low (section 2.6.5.1)

Nd doping had only a minor effect on the band gap, which was preserved for thin films sputtered from mixed oxide targets containing 5 and 10 wt% Nd_2O_3, even though these films do not show the anatase structure. This can be explained by assuming that the unknown crystalline phase observed at the high dopant levels is embedded in an amorphous TiO_2 matrix. If the band gap of this crystalline phase is higher than that of anatase, then latter will determine the observed effective band gap.

For none of the doped thin films any presence of donor or acceptor levels in the band gap was indicated in the transmission spectra. The absorption edges showed a smooth, continuous decrease of the transmission (not considering the interference fringes) with decreasing wavelength, which was not different from the absorption edge of the pure TiO_2 thin films. Accord-

ing to literature, the presence of the dopants should result in acceptor states for Fe and donor states for Nd (and V if present in the 5+ state) within the band gap (section 2.6.5.1). The reasons for the different behavior of the doped thin films lies in the high dopant concentrations used. In this case the discrete dopant levels merge to a continuous impurity band [Pankove71].

4.4.7 Photocatalytic activity

The results will again be presented per additive to directly compare the two different doping methods. The effect of the addition of Fe, Nd and V will be discussed in sections 4.4.7.1, 4.4.7.2 and 4.4.7.3, respectively. Possible relationships between the structural, optical and photocatalytic properties will be discussed in section 4.4.7.4.

The Fe-doped films, when sputtered from mixed oxide targets, showed a strong reduction in band gap energy with increasing amount of dopant. Therefore, their photocatalytic activity was tested by cutting out the UV part of the lamp spectrum (please refer to section 4.3.5.2). These results will also be included in section 4.4.7.1.

4.4.7.1 Dependence on Fe-addition

Figure 4. 100 shows the dependence of the photocatalytic activity on the amount of dopant for the thin films sputtered from the mixed oxide targets (left) and the ion implanted films (right). For the as deposited and as received films the photocatalytic activity decreases slightly with increasing Fe-content, which is less obvious for the ion implanted films where the concentration is lower. The low activity measured for the film implanted with 0.5 at% is most likely an artifact.

Upon annealing the photocatalytic activity decreases with increasing Fe-content for the films sputtered from mixed oxide targets, while it increases or remains unchanged for the ion implanted films. One has to remember that the implanted films showed a visible sub-stoichiometry, but this does not seem to have affected their photocatalytic activity. As discussed in section 2.5.1.4 the effect of sub-stoichiometry is still a matter of discussion.

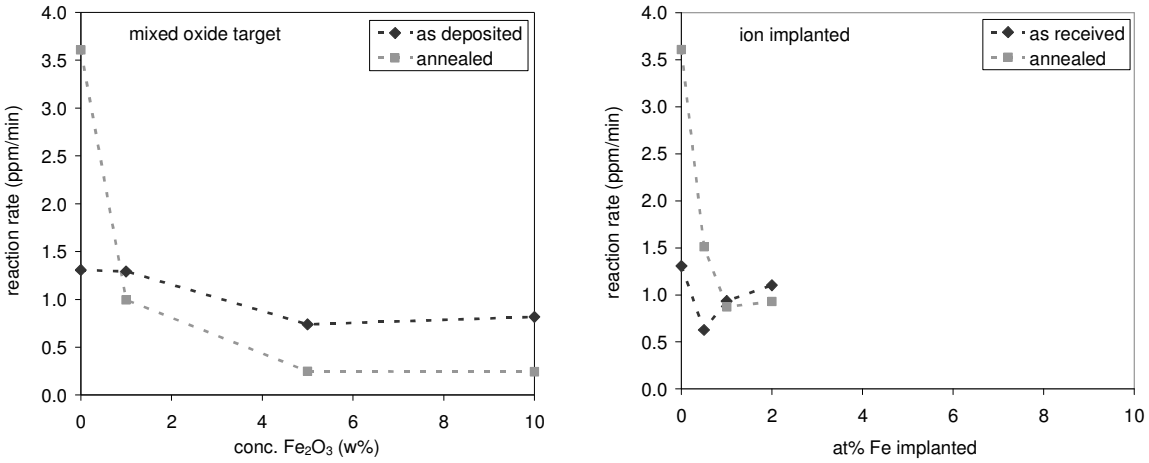

Figure 4. 100:

Dependence of the photocatalytic activity on the Fe_2O_3 content in the Fe_2O_3-TiO_2 mixed oxide targets (left) and the implanted Fe-ion concentration (right) of thin films sputtered at 60 W and 1.4 Pa; as deposited/ received and annealed at 673 K/ 1 h.

In section 2.6.5.1 it was mentioned that increasing concentrations of Fe decreased the photocatalytic activity in UV (for crystalline films), which is confirmed here. This effect is much stronger for annealed films than for as deposited and as received films. With latter, interestingly, the effect of dopant addition is not very strong. The polishing effect on the surface (section 4.4.1.2) observed for the ion implanted films, does not seem to have influenced the photocatalytic activity of the thin films significantly. Additionally, the film is most likely not doped through the whole thickness, so that part of the column-grain sides is still pure and, therefore, more active TiO_2. Possibly the two effects compensate each other.

Note, that the normally strong positive effect of crystallization is off-set by a much stronger effect caused by the presence of the dopant. The film sputtered from the target containing 10wt% Fe_2O_3 remains XRD amorphous after annealing, but still shows the reduction of the photocatalytic activity.

Photocatalytic activity with VIS light

A thin film deposited from the 10 wt% Fe_2O_3/TiO_2 mixed oxide target (as deposited) was tested using only the VIS light emitted from the UV lamp. For this the 395 nm cut-off filter was used (section 3.1.2.1). A second layer was tested using the full lamp spectrum to have a direct reference. The results are summarized Table 4. 8 on the following page:

Illumination	Reaction rate (ppm/min)
Full lamp	0.545
395 nm filter	0.113
No UV (P25)	0.174

Table 4. 8: Photocatalytic activity of thin films deposited from a 10 wt% Fe_2O_3/TiO_2 mixed oxide target (as deposited), with full lamp spectrum and only with VIS part of lamp spectrum.

The photocatalytic activity using the full lamp spectrum is somewhat lower than shown in Figure 4. 100. The activity of the film under VIS light is comparable to the black rate measured with P25, even though the band gap of the doped film has shifted to VIS light. This could have as possible reasons: (i) The intensity of the VIS-light having an energy above the band gap of the film is too low to see any measurable photocatalytic activity. (ii) The band gap is higher than the value of 2.9 eV as calculated assuming an indirect forbidden transition. (iii) The absorption at wavelengths between 395 nm and the band gap is not sufficiently high to yield a strong photocatalytic activity, at 395 nm the transmission is still 35%. (iv) The photocatalytic active phase in the thin films is only the TiO_2 phase and not the mixed oxide phase (see discussion 4.4.6.4). The rather high transmission at 395 nm indicates that the active band gap is higher than 2.9 eV (443 nm). The lamp spectrum (Figure 3. 6, p. 116) shows that there is still rather high VIS activity below 445 nm. Therefore we can conclude that most likely the low VIS activity of the Fe-doped thin films is due to the photocatalytically active phase being the TiO_2 phase, which has a band gap energy of higher than 3.2 eV.

4.4.7.2 Dependence on Nd-addition

Figure 4. 101 shows the effect of Nd-incorporation into the TiO_2 films on the photocatalytic activity. For the thin films deposited from Nd_2O_3/ TiO_2 mixed oxide targets the photocatalytic activity decreases with increasing Nd-content. Annealing results in a further decrease of the photocatalytic activity. This is opposite to the behavior seen for pure TiO_2 thin films (section 4.3.5), where a strong increase was observed.

The as received ion implanted films show a similar behavior as the as deposited films from mixed oxide targets. The annealed ion implanted films show a rather scattered behavior, but on average their photocatalytic activity is approximately the same as for the as received films. Again, the polishing effect on the surface (section 4.4.1.2) observed for the ion im-

planted films, does not seem to have influenced their photocatalytic activity significantly, or is compensated by the not complete doping of the thin film.

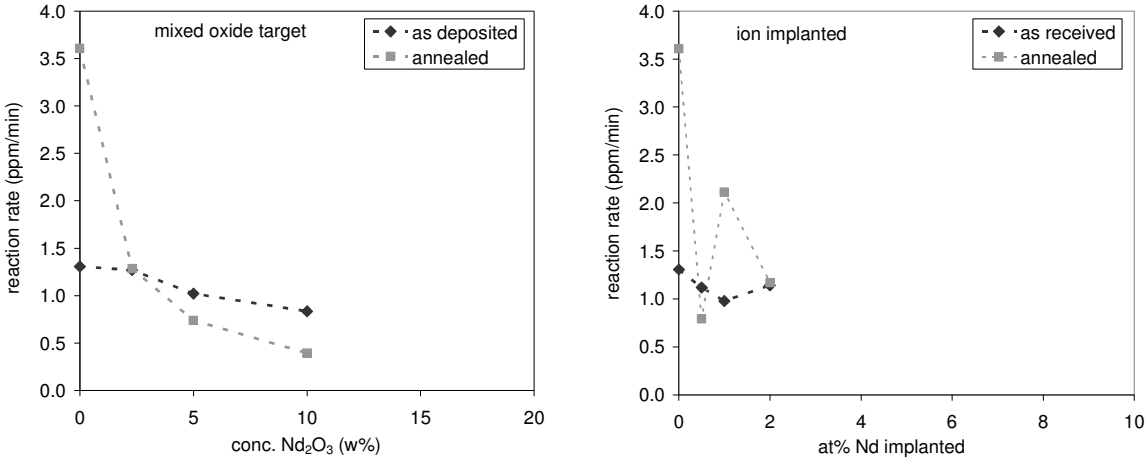

Figure 4. 101:

Dependence of the photocatalytic activity on the Nd_2O_3 content in the Nd_2O_3-TiO_2 mixed oxide targets (left) and the implanted Nd-ion concentration (right) of thin films sputtered at 60 W and 1.4 Pa; as deposited/ received and annealed at 673 K/ 1 h.

4.4.7.3 Dependence on V addition

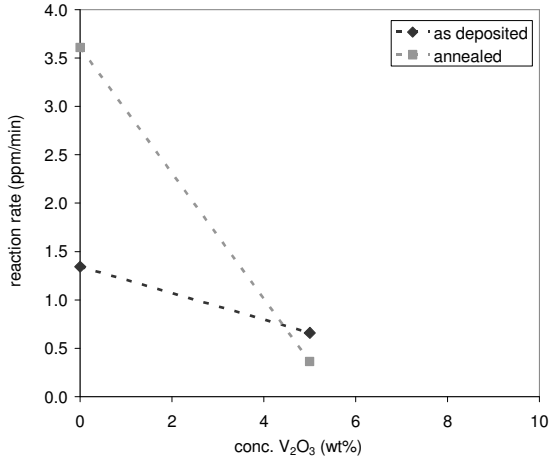

Figure 4. 102:

Dependence of the photocatalytic activity on the V_2O_3 content in the V_2O_3-TiO_2 mixed oxide targets of thin films sputtered at 60 W and 1.4 Pa; as deposited and annealed at 673 K/ 1 h.

For the thin films sputtered from the 5 wt% V_2O_3/TiO_2 mixed oxide target the same trend as for the other two dopants can be observed, namely that the photocatalytic activity is decreased upon addition of V, with the annealed film showing a lower photocatalytic activity than the as deposited film (Figure 4. 102).

4.4.7.4 Discussion of the photocatalytic activity

In summary, the effect of the dopants investigated on the photocatalytic activity was similar, independent of the dopant and the doping technique. This indicates that the presence of the impurity itself is the cause for the negative effect. Compared to the dopant levels reported in literature the levels used in this study were rather high, with exception of possibly the implanted concentration of 0.5 at% for Fe and Nd. What is also striking is that the negative effect is less for the amorphous phase, while it is very strong for the annealed samples. This indicates that there are structural factors controlling the photocatalytic activity. A more detailed discussion of this issue follows in the subsequent section.

4.4.8 Discussion of the doped TiO_2 thin films

In this section possible relationships between the photocatalytic activity and the structural and optical properties of the doped thin films will be discussed. First some general observations and conclusions will be highlighted (section 4.4.8.1). Then influences of doping on the microstructure (section 4.4.8.2), crystallinity (section 4.4.8.3) optical (section 4.4.8.4) and photocatalytic (section 4.4.8.5) properties will be summarized.

4.4.8.1 General observations

The most important observation is that the methods of doping implemented in this study and/ or the elements/ concentrations used had a negative effect on the photocatalytic activity of the TiO_2 thin films. The reasons for this most likely lie in changes to the electronic structure and surface composition of the material, as will be discussed further below.

Ion implantation caused a polishing effect on the surface (section 4.4.1.2). The photocatalytic activity of the Fe and Nd-doped TiO_2 thin films did not depend on the doping technique, so that surface polishing due to ion implantation had no effect. This indicates that (i) the roughness of the column-grain tops does not influence the photocatalytic activity of the thin films and/ or (ii) the limited implantation depth leaves part of the column-grains dopant-free so that these surfaces have the same reactivity as pure TiO_2. Additionally, for the thin films implanted with 2 at% Nd the implantation profile was not as intended. Most likely this the case for all other implanted films. The reason is the partially ionic nature of the bonding in TiO_2 which makes it very difficult to predict the implantation behavior of a given ion beam.

When annealing the thin films several changes in their crystallization behavior occurred. The first is, that the normally strong positive effect of crystallization on the photocatalytic

activity is off-set by a much stronger effect caused by the presence of the dopant. This results in the reaction rate of the annealed doped films being even smaller than that of the as deposited/ received films. The second observation is, that doping affected the development of a preferred out of plane orientating. For Fe the ion implanted films all showed an almost random orientation, while the films sputtered from mixed oxide targets showed a strong (004) preferred orientation (when crystalline). The crystallization behavior of the Nd-doped films was found to depend on the doping technique for Nd concentration above 1at%. At and below this concentration the thin films crystallized similar to the pure TiO_2 thin films, namely with a (004) preferential out of plane orientation. Since for both dopants no difference in photocatalytic activity was observed between the two doping techniques it must be concluded that the crystallographic orientation does not play a role.

It was not possible to calculate the porosity of the doped samples since the doping itself most likely influences the refractive index in an unpredictable way.

4.4.8.2 Microstructure

The thin films sputtered from mixed oxide targets showed an influence of the dopant in higher concentrations for Nd and to a less extent for V, but not for Fe. The microstructure of the thin films deposited from mixed oxide targets was found to depend strongly on the amount of Nd_2O_3 in the target. The films sputtered from the 2.3 wt% mixed oxide target looked quite similar to the pure TiO_2 films. For higher Nd_2O_3 content the layer density increased. The films deposited from a target containing 10 wt% Nd_2O_3 showed a quite different microstructure, having a very smooth surface, and no column-grain structure could be identified in cross sectional SEM for both the as deposited as well as the annealed film. The increasing film density should contribute to the decreasing photocatalytic activity of the Nd-doped thin films. There were some microstructural differences between the pure and the V-doped thin films but it was not possible to draw any conclusions about the film density from the SEM images.

For the ion implanted films a ‘polishing’ of the surface was observed. For the Nd implanted films an altered top layer of about 100 nm was seen, but not for the Fe-implanted films. For all doped films no second phases could be observed in SEM, before or after heat treatment. This is not surprising, when looking at the deposition and annealing conditions. During deposition from the mixed oxide targets one would expect, on a macroscopic scale, a statistical distribution of the dopant throughout the thin film. On the local scale, though, it is probable that ordered structures are formed which can act as nucleation sites for crystal

growth (section 4.3). It can, therefore, be expected that on local scale the dopant distribution is not completely random, which upon annealing can lead to further segregation. This segregation cannot be on a large scale, though, since the ESCA depth profile of the ion implanted sample showed that the implantation profile is not affected by the anneal treatment (with a depth resolution of 10 nm and a lateral resolution of mm). The major problem with determining the dopant distribution is that no experimental technique was available that allowed investigation on a nanometer scale. For the ion implantation one expects a random distribution on the local scale, but as shown by the ESCA depth profile, the distribution throughout the film is inhomogeneous. Upon heat treatment some local relaxation can be expected, but the crystallization behavior of the films indicated that the initial local structure of the thin films was destroyed in the implanted zone.

4.4.8.3 Crystallinity

The XRD spectra showed that the thin films doped with Fe and V all crystallized in the anatase structure, with exception of 10 wt% Fe_2O_3 which remained amorphous. No second crystalline phase could be identified. This is also not expected since the low anneal temperatures do not allow for re-structuring of the column-grains (section 4.3). It is impossible to detect an amorphous phase from XRD spectra, so that it cannot be excluded that such a second phase is indeed present due to incomplete crystallization. As a result there is the possibility that the dopants remain mostly in the amorphous phase so that only a (very) small amount is incorporated in the crystalline phase. This effect was reported in [Ball06b] and was referred to as ‘self-cleaning effect of nano-particles’. This segregation should lead to a higher dopant concentration at the thin film surface which has been reported to be detrimental to the photocatalytic activity of Ti_2O (section 2.6.5.1). On the other hand, ESCA analysis did not show any increased dopant concentration at the sample surface so that segregation (to the surface) is most likely not possible with the thin film preparation methods used.

While Fe and V behave rather similar as dopants towards crystallization, the films doped with Nd showed anatase crystallization only for the lowest concentration. At higher concentrations a not identified other crystalline phase was formed which, most likely, is a Nd-Ti-O compound. Here also only one crystalline phase was detected. In the case of Nd the dopant remains in the amorphous phase for low concentrations, but for higher Nd concentrations the dopant rich phase and not anatase crystallizes. The same arguments against restructuring of the column-grains during crystallization are valid for Nd-doped samples as well.

4.4.8.4 Optical properties

The red-shift of the band gap reported in literature was observed for the Fe and V doped films, which was stronger in the annealed films. Additionally, the results indicated that a shift in band gap transition mode from indirect allowed to indirect forbidden occurred with increasing Fe and V content, especially after annealing. For the Nd doped films a very small red shift of the band gap was observed, and the band gap was not influenced significantly by the anneal treatment. For all dopants no impurity levels inside the band gap could be detected in the transmission spectra which was linked to the high dopant levels.

It was suggested that the observed band gap of the thin films could be explained by assuming the presence of two phases. The first phase would be a highly doped or mixed oxide phase, the second a (very) low doped TiO_2 phase. The phase with the lower optical band gap determines the observed band gap of the thin film. In the case of the Fe and V doped films it was indicated that the unknown phase had the lower band gap, because the nature of the band gap transition was changed and there was a strong effect of the dopant on the band gap. In the case of Nd doping it was indicated that the band gap of TiO_2 was dominating, as there was little influence of the dopant on the band gap.

Little information could be gained from the refractive index as it was not possible to calculate the porosity due to the unknown sample structure.

4.4.8.5 Photocatalytic activity

The introduction of dopants into TiO_2 thin films caused a variety of structural and optical changes, but the effect on the photocatalytic activity was similar for all types of dopants and methods, namely that it decreased with increasing amount of additive and was further lowered after a heat treatment. This common behavior could be explained by assuming that the thin films consisted of two phases, one being (anatase) TiO_2 and the other being a dopant rich phase. As discussed in section 4.4.8.2 dopant diffusion during the anneal treatment is limited. On the other hand, in nano-sized grains the dopant is likely to segregate to the grain boundaries, forming a second phase. In all cases the second phase was not detected in XRD, with exception of the annealed films doped with a high concentration of Nd where only this phase was found. The volume of the dopant rich phase can be expected to increase with increasing amount of dopant and after a heat treatment, which is likely to cause segregation. If the photocatalytic activity of the dopant rich phase is lower than that of TiO_2 this would explain the decrease in photocatalytic activity with increasing dopant level and after heat treatment.

For the thin films deposited from Nd_2O_3/ TiO_2 mixed oxide targets possibly an increase in film density (as observed in SEM) could also be contributing to the decrease in photocatalytic activity. The negative effect of increasing density was described already for the pure TiO_2 thin films in section 4.3.5.3.

Concerning the dopant distribution on the nano-scale only theoretical considerations can be made since it was impossible to measure with the available equipment. For the as deposited and as implanted films one can expect that there is a long range statistical mixture of the dopant and Ti in the thin film. As already discussed in section 4.4.8.2 there are indications that there is some local ordering of the dopant atoms (at least in the sputtered films). The XRD amorphous structure is, by definition, full of defects so that the dopant atoms do not change the situation strongly. One will have to take into account that the number of active sites at the surface will be lower due to some Ti being replaced by a dopant cation, which is, presumably, not photocatalytically active.

The stoichiometry of the cations was not determined. For Nd the only possibility is the +3 state. For iron, indications in literature are, that also the +3 state is the most likely. For V the possibility of the +4 and the +5 state exists. The fact that the band gap of V could be explained by the presence of a V rich amorphous phase indicates that V has a higher solubility in the amorphous than in the anatase crystal phase. As discussed in section 2.6.5.1 V^{4+} has a high and V^{5+} a low solubility in anatase TiO_2. The conclusion is, that V most likely is present in the 5+ state.

Interestingly the ‘polished’ surface and altered top layer observed after ion implantation did not influence the photocatalytic properties of the thin films; they follow the same dependencies as the films sputtered from mixed oxide targets. This indicates that the surface structure of the column-grains is of less importance as compared to their density and spacing or is compensated by the remaining unchanged part of the column-grains which consist of pure TiO_2.

5 Conclusions and outlook

During this thesis a batch reactor for testing the photocatalytic activity of thin films was developed, the relationships between microstructure, optical properties and photocatalytic activity of TiO_2 thin films were investigated and the effect of dopant addition on the thin film properties was studied.

The development of a photocatalytic test reactor in form of a batch reactor was successful. A reproducible test system has been developed. The only drawback was the lack of a reproducible external standard as no commercial TiO_2 thin film with good photocatalytic properties could be found.

The sputter deposition of TiO_2 thin films was studied and TiO_2 thin films could be deposited reproducibly by sputter deposition from sub-stoichiometric TiO_{2-x} targets. The effect of sputter deposition from M_2O_3/ TiO_2 (M = Fe, Nd, V) mixed oxide targets was studied to see the influence of the additives on the sputtering behavior.

First the influence of the deposition parameters on the thin film structure, optical and photocatalytic properties was studied for the pure TiO_2 thin films. It was discovered that the thin films microstructure played a major role for the photocatalytic activity, the most active films showing the highest porosity. Additionally the thin film thickness was found to be very important below 350-400 nm. The experiments performed with light of different wavelengths showed that the photocatalytic activity was not diffusion limited up to a film thickness of 1 µm. Most likely the porous microstructure of the thin films played a major role for this behavior. It became clear that in order to determine the influence of parameters like band gap, crystallite size, lattice strain, etc. it will be important to keep the microstructure (i.e. the porosity, surface area, etc.) unchanged and work at the same film thickness. In literature these two factors are often not accounted for when discussing the influence of deposition and post deposition treatments on the photocatalytic activity of thin films.

Secondly, the effect of dopants incorporated by sputter deposition from M_2O_3/ TiO_2 targets and ion implantation was studied for M_2O_3 concentrations in the target between 1 and 10 wt% (M = Fe, Nd, V) and implanted ion concentrations of 0.5 to 2.0 at% (Fe, Nd), respectively. For the films deposited from mixed oxide targets it was found that Fe and V had little effect on the thin film microstructure while Nd had a strong effect. Ion implantation resulted in a polished surface structure, which had little influence on the photocatalytic activity,

though. The crystallization behavior of the thin films was strongly influenced by the dopant addition. Overall the addition of the dopants was detrimental to the photocatalytic activity, decreasing it slightly for the as deposited films and leading to a decreased activity after annealing. It was suggested that this is due to dopant segregation to the grain boundaries. Diffusion to the film surface was not detected with ESCA. A shift in optical band gap to VIS was observed for V and Fe doped films. The photocatalytic activity was too low to measure VIS light activity for thin films where a red shift in optical band gap was observed (Fe). In conclusion, the method of doping and/ or the dopant elements/ concentrations used in this thesis was not successful for improving the photocatalytic activity or yielding VIS light active films. Another conclusion is that doping to improve the VIS light photocatalytic activity is not straightforward but will require quite some fine tuning, especially regarding the red shift of the band gap. However, one will have to ensure that the doping method does not result in microstructural changes which have a profound influence on the photocatalytic activity.

Possibilities for future research

There are many aspects governing the photocatalytic activity of TiO_2. This thesis goes beyond the mere photocatalytic activity of d.c. magnetron sputter deposited TiO_2 thin films, because the structural and optical characterization of these materials was also performed. There were still many questions left unanswered and some of the most intriguing questions are presented here as suggestions for further research.

1) Structure of the XRD amorphous thin films

The experimental results show that the structure of the amorphous films has to be influenced by the thin film deposition conditions. Possibly, some nucleation sites are formed, i.e. very small crystallites, which then grow during the heat treatment step. It would be interesting to see whether indeed these crystallites exist, and more in general to investigate the local structure of the material, especially the nature of the TiO-bonding (bond distances and coordination numbers). For these investigations more complex analysis techniques would be needed. Visualization of small crystallites can be done using (HR)TEM, which, unfortunately, is not straightforward for brittle ceramic films. A technique suitable for investigating the local structure in matter is EXAFS/ XAS (Extended X-Ray Absorption Fine Structure/ X-ray Absorption Spectroscopy). A difficulty may be the presence of irregular bonding environments in the amorphous films that could lead to signals which are difficult to interpret.

2) Nature of the band gap transition in anatase and amorphous TiO_2 thin films

Even though there exists extended literature on the photocatalytic activity of anatase TiO_2 and how to shift its band gap to visible light, there is little known about the nature of the band gap transition in anatase and nothing for amorphous TiO_2. In order to discuss the influence of the band gap on the photocatalytic properties, especially with respect to doping, it will be important to know more about this issue. This could be obtained from careful optical measurements on thicker films and single crystals.

3) Thickness dependence of the photocatalytic activity

In this thesis it was tried to shed some light on the nature of the thickness dependence of the photocatalytic activity of TiO_2 thin films. Unfortunately the columnar microstructure of the films did not allow to measure the diffusion length of the charge carriers. In order to solve this matter it will be necessary to work with a highly dense thin film, which due to its low surface area will have a very low photocatalytic activity. In order to have measurable organic breakdown it will be necessary to use larger sample sizes to enlarge the surface area.

4) Photocatalytic activity of doped TiO_2 under VIS light (> 400 nm) illumination

This issue is very intriguing but not very well understood. It seems that not only the nature and concentration of the dopant but also its location in the material are important. According to the investigations presented in this thesis high amounts of dopant are needed to shift the band gap into the VIS range. The resulting photocatalytic properties were worse than those of pure TiO_2, especially after annealing. From literature it seems that small dopant levels may be more successful. Here the red-shift of the band gap can be expected to be small, though. In this context it will be important to determine the exact dopant concentration and distribution in the thin films. A possible technique may be SIMS.

It will be necessary to examine the importance of the dopant location. It may be interesting to devise a film composition were the dopant is present in the bulk but not at the surface, which has been proposed in [Anpo03]. This means that it has to be investigated whether it is beneficial to preserve the photocatalytically active TiO_2 surface while altering the electronic properties of the bulk.

For the type of dopant there is a discussion whether cationic or anionic dopants will be more successful. One promising dopant is N^{3-}, which can be incorporated into TiO_2 thin films by adding N_2 to the sputtering gas. Another issue is the concentration of oxygen vacancies in the material. It may be interesting to try to change the O_2 concentration in the sputter gas. It

will be necessary though, to use other methods than ESCA to asses the oxygen concentration in the sputter deposited films.

5) Reactivity of the (doped) thin films towards other volatile organic compounds (VOC's)

The reactivity of a given photocatalyst may vary with the organic compound investigated. It will be interesting to test the thin films deposited in this thesis with other (types) of VOC's.

Summary

In this thesis the first and main goal was to investigate the effect of structural and optical properties of TiO_2 thin films on their photocatalytic activity. The thin film deposition technique implemented was d.c. magnetron sputtering. Prior to thin film deposition the sputtering behavior of the sub-stoichiometric TiO_{2-x} ceramic targets was determined and compared to reactively sputtering from metallic Ti targets. As a result of this study it was chosen to continue with sub-stoichiometric TiO_{2-x} ceramic targets. This technique allows to control the thin film structure by varying the deposition parameters. Using TiO_{2-x} targets allowed for sputtering in pure Ar to obtain stoichiometric TiO_2 thin films. The deposition parameters varied for thin film deposition were the applied d.c. power (60 - 180 W) and the Ar-pressure (0.47 - 2.2 Pa). The as deposited thin films were XRD amorphous and could be crystallized by heating to temperatures above 573 to 673 K, depending on the deposition parameters. For all films the microstructure, film density/porosity, crystallization behavior, refractive index, optical band gap and photocatalytic activity were determined.

The thin films were found to consist of column-grains extending through the thickness of the film. The density/porosity of the thin films, i.e. the spacing of the column-grains was dependent on the deposition conditions. The porosity increased strongly with Ar-pressure (from 5 to 25%) and decreased less strongly with increasing sputtering power (from 22.5 to 11%), but was not significantly affected by the annealing conditions. The crystalline thin films showed a random orientation at the lowest Ar-pressure and an increasing preferential (004) out of plane orientation with increasing Ar-pressure. This preferential orientation was reduced with increasing sputtering power but not affected by the annealing conditions. The band gap of the thin films increased with Ar-pressure and showed a small decrease with increasing sputtering power. Annealing resulted in an increase of the band gap at high Ar-pressures and a decrease at low Ar-pressures.

The photocatalytic activity of both the as deposited as well as the films crystallized by annealing was investigated and linked to the deposition conditions. It was found that the film density/porosity (i.e. film microstructure) and crystallinity were the most important factors. Increasing the porosity by increasing the Ar-pressure resulted in a more than 5-fold increase of the photocatalytic activity. Crystallization resulted in a more than 2-fold increase. The photocatalytic activity was found to be the highest for the thin films deposited at 60 W and 1.4 - 2.2 Pa and crystallized by an anneal treatment at temperatures of 673 K or higher. These

films show a photocatalytic activity of 3.5 ppm/min towards the breakdown of ethanol in the test reactor developed during this study. These results compare well to the photocatalytic activity measured for a P25 reference coating. Another important factor determining the photocatalytic activity of the thin films was their thickness. Results in literature reporting a steep increase of the photocatalytic activity with increasing film thickness up to a saturation thickness were confirmed. The activity of the films was found to be proportional to the number of absorbed photons, meaning that the thickness dependence of the activity was controlled by the absorption of light. This was interpreted to be a result of the column-grain structure and the porous nature of the thin films, which allows the charge carriers to react at the sides of the column-grains.

A second goal of this study was to investigate the effect of dopants/ additives on the structural development as well as the optical and photocatalytic properties of the TiO_2 thin films. Doped films were prepared by deposition from M_2O_3/ TiO_{2-x} mixed oxide targets (M = Fe, Nd, V) and ion implantation (Fe, Nd) into as deposited TiO_2 thin films. Prior to thin film deposition the effect of adding a second oxide to the TiO_2 targets on the sputtering behavior was investigated. For thin film deposition the parameters resulting in the best photocatalytic activity for pure TiO_2 thin films (60 W, 1.4 Pa, as deposited and annealed at 673 K/ 1 h) were chosen for investigating the effect of dopant concentration. The concentrations of the dopants for the mixed oxide targets were between 1 and 10 at%. For ion implantation it was aimed at introducing the dopants into the top 40 nm of the thin film in concentrations between 0.5 and 2 at%.

The influence of the dopants on the properties of the TiO_2 thin films was rather complex and sometimes dependent on the doping technique. While the changes in microstructure, crystallization behavior and optical properties varied among the dopants, the deposition method and concentration, their effect on the photocatalytic activity was quite comparable. In all cases the photocatalytic activity decreased moderately with increasing dopant content for the as deposited layers, resulting in a decrease of about 1/3 for the highest dopant concentrations. The strongest difference to the pure TiO_2 films was noticed upon annealing: where for latter a more than double increase in photocatalytic activity was seen, the former showed a decrease, so that the annealed doped thin films had an activity of less than 1/7 of that of the pure TiO_2 film. Even though the photocatalytic activity of TiO_2 could not be improved valuable knowledge on the effect of introducing additives into TiO_2 thin films was gained.

A third goal of this thesis was to develop a reliable reactor and procedure for testing the photocatalytic activity of the (doped) TiO_2 thin films. The choice was a batch reactor which operated with a controlled, dry atmosphere consisting of 80% Ar and 20% O_2 to simulate air. The photocatalytic reaction chosen for comparing the reactivity of the thin films was the breakdown of ethanol to acetaldehyde. Into the reactor a chosen amount of organic test substance could be injected. For illumination a high pressure mercury arc lamp was used. This specialized reactor allowed to investigate the effect of incoming light intensity, humidity, concentration of ethanol and substrate temperature. As a standard to ensure the functioning of the reactor a spin coated layer of Degussa P25 powder was used. The final choice of standard conditions for photocatalytic testing were an ethanol concentration of 273 ppm (containing 5 vol% water from the ambient atmosphere), a lamp input power of 100 W and a substrate temperature of 313 K. To determine the reaction rate the initial slope of the decay in ethanol concentration was used.

During this study a batch reactor for testing the photocatalytic activity of thin films was developed, the relationships between microstructure, optical properties and photocatalytic activity of TiO_2 thin films were investigated and the effect of dopant addition on the thin film properties was studied. Even though valuable information was obtained some questions still remain unanswered. Among these are (i) the true nature of the XRD amorphous films, (ii) the nature of the band gap transition in anatase, and (iii) the photocatalytic activity of doped TiO_2 thin films under VIS light illumination.

Samenvatting

Het eerste en voornaamste doel van deze thesis was het verband te onderzoeken tussen de microstructuur en optische eigenschappen van TiO_2 dunne films en hun fotokatalytische werking. De dunne films werden afgezet via d.c. magnetron sputteren. Alvorens het onderzoek i.v.m. de depositie aan te vatten, werd het sputtergedrag van de substoichiometrische TiO_{2-x} keramische targets nagegaan en vergeleken met het reactief sputteren van een metallische Ti target. Op basis hiervan werd gekozen voor het gebruik van substoichiometrische TiO_{2-x} keramische targets. Deze techniek laat toe de filmstructuur te beïnvloeden d.m.v. de depositieparameters. Bovendien konden door het gebruik van TiO_{2-x} keramische targets stoichiometrische TiO_2 films afgezet worden met uitsluitend argon als sputtergas. De parameters die voor de depositie veranderd werden, zijn het aangelegde elektrische vermogen (60 – 180 W) en de argon gasdruk (0.47 - 2.2 Pa). De afgezette dunne films waren XRD-amorf maar werden kristallijn door een hittebehandeling achteraf ("gloeien") bij temperaturen van 573 tot 673 K (de temperatuur is afhankelijk van de depositieparameters). Voor alle dunne films werden de microstructuur, de film dichtheid/ porositeit, de kristallisatie, de brekingsindex, de optische verboden zone en de fotokatalytische activiteit bepaald.

De afgezette dunne films zijn opgebouwd uit kolommen die zich doorheen de ganse filmdikte uitstrekken. De dichtheid/ porositeit van de dunne films, m.a.w. de spatiëring tussen de kolommen, was afhankelijk van de depositieparameters. De porositeit nam sterk toe met stijgende argon gasdruk (van 5 tot 25 %) en daalde lichtjes met stijgend elektrisch vermogen (van 22.5 tot 11 %). De porositeit werd echter niet relevant beïnvloed door de hittebehandeling achteraf. De kristallijne dunne films vertoonden een willekeurige kristaloriëntatie bij de laagste gasdrukken, met oplopende argon gasdruk werd de preferentiële (004) oriëntatie sterker. Deze oriëntatie werd zwakker voor toenemend sputtervermogen maar werd niet beïnvloed door de hittebehandeling achteraf. De verboden zone werd groter met toenemende argon gasdruk en nam lichtjes af met toenemend sputtervermogen. De hittebehandeling achteraf leidde bij lagen afgezet bij hoge argon gasdruk tot een toename van de verboden zone, bij lage argon gasdruk daarentegen verkleinde de verboden zone.

De fotokatalytische activiteit van zowel de afgezette amorfe films als van gegloeide kristallijne films werd nagegaan en het verband met de depositieparameters werd onderzocht. Het bleek dat de filmdichtheid/ porositeit en het kristallijne karakter de grootste invloed hadden. Toenemende porositeit van de lagen, bekomen via het verhogen van de argon gasdruk tijdens

depositie, leidde tot een vijfmaal hogere fotokatalytische activiteit. Het kristallijn maken via gloeien leidde tot een meer dan tweemaal hogere activiteit. De hoogste fotokatalytische activiteit werd waargenomen bij films afgezet bij 60 W en 1.4 - 2.2 Pa die een hittebehandeling ondergingen bij een temperatuur van 673 K of hoger. Deze films hebben een fotokatalytische activiteit van 3.5 ppm/min voor het afbreken van ethanol in de testreactor ontwikkeld voor deze thesis. Deze waarden zijn vergelijkbaar met de waarden gemeten voor een P25 referentiefilm. Een andere belangrijke factor voor de fotokatalytische activiteit van de films is hun dikte. In de literatuur wordt vermeld dat de fotokatalytische activiteit sterk toeneemt met de dikte tot een bepaalde waarde. Boven deze kritische waarde wordt de activiteit bijna onafhankelijk van de dikte. Dit gedrag werd ook in deze thesis waargenomen. De activiteit van de films was evenredig met het aantal geabsorbeerde fotonen, dit betekent dat de dikte afhankelijkheid van de activiteit te wijten is aan de lichtabsorptie. Dit werd toegeschreven aan de kolomstructuur en het poreuze karakter van de films daar deze het mogelijk maken dat ladingsdragers kunnen reageren op de zijwanden van de kolommen.

Een tweede doel van de studie was het onderzoeken van de invloed van dopering op de microstructuur en optische en fotokatalytische eigenschappen van TiO_2 lagen. Gedopeerde films werden aangemaakt via sputterdepositie met een M_2O_3/ TiO_{2-x} gemengde oxide target (M = Fe, Nd of V) en via ionenimplantatie (van Fe, Nd) in een reeds afgezette TiO_2 film. Vooraleer films te groeien m.b.v. de gemengde oxidetargets werd eerst het sputtergedrag met dergelijke targets onderzocht. Om de invloed van het doperen na te gaan, werden de depositieparameters gebruikt die resulteerden in de beste fotokatalytische eigenschappen van de pure TiO_2 films (60 W, 1.4 Pa en, indien een nabehandeling werd gedaan, gloeien bij 673 K gedurende 1 uur). De doperingsconcentratie van de gemengde oxide targets varieerde tussen 1 en 10 at%. Bij de ionenimplantatie was het de bedoeling het doperingsmateriaal te implanteren in de bovenste 40 nm van de film met een concentratie tussen 0.5 en 2 at%.

De invloed van het doperingsmateriaal op de eigenschappen van de TiO_2 films was vrij complex en afhankelijk van de gebruikte doperingstechniek. De invloed op de microstructuur, kristallisatie en optische eigenschappen hing af van het doperingsmateriaal, de gebruikte techniek en de aangebrachte concentratie. Desondanks was het effect op de fotokatalytische activiteit in alle gevallen ruwweg hetzelfde: het verhogen van de doperingsconcentratie leidde tot een lagere fotokatalytische activiteit, bij de hoogste concentraties liep dit op tot een reductie met ongeveer 1/3. Het grootste verschil met de zuivere TiO_2 films bleek tijdens het nabehandelen: voor de zuivere films leidde gloeien tot een verdubbeling van fotokatalytische acti-

viteit, voor de gedopeerde films werd echter een daling vastgesteld, zodat de nabehandelde gedopeerde films slechts een activiteit van ongeveer 1/7 van de zuivere films hadden. Ook al kon de fotokatalytische activiteit niet verhoogd worden, toch werd waardevolle informatie bekomen over het effect van dopering op de eigenschappen van de TiO_2 lagen.

Een derde doel van de thesis was het ontwerpen van een betrouwbare reactor en procedure om de fotokatalytische activiteit van de aangemaakte (gedopeerde) TiO_2 lagen na te gaan. De keuze viel op een *batch reactor* met een gecontroleerde atmosfeer bestaande uit 80 % argon en 20 % zuurstof (om lucht te simuleren). De fotokatalytische reactie die gekozen werd om de activiteit van de verschillende films te meten was het afbreken van ethanol tot acetaldehyde. Daartoe werd in de reactor een welbepaalde hoeveelheid van de organische testsubstantie geïnjecteerd. Als belichtingsbron werd een hoge druk kwikbooglamp gebruikt. De speciaal voor deze thesis ontwikkelde reactor liet toe om de invloed van de intensiteit van het invallende licht, de luchtvochtigheid, de ethanol beginconcentratie en de substraattemperatuur op de fotokatalytische reactie na te gaan. Om de reactorwerking na te gaan werd als referentiemateriaal een *spin coated* film van Degussa P25 poeder gebruikt. De instellingen die standaard gebruikt werden om de afgezette films te evalueren waren: een ethanol beginconcentratie van 273 ppm (met 5 vol% water van de omringende atmosfeer), een lampvermogen van 100 W en een substraattemperatuur van 313 K. Om de reactiesnelheid na te gaan werd de initiële helling bepaald van de dalende curve die de ethanolconcentratie aangeeft.

Gedurende dit doctoraatswerk werden fotokatalytisch actieve lagen op basis van TiO_2 afgezet m.b.v. magnetron sputteren. Een *batch reactor* werd ontwikkeld voor het bepalen van de fotokatalytische activiteit van die dunne films. De relatie tussen de microstructuur, de optische en de fotokatalytische eigenschappen van de TiO_2 films werd onderzocht net als de invloed van dopering van het zuivere TiO_2 op die eigenschappen. Ondanks het feit dat heel wat relaties en inzichten bekomen werden, blijven een aantal vragen open. De voornaamste zijn (i) de werkelijke aard van de XRD amorfe films die afgezet worden, (ii) de aard van de overgangen bij het absorberen van een foton in anataas en (iii) de fotokatalytische activiteit van gedopeerde TiO_2 dunne films bij belichting met zichtbaar licht.

Appendix

A.1 Crystal field splitting of an octahedral complex

A.1.1 High spin configuration of Fe^{3+}

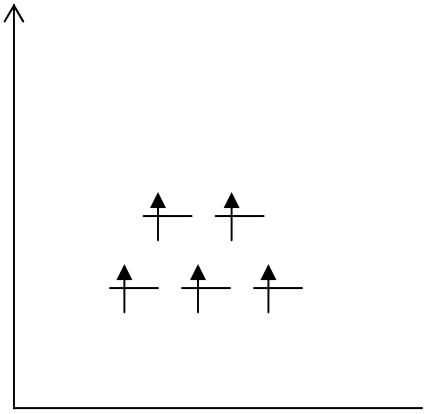

A.1.2 Low spin configuration of Fe^{3+}

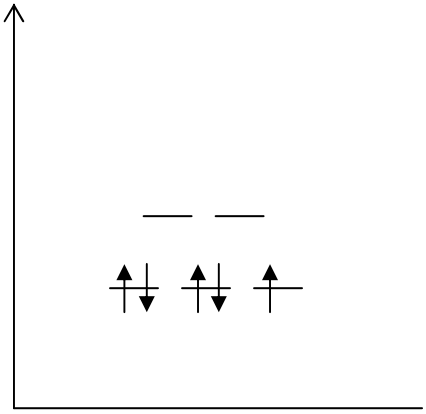

A.2 References for deposition of amorphous/weakly crystalline, anatase or rutile thin films by r.f. and d.c. magnetron sputtering

For the blank fields in the table no information was given in the respective reference.

a) r.f. magnetron sputtering

Reference	**target material and diameter**	**total pressure p_t or Ar-flow**	**O_2-content Or Ar-flow**	**substrate T**	**target to substrate distance**	**discharge parameters**	**Observed phases**
[Asanuma03]	Ti, 100mm	1-10x10^{-2} torr (1.33-13.3 Pa)	pure O_2	200°C	60mm	P=140W/ 200W	a, r, w
[Zeman02]	Ti, 75mm	0.18-1.5 Pa	20-85%	120°C	80mm	P=300W	a, r, w
[Yamagishi03]	Ti	0.3-3 Pa	p_{O2}/p_t =30% (fully reactive)	200°C		P=200W	a, r, w
[Okimura01]		0.27, 2.7 Pa	flowO_2/flowAr =3sccm/50sccm	270-280°C		P=200W	a, r
[Miao02]	TiO_2, 2 in	p(Ar) = 0.1-1 Pa	0.1-0.7 sccm	RT-600°C	150mm		a, r

Observed phases: a=anatase; r=rutile, w=amorphous/weakly crystalline

b) d.c. magnetron sputtering

Reference	**target material, diameter**	**total pressure p_t**	**O_2-content**	**substrate T**	**target to substrate distance**	**discharge parameters**	**Observed phases**
[Liu05]	Ti,	p(Ar)=0.85 Pa	p(O2)=0.15-0.4 Pa		100mm	0.6 A	a, w
[Kim02c]	Ti, 75mm	2x10^{-3} torr (0.27 Pa), 3x10^{-2} torr (4 Pa)	p_{O2}/p_t = 10-28 %			P = 150-450 W	a, w
[Takahashi02]	Facing targets, Ti, 68x48mm	$flow_{Ar}$=30cm^3	$flow_{O2}$=5cm^3		23-63 mm	P=320-400W, 0.5A, 640-800V	a, w
[Takahashi06]	Ti,	0.2-5 Pa	Ar:O_2=80:20		40-70mm	P=200W	a, w
[Barnes05]	Ti, 180mm	0.27-1.5 Pa	$flow_{O2}$=20sccm, $flow_{Ar}$=20-100sccm	<100°C	30-250mm	P=200-800W V=485±5V	a,w
[Zhang04]	Ti, 125x378m	0.33-0.56 Pa	p_{Ar}/p_{02}=1.5-2.81	up to 130°C	150mm	2.5A	a
[Vale06]	Ti, 30mm erosion zone	0.35-1 Pa	15:1, 5:1=Ar:O_2-mix		120mm	V adjusted to keep dep. rate 0.1nm/s	r, a

Observed phases: a=anatase; r=rutile, w=amorphous/weakly crystalline

A.3 Calibration steps implemented in the measurement program written with the QuadStar software [software2]

1. QMS offset: Defines the zero point of the ion current signal received by the detector. This calibration is needed to correct for the offset in the ion current.
2. MSC (Mass scale calibration): Defines the actual position of the maximum of the mass/ charge peak, which will usually be shifted slightly from the theoretical value. For example the mass/charge peak at 28 amu may be at 27.8 or 28.2. If the measured value deviates by 0.5 from the actual value an error is reported. This calibration is needed to perform accurate MID/ MCD measurements.

Both calibrations are performed at the beginning of each measurement cycle, because drift in the signals can occur with time.

Publications and conference contributions

International, refereed Papers:

- *K. Eufinger, D. Poelman, H. Poelman, R. De Gryse, G.B. Marin, "Effect of microstructure and crystallinity on the photocatalytic activity of TiO_2 thin films deposited by d.c. magnetron sputtering, manuscript in preparation*
- *K. Eufinger, D. Poelman, H. Poelman, R. De Gryse, G.B. Marin, 'TiO$_2$ thin films for photocatalytic applications,' invited review article for 'Thin Solid Films: Process and Applications', by S.-C. Nam (ed), Research Signpost, manuscript in preparation*
- *K. Eufinger, D. Poelman, H. Poelman, R. De Gryse, G.B. Marin, "Photocatalytic activity of d.c. magnetron sputter deposited XRD amorphous TiO_2 thin films," submitted to Applied Surface Science, November 2006*
- H. Tomaszewski, K. Eufinger, H. Poelman, D. Poelman, R. De Gryse, P. Smet, G.B. Marin, "Effect of the substrate sodium content on the crystallization and photocatalytic activity of TiO_2 films prepared by d.c. magnetron sputtering," International Journal of Photoenergy, (2007) ID 95213
- *H. Poelman, K. Eufinger, D. Depla, D. Poelman, R. De Gryse, B.F. Sels, G.B. Marin, "Magnetron Sputter Deposition for Catalyst Synthesis," Applied Catalysis A: General, available online via Science Direct, February 2007*
- M. Olea, I. Sack, V. Balcaen, G.B. Marin, H. Poelman, K. Eufinger, D. Poelman, R. De Gryse, J.S. Paul, B.F. Sels and P.A. Jacobs, "DC magnetron sputter deposited vanadia catalysts for oxidation processes," Applied Catalysis A: General, **318** (2007) 37-44
- H. Poelman, B.F. Sels, M. Olea, K. Eufinger, J.S. Paul, B. Moens, I. Sack, V. Balcaen, F. Bertinchamps, E.M. Gaigneaux, P.A. Jacobs, G.B. Marin, D. Poelman, R. De Gryse, "New supported vanadia catalysts for oxidation reactions prepared by sputter deposition," Journal of Catalysis **245** (2007)156-172
- K. Eufinger, E.N. Janssen, H. Poelman, D. Poelman, R. De Gryse, G.B. Marin, "The effect of argon pressure on the structural and optical characteristics of TiO_2 thin films deposited by d.c. magnetron sputtering," Thin Solid Films **515** (2006) 425-429
- K. Eufinger, H. Tomaszewski, D. Depla, H. Poelman, D. Poelman, R. De Gryse, "The d.c. magnetron sputtering behavior of TiO_{2-x} targets with added Fe_2O_3 or Nd_2O_3," Thin Solid Films **515** (2006) 683-686
- G. Buyle, D. Depla, K. Eufinger, R. De Gryse "Calculation of the effective gas interaction probabilities of secondary electrons in a dc magnetron discharge" Journal of Physics D: Applied Physics **37** (2004) 1639-1647
- I. Sack, M. Olea, H. Poelman, K. Eufinger, R. De Gryse, G.B. Marin, "TAP studies on the reoxidation of some partially reduced vanadia-based catalysts," Catalysis Today **91-92** (2004) 149-153
- G. Buyle, D. Depla, K. Eufinger, J. Haemers, W. De Bosscher, R. De Gryse "Simplified model for the DC planar magnetron discharge," Vacuum **74** (2004) 353-358
- G. Buyle, D. Depla, K. Eufinger, J. Haemers, R. De Gryse, W. De Bosscher, "Simplified model for calculating the pressure dependence of a direct current planar magnetron discharge," Journal of Vacuum Science and Technology A **21** [4] (2003) 1218-1224

- G. Buyle, W. De Bosscher, D. Depla, K. Eufinger, J. Haemers, R. De Gryse, "Recapture of secondary electrons by the target in a DC planar magnetron discharge, Vacuum **70** [1] (2003) 29-35
- G. Buyle, D. Depla, K. Eufinger, J. Haemers, R. De Gryse, "Importance of recapture of secondary electrons in cylindrical and planar magnetron discharges," Czech Journal of Physics, **52** Suppl. D (2002) 615-623
- D. Depla, A.Colpaert, K. Eufinger, A. Segers, J. Haemers, R. De Gryse, "Target voltage behavior during DC sputtering of Silicon in an argon/nitrogen mixture," Vacuum **66** [1] (2002) 9-17

Non-refereed papers:

- K. Eufinger, D. Poelman, H. Poelman, R. De Gryse, G.B. Marin, "Influence of the d.c. magnetron sputter deposition process on the photocatalytic activity of amorphous TiO_2 thin films," Vacuum Technology and Coating **8** [1] (2007), 44-49
- G. Buyle, D. Depla, K. Eufinger, J. Haemers, R. De Gryse, W. De Bosscher, "Simplified model for the DC planar magnetron discharge," Belvac News **19** [2] (2003) 8-16
- A. Segers, D. Depla, K. Eufinger, J. Haemers, R. De Gryse, "Instabilities in the Reactive Sputtering of Electrical Insulating Compounds," Belvac News **19** (4) (2003) 28-41

Proceedings:

- K. Eufinger, D. Poelman, H. Poelman, R. De Gryse, G.B. Marin, "Influence of the d.c. magnetron sputter deposition process on the photocatalytic activity of amorphous TiO_2 thin films," Proceedings of the 49th Annual Technical Conference of the Society of Vacuum Coaters, Washington DC, April 24-27 (2006) 480-484
- G. Buyle, D. Depla, K. Eufinger, R. De Gryse, W. De Bosscher, "Monte Carlo Simulation of Anomalous Erosion in Large Area Sputter Magnetrons," Proceedings of the 48th Annual Technical Conference of the Society of Vacuum Coaters, Denver, Co, April 23-28 (2005)
- G. Buyle, D. Depla, K. Eufinger, J. Haemers, W. De Bosscher, R. De Gryse, "Characterization of the Electron Movement in Varying Magnetic Fields and the Resulting Anomalous Erosion," Proceedings of the 47th Annual Technical Conference of the Society of Vacuum Coaters, Dallas, Tx, April 24-29 (2004)
- A. Segers, D. Depla, K. Eufinger, J. Haemers, R. De Gryse, "Instabilities in the reactive Sputtering of Electrical Insulating Compounds," The third edition of lectures on 'Nouvelles Tendances en Procédés Magnetron et Arc pour le Dépôt de Couches Minces' book of abstracts (2003)
- I. Sack, M. Olea, H. Poelman, K. Eufinger, R. De Gryse, G.B. Marin, "TAP studies on the reoxidation of some partially reduced vanadia-based catalysts," Proceedings of Innovative Selective Oxidations : Nano-scale and Dynamic Aspects (ISO 2003) Innsbruck, Austria, August 31 - September 4 (2003)
- G. Buyle, D. Depla, K. Eufinger, J. Haemers, W. De Bosscher, R. De Gryse "Simplified model for the DC planar magnetron discharge," The 7th International Symposium on Sputtering & Plasma Processes ISSP, Kanazawa Institute of Technology, Kanazawa, Japan, June 11-13 (2003) 67-70

- G. Buyle, D. Depla, W. De Bosscher, K. Eufinger, J. Haemers, R. De Gryse, "Dissection of the Planar Magnetron Discharge," Proceedings of the 46th Annual Technical Conference of the Society of Vacuum Coaters, San Francisco Ca, May 3-8 (2003)
- G. Buyle, D. Depla, K. Eufinger, W. De Bosscher, J. Haemers, R. De Gryse, "Influence of Recapture of Secondary Electrons on the Magnetron Sputter Deposition Process," Proceedings of the 45th Annual Technical Conference of the Society of Vacuum Coaters, Orlando FL, April 13-18 (2002) 346-353
- A. Segers, D. Depla, K. Eufinger, J. Haemers, R. De Gryse, "Arc Discharges in the reactive Sputtering of Electrical insulating compounds," Proceedings of the 45th Annual Technical Conference of the Society of Vacuum Coaters, Orlando FL, April 13-18 (2002) 30-35
- R. De Gryse, D. Depla, K. Eufinger, "Poisoning in reactive sputtering as seen from the target voltage behavior," Proceedings of the 14th International Conference on Vacuum Web Coating, Reno NV, ed. R. Bakish (2000) 190
- R.C. Buchanan, R.D. Roseman and K.R. Eufinger, "Electrical and Mechanical Properties of Core-Shell Type Structures in Doped $BaTiO_3$." Proceedings of the 10th IEEE International Symposium on Applications of Ferroelectrics (ISAF '96), East Brunswick, NJ, (1996) 887-890.
- R.C. Buchanan, R.D. Roseman and K.R. Eufinger, "Electrical and Mechanical Properties of Core-Shell Structures Developed in Doped $BaTiO_3$," Proceedings of the 7th U.S.-Japan Seminar on Dielectric and Piezoelectric Ceramics, Tsukuba, Japan (1995)

Invited Presentations:

- K. Eufinger, D. Poelman, H. Poelman, R. De Gryse*, G.B. Marin, "Photocatalytic activity of d.c. magnetron sputter deposited XRD amorphous TiO_2 thin films," Presented at the 13th International Conference on Solid Films and Surfaces (ICSFS 13) in San Carlos de Bariloche, Patagonia, Argentina, Nov. 6 -10 (2006)
- R. C. Buchanan* and K.R. Eufinger, "Dielectric Properties of Nd_2O_3 Doped $BaTiO_3$ Ceramics with Diffuse Phase Transition," American Ceramic Society 100th Annual Meeting, Cincinnati, OH. May (1998)
- R.C. Buchanan*, R.D. Roseman and K.R. Eufinger, "Electrical and Mechanical Properties of Core-Shell Structures Developed in Doped $BaTiO_3$ Ceramics," Seventh U.S.-Japan Seminar on Dielectric and Piezoelectric Ceramics, Tsukuba, Japan, Nov. 15-17 (1995)

Other Presentations:

1. K. Eufinger, D. Poelman, H. Poelman, R. De Gryse*, G. B. Marin, "Influence of the d.c. magnetron sputter deposition process on the photocatalytic activity of amorphous TiO_2 thin films," 49th Annual Technical Conference of the Society of Vacuum Coaters, Washington DC, April 24-27 (2006)
2. K. Eufinger*, E.N. Janssen, H. Poelman, D. Poelman, R. De Gryse, G.B. Marin, "The effect of argon pressure on the structural and optical characteristics of TiO_2 thin films deposited by d.c. magnetron sputtering," 13th International Congress on Thin films/ 8th International Conference on Atomically Controlled Surfaces, Interfaces and Nanostructures (ICTF13/ACSIN 8), June 19-23 (2005)
3. K. Eufinger*, H. Tomaszewski, D. Depla, H. Poelman, D. Poelman, R. De Gryse, "The d.c. magnetron sputtering behavior of TiO_{2-x} targets with added Fe_2O_3 or Nd_2O_3," 13th International Congress on Thin films/ 8th International Conference on Atomically Controlled Surfaces, Interfaces and Nanostructures (ICTF13/ACSIN 8), June 19-23 (2005) (Poster)
4. G. Buyle*, D. Depla, K. Eufinger, R. De Gryse, W. De Bosscher, "Monte Carlo Simulation of Anomalous Erosion in Large Area Sputter Magnetrons," 48th Annual Technical Conference of the Society of Vacuum Coaters, Denver, Co, April 23-28 (2005)
5. G. Buyle*, D. Depla, K. Eufinger, J. Haemers, R. De Gryse, "Simplified Model for the DC Planar Magnetron Discharge," Reactive Sputtering and related Phenomena III, Ghent, Belgium, December 9-10 (2004)
6. M. Olea*, I. Sack, V. Balcaen, G.B. Marin, H. Poelman, K. Eufinger, R. De Gryse, J.S. Paul, B.F. Seels, P.A. Jacobs, "D.C. magnetron sputtered catalysts for oxidation processes," 228th National Meeting and Exposition of the American Chemical Society, Philadelphia PA, August 22-26 (2004)
7. K. Eufinger*, H. Poelman, D. Poelman, R. De Gryse, G.B. Marin, "DC magnetron sputtered TiO_2 thin films for photocatalytic applications," Workshop on "Catalyst Design Through Characterisation and Modelling", Gent, Belgium, May 28 (2004)
8. H. Poelman*, K. Eufinger, J.S. Paul, B.F. Sels, P.A. Jacobs, R. De Gryse, "VO_x/ TiO_x model catalysts prepared by sputter deposition onto inert carriers," Workshop on "Catalyst Design Through Characterisation and Modelling", Gent, Belgium, May 28 (2004)
9. G. Buyle*, D. Depla, K. Eufinger, J. Haemers, W. De Bosscher, R. De Gryse, "Characterization of the Electron Movement in Varying Magnetic Fields and the Resulting Anomalous Erosion," 47th Annual Technical Conference of the Society of Vacuum Coaters, Dallas, Tx, April 24-29 (2004)
10. H. Poelman, K. Eufinger*, R. De Gryse, I. Sack, M. Olea, G.B. Marin, "Physical and chemical characterization of VO_x/ TiO_x model catalyst prepared by sputter deposition on inert carriers," 10th NICE Workshop on Non-Thermal Induction of Catalysis, Frankfurt/ Main (Germany) Nov. 6-7 (2003) (Poster)
11. H. Poelman*, K. Eufinger, R. De Gryse, I. Sack, M. Olea, G.B. Marin, "Physical and chemical characterization of VO_x/ TiO_x model catalyst," ECASIA 2003 (Poster)
12. I. Sack*, M. Olea, H. Poelman, K. Eufinger, R. De Gryse, G.B. Marin, "TAP studies on the reoxidation of some partially reduced vanadia-based catalysts," EuropaCat IV, Innsbruck (Austria), August 31-September 4 (2003)

13. G. Buyle*, D. Depla, K. Eufinger, J. Haemers, W. De Bosscher, R. De Gryse, "Simplified model for the DC planar magnetron discharge," The Seventh International Symposium on Sputtering & Plasma Processes ISSP 2003, Kanazawa Institute of Technology, Kanazawa, Japan, June 11-13 (2003)
14. G. Buyle*, D. Depla, W. De Bosscher, K. Eufinger, J. Haemers, R. De Gryse, "Dissection of the Planar Magnetron Discharge," 46th Annual Technical Conference of the Society of Vacuum Coaters, San Francisco Ca, May 3-8 (2003)
15. G. Buyle*, D. Depla, K. Eufinger, W. De Bosscher J. Haemers,R. De Gryse, "Simplified Model for Calculating the Pressure Dependence of a DC Planar Magnetron Discharge and Experimental Verification", AVS 49th International Symposium, Denver, Co, November 4-8 (2002)
16. G. Buyle*, D. Depla, K. Eufinger, J. Haemers, R. De Gryse, "Importance of recapture of secondary electrons in cylindrical and planar magnetron discharges," Symposium of Plasma Physics and Technology, Prag, Czechia, June 10-13 (2002)
17. G. Buyle*, D. Depla, W. De Bosscher, K. Eufinger, J. Haemers, R. De Gryse, "Low Pressure Behaviour of the Sputter Magnetron Discharge," IEEE International Conference on Plasma Science (ICOPS), Banff, Alberta, Canada, May 26-30 (2002)
18. G. Buyle*, D. Depla, K. Eufinger, W. De Boscher, J. Haemers, R. De Gryse, "Influence of Recapture of Secondary Electrons on the Magnetron Sputter Deposition Process," 45th Annual Technical Conference of the Society of Vacuum Coaters, Orlando FL, April 13-18 (2002)
19. A. Segers, D. Depla, K. Eufinger, J. Haemers, R. De Gryse*, "Arc Discharges in the reactive Sputtering of Electrical insulating compounds," 45th Annual Technical Conference of the Society of Vacuum Coaters, Orlando FL, April 13-18 (2002)
20. D. Depla, K. Eufinger, J. Haemers, A. Segers, R. De Gryse*, "Arc Discharges in Reactive Sputtering," CIP', Antibes, France, June 10-14 (2001)
21. K.R. Eufinger*, R.D. Roseman, R.C. Buchanan, "Core-Shell Microstructures in Donor Doped $BaTiO_3$ Ceramics," American Ceramic Society 97th Annual Meeting Cincinnati, OH April/May (1995)

References

[Anderson97] O. Anderson, C.R. Ottermann, R. Kuschnereit, P. Hess, K. Bange, "Density and Young's modulus of TiO_2 films," Fresenius Journal of Analytical Chemistry 358 (1997) 315-318

[Anpo03] M. Anpo, M. Takeuchi, "The design and development of highly reactive titanium oxide photocatalyst operating under visible light irradiation," Journal of Catalysis 216 (2003) 505-516

[Asahi01] R. Asahi, T. Morikawa, T. Ohwaki, K. Aoki, Y. Taga, "Visible-Light Photocatalysis in Nitrogen-doped Titanium Oxides," Science 293 (2001) 269-271

[Asanuma03] T. Asanuma, T. Matsutani, C. Liu, T. Mihara, M. Kiuchi, "Structural and Optical Properties of Titanium Dioxide Films Deposited by Reactive RF Magnetron Sputtering Method," Proceedings of *The Seventh International Symposium on Sputtering and Plasma Process (ISSP 2003)*, Kanazawa Institute of Technology, Kanazawa, Japan, June 11-13, 2003, 447-450

[Atkins90] P.W. Atkins, "Physical chemistry," 4^{th} edition, Oxford University Press, Oxford (1990)

[Augugliaro99] V. Augugliaro, S. Coluccia, V. Loddo, L. Marchese, G. Martra, L. Palmisano, M. Schialvello, "Photocatalytic oxidation of gaseous toluene on anatase TiO_2 catalyst: mechanistic aspects and FT-IR investigation," Applied Catalysis B, Environmental 20 (1999) 15-27

[Bak03a] T. Bak, J. Nowotny, M. Rekas, C.C. Sorrell, "Defect chemistry and semiconducting properties of titanium dioxide: I. Intrinsic electronic equilibrium," Journal of Physics and Chemistry of Solids, 64 (2003) 1043-1056

[Bak03b] T. Bak, J. Nowotny, M. Rekas, C.C. Sorrell, "Defect chemistry and semiconducting properties of titanium dioxide: II. Defect diagrams," Journal of Physics and Chemistry of Solids, 64 (2003) 1057-1067

[Bak03c] T. Bak, J. Nowotny, M. Rekas, C.C. Sorrell, "Defect chemistry and semiconducting properties of titanium dioxide: III. Mobility and electronic charge carriers," Journal of Physics and Chemistry of Solids, 64 (2003) 1069-1087

[Bak03d] T. Bak, T. Burg, S.-J.L. Kang, J. Nowotny, M. Rekas, L. Sheppard, C.C. Sorrell, E.R. Vance, Y. Yoshida, M. Yamawaki, "Charge transport in polycrystalline titanium dioxide," Journal of Physics and Chemistry of Solids, 64 (2003) 1089-1095

[Ball06a] P. Ball, "Nanoparticles in sun creams can stress brain cells," news@nature.com, June 16 (2006)

[Ball06b] P. Ball, "Why nanotech fails the dope test," nanozone news, Nature Materials Update, June 22 2006

[Bally98] A.R. Bally, E.N. Korobeinikova, P.E. Schmid, F. Lévy, F. Bussy, "Structural and electrical properties of Fe-doped TiO_2 thin films," Journal of Physics D: Applied Physics 31 (1998) 1149-1154

[Barnes05] M.C. Barnes, S. Kumar, L. Green, N.-M. Hwang, A.R. Gerson, "The mechanism of low temperature deposition of crystalline anatase by reactive DC magnetron sputtering," Surface and Coatings Technology 190 (2005) 321-330

[Baroch05] P. Baroch, J. Musil, J. Vlček, K.H. Nam, J.G. Han, "Reactive magnetron sputtering of TiO_X films," Surface & Coatings Technology 193 (2005) 107-111

[Beermann02] N. Beermann, G. Boschloo, A. Hagfeld, "Trapping of electrons in nanostructured TiO_2 studied by photocurrent transients," Journal of Photochemistry and Photobiology A: Chemistry 152 (2002) 213-218

[Belkind98] A. Belkind, F. Jansen, "Anode effects in magnetron sputtering," Surface and Coatings Technology, 99 (1998) 52-59

[Belver06a] C. Belver, R. Bellod, A. Fuerte, M. Fernández-García, "Nitrogen-containing TiO_2 photocatalysts Part 1. Synthesis and solid characterization," Applied Catalysis B: Environmental 65 (2006) 301-308

[Belver06b] C. Belver, R. Bellod, S.J. Steward, F.G. Requejo, M. Fernández-García, "Nitrogen-containing TiO_2 photocatalysts Part 2. Photocatalytic behavior under sunlight excitation," Applied Catalysis B: Environmental 65 (2006) 309-314

[Berg05] S. Berg, T. Nyberg "Fundamental understanding and modeling of reactive sputtering processes," Thin Solid Films 476 (2005) 215-230

[Berger93] H. Berger, H. Tang, F. Lévy, "Growth and Raman spectroscopic characterization of TiO_2 anatase single crystals," Journal of Crystal Growth 130 (1993) 108-112

[Bessekhouad2004] Y. Bessekhouad, D. Robert, J-V. Weber, N. Chaoui "Effect of alkaline doped TiO_2 on photocatalytic efficiency," Journal of Photochemistry and Photobiology A: Chemistry 167 (2004) 49-57

[Buyle04] G. Buyle, D. Depla, K. Eufinger, R. De Gryse "Calculation of the effective gas interaction probabilities of secondary electrons in a dc magnetron discharge," Journal of Physics D: Applied Physics 37 (2004) 1639-1647

[Byun00] D. Byun, Y. Jin, B. Kim, J. K. Leen D. Park, "Photocatalytic TiO_2 deposition by chemical vapor deposition," Journal of Hazardous Materials B, 73 (2000) 199-206

[Cao04] Y. Cao, W. Yang, Y. Chen, H. Du, P. Yue, "Effect of chemisorbed surface species on the photocatalytic activity of TiO_2 nanoparticle films," Applied Surface Science 236 (2004) 223-230

[Cangiani03] G. Cangiani, "Ab-initio study of the properties of TiO_2 rutile and anatase polytypes," PhD Thesis, Faculte de sciences de base section de physique, École Polytechnique Fédérale de Lausanne (2003)

[Carneiro05] J.O. Carneiro, V. Teixeira, A. Portinha, L. Dupák, A. Magalhães, P. Coutinho, "Study of the deposition parameters and Fe-dopant effect in the photocatalytic activity of TiO_2 films prepared by dc reactive magnetron sputtering," Vacuum 78 (2005) 37-46

[Carp04] O. Carp, C.L. Huisman, A. Reller, "Photoinduced reactivity of titanium dioxide," Progress in Solid State Chemistry 32 (2004) 33-177

[Chapman80] B. N. Chapman, "Glow Discharge Processes," John Wiley & Sons, New York (1980)

[Chen04] S.-Z. Chen, P.-Y. Zhang, D.-M. Zhuang, W.-P. Zhu, "Investigation of nitrogen doped TiO_2 photocatalytic films prepared by reactive magnetron sputtering," Catalysis Communications 5 (2004) 677-680

[Chiker03] F. Chiker, J.Ph. Nogier, J.L. Bonardet, "Sub-monolayer V_2O_5-anatase TiO_2 and Eurocat catalyst: IR, Raman and XPS characterization of VO_x dispersion," Catalysis today 78 (2003) 139-147

[Ching04] W.H. Ching, M. Leung, D.Y.C. Leung, "Solar photocatalytic degradation of gaseous formaldehyde by sol-gel TiO_2 thin film for enhancement of indoor air quality," Solar Energy 77 (2004) 129-135

[Colbeau-Justin03] C. Colbeau-Justin, M. Kunst, D. Huguenin, "Structural influence on charge-carrier lifetimes in TiO_2 powders studied by microwave absorption," Journal of Materials Science 38 (2003) 2429-2437

[Colón03] G. Colón, M.C. Hidalgo, J.A. Navío, "Photocatalytic behaviour of sulphated TiO_2 for phenol degradation," Applied Catalysis B: Environmental 45 (2003) 39-50

[Cornu02] PhD Thesis by Catherine J.G.Cornu, California Institute of Technology, Pasadena, California, 2002, (Submitted September 24, 2001)

[Cullity78] B.R. Cullity, Elements of X-ray diffraction, 2nd edition, Addison-Wesley Publishing company, INC. Reading, Massachusetts, (1978)

[Damm05] C. Damm, D. Völtzke, H.-P. Abicht, G. Israel, "Influence of TiO_2 particles on the photocatalytic acrylate polymerization," Journal of Photochemistry and Photobiology A: Chemistry 174 (2005) 171-179

[Daude77] N. Daude, C. Gout, C. Jouanin, "Electronic band structure of titanium dioxide," Physical Review B 15 [6] (1977) 3229-3235

[de Almeida Filho06] C. de Almeida Filho, A. J.G. Zarbin, "Hollow porous carbon microspheres obtained by the pyrolysis of TiO_2/poly(furfuryl alcohol) composite precursors," Carbon 44 (2006) 2869-2876

[Demeestere03] K. Demeestere, J. Dewulf, H. Van Langemhove, B. Sercu, "Gas-solid adsorption of selective volatile organic compounds on titanium dioxide Degussa P25", Chemical Engineering Science 58 (2003) 2255-2267

[Depla01] D. Depla, R. De Gryse, "Influence of oxygen addition on the target voltage during reactive sputtering of aluminium," Plasma Sources Science and Technology 10 (2001) 547-555

[Depla06a] D. Depla, H. Tomaszewski, G. Buyle, R. De Gryse, "Influence of the target composition on the discharge voltage during magnetron sputtering," Surface and Coatings Technology 201 (2006) 848-854

[Depla06b] D. Depla, J. Haemers, R. De Gryse, "Discharge voltage measurements during reactive sputtering of oxides," Thin Solid Films 515 (2006) 468-471

[Depla06c] D. Depla, S. Heirwegh, S. Mahieu, J. Haemers, R. De Gryse, "Understanding the discharge voltage behaviour during reactive sputtering of oxides" Journal of Applied Physics, accepted for publication (2006)

[Diallo05] M.S. Diallo, N. Savage, "Nanoparticles and water quality," Journal of Nanoparticle Research 7 (2005) 325-330

[Dumitriu00] D. Dumitriu, A.R. Bally, C. Ballif, P. Hones, P.E. Schmid, R. Sanjinés, F. Lévy, V.I. Pârvulescu, "Photocatalytic degradation of phenol by TiO_2 thin films prepared by sputtering," Applied Catalysis B: Environmental 25 (2000) 83-92

[Einaga99] H. Einaga, S. Futamura, T. Ibusuki, "Photocatalytic decomposition of benzene over TiO_2 in a humidified airstream," Physical Chemistry Chemical Physics 1 (1999) 4903-4908

[Einaga02] H. Einaga, S. Futamura, T. Ibusuki, "Heterogeneous photocatalytic oxidation of benzene, toluene, cyclohexene and cyclohexane in humidified air: comparison of decomposition behavior on photoirradiated TiO_2 catalyst," Applied Catalysis B: Environmental 38 (2002) 215-225

[Eurocat97] Applied Catalysis A 157 (1997), special issue

[Fallet06] M. Fallet, S. Permpoon, J.L. Deschanvres, M. Langlet, "Influence on the physico-structural properties on the photocatalytic activity of sol-gel derived TiO_2 thin films," Journal of Materials Science 41 (2006) 2915-2927

[Fernández95] A. Fernández, G. Lassaletta, V.M. Jiménez, A. Justo, A.R. González-Elipe, J.-M. Herrmann, H. Tahiri, Y. Ait-Ichou, "Preparation and characterization of TiO_2 photocatalysts supported on various rigid supports (glass, quartz and stainless steel). Comparative studies of photocatalytic activity in water purification," Applied Catalysis B: Environmental 7 (1995) 49-63

[Fernández-García04] M. Fernández-García, A. Martínez-Arias, J.C. Hanson, J.A. Rodriguez, "Nanostructured Oxides in Chemistry: Characterization and Properties," Chem. Rev. 104 (2004) 4063-4104

[Franch04] M.I. Franch, J.A. Ayllón, J. Peral; X. Doménech, "Fe(III) photocatalyzed degradation of low chain carboxylic acids implications of the iron salt," Applied Catalysis B: Environmental 50 (2004) 89-99

[Fujishima72] A. Fujishima, K. Honda, "Electrochemical Photolysis of Water at a Semiconductor Electrode," Nature 238 (1972) 37-38

[Fujishima00] A. Fujishima, T.N. Rao, D.A. Tryk, "Titanium dioxide photocatalysis," Journal of Photochemistry and Photobiology C: Photochemistry Reviews 1 (2000) 1-21

[Gao04] W. Gao, C.M. Wang, H.Q. Wang, V.E. Henrich, E.I. Altman, "Growth and surface structure of vanadium oxide on anatase (001)," Surface Science 559 (2004) 201-213

[Gao06] W. Gao, E.I. Altman, "Growth and structure of vanadium oxide on anatase (101) terraces," Surface Science 600 (2006) 2572-2580

[Greenwood84] N.N. Greenwood and A. Earnshaw, "Chemistry of the elements," Pergamon Press, Oxford, (1984)

[Guan05] K. Guan, "Relationship between photocatalytic activity, hydrophilicity and self-cleaning effect of TiO_2/ SiO_2 thin films," Surface Coatings and Technology 191 (2005) 155-160

[Hashimoto02] S. Hashimoto, A. Tanaka, "Alteration of Ti 2p XPS spectrum for titanium oxide by low-energy Ar-ion bombardment," Surface and Interface Analysis 34 (2002) 262-265

[Hattori00] A. Hattori, T. Kawahara, T. Uemoto, F. Suzuki, H. Tada, S. Ito, "Ultrathin SiO_x Fil; Coating Effect on the Wettability Change of TiO_2 Surfaces in the Presence and Absence of UV light Illumination," Journal of Colloid and Interface Science 232 410-413 (2000)

[Hong05] N. H. Hong, J. Sakai, W. Prellier, A. Ruyter, "Room temperature ferromagnetism in anatase $TiO_{0.95}V_{0.5}O_2$ thin films," Physica B 355 (2005) 295-298

[Hove06] M.A. Hove, “From surface science to nanotechnology,” Catalysis Today 113 (2006) 133-140

[Ihara03] T. Ihara, M. Miyoshi, Y. Iriyama, O. Matsumoto, S. Sugihara, “Visible-light-active titanium oxide photocatalyst realized by an oxygen-deficient structure and by nitrogen doping,” Applied Catalysis B: Environmental 42 (2003) 403-409

[Iketani04] K. Iketani, R.-D. Sun, M. Toki, K. Hirota, O. Yamaguchi, “Sol-gel-derived $V_xTi_{1-x}O_2$ films and their photocatalytic activities under visible light irradiation,” Materials Science and Engineering B 108 (2004) 187-193

[Ismail03] A. A. Ismail; I.A. Ibrahim, R. M. Mohamed, “Sol-gel synthesis of vanadia-silica for photocatalytic degradation of cyanide,” Applied Catalysis B: Environmental 45 (2003) 161-166

[Ismat Shah02] S. Ismat Shah, W. Li, C.P. Huang, C. Ni, “Study of Nd^{3+}, Pd^{2+}, Pt^{4+}, Fe^{3+} dopant effect on photoreactivity of TiO_2 nanoparticles,” PNAS (Proceedings of the National Academy of Sciences) 99, suppl. 2 (2002) 6482-6486

[Janssen05] Els Janssen, “Fotokatalytische activiteit van dunne TiO_2-filmen,” Proefschrift Licenciat, Ghent University, Ghent, Belgium (2005)

[Jung99] K.Y. Jung, S.B. Park, “Anatase-phase titania: preparation by embedding silica and photoactivity for the decomposition of trichloroethylene,” Journal of Photochemistry and Photobiology A: Chemistry 127 (1999) 117-122

[Jung02] K.Y. Jung, S.B. Park, S.-K. Ihm, “Linear relationship between the crystallite size and the photoactivity of non-porous titania ranging from nanometer to micrometer size,” Applied Catalysis A: General 224 (2002) 229-237

[Jung04] K.Y. Jung, S.B. Park, “Photoactivity of SiO_2/TiO_2 and ZrO_2/TiO_2 mixed oxides prepared by sol-gel method,” Materials Letters 58 (2004) 2897-2900

[Jung05] S.-C. Jung, S.-J. Kim, N. Imaishi, Y.-I. Cho, “Effect of TiO_2 thin film thickness and specific surface area by low-pressure metal-organic chemical vapor deposition on photocatalytic activities,” Applied Catalysis B: Environmental 55 (2005) 253-257

[Kamei00] M. Kamei, T. Mitsuhashi, "Hydrophobic drawings on hydrophilic surface of single crystalline titanium dioxide: surface wettability control by mechanochemical treatment," Surface Science 463 (2000) L609-L612

[Karches02] M. Karches, M. Morstein, P.R. von Rohr, R.L. Pozzo, J.L. Giombi, M.A. Baltanás, “Plasma CVD-coated glass beads as photocatalyst for water decontamination,” Catalysis Today 72 (2002) 267-279

[Katsumata06] K.-I. Katsumata, A. Nakajima, T. Shiota, N. Yoshida, T. Watanabe, Y. Kameshima, K. Okada, “Photoinduced surface roughness variation in polycrystalline TiO_2 thin films,” Journal of Photochemistry and Photobiology A: Chemistry 180 (2006) 75-79

[Kim02a] S.B. Kim, S.C. Hong, “Kinetic study for photocatalytic degradation of volatile organic compounds in air using thin film TiO_2 photocatalyst,” Applied Catalysis B: Environmental 35 (2002) 305-315

[Kim02b] B. Kim, D. Byun, J.K. Lee, D. Park, “Structural Analysis on Photocatalytic Efficiency of TiO_2 by Chemical Vapor Deposition,” Japanese Journal of Applied Physics 41 (2002) 222-226

[Kim02c] S.-H. Kim, Y.-L. Choi, Y.-S. Song, D. Y. Lee, S.-J. Lee, "Influence of sputtering parameters on microstructure and morphology of TiO_2 thin films," Materials Letters, 57 (2002) 343-348

[Kinbara92] A. Kinbara, E. Kusano, S. Baba "TiO_x film formation process by reactive sputtering," Journal of Vacuum Science and Technology A 10 [4], Jul/Aug 1992, 1483-1487

[Kominami03] H. Kominami, Y. Ishii, M. Kohno, S. Konishi, Y. Kera, B. Ohtani, "Nanocrystalline brookite-type titanium (IV) oxide photocatalysts prepared by a solvothermal method: correlation between their physical properties and photocatalytic activities," Catalysis Letters 91 [1-2] (2003) 41-47

[Li 02] W. Li, S. Ismat Shah, C.-P. Huang, O. Jung, C. Ni, "Metallorganic chemical vapor deposition and characterization of TiO_2 nanoparticles," Materials Science and Engineering B 96 (2002) 247-253

[Lichtin98] N.N. Lichtin, M. Sadeghi, "Oxidative photocatalytic degradation of benzene vapor over TiO_2," Journal of Photochemistry and Photobiology A: Chemistry 113 (1998) 81-88

[Lindic05] M.-H. Lindic, B. Pecquenard, P. Vinatier, A. Levasseur, H. Martinez, D. Gonbeau, P.-E. Petit, G. Ouvrard, "Characterization of fr sputtered TiO_yS_z thin films," Thin Solid Films 484 (2005) 113-123

[Linsebigler95] A. L. Linsebigler, G. Lu, J. T. Yates Jr, "Photocatalysis on TiO_2 Surfaces: Principles, Mechanisms and Selected Results," Chem. Rev. 95 (1995) 735-758

[Liu05] B. Liu, X. Zhao, Q. Zhao, C. Li, X. He, "The effect of O_2 partial pressure on the structure and photocatalytic property of TiO_2 films prepared by sputtering," Materials Chemistry and Physics 90 (2005) 207-212

[Liu06] B. Liu, X. Zhao, L. Wen, "The structural and photoluminescence studies related to the surface of the TiO_2 sol prepared by wet chemical method," Materials Science and Engineering B 134 (2006) 27-31

[Long06] M. Long, W. Cai, Z. Wang, G. Liu "Correlation of electronic structures and crystal structures with photocatalytic properties of undoped, N-doped and I-doped TiO_2," Chemical Physics Letters 420 (2006) 71-76

[Lowekamp98] J.B. Lowekamp, G.S. Rohrer, P.A. Morris Hotsenpiller, J.D. Bolt, W.E. Farneth "The Anisotropic Photochemical Reactivity of Bulk TiO_2 Crystals," The Journal of Physical Chemistry B 102 (1998) 7323-27

[Madhusudan Reddy02] K. Madhusudan Reddy, Sunkara V. Manorama, A. Ramachandra Reddy, "Bandgap studies on anatase titanium dioxide nanoparticles," Materials Chemistry and Physics 78 (2002) 239-245

[Mahieu06a] PhD Thesis, Ghent University, Ghent, Belgium (2006)

[Mahieu06b] S. Mahieu, P. Ghekiere, D. Depla, R. De Gryse, "Biaxial alignment in sputter deposited thin films," Thin Solid Films 515 (2006) 1229-1249

[Marin2000] G.B. Marin, Cursus Chemische Reactoren 1&2, Ghent University, Ghent, Belgium, (2000)

[Manifacier76] J.C. Manifacier, J. Gasiot, J.P. Fillard, "Simple method for determination of optical-constants n, k and thickness of a weakly absorbing thin film," Journal of Physics E: Scientific Instruments 9 (1976) 1002-1004

[Martin97] N. Martin, C. Rousselot, D. Rondot, F. Palmino, R. Mercier, "Microstructure modification of amorphous titanium oxide thin films during anneal treatment," Thin Solid Films 300 (1997) 113-121

[Martin01] N. Martin, A.M. Santo, R. Sanjinés, F. Lévy, "Energy distribution of ions bombarding TiO_2 thin films during sputter deposition," Surface and Coatings Technology 138 (2001) 77-83

[Mathieu78] H. Mathieu, J. Pascual, J. Camassel, "Uniaxial stress dependence of the direct-forbidden and indirect-allowed transition of TiO_2," Physical Review B 18 [12] (1978) 6920-6929

[Martra99] G. Martra, S. Coluccia, L. Marchese, V. Augugliaro, V. Loddo, L. Palmisano, M. Schialvello, "The role of H_2O in the photocatalytic oxidation of toluene in vapor phase on anatase TiO_2 catalyst A FTIR study," Catalysis Today 53 (1999) 695-702

[Miao02] L. Miao, P. Jin, K. Kaneko, S. Tanemura, "Sputter deposition of polycrystalline and epitaxial TiO_2 films with anatase and rutile structure," Proceedings of the Advanced Nanomaterials and Nanodevices (IUMRS-ICEM), Xi'an, China 10-14 June 2002, 943-963

[Miao05] L. Miao, S. Tanemura, H. Watanabe, S. Toh, K. Kaneko, "Structural and compositional characterization of N_2-H_2 plasma surface treated TiO_2 thin films," Applied Surface Science 244 (2005) 412-417

[Mills97] A. Mills, S. Le Hunt, "An overview of semiconductor photocatalysis," Journal of Photochemistry and Photobiology A: Chemistry 108 (1997) 1-35

[Mills02] A. Mills, N. Elliot, I.P Parkin, S. O'Neill, R. J. Clark, "Novel TiO_2 CVD films for semiconductor photocatalysis," Journal of Photochemistry and Photobiology A: Chemistry 151 (2002) 171-179

[Mills03] A. Mills, A. Lepre, N. Elliot, S. Bhopal, I.P. Parkin, S.A. O'Neill, "Characterisation of the photocatalyst Pilkington Activ^{TM}: a reference film photocatalyst?", Journal of Photochemistry and Photobiology A: Chemistry 160 (2003) 213-224

[Miyagi04] T. Miyagi, M. Kamei, T. Mitsuhashi, T. Ishagashi, A. Yamazaki, "Charge separation at the rutile/anatase interface: a dominant factor of photocatalytic activity," Chemical Physics Letters, 390 (2004) 399-402

[Möller01] W. Möller, "Fundamentals of Ion-Surface Interaction," Short resume of a lecture held at the Technical University of Dresden, Issue Winter 2001/2002

[Monticone00] S. Monticone, R. Tufeu, A.V. Kanaev, E. Scolan, C. Sanchez, "Quantum size effect in TiO_2 nano particles: does it exist?," Applied Surface Sciences 162-163 (2000) 565-570

[Moradi91] M. Moradi, C. Nender, S. Berg, H-O. Blom, A. Belkind, Z. Orban, "Modelling of multicomponent reactive sputtering," Journal of Vacuum Science and Technology A 9 [3], May/ Jun 1991, pp. 619-624

[Miyashita03] K. Miyashita, K. Tokuda, T. Ubukata, "Photo-catalytic oxidation and hydrophilicity of sputter-deposited Si-overlayer on TiO_2 film," Proceedings of *The Seventh International Symposium on Sputtering and Plasma Process (ISSP 2003)*, Kanazawa Institute of Technology, Kanazawa, Japan, June 11-13, 2003, 202-205

[Nakamura00a] M. Nakamura, T. Aoki, Y. Hatanaka, D. Korzec, J. Engemann, "Comparison of hydrophilic properties of amorphous TiO_x films obtained by radio frequency sputtering and plasma-enhanced chemical vapor deposition," J. Mater. Res. 16 [2] (2000) 621-626

[Nakamura00b] M. Nakamura, T. Aoki, Y. Hatanaka, “Hydrophilic characteristics of r.f.-sputtered amorphous TiO_2 film,” Vacuum 59 (2000) 506-513

[Nam04] H.-J. Nam, T. Amemiya, M. Murabayashi, K. Itoh, “Photocatalytic activity of Sol-Gel TiO_2 Thin Films on Various Kinds of Glass Substrates: The Effects of Na^+ and Primary Particle Size,” Journal of Physical Chemistry B 108 (2004) 8254-8259

[NIST] National Institute of Standards and Technology, U.S.A., www.nist.gov

[Ohno01] T. Ohno, K. Sarukawa, K. Tokieda, M. Matsumura, “Morphology of a TiO_2 Photocatalyst (Degussa, P-25) Consisting of Anatase and Rutile Crystalline Phases,” Journal of Catalysis 203 (2001) 82-86

[Ohno03] T. Ohno, K. Tokieda, S. Higashida, M. Matsumara, “Synergism between rutile and anatase TiO_2 particles in photocatalytic oxidation of naphthalene,” Applied Catalysis A: General 244 (2003) 383-391

[Ohno04] T. Ohno, M. Akiyoshi, T. Umebayashi, K. Asai, T. Mitsui, M. Matsumara, “Preparation of S-doped TiO_2 photocatalysts and their photocatalytic activities under visible light,” Applied Catalysis A: General 265 (2004) 115-121

[Ohsaki99] H. Ohsaki, Y. Tachibana, A. Hayashi, A. Mitsui, Y. Hayashi ,"High rate sputter deposition of TiO_2 from TiO_{2-x} target," Thin Solid Films, 351 (1999) 57-60

[Ohsaki01] H. Ohsaki, Y. Tachibana, A. Mitsui, T. Kamiyama, Y. Hayashi, “High rate deposition of TiO_2 by DC sputtering of the TiO_{2-x} target,” Thin Solid Films 392 (2001) 169-173

[Okimura01] K. Okimura, “Low temperature growth of rutile TiO_2 thin films in modified r.f. magnetron sputtering,” Surface and Coatings Technology 135 (2001) 286-290

[Pankove71] J.I. Pankove, Optical processes in semiconductors, Dover Publications, Inc., New York (1971)

[Persoone05] P. Persoone, S. Diericks, S. Luys, W. De Bosscher, “Sputter deposited titanium oxide coatings for plasma display filters,” Proceedings of the 48th Annual Technical Conference of the Society of Vacuum Coaters, Denver, Co, April 23-28 (2005) 180-183

[Pfeiffer02] Mass Spectrometer, Sales and information brochure, Pfeiffer Vacuum Inc, Nashua, NH (2002)

[Poelman03] D. Poelman, Ph.F. Smet, “Methods for the determination of the optical constants of thin films from single transmission measurements: a critical review,” Journal of Physics D: Applied Physics 36 (2003) 1850-1857

[Poelman04] H. Poelman, H. Tomaszewski, D. Poelman, D. Depla, R. De Gryse “Effect of the oxygen deficiency of ceramic TiO_{2-x} targets on the deposition of TiO_2 thin films by DC magnetron sputtering,” Surface and Interface Analysis 36 [8] (2004) 1167-1170

[Prabakar06] K. Prabakar, T. Takahashi, T. Nezuka, T. Nakashima, Y. Kubota, A. Fujishima, “Effect of nitrogen on the photocatalytic activity of TiO_XN_Y thin films,” Journal of Vacuum Science and Technology A 24 [4] (2006) 1156-1160

[Safi00] I. Safi, “Recent aspects concerning DC reactive magnetron sputtering of thin films: a review,” Surface and Coatings Technology 127 (2000) 203-219

[Sakai98] N. Sakai, R. Wang, A. Fujishima, T. Watanabe, K. Hashimoto, “Effect of Ultrasonic Treatment on Highly Hydrophilic TiO_2 Surfaces,” Langmuir 14 (1998) 5918-5920

[Sakthivel06] S. Sakthivel, M.S. Hidalgo, D.W. Bahnemann, S.-U. Geissen, V. Murugesan, A. Vogelpohl, "A fine route to tune the photocatalytic activity of TiO_2," Applied Catalysis B: Environmental 63 (2006) 31-40

[Salinaro99] A. Salinaro, A.V. Emeline, J. Zhao, H. Hidaka, V.K. Rybabchuk, N. Serpone, "Terminology, relative photonic efficiencies and quantum yields in heterogeneous photocatalysis. Part II: Experimental determination of quantum yields," Pure & Applied Chemistry 71 [2] (1999)321-335

[Serpone99] N. Serpone, A. Salinaro, "Terminology, relative photonic efficiencies and quantum yields in heterogeneous photocatalysis. Part I: Suggested Protocol," Pure & Applied Chemistry 71 [2] (1999)303-320

[Schiavello97], "Heterogeneous photocatalysis," Wiley Series in Photoscience and Photoengineering, volume 3, M. Schiavello (ed), John Wiley & Sons, Chichester (1997)

[Schiller97] S. Schiller, V. Kirchoff, F. Milde, M. Fahland, N. Schiller, "Pulsed Plasma Activated Deposition of Plastic films," Society of Vacuum Coaters, 40th Annual technical Conference Proceedings (1997), 327-332

[Schiller80] S. Schiller, G. Beister, S. Schneider, W. Sieber, "Features of *in situ* measurements on absorbing TiO_x films produced by reactive d.c. magnetron-plasmatron sputtering," Thin Solid Films 72 (1980) 475-483

[Schroder98] D. K. Schroder, "Semiconductor material and device characterization," 2nd ed. John Wiley & Sons, New York (1998)

[Segers03] A. Segers, D. Depla, K. Eufinger, J. Haemers, R. De Gryse, "Instabilities in the Reactive Sputtering of Electrical Insulating Compounds," BELVAC News. 19: (4) (2003) 28-41

[Smith94] "Thin Film Deposition, Principles and Practice," Chap. 5: Deposition, pp. 119-219, by Donald L. Smith, McGraw-Hill, Inc., New York (1994)

[Sproul05] W.D. Sproul, D.J. Christy, D.C. Carter, "Control of reactive sputtering processes," Thin Solid Films 491 (2005) 1-17

[Software1] CaRIne Crystallography, Divergent S.A., France

[Software2] Quadstar 32 bit, mass spectrometer software, Pfeiffer Vacuum Inc, Nashua, NH (2003)

[Swanepoel83] R. Swanepoel, "Determination of the thickness and optical-constants of amorphous-silicon," Journal of Physics E: Scientific Instruments 16 (1983) 1214-1222

[Tachibana00] Y. Tachibana, H. Ohasaki, A. Hayashi, A. Mitsui, Y. Hayashi, "TiO_{2-x} sputter for high rate deposition of TiO_2," Vacuum 59 (2000) 836-843

[Tada97] H. Tada, M. Tanaka, "Dependence of TiO_2 Photocatalytic Activity upon Its Film Thickness," Langmuir 13 (1997) 360-364

[Takahashi02] T. Takahashi, H. Nakabashi, W. Mizuno, "Effects of plasma exposure on structural and optical properties of TiO_2 films deposited by off-axis target sputtering," Journal of Vacuum Science and Technology A 20 [6] (2002) 1916-1920

[Takahashi06] T. Takahashi, K. Prabakar, T. Nezuka, T. Yamazaki, T. Nakashima, Y. Kubota, A. Fujishima, "Sputtering pressure dependent photocatalytic properties of TiO_2 thin films," Journal of Vacuum Science and Technology A 24 [4] (2006) 1161-1165

[Takeda01] S. Takeda, S. Suzuki, H. Odaka, H. Hosono, "Photocatalytic TiO_2 thin film deposited onto glass by DC magnetron sputtering," Thin Solid Films 392 (2001) 338-344

[Takenaka97] S. Takenaka, T. Tanaka, T. Funabiki, S. Yoshida, "Reaction mechanism of photooxidation of propane over alkali-metal-ion-modified silica-supported vanadium pentoxide under irradiation by visible light," Journal of the Chemical Society, Faraday Transactions 93 [23] (1997) 4151-4158

[Takeshita06] K. Takeshita, A. Yamakata, T.-A. Ishibashi, H. Onishi, K. Nishijima, T. Ohno, "Transient IR study of charge carriers photogenerated in sulfur-doped TiO_2," Journal of Photochemistry and Photobiology A: Chemistry 177 (2006) 269-275

[Tanemura05] S. Tanemura, L. Miao, H. Watanabe, Y. Mori, "Spectroscopic ellipsometry study on TiO_2 thin films modified by N_2-H_2 plasma surface treatment," Applied Surface Science 244 (2005) 546-549

[Thornton77] J. A. Thornton, "High rate thick film growth," Annual Reviews in Materials Science 7 (1977) 239-260

[Thornton78] J.A. Thornton, A.S. Penfold, "Cylindrical Magnetron Sputtering," pp. 75-113 in *Thin Film Processes*, edited J.L. Vossen, W.Kern, Academic Press Inc. (1978)

[Tjong04] S.C. Tjong, H. Chen, "Nanocrystlline materials and coatings," Materials Science and Engineering R 45 (2004) 1-88

[Tokita03] S. Tokita, N. Tanaka, S. Ohshio, H. Saitoh, "Photoinduced Surface Reaction of Highly Oriented Anatase Polycrystalline Films Synthesized Using a CVD Apparatus Operated in Atmospheric Pressure Regime," Journal of the Ceramic Society of Japan 111 [6] (2003) 433-435

[Tomaszewski03] H. Tomaszewski, H. Poelman, D. Depla, D. Poelman, R. De Gryse, L. Fiermans, M.F. Reyniers, G. Heynderickx, G.B. Marin "TiO_2 films prepared by DC magnetron sputtering from ceramic targets," Vacuum 68 (2003) 31-38

[Tomaszewski04] Personal communications Henry Tomaszewski

[Vale06] A. Vale, N. Chaure, M. Simonds, A.K. Ray, N. Bricklebank, "Sputtered rutile stoichiometric TiO_2 nanocrystalline films," Journal of Material Science: Materials in Electronics 17 (2006) 851-855

[Valentin05] C. Di Valentin, G. Pacchioni, A. Selloni, S. Livraghi, E. Giamello, "Characterization of paramagnetic species in N-doped TiO_2 powders by EPR spectroscopy and DFT calculations," Journal of Physical Chemistry B 109 [23] (2005) pp11414 (Abstract)

[Vancoppenolle99] V. Vancoppenolle, P.Y. Jouan, M. Wautelet, J.-P. Dauchot, M. Hecq "Glow discharge mass spectrometry study of the deposition of TiO_2 thin films by direct current reactive magnetron sputtering of a Ti target," Journal of Vacuum Science and Technology A 17 (6) Nov/Dec (1999) 3317-3321

[Vittadini05] A. Vittadini, M. Casarin, M. Sambi, A. Selloni, "First-principle studies of vanadia-titania catalysts: Beyond the monolayer," Journal of Physical Chemistry B 109 [46] (2005) pp21766-21771 (Abstract)

[Vorontsov04] A.V. Vorontsov, V.P. Dubovitskaya, "Selectivity of photocatalytic oxidation of gaseous ethanol over pure and modified TiO_2," Journal of Catalysis 221 (2004) 102-109

[Wada98] K. Wada, H. Yamada, Y. Watanabe, T.-a. Mitsudo, "Selective photo-assisted catalytic oxidation of methane and ethane to oxygenates using supported vanadium oxide catalysts," Journal of the Chemical Society, Faraday Transactions 94 [12] (1998) 1771-1778

[Wang2004] Q. Wang, G. Lan, E. C. Dikey, "Grain boundary segregation in yttrium-doped polycrystalline TiO_2," Acta Materialia 52 (2004) 809-820

[Wang05a] Y. Wang, D.J. Doren, "First-principle calculations on TiO_2 doped by N, Nd, and vacancy," Solid State Communications 136 (2005) 186-189

[Wang05b] Y. Wang, D.J. Doren, "Electronic structures of V-doped anatase TiO_2," Solid States Communications 136 (2005) 142-146

[Wang06a] S.-F. Wang, Y.-F. Hsu, Y.-S. LEE, "Microstructural evolution and optical properties of doped TiO_2 films prepared by RF magnetron sputtering," Ceramics International 32 (2006) 121-125

[Wang06b] X.H. Wang, J.G. Li, H. Kamiyama, T. Ishigaki, "Fe-doped TiO_2 nanopowders by oxidative pyrolysis of organometallic precursors in induction thermal plasma: synthesis and structural characterization," Thin Solid Films 506-507 (2006) 278-282

[Weibel06a] A. Weibel, R. Bouchet, P. Knauth, "Electrical properties and defect chemistry of anatase (TiO_2)," Solid State Ionics 177 (2006) 229-236

[Weibel06b] A. Weibel, R. Bouchet, P. Bouvier, P. Knauth, "Hot compaction of nanocrystalline TiO_2 (anatase) ceramics. Mechanism of densification: Grain size and doping effects," Acta Materialia (2006) 3575-3583

[Weinberger95] B.R. Weinberger, R.B. Garber, "Titanium dioxide photocatalysts produced by reactive magnetron sputtering," Applied Physics Letters 66 [18] (1995) 2409-2411

[Westwood03] W. Westwood, "Sputter deposition," volume #2 of the AVS Education Committee Book Series, (2003)

[Wikipedia1] http://en.wikipedia.org/wiki/Ion_implantation

[Wikipedia2] http://en.wikipedia.org/wiki/Mesopore, /Macropore, /Micropore

[Wong06] M.-S. Wong, H.P. Chou, T.-S. Yang, "Reactively sputtered N-doped titanium oxide films as visible light photocatalyst," Thin Solid Films 494 (2006) 244-249

[Wunderlich04a] W. Wunderlich, T. Oeckermann, L. Miao, N.T. Hue, S. Tanemura, M. Tanemura, "Electronic roperties of Nano-porous TiO_2- and ZnO-Thin Films – comparison of simulations and experiments," Journal of Ceramic Processing Research 5 [4] (2004) 343-354

[Wunderlich04b] W. Wunderlich, L. Miao, M. Tanemura, S. Tanemura, P. Jin, K. Kaneko, A. Terai, N. Nabatova-Gabin, R. Belkada, "Ab-initio calculations of the Optical band-gap of TiO_2 thin films," International journal of Nanoscience 3 [4-5] (2004) 439-445

[www1] www.almazoptics.com/TiO_2.htm

[www2] www.shinkosha.com/e/new_material/nm09_e.htm

[www3] http://www.ee.ucl.ac.uk/~mflanaga/java/RefractiveIndex.html#lore

[www4] http://www.leb.e-technik.uni-erlangen.de/lehre/mm/html/implant.htm

[Yamagishi03] M. Yamagishi, S. Kuriki, Y. Shigesato, "Thin film TiO_2 photocatalyst deposited by reactive magnetron sputtering," Thin Solid Films 442 (2003) 227-231

[Yamashita02] H. Yamashita, M. Harada, J. Misaka, M. Takeuchi, K. Ikeue, M. Anpo, "Degradation of propanol diluted in water under visible light irradiation using metal ion-implanted titanium dioxide photocatalysts," Journal of Photochemistry and Photobiology A: Chemistry 148 (2002) 257-261

[Yamashita03] H. Yamashita, M. Harada, J. Misaka, M. Takeuchi, B. Neppolian, M. Anpo, "Photocatalytic degradation of organic compounds in water using visible light-responsive metal ion-implanted TiO_2 catalysts: Fe ion-implanted TiO_2," Catalysis Today 84 (2003) 191-196

[Yates06] H.M. Yates, M.G. Nolan, D.W. Sheel, M.E. Pemble, 'The role of nitrogen doping on the development of visible light-induced photocatalytic activity in thin TiO_2 films grown on glass by chemical vapour deposition," Journal of Photochemisty and Photobiology A: Chemistry 179 (2006) 213-223

[Yin04] S. Yin, H. Hasegawa, D. Maeda, M. Ishitsuka, T. Sato, "Synthesis of visible-light-active nanosized titania photocatalyst by low temperature dissolution-reprecipitation process," Journal of Photochemistry and Photobiology A: Chemistry 163 (2004) 1-8

[Zallen06] R. Zallen, M.P. Moret, "The optical absorption edge of brookite TiO_2," Solid States Communications 137 (2006) 154-157

[Zeman02] P. Zeman, S. Takabayashi, "Effect of total and oxygen partial pressures on structure of photocatalytic TiO_2-films sputtered on unheated substrate," Surface and Coatings Technology 153 (2002) 93-99

[Zeman03] P. Zeman, S. Takabayashi, "Nano-scaled photocatalytic TiO_2 thin films prepared by magnetron sputtering," Thin Solid Films 433 (2003) 57-62

[Zhang03a] W. Zhang, Y. Li, SH. Zhu, F. Wang, "Fe-doped photocatalytic TiO_2 film prepared by pulsed dc reactive magnetron sputtering," Journal of Vacuum Science and Technology A 21 [6] (2003) 1877-1879

[Zhang03b] W. Zhang, Y. Li, S. Zhu, F. Wang, "Surface modification of TiO_2 film by iron doping using reactive magnetron sputtering," Chemical Physics Letters 373 (2004) 333-337

[Zhang03c] W. Zhang, Y.L. Shenglong Zhu, F. Wang, "Surface modification of TiO_2 thin film by iron doping using reactive magnetron sputtering," Chemical Physics Letters 373 (2003) 333-337

[Zhang04] W. Zhang, Y. Li, S. Zhu, F. Wang, "Influence of argon flow rate on TiO_2 photocatalyst film deposited by dc reactive magnetron sputtering," Surface and Coatings Technology 182 (2004) 192-198

[Zheng01] S.K. Zheng, T.M. Wang, G. Xiang, C. Wang, "Photocatalytic activity of nanostructured TiO2 thin films prepared by dc magnetron sputtering method," Vacuum 62 (2001) 361-366

[Zielinska2005] B. Zielińska, A.W. Moraski, "TiO_2 photocatalyst promoted by alkali metals," Applied Catalysis B: Environmental 55 (2005) 221-226

[Zhu05] K.-R. Zhu, M.-S. Zhang, J.-M. Hong, Z. Yin, "Size effect on phase transition sequence of TiO_2 nanocrystal," Materials Science and Engineering A 403 (2005) 87-93

Faculteit Wetenschappen
Vakgroep Vaste-stofwetenschappen
Krijgslaan 281 S1
9000 Gent